Faculty of Mathematics and Physics
Charles University
Prague

Olena Gamaliy

Hyperfine interactions in magnetic iron oxides with nonmagnetic substitutions

Doctoral Thesis

2006

Contents

1. Introduction

Magnetic materials, including magnetic iron oxides, are important for different technical applications as well as for basic research in condensed matter field. Their physical properties can be sufficiently affected by the presence of defects or substitutions.

Experimental techniques utilizing hyperfine interactions for study of electronic and magnetic structures of solids are usually greatly appreciated for a possibility of microscopic characterization since hyperfine parameters depend on a nearest neighbourhood of an ion with a studied nucleus. The method offering the best resolution is the Nuclear Magnetic Resonance (NMR). It provides possibility to study separately resonant responses corresponding to different crystallographic positions in a given structure.

Proposed thesis is focused on the study of hyperfine interactions in magnetic iron oxides by means of NMR technique. The thesis takes into consideration two basic magnetic iron oxides: yttrium iron garnet (YIG, chemical formula $Y_3Fe_5O_{12}$) and magnetite (Fe_3O_4). The matter of interest is hyperfine interactions in nominally pure materials as well as the changes induced in the systems in question by substitutions in different crystallographic positions. The goal is to investigate changes in NMR spectra and relaxations induced by different substitutions and to contribute to explanation of the influence of the substitutions on the change of hyperfine parameters and some macroscopic properties of the materials.

YIG contains two magnetic sublattices constituted by trivalent iron cations and has rather simple temperature dependence of structural and magnetic properties in contrast to the magnetite. As a result, this compound is a very suitable test system for a verification of general and specific models dealing with the influence of substitutions on hyperfine interactions. The present thesis investigates NMR spectra of thin epitaxial films of yttrium iron garnets containing diamagnetic substitutions (Al^{3+}, In^{3+}, La^{3+}, Ca^{2+}, Bi^{3+}) in different crystallographic positions. The spin-lattice and spin-spin relaxations in substituted systems were systematically studied too. In addition, the first NMR study of completely substituted BiIG is presented.

Magnetite is probably the first magnetic material which has been used by mankind since 1500 B.C. It contains two magnetic sublattices. Structural unit of the pure magnetite is rather simple since it has only two types of atoms: iron and oxygen. However, as the chemical formula

of magnetite implies two trivalent and one bivalent iron cations the issues related to valencies of iron ions and a charge ordering arise in this system. At the specific temperature known as the Verwey temperature [Verw41] magnetite undergoes a phase transition. Despite a long time (more than 60 years) that has passed since this transition was discovered, the nature of it is not completely understood. The character of the transition and some properties of magnetite below and above the transition are strongly affected by defects and substitutions present in a sample. Therefore, a systematic study of substitution effects on magnetite could lead to a better understanding of magnetite system in general and particularly the nature of the Verwey transition itself. In the thesis the results of NMR study of magnetites with diamagnetic substitutions of Al and Ga are presented. The studied substitutions in magnetites preferentially occupy different crystallographic positions.

The thesis consists of 5 chapters. Following the Introduction (Chapter1), the Chapter 2 concerns principles of NMR technique in magnetically ordered systems. The next Chapter 3 embraces general properties and preceding NMR investigations of studied magnetic oxides: yttrium iron garnets and magnetites. The new experimental results obtained within the work on the thesis, their interpretation and discussion are comprised in Chapter 4. This chapter is supplemented with running recapitulations of the results on studied garnets (paragraph 4.1.5) and magnetites (paragraph 4.2.5). In the Summary of the thesis (Chapter 5), the main results are summarized. The thesis is also supplemented with References to the mentioned literature and the list of author's articles in Appendix.

2. NMR in magnetically ordered systems

2.1. Principles of NMR

Let us consider an isolated nucleus having magnetic moment **μ:**

$$\mu = \gamma \hbar I \tag{2.1.1}$$

where γ is gyromagnetic ratio, $\hbar$ is Planck's constant, ***I*** is a spin of the nucleus.

The application of the magnetic field $\boldsymbol{B_0}$ produces interaction energy of the nucleus of amount $-\boldsymbol{\mu B_0}$. Taking the field $\boldsymbol{B_0}$ to be along the z-direction, we find corresponding Hamiltonian in the form:

$$\hat{H} = -\gamma \hbar B_0 I_z \tag{2.1.2}$$

The corresponding eigenvalues of this Hamiltonian are

$$E = -\gamma \hbar B_0 m, \qquad m = I, I-1, \ldots, -I \tag{2.1.3}$$

In the case of ^{57}Fe nucleus which has spin I=1/2 the energy levels are illustrated in the Fig. 2.1.1. The energy distance between levels is $\gamma \hbar B_0$.

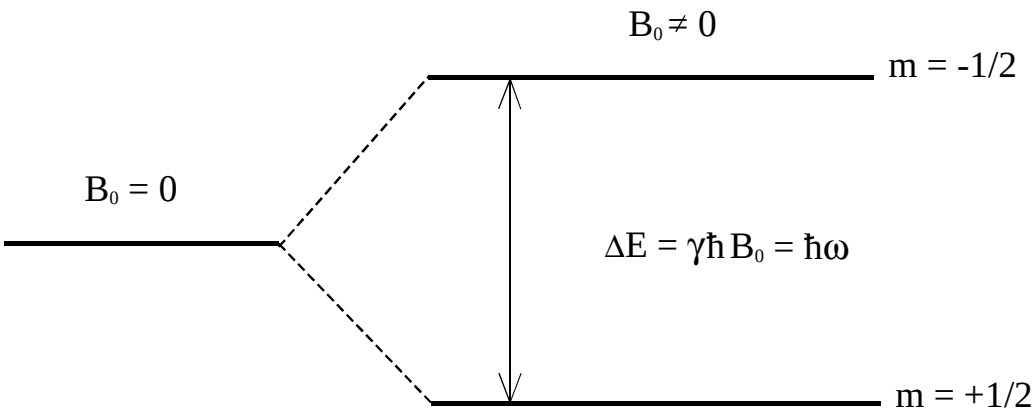

Figure 2.1.1. Energy levels of the ^{57}Fe nucleus in the magnetic field B_0.

To detect the presence of such set of levels one need to have an interaction that can cause transition between levels. The coupling used to produce magnetic resonance is an alternating magnetic field applied perpendicular to the static field.

The condition for the resonance is

$$\omega = \gamma B_0 \tag{2.1.4}$$

The equation of motion of the nucleus magnetic moment in the external generally time dependent magnetic field can be written in the form:

$$\frac{d\boldsymbol{\mu}}{dt} = \gamma [\boldsymbol{\mu} \times \boldsymbol{B}] \tag{2.1.5}$$

In the case when we are dealing with NMR in condensed matter, the total magnetization of nuclei in the unit volume is considered.

$$\boldsymbol{m} = \frac{1}{V} \sum_j \boldsymbol{\mu}_j \tag{2.1.6}$$

In condensed matter, a nucleus magnetic moment cannot be considered as an isolated moment. It is necessary now to take into account interactions inside nuclei system and between the nuclei moments and the other systems in the matter, widely called 'lattice'. Corresponding phenomenological equations of motion for nuclear magnetization in the external magnetic field were first written by F.Bloch [Bloc46]. Under assumption that static external magnetic field is applied along z-direction, the Bloch equations have the form:

$$\begin{aligned} \frac{dm_x}{dt} &= \gamma [\boldsymbol{m} \times \boldsymbol{B}]_x - \frac{1}{T_2} m_x \\ \frac{dm_y}{dt} &= \gamma [\boldsymbol{m} \times \boldsymbol{B}]_y - \frac{1}{T_2} m_y \\ \frac{dm_z}{dt} &= \gamma [\boldsymbol{m} \times \boldsymbol{B}]_z + \frac{1}{T_1}(m_0 - m_z) \end{aligned} \tag{2.1.7}$$

Here $\boldsymbol{B}=\boldsymbol{B_0}+\boldsymbol{B_1}$ is a sum of the static external field $\boldsymbol{B_0}$ and the alternating perpendicular field $\boldsymbol{B_1}$, m_0 is an equilibrium value of the nuclear magnetization, T_2 is characteristic relaxation time for x- and y-components of the magnetization (transversal components), T_1 is characteristic relaxation time for z-component of the nuclei magnetization (longitudinal component). The presence of the relaxation terms in the equations reflects existence of weak interaction of nuclear magnetic moments between each other and with the lattice.

Bloch equations (2.1.7) work with good approximation in liquids. In solids, however, the interaction between nuclei spin system and the lattice can not be further assumed as small. For the correct description of the nuclear magnetization behavior in these cases more sophisticated

analysis must be applied [Slic90]. In practice due to complexity of sophisticated analysis Bloch equations are often used as a rough approximation allowing getting some qualitative results.

2.2. Pulsed NMR

2.2.1 Spin echo technique

Let us consider a group of nuclear spins in thermal equilibrium situated in a static magnetic field $\boldsymbol{B_0}$ applied along z-direction. Linearly polarized radio frequency field $\boldsymbol{B_1}$ is applied in the perpendicular with respect to z-axis direction and $|\boldsymbol{B_1}|<<|\boldsymbol{B_0}|$. The thermal equilibrium magnetization $\boldsymbol{m_0}$ lies along $\boldsymbol{B_0}$, thus $\boldsymbol{m_0}=(0,0,m_0)$. Let assume that $|\boldsymbol{B_1}|=2B_1\cos\omega t$. Then Bloch's equations (2.1.7) in the coordinate system that rotates about z-direction with frequency ω can be written in the form:

$$\begin{aligned}
\frac{dm_x}{dt} &= \gamma\left[\boldsymbol{m}\times\boldsymbol{B}_{eff}\right]_x - \frac{1}{T_2}m_x \\
\frac{dm_y}{dt} &= \gamma\left[\boldsymbol{m}\times\boldsymbol{B}_{eff}\right]_y - \frac{1}{T_2}m_y \\
\frac{dm_z}{dt} &= \gamma\left[\boldsymbol{m}\times\boldsymbol{B}_{eff}\right]_z + \frac{1}{T_1}(m_0 - m_z)
\end{aligned} \qquad (2.2.1)$$

where $\boldsymbol{B_{eff}}$ = (0, B_1, B_0 - ω/γ) is an effective magnetic field acting on the magnetic moments in the rotating coordinate system. To obtain (2.2.1), the linearly polarized field $\boldsymbol{B}_1$ was considered as a sum of two circularly polarized fields of equal amplitude B_1 but opposite direction of rotation, and the field rotating oppositely to the Larmor precession of nuclei in the external field $\boldsymbol{B}_0$ was neglected. Let us denote $\omega_0 = \gamma B_0$ and $\omega_1 = \gamma B_1$. The corresponding set of the equation (2.2.1) has then the form:

$$\begin{aligned}
\frac{dm_x}{dt} &= -\frac{1}{T_2}m_x + (\omega_0 - \omega)m_y - \omega_1 m_x \\
\frac{dm_y}{dt} &= -\frac{1}{T_2}m_y - (\omega_0 - \omega)m_x \\
\frac{dm_z}{dt} &= \omega_1 m_x + \frac{1}{T_1}(m_0 - m_z)
\end{aligned} \qquad (2.2.2)$$

Let now apply to the nuclei spin system the radio frequency field B_1 as a pulse with the length $\tau_1 << T_1, T_2$. In the time interval $t = (0, \tau_1)$ the relaxation terms of the equations (2.2.2) can be neglected and corresponding solution can be written (for positive γ) as:

$$
\begin{aligned}
m_x(t) &= -m_0 \frac{\omega_1}{\omega_1'} \sin(\omega_1' t) \qquad \text{where } \omega_1' = \sqrt{(\omega_0 - \omega)^2 + \omega_1^2} \\
m_y(t) &= -m_0 \frac{(\omega_0 - \omega)\omega_1}{\omega_1'^2} \cos(\omega_1' t) \\
m_z(t) &= m_0 \frac{\omega_1^2}{\omega_1'^2} \cos(\omega_1' t) + m_0 \left(1 - \frac{\omega_1^2}{\omega_1'^2}\right)
\end{aligned}
\qquad (2.2.3)
$$

It can be seen that nuclear magnetization rotates about effective field direction $\boldsymbol{B_{eff}}$=(0, B_1, B_0-ω/γ) with angular frequency ω_1'. If the frequency ω of the radio frequency field tends to be ω_0 then $\omega_1' \cong \omega_1$ and rotation takes place in the (x,z) plane. Choosing the length of the pulse in such a way that $\omega_1' \tau_1 = \pi/2$ one will have at the end of the pulse the direction of the nuclear magnetization $\boldsymbol{m}(\tau_1)$ = (-m_0, 0, 0). Such type of a pulse is called "$\pi/2$ pulse".

At time $t > \tau_1$ radio frequency field is switched off, thus ω_1=0, and solution of the corresponding Bloch equations turns out:

$$
\begin{aligned}
m_+(t) &= -m_0 \, e^{-\frac{t}{T_2}} \, e^{i(\omega_0 - \omega)t} \\
m_z(t) &= m_0 \left(1 - e^{-\frac{t}{T_1}}\right)
\end{aligned}
\qquad (2.2.4)
$$

Here $m_+ = m_x + i\, m_y$.

As can be seen from (2.2.4) transversal component of the nucleus magnetization relaxes to zero with characteristic time T_2 (spin-spin relaxation time), and longitudinal component relaxes to the equilibrium magnetization with characteristic time T_1 (spin-lattice relaxation time).

At a time moment $t_{12} << T_1$, $t_{12} < T_2$ the second pulse is applied. The length of the pulse is $\tau_2 << T_1, T_2, t_{12}$. If the frequency ω of the radio frequency field tends to be ω_0 then $\omega_1' \cong \omega_1$ and rotation takes place around y-direction. Choosing the length of the second pulse in such a way that $\omega_1' \tau_2 = \pi$ (the so-called "π-pulse") one will have at a time $t = t_{12} + \tau_2$ the nuclear magnetization as:

$$m_+(t_{12}+\tau_2) = -m_0\, e^{-\frac{t_{12}}{T_2}}\, e^{i(\omega_0-\omega)t_{12}}$$
$$m_z(t_{12}+\tau_2) = m_0\left(1-e^{-\frac{t_{12}}{T_1}}\right) \qquad (2.2.5)$$

Keeping in view that $t_{12}<<T_1$ one can see that $m_z \cong 0$.

After the end of the second pulse $t > t_{12}+\tau_2$, $\omega_1=0$ and the corresponding solutions can be written in the form:

$$m_+(t) = m_0\, e^{-\frac{t}{T_2}}\, e^{i(\omega_0-\omega)(t-2t_{12})}$$
$$m_z(t) = m_0\left(1-e^{-\frac{t}{T_1}}\right) \qquad (2.2.6)$$

In the real system, however, there is always some inhomogeneity of the magnetic field. It can be taken into account by introducing of some distribution function $g(\omega_0-\overline{\omega}_0)$ for the resonant frequency. For that function

$$\int_{-\infty}^{+\infty} g(\omega_0-\overline{\omega}_0)\,d\omega_0 = 1$$
$$\overline{\omega}_0 = \int_{-\infty}^{+\infty} \omega_0 g(\omega_0-\overline{\omega}_0)\,d\omega_0 \qquad (2.2.7)$$
$$\sigma^2 = \int_{-\infty}^{+\infty} (\omega_0-\overline{\omega}_0)^2 g(\omega_0-\overline{\omega}_0)\,d\omega_0$$

Under assumptions of the homogeneous excitation $\sigma << \omega_1$ with frequency of the *rf* field close to the average value of the resonant frequency $|\overline{\omega}_0-\omega| < \omega_1$ the first equation (2.2.4) can be generalized:

$$m_+(t) = -m_0\, e^{-\frac{t}{T_2}}\, e^{i(\overline{\omega}_0-\omega)t} \int_{-\infty}^{+\infty} g(\omega_0-\overline{\omega}_0)\cdot e^{-i(\omega_0-\overline{\omega}_0)t}\,d\omega_0 \qquad (2.2.8)$$

Nonstationary signal of magnetic resonance detected by means of *rf* voltage induced in the probe coil (see chapter 2.6 about the experimental arrangement) by the transversal component m_+ described by the equation (2.2.8) is called the free induction decay (FID). As was already mentioned, there is always some magnet inhomogeneity of the magnetic field B_0 and as a result, the inhomogeneity –induced spread in precession frequency causes the spins in one portion of the sample to get out of phase with those in other portions. As the separate parts get

out of phase, the resultant signal decays faster than corresponds to T_2. According to the Bloch equations, the free induction decays exponentially with characteristic time constant T_2. After the second "π-pulse" applied, as can be seen from the equation (2.2.6) (or generalized equation (2.2.9)), at time $2t_{12}$ the refocusing takes place and as a result the spin echo appears.

$$m_+(t) = m_0\, e^{-\frac{t}{T_2}}\, e^{i(\overline{\omega}_0-\omega)(t-t_{12})} \int_{-\infty}^{+\infty} g(\omega_0-\overline{\omega}_0)\cdot e^{-i(\omega_0-\overline{\omega}_0)(t-t_{12})}\, d\omega_0 \qquad (2.2.9)$$

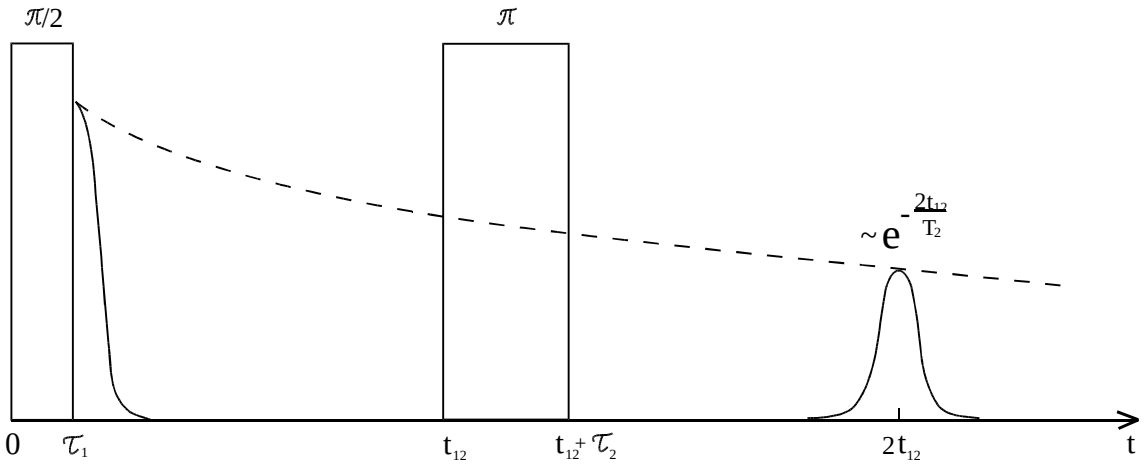

Figure 2.2.1. The formation of a spin echo by means of a π/2-π pulse sequence (schematic plot).

The value of the magnetization producing the echo signal as can be seen from (2.2.6) obeys

$$m_+(2t_{12}) = m_0\, e^{-\frac{2t_{12}}{T_2}} \qquad (2.2.10)$$

This expression can be used for measurements of the T_2 relaxation time. For that purpose the dependence of spin echo on time t_{12} should be measured.

2.2.2. Signal to noise improvement by the Carr-Purcell sequence.

A special problem arises in experiments on samples with a long spin-lattice relaxation time T_1, which determines the time when the echo sequence may be repeated in the cycle of averaging (in many YIG samples T_1 is longer than 1 second at low temperatures). Under the circumstances, an efficient averaging is very time consuming. However, if the transverse

relaxation time T_2 is long as well, the Carr-Purcell pulse sequence allows to increase substantially the number of signals to be averaged [Slic90].

Suppose at $t=0$ one applies a $\pi/2$ pulse in which B_1 lies along the positive x-direction in the rotating frame with the *rf* frequency ω exactly at the Larmor frequency ω_0. Such a pulse turns the magnetization to lie along +y-axis. If one applies a π pulse at $t=t_{12}$, also with B_1 along the +x-axis, an echo is formed at $2t_{12}$ with the magnetization along the –y-axis. If now one applies a π pulse at $3t_{12}$, another echo will form at $4t_{12}$, this time along +y-direction. In this manner, π pulses at $(2n+1)t_{12}$ $(n=0,1,2,\ldots)$ form echoes at $(2n+2)t_{12}$,the echoes forming along the –y-axis for odd n, and the +y-axis for even n.

A sequence of such pulses is shown in figure 2.2.2. Echoes shown by doted curves correspond to echoes forming along negative y-direction.

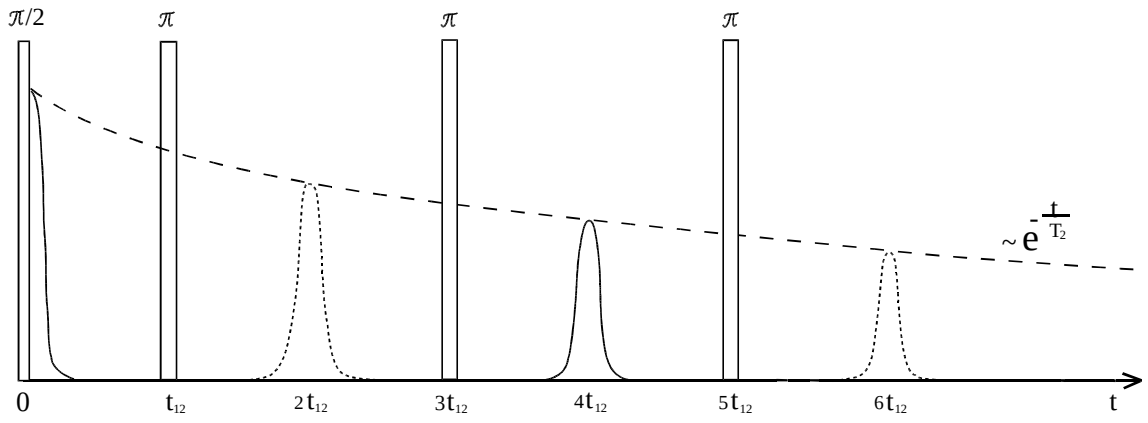

Figure 2.2.2. The Carr-Purcell sequence and the resulting echoes.

Such sequence of *rf* pulses and echoes can be repeated many times. Thus, significant number of echoes can be obtained during only one excitation. The Carr-Purcell echoes are then summed up in order to improve the signal/noise ratio. The number of useful echoes is limited by the minimal possible distance of the pulses and by the transversal relaxation time T_2. Care is needed when T_2 depends on the frequency, because if this is the case, the spectrum deduced from the “early echoes” and the “late echoes” is different.

More sophisticated versions of the Carr-Purcell concepts are used to eliminate imperfections in calibrating of $\pi/2$ and π pulses. The basic Meiboom-Gill modification uses a $\pi/2$ phase shift of rf field for π pulses with respect to the $\pi/2$ pulse: B_1 in the rotating frame is along *x*- axis for the $\pi/2$ pulse but parallel to y-axis for all following π pulses (and spin echoes

are then formed along +y). While the basic Carr-Purcell sequence gives a cumulative error for the echoes intensities in the echo train, in the Meiboom-Gill modification the error is compensated after even π pulses.

The Carr-Purcell pulse series (with the Meiboom-Gill modification) can serve also to determine T_2 when the dependence of the spin echo on its position in the echo train is measured.

2.3. Hyperfine interactions of ^{57}Fe nucleus in magnetic oxides.

NMR spectrum consists of the superposition of signals from all the nuclei of a given isotope in a sample. Each of those nuclei gives rise to a signal at a resonance frequency which is proportional to the magnitude of the local magnetic field at a position of that nucleus. The constant of proportionality (nuclear gyromagnetic ratio γ) is given by an isotope in question.

2.3.1. Origin of the local field in magnetically ordered iron oxides.

NMR in magnetically ordered iron oxides is the most often measured on ^{57}Fe isotope (nuclear spin 1/2, γ=1.377 MHz/T) in trivalent cations Fe^{3+}. Dominating contribution to the local magnetic field on a resonating nucleus of an iron ion gives the hyperfine field which is caused by an interaction with spin and orbital moments of own electronic shells, magnetically polarized due to their interactions with surroundings. Dipolar field, caused by magnetic moments of the rest of ions in the lattice, and an external magnetic field (if applied) are by an order of magnitude smaller.

Hyperfine field on the nucleus of a free Fe^{3+} ion in a ground state (spin 5/2, zero orbital moment) is caused by Fermi contact interactions of 1s, 2s and 3s electrons polarized by exchange interactions with 3d electrons, other contributions due to the spherical symmetry of an ion are zero.

The magnitudes of the hyperfine field were reported to be 63T [Sawa74] and ≈71 T [Noff85]. The field is oriented antiparallel to the direction of the magnetic moment of an ion. Because iron garnets are believed to be ionic compounds (in an ideal, stoichiometric YIG all the cations are trivalent, while the formal valency of oxygen is -2) it is possible for the studying of hyperfine

field on iron nuclei to start from the magnitude of the hyperfine field of a free iron ion and to describe the effect of a crystal structure as corrections to that magnitude. The following mechanisms are believed to be of the main importance:

Neighboring O^{2-} anions (ligands) affect the magnitude of the hyperfine field first of all due to a definite contribution of a covalence in bonds Fe^{3+} - O^{2}, i.e. due to an electron transfer from valence band of O^{2-} anion to 3d, 4s and 4p orbits of Fe^{3+} ion [Namt71, Boek72, Boro91, Nage85]. This contribution reduces the resonance frequencies compared to ones of free ions down to 30MHz and also makes the hyperfine field anisotropic.

As a result of an influence of other neighbors (i.e. cations neighboring with oxygen ligands) is a supertransfer interaction given by the transfer of a spin density between cations through intermediate oxygen ligands [Sawa74, Woud71, Wats67]. The mentioned dependence of the supertransfer interaction on the spin transfer between Fe^{3+} cations intermediated by an oxygen ion is given by a close dependence between supertransfer and superexchange interactions [Boek72, Woud71, Toma95], despite different details of the mechanisms. One can, for instance, expect that the supertransfer field will have, similar to the exchange interaction, a strong dependence on the angle α of the bond Fe^{3+}-O^{2-}-Fe^{3+}. The supertransfer hyperfine field is caused by the overlap distortions of the central cation *4s* orbitals by the ligand orbitals which have been unpaired by transfer into unoccupied *3d* orbitals of the neighboring cations. The supertransfer hyperfine field value depends on the Fe^{3+}- O^{2-}– Fe^{3+} bond angle α according to [Sawa74] as $B_{sthf} = a + b\cos^2\alpha$. The value of supertransfer hyperfine field is approximately 1T by order of magnitude. Following [Sawa74] the contribution to the supertransfer field given by a neighboring cation is oriented according to the direction of a magnetic moment of that neighbor. For an antiparallel orientation of the moments of a central iron ion and of that neighbor the hyperfine field will then increase. Experimental investigations of mechanisms of hyperfine interactions in magnetic oxides [Sawa74, Doro87, Doro89, Doro92] revealed that besides the mentioned dependence of the hyperfine field on the angle α, the increase of the covalence degree in the bond with decreasing distance Fe^{3+}-O^{2-} leads to a reduction of the hyperfine field and that the change of supertransfer interactions on the contrary increases the hyperfine field.

2.3.2. Mathematical description.

The effective local field on the nucleus originates from the hyperfine interaction of the nuclear spin with electrons. By the hyperfine interaction the interaction of a nuclear spin with all electrons present in the system is implied.

A description of a magnetic field on a nucleus of a magnetic ion comes out in general from the expression for the magnetic field induced by an electron [Abra63, Free67]. The contribution of an electron system to the local field at the position of the nucleus is given by the quantum-mechanical average value of a sum of field operators from all the electrons. Evidently, by this way the electron system of the material (and respectively the interactions leading to a magnetic ordering) and also the local field appear in that dependence. However, theoretical calculations of the electronic structure of magnetic oxides are not feasible yet and our knowledge of the local fields at nuclei of transition elements is still limited. When analyzing the hyperfine interactions we are thus forced to use semi-empirical models in combination with independent experimental results.

A natural approximating step to the relations for evaluation of experimental results is the expression of contributions of the hyperfine interactions to the local field by means of the sum of terms linearly dependent on components of electronic magnetic moments of ions in the lattice [Kurk90]. The more distant ions will then give rise mostly by the field of elementary magnetic dipoles only.

The ^{57}Fe nucleus has spin *I=1/2*. As a consequence only the magnetic part of the hyperfine interaction is relevant and it may be represented by an interaction of the nuclear spin with an effective magnetic field $\boldsymbol{B_{hf}}$:

$$\hat{H} = -\boldsymbol{\mu}\, \boldsymbol{B}_{hf} \qquad (2.3.1)$$

where $\boldsymbol{\mu}$ is the nuclear magnetic moment operator.

To discuss the hyperfine field $\boldsymbol{B_{hf}}$ on the given nucleus, the system is divided into three regions: an own electronic shell around the nucleus (including the electron transfer and supertransfer from neighbouring oxygen ions and cations), atoms within the Lorentz sphere and the rest of the system. The hyperfine field, thus, can be divided into two parts: dipolar part, corresponding to the interaction of the nuclear spin with magnetic moments of ions presenting in the system, and dominating part of hyperfine field, caused by the magnetic interaction with electrons within atomic sphere.

If external magnetic field is applied to the system the general expression for the local effective field acting on the nuclei can be written as:

$$\boldsymbol{B}_{eff} = \boldsymbol{B}_{ext} + \boldsymbol{B}_{hf}^{dip} + \boldsymbol{B}_{hf}^{atomic} \tag{2.3.2}$$

2.3.2.1. Dipolar field contribution of the surrounding magnetic ions.

The dipolar part of the hyperfine field caused by the magnetic moments inside the Lorentz sphere but outside the atomic sphere can be written in the form:

$$\boldsymbol{B}_{dip}^{in} = -\frac{\mu_0}{4\pi}\sum_{i=1}^{N_{in}}\left(\frac{\boldsymbol{\mu}_i}{R_i^3} - 3\frac{(\boldsymbol{\mu}_i \boldsymbol{R}_i)}{R_i^5}\boldsymbol{R}_i\right) \tag{2.3.3}$$

where N_{in} is a number of magnetic ions inside the Lorentz sphere, $\boldsymbol{R}_i$ is a radius-vector from the nucleus to the point where the i^{th} moment $\boldsymbol{\mu}_i$ is situated, μ_0 is a magnetic vacuum permeability.

The Lorentz sphere must be taken sufficiently large, so that the field in (2.3.3) is practically independent of its radius.

If the magnetic moments of different ions are collinear then $\boldsymbol{\mu}_i = \mu_i \boldsymbol{n}$, where $\boldsymbol{n}$ is the unit vector in the direction of the magnetic moment of ion containing considered nucleus, and the expression (2.3.3) can be rewritten in a form:

$$\begin{aligned} \left(\boldsymbol{B}_{dip}^{in}\right)_\alpha &= \sum_{\beta=1}^{3}\left(A_{\alpha\beta}^{dip}\, n_\beta\right) \\ A_{\alpha\beta}^{dip} &= \frac{\mu_0}{4\pi}\sum_{i=1}^{N_{in}}\left(\frac{3\, x_\alpha x_\beta - R_i^2\delta_{\alpha\beta}}{R_i^5}\mu_i\right), \qquad \alpha,\beta = 1,2,3 \end{aligned} \tag{2.3.4}$$

Here $A_{\alpha\beta}^{dip}$ are components of the symmetrical tensor of the second order with zero trace. Choosing the corresponding coordinate system axes in the directions of the principal axes of a tensor $\vec{\vec{A}}^{dip}$ one obtains $A_{\alpha\beta}^{dip} = 0$ for $\alpha \neq \beta$ and, because the trace of the tensor is zero, only two components of the tensor are independent. If moreover, the system has tetragonal, trigonal or hexagonal symmetry and assuming z-axis as symmetry axis the number of independent components reduces to one: $2A_{11}^{dip} = 2A_{22}^{dip} = -A_{33}^{dip}$. In this case projection of the considered dipolar part of the field on the magnetization direction can be written in the form [Robe62]:

$$\left(\boldsymbol{B}_{dip}^{in}\right)_M = \frac{1}{2}A_{33}^{dip}\left(3\cos^2\theta - 1\right) \tag{2.3.5}$$

where θ is an angle between the magnetization direction and a local symmetry axis z.

The contribution of the magnetic moments outside Lorentz sphere can be calculated in such a way: because of large distances between considered nucleus and magnetic ions outside Lorentz sphere, discrete magnetic moments of these ions can be considered as continuum with magnetization ***M***. Under this assumption the corresponding contribution can be expressed in a form:

$$\boldsymbol{B}_{dip}^{out} = \frac{\mu_0}{4\pi} grad\left\{ \int_v \frac{div\ \boldsymbol{M(r)}}{r} dV - \int_S \frac{\boldsymbol{M(r)}}{r} d\,\boldsymbol{S} - \int_\sigma \frac{\boldsymbol{M(r)}}{r} d\,\boldsymbol{\sigma} \right\} \qquad (2.3.6)$$

Here in the first term one should integrate through the volume *V* of the whole system without the Lorentz sphere; at the second term integration is going on at the surface *S* of the system; third term should be integrated at the surface of the Lorentz sphere σ.

In the case of ellipsoidal one domain sample one has homogenous magnetization **M**(r)=**M** and the first integral in (2.3.6) is zero. Second term represents demagnetizing field:

$$\boldsymbol{B}_{dip}^{dem} = -\vec{\vec{N}}\,\boldsymbol{M}\,, \qquad N_{\alpha\beta} = \int_S \frac{r_\alpha\, dS_\beta}{r^3} \qquad (2.3.7)$$

Here $\vec{\vec{N}}$ is a tensor of the demagnetizing constants. The third integral represents so-called Lorentz field:

$$\boldsymbol{B}_{dip}^{L} = \frac{\mu_0}{3}\boldsymbol{M} \qquad (2.3.8)$$

In the case of spherical sample the demagnetizing factor *N=1/3* and Lorentz field and the demagnetizing field are compensated.

The dipolar field contribution $\boldsymbol{B}_{hf}^{dip} = \boldsymbol{B}_{dip}^{in} + \boldsymbol{B}_{dip}^{dem} + \boldsymbol{B}_{dip}^{L}$ to the hyperfine field makes only a small part of a total $\boldsymbol{B_{hf}}$, its magnitude being at least by two orders smaller comparing to $\boldsymbol{B_{hf}}$.

2.3.2.2. Hyperfine field caused by electrons within atomic sphere.

The dominating part of the hyperfine field acting on the nuclei originates from the hyperfine interaction of a magnetic moment of a nucleus with spin and orbital moments of electrons within an atomic sphere. It consists of three parts: Fermi contact term caused by s-electrons, which have nonzero density at the nucleus; dipolar interaction with the electrons

outside the nucleus, dipolar interaction with an orbital moment of electrons. Corresponding effective field could be written as [Abra61]

$$\boldsymbol{B}_{hf}^{at} = g\mu_0\mu_B \sum_i \left\{ -\frac{8\pi}{3}\boldsymbol{S}_i\,\delta(\boldsymbol{r}_i) + \left(\frac{\boldsymbol{S}_i}{r_i^3} - 3\frac{\boldsymbol{S}_i\boldsymbol{r}_i}{r_i^5}\boldsymbol{r}_i \right) - \frac{\boldsymbol{l}_i}{r_i^3} \right\} \qquad (2.3.9)$$

where $\boldsymbol{l}_i$, $\boldsymbol{S_i}$ represent electron orbital and electron spin operators, respectively; μ_B is Bohr magneton; g is the electronic spectroscopic splitting factor, $\delta(\boldsymbol{r}_i)$ is Dirac delta-function.

The last term in (2.3.9) describes the electron orbital moment contribution to the hyperfine field. The orbital contribution of electrons equals to zero in the case of electrons in *s* state, for filled or half-filled shells or due to the influence of crystal field when orbital moment is "frozen". The dipolar field contribution is zero in the case of *s* states with spherical electron distribution. Fermi contact contribution (the first term in (2.3.9)) is nonzero only for *s* electrons.

The dominating contribution to the hyperfine field on the iron nucleus arises from the Fermi contact term. In the case of atoms having magnetic moments, large hyperfine fields originate from the exchange polarization of the core electrons by uncompensated spin of not completely filled shell. Due to core polarization inner 1s, 2s, 3s filled shells contribute to the hyperfine field by means of Fermi contact interaction.

In the case of ion in *s* state or in the case of frozen orbital moment the hyperfine field on the nuclei caused by electrons within atomic sphere could be written in a form:

$$\boldsymbol{B}_{hf}^{at} = \vec{\vec{A}}\,\boldsymbol{S} \qquad (2.3.10)$$

Here $\vec{\vec{A}}$ is a tensor of hyperfine interaction, $\boldsymbol{S}$ is a total spin of the ion.

$\vec{\vec{A}}$ is a symmetrical tensor of second order. Choosing the corresponding coordinate system axes in the directions of the principal axes of a tensor $\vec{\vec{A}}$ one obtains only three independent components. If moreover the system has tetragonal, trigonal or hexagonal symmetry and assuming z-axis as symmetry axis the number of independent components reduces to two and for the projection of hyperfine field to magnetization direction one can write [Robe62]:

$$B_{hf}^{at} = a + b\,\left(3\cos^2(\theta) - 1\right) \qquad (2.3.11)$$

Here θ is an angle between a local symmetry axes and a total spin of the ion.

2.3.2.3. Electric quadrupole effects in magnetically ordered systems.

If a nuclear spin I>1/2 then the nucleus possesses a quadrupolar electric momentum and the internal electric (inhomogeneous) fields will be affecting NMR parameters. In a coordinate system (x,y,z) of the main axes of that tensor the effective quadrupole Hamiltonian has a form [Abra63]:

$$H_Q = \frac{1}{2}\hbar\omega_Q\left[I_z^2 - \frac{1}{3}I(I+1) + \frac{1}{6}\eta\left(I_+^2 + I_-^2\right)\right]$$
$$\hbar\omega_Q = \frac{3e^2qQ}{2I(2I-1)}, \qquad eq = V_{zz}, \qquad \eta = \frac{V_{xx} - V_{yy}}{V_{zz}}, \qquad I_\pm = I_x \pm iI_y \tag{2.3.12}$$

Q - quadrupolar momentum of a nucleus.

In particular, if the symmetry of a tensor of electric field gradient $V_{\alpha\beta}$ affecting the nucleus is lower than cubic, but the electric quadrupolar interaction is relatively weak (it can be considered as a first order correction to Zeeman energy levels), the splitting of NMR lines into 2∗I lines will appear [Turo69].

The electric field gradient (EFG) on nuclei and atoms of transition elements is mostly caused by electrons of unpaired d- or f- orbitals. Main axes of EFG and a tensor of hyperfine interactions usually coincide. However the axis of quantization of nuclear spins (directing along local magnetic fields) may coincide with no one of those axes, because the equilibrium orientation of electronic spins, which mainly defines the direction of the local field on a nucleus, establishes as a result of competing processes: exchange, magnetocrystalline anisotropy and an external magnetic field.

The quadrupole interaction can affect also the relaxation times T_1 and T_2 coupled with fluctuations of local hyperfine fields on nuclei – the effects considered in paragraph 2.5.

2.4. The enhancement factor of *rf* field in magnetically ordered systems.

As early as first results of NMR experiments in magnetically ordered systems appeared, it was noticed that quantum resonant transitions of the nuclear spins are induced not by the external radio frequency field $\boldsymbol{b}_{rf}$ directly but the alternating transversal part of the local field

$\boldsymbol{B}_{loc}^{\perp}$ acting on the nuclei. As far as $\left|\boldsymbol{B}_{loc}^{\perp}\right| >> \left|\boldsymbol{b}_{rf}\right|$ the so-called enhancement effect of the *rf* field takes place.

Let us consider what is going on in the magnetically ordered system when external *rf* field is applied. The electron magnetization follows the direction of the effective magnetic field, which results from the vector sum of the static magnetic fields determining the easy magnetization direction in the system. Applying the external transversal *rf* field $\boldsymbol{b}_{rf}$ will change the effective field direction.

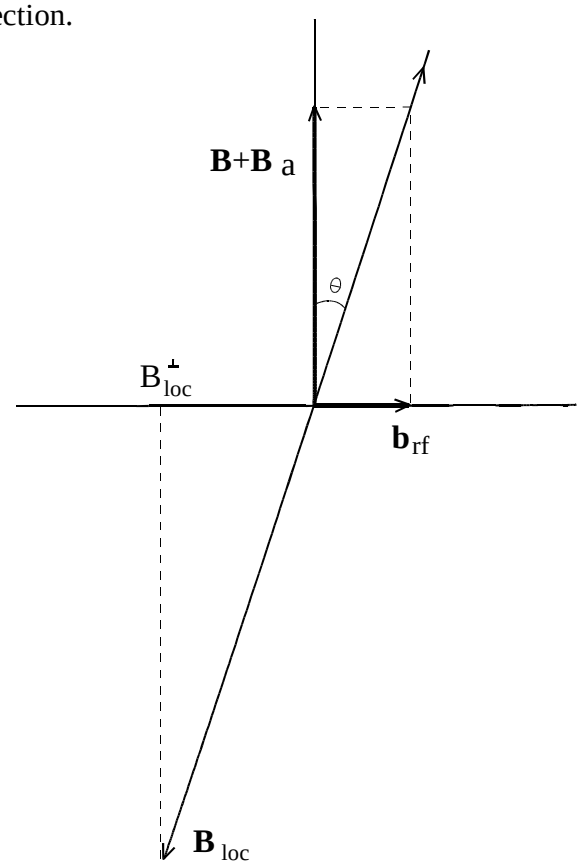

Figure 2.4.1. Effect of the *rf* field enhancement. Here $\mathbf{B}_a$ is effective field of magnetic anisotropy, **B** is an external magnetic field.

As far as magnetization should follow the effective field direction the transversal component of the magnetization and as a consequence the transversal component of the local field will appear. Thus nuclear spins suffer the influence of additional alternating magnetic field $\boldsymbol{B}_{loc}^{\perp}$ besides external magnetic field $\boldsymbol{b}_{rf}$

$$B_{loc}^{\perp} \cong B_{loc}\,\theta = \frac{B_{loc}}{B + B_a} b_{rf} = \eta\, b_{rf} \qquad (2.4.1)$$

The enhancement factor $\eta = \frac{B_{loc}^{\perp}}{b_{rf}} = \frac{B_{loc}}{B + B_a}$ in zero external magnetic fields can achieve for the ferric oxides the values up to 10^2.

Even greater alternating magnetic field act on the nuclei located within the domain wall. When the external alternating magnetic field is applied the reversible oscillations of the domain walls take place in many domains system. During these oscillating displacements, especially strong deviations feel the local magnetization vectors inside domain walls. As far as $B_{loc}^{\perp}$ is proportional to a deviation angle, the corresponding enhancement factor for the nuclei inside domain walls turns out to be 10-100 times greater than for nuclei inside domains.

2.5. Spin relaxation in magnetically ordered systems.

Analogously with similar phenomena in other areas of spectroscopy, the process by which an arbitrary density operator returns to the equilibrium operator is called nuclear magnetic, or spin, relaxation. Although pulse NMR techniques permit generation of off-diagonal density matrix elements, eventually the density operator returns to an equilibrium state in which all off-diagonal elements of the density operator have decayed to zero and the populations of the energy levels of the system (diagonal elements of the density operator) have been restored to the Boltzmann distribution [Abra61]. The following section will describe the general features of spin relaxation and some important consequences of spin relaxation processes for NMR experiments.

Nuclear spin relaxation is a consequence of coupling of a spin to the surroundings. The surroundings modifies the local magnetic field at the location of a nucleus and thereby contributes to the relaxation.

Transverse components of the local field are responsible for *non-adiabatic* contributions to relaxation. If the fluctuating transverse magnetic fields at the location of a nucleus contain components with frequencies corresponding to the energy differences between eigenstates of the spin system, then transitions between eigenstates can occur. In this case, transition of the spin system from a higher (lower) energy state to a lower (higher) energy state is accompanied by an energy-conserving transition of the lattice from a lower (higher) to higher (lower) energy state. A transition of the spin system from higher energy to lower energy is more probable because the lattice is always in thermal equilibrium and has a larger population in the lower energy state.

Thus, exchange of energy between the spin system and the lattice brings the spin system into thermal equilibrium with the lattice and the populations of the stationary states return to the Boltzmann distribution. Furthermore, transitions between stationary states caused by non-adiabatic processes decrease the lifetimes of these states and introduce uncertainties in the energies of the nuclear spin states through a Heisenberg uncertainty relationship. As a result, the Larmor frequencies of the spins vary randomly and the phase coherence between spins is reduced over time. Consequently, non-adiabatic fluctuations that cause transitions between states result in both thermal equilibration of the spin state populations and decay of off-diagonal elements of density operator.

Fluctuating fields parallel to the main static field are responsible for *adiabatic* contributions to relaxation. The fluctuating fields generate variations in the total magnetic field in the *z*-direction, and consequently, in the energies of the nuclear spin energy levels. Thus, adiabatic processes cause the Larmor frequencies of the spins to vary randomly. Over time, the spins gradually lose phase coherence and off-diagonal elements of the density matrix decay to zero. The populations of the states are not altered and no energy is exchanged between the spin system and the lattice because transitions between stationary states do not occur.

Magnetic relaxation which does not change the full energy of the spin system, but redistribute it between degrees of freedom of magnetic moments, is called the *spin-spin relaxation*.

Magnetic relaxation changing the full energy of the spin system is called *spin-lattice relaxation*. It establishes the thermal equilibrium between the spin system and the 'lattice' (i.e. the heat reservoir representing other degrees of freedom in the matter).

2.5.1. Relaxation in the Bloch equations

In the simplest theoretical approach to spin relaxation, the relaxation of isolated spins is characterized in the Bloch equations (2.1.7) by two phenomenological first order rate constants: the *spin-lattice* or *longitudinal* relaxation rate constant, R_1, and the *spin-spin* or *transverse* relaxation rate constant, R_2,

$$\frac{dm_x}{dt} = \gamma\ [\mathrm{m}\times\mathrm{B}]_x - \frac{1}{T_2} m_x = \gamma\ [\mathrm{m}\times\mathrm{B}]_x - R_2 m_x$$
$$\frac{dm_y}{dt} = \gamma\ [\mathrm{m}\times\mathrm{B}]_y - \frac{1}{T_2} m_y = \gamma\ [\mathrm{m}\times\mathrm{B}]_x - R_2 m_x \qquad (2.5.1)$$
$$\frac{dm_z}{dt} = \gamma\ [\mathrm{m}\times\mathrm{B}]_z + \frac{1}{T_1}(m_0 - m_z) = \gamma\ [\mathrm{m}\times\mathrm{B}]_z + R_1(m_0 - m_z)$$

Here (as in paragraph 2.1) T_2 is a characteristic relaxation time for x- and y-components of the magnetization (transversal components), T_1 is characteristic relaxation time for z-component of the nuclei magnetization (longitudinal component). Rate constants rather than time constants, are utilized; the two quantities are reciprocals of each other (for example $T_1 = 1/R_1$). The spin-lattice relaxation rate constant describes the recovery of the longitudinal magnetization to the thermal equilibrium, or, equivalently, returns the populations of the energy levels of the spin system (diagonal elements of the density operator) to the equilibrium Boltzmann distribution. The spin-spin relaxation rate constant describes the decay of the transverse magnetization to zero, or equivalently, the decay of transverse “single quantum coherences” (off-diagonal elements of the density matrix) [Abra61]. Non-adiabatic processes contribute to both spin-lattice and spin-spin relaxation. Adiabatic processes only contribute to spin-spin relaxation; spin-lattice relaxation is not affected because adiabatic processes do not change the populations of stationary states.

The Bloch formulation provides qualitative insights into the effects of relaxation on the NMR experiment, and the phenomenological rate constants can be measured experimentally. For example, the Bloch equations predict that the free induction decay (FID) is the sum of exponentially damped sinusoidal functions and that, following a pulse sequence that perturbs a spins system from equilibrium, R_2 governs the length of time that the FID can be observed (supposing ideally homogeneous static magnetic field, however usually the duration of FID is restricted by inhomogeneity of that field) and R_1 governs the minimum time required for equilibrium to be restored. The Bloch formulation does not provide a microscopic explanation of the origin or magnitude of the relaxation rate constants, nor is it extendible to more complex, coupled spin systems.

2.5.2. Relaxation mechanisms in magnetically ordered systems.

All the relaxation mechanisms which are relevant for resonance properties of nonmagnetic solids are relevant also for magnetic crystals. However there are some peculiarities which are the consequence of properties of electron system in magnetic crystals. The main such peculiarity is the existence of collective spin excitations described (at low temperatures) in terms of spin waves [Turo69]. Spin waves (or magnons) interacting with nuclear spins via hyperfine coupling, dipole-dipole or other interactions, can be dispersed, absorbed or emitted by nuclear spins, besides spin waves can be transformed into lattice vibrations – phonons. The dominant role of spin waves in relaxation processes can be described by the next two types of effects:

1) Spin waves being directly dispersed on a nuclear spin (by themselves or with an assistance of phonons) establish on a nucleus fluctuating local magnetic fields. The latter can induce a quantum transitions between nuclear quasizeeman levels.
2) Emission of a spin wave by one nucleus and absorption it by another one leads to indirect (Suhl-Nakamura) interaction of nuclear spins.

There is a sufficient difference between these two types of effects. The first type can take place also for some single nuclear spin in magnetically ordered system. That is why they should be taken into account at any small concentration of magnetic nuclei. The effects of the second type play a sufficient role at large enough concentration of magnetic nuclei and therefore are especially significant for completely magnetic isotopic content of nuclei under consideration.

At large enough concentration of magnetic nuclei the first place for the reason of NMR line homogeneous broadening stands Suhl-Nakamura mechanism of the interaction of nuclear spins via spin waves. It gives at a first approximation the linewidth which does not depend on the temperature.

At small concentrations of magnetic isotope the universal mechanism of the NMR line broadening probably does not exist [Turo69]. For insulators, the reason of the broadening could be different types of dispersion of spin waves on a nuclear spin. In terms of magnons those would be one-magnon processes in the case when there is a strong damping of longwave spin waves at NMR frequency (caused for instance by their interaction with rapidly relaxing magnetic impurities, as in the case of YIG at $T<20K$ [Turo69]). Another example is the presence in the system of Fe ions with different valences resulting in a possibility of electron migration as a reason of sufficient effects on nuclear magnetic relaxation in magnetite Fe_3O_4 [Mizo66]). In this case the same mechanism will be the important reason of the spin-lattice relaxation. In other cases the reason of line broadening could be two-magnon processes of dispersion (as in the case of YIG at $T>20K$) [Turo60]. If the hyperfine interactions are anisotropic then the same

processes will be responsible for the longitude relaxation. Another contribution to the spin-lattice relaxation in magnetic insulators could be different mechanisms of the interaction of nuclear spins with lattice vibrations (one- and two-phonon processes) and also specific for magnetic crystals more complicated processes of dispersion under combined assistance of magnons and phonons.

Quadrupole interaction could affect also the relaxation times T_1 and T_2 coupled with fluctuations of local hyperfine fields on nuclei. The first quadrupolar effect is the affection of the probabilities of nuclear transitions: if at H_Q=0 in first approximation an average probability of nuclear transitions $W_{m\rightarrow m\pm1} \sim 1/T_1$ equals 0, then at $H_Q \neq 0$ the transitions between two levels m and $m\pm1$ could be allowed. Another effect is the affection of the symmetry of the EFG by lattice vibrations. Lattice vibrations affect even the cubic symmetry of EFG in cubic crystals leading to one-phonon processes of spin-lattice relaxation ($1/T_1 \sim T$) and also to two-phonon Raman processes ($1/T_1 \sim T^7$ for low temperatures and $1/T_1 \sim T^2$ for high temperatures) [Turo69]. The calculation of a velocity of the longitudinal relaxation for this mechanism almost does not depend on if the crystal is magnetic or not [Abra63].

2.6. Experimental details.

2.6.1 Pulse NMR spectrometer.

The NMR spectra in this Thesis were measured by the spin echo method using the pulse phase-coherent spectrometer with an averaging technique and fast Fourier transformation (FFT). Measurements were performed partially at the Research Centrum of Juelich (Germany) on the commercially manufactured spectrometer (SMIS) adapted for the broad-line NMR spectroscopy and later on the same spectrometer at the Faculty of Mathematics and Physics, Charles University. The block scheme of the spectrometer is shown in the figure 2.6.1.1.

The spectrometer is governed by the PC. The RF generator produces continuous radio frequency signals with the frequency f_0 and $f_0 + f_B$. Afterwards continuous signal with the frequency f_0 is modulated by the pulse sequence produced by the pulse generator and is amplified by the RF amplifier (power output 300W). The attenuator establishes optimal (for obtaining of the spin echo signal) magnitude of the pulses going to the probe. The duration and amplitude of pulses for spectra in this thesis were for each sample (and temperature) optimized to obtain NMR

signal originated from nuclei in magnetic domains. The measured samples were placed either in the coil of the tuned resonant circuit or the broadband probe was used. After the pulses were applied the echo signal is detected. The echo signal is then sent to the low-noise broadband preamplifier and to the mixer, where the spin echo signal is mixed with the reference continuous signal of the frequency f_0+f_B received from the RF generator. The result of the mixing is spin echo signal modulated on the intermediate frequency f_B. The spin echo signal, amplified in the intermediate-frequency amplifier, is then digitized by the AD converter.

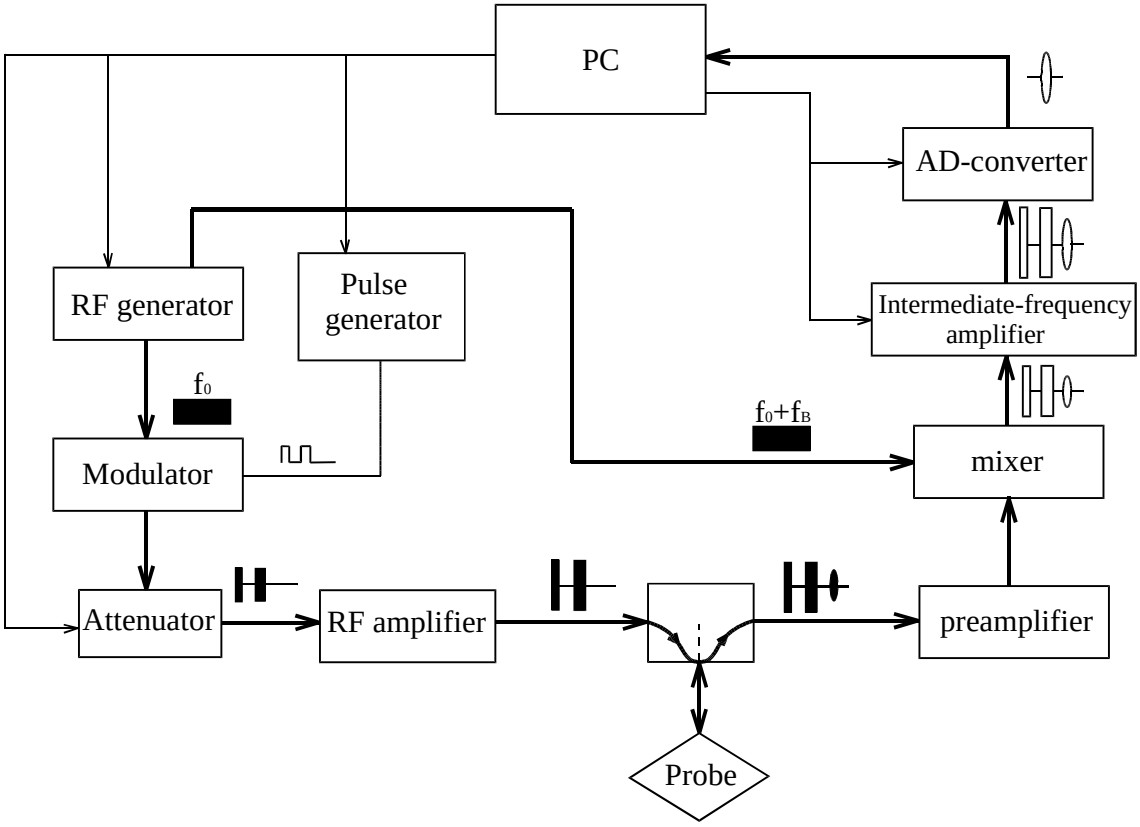

Figure 2.6.1.1. Block scheme of the pulsed NMR spectrometer used in the measurements.

Digitized spin echo signal is averaged in the PC memory in order to improve the signal/noise ratio. The resulting signal/noise ratio is proportional to $n^{1/2}$, where n is number of averaged signals. NMR signal spectrum is obtained by the fast Fourier transformation of the averaged time dependent spin echo signal.

Basic technical parameters of the pulse coherent spectrometer used in the measurements are collected in Table 2.6.1.1.

Frequency range	10 MHz - 300 MHz
Maximal output of excitation pulses	300 W
Length range of the excitation pulses	0.1 μs – 40 μs
Repetition time range of the pulse series	0.01 s – 327s
Pulse separation range	7 μs – 3200 μs

Table 2.6.1.1. Basic technical characteristics of the pulse phase coherent NMR spectrometer.

2.6.2 NMR probes.

In order to excite (or detect) radio frequency signal in (from) the sample, it should be placed in either resonant circuit or in the broadband probe. In the figure 2.6.2.1 classical parallel resonant circuit consisting of the radio frequency coil with the sample and of the continuously adjustable capacitor is shown.

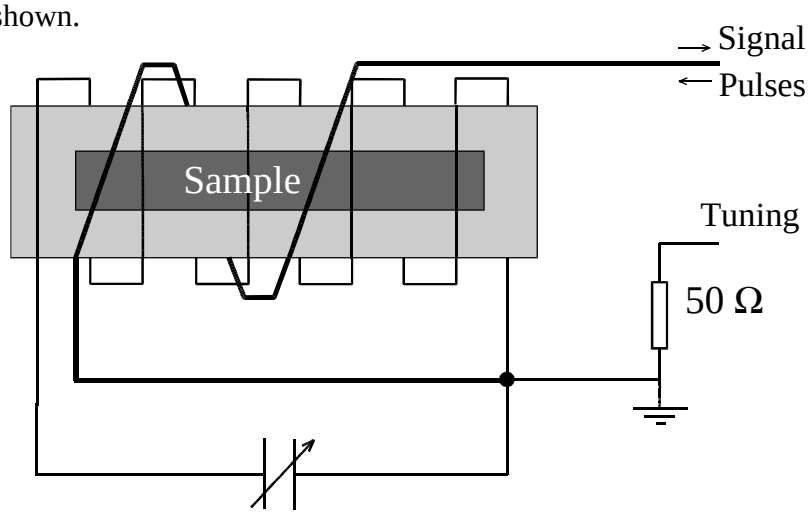

Figure 2.6.2.1. Tuned NMR probe.

Exciting and detecting routes are realized by 50Ω BNC cable. Tuning route with attached 50Ω resistor allows to tune the resonant circuit at the required frequency.

The disadvantage of such type of the NMR probe is necessity of resonant circuit tuning for each excitation frequency that makes impossible to make spectrometer fully automated.

In order to make spectrometer entirely automated, broadband NMR probe should be made [Wagn94].

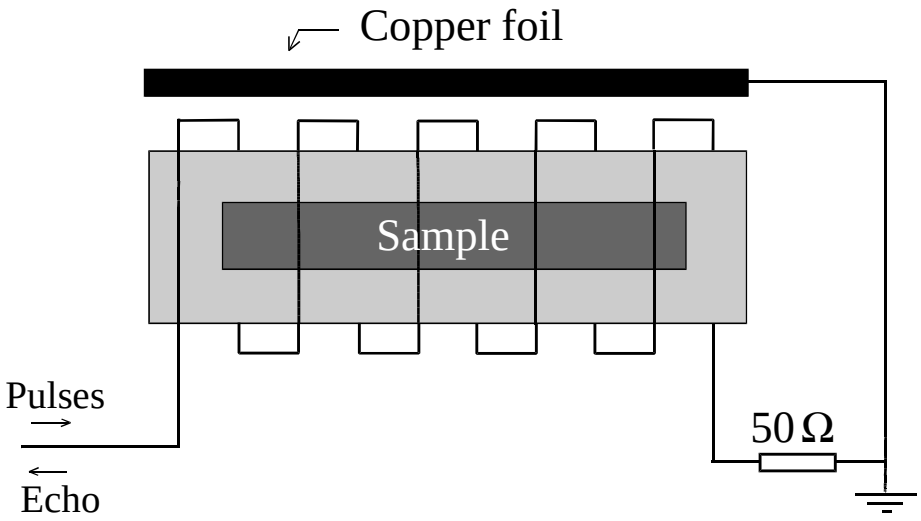

Figure 2.6.2.2. Broadband NMR probe.

The broadband NMR probe is made as radio frequency coil with approximately 10 loops for the frequency region of 57Fe NMR in magnetic iron oxides. The surface of the coil is covered by isolated and earthed thin copper foil. The frequency range of a probe made in such a way is practically constant at the range 10 – 100 MHz. In the case of measurements with broadband probe, it is not necessary furthermore to tune resonant circuit at each frequency that makes NMR measurements entirely automated. However, the sensitivity of such probe is estimated to be approximately five times lower than for the case of classical tuning NMR probe and, as a result, when one deals with weak signals (for example, satellite lines caused by the presence of some defects in small concentration) it is still necessary to use tuning NMR probe for the measurements.

2.6.3 NMR signal processing.

Spectrometer being coherent allows averaging of individual spin echo signals on the intermediate frequency f_B, which comes to PC from AD converter. Individual spin echo signals are summed up and the arithmetical mean value is calculated.

In the figure 2.6.3.1 one is shown how the signal to noise ratio can be improved by the increasing of number n of spin echo signals taken for an averaging. Theoretically signal to noise ratio can be described by the following expression [Engl94]:

$$\frac{A_{signal}}{A_{noise}} \approx \sqrt{n} \qquad (2.6.3.1)$$

Here A_{signal} and A_{noise} are amplitude of the signal and an effective amplitude of the noise respectively. Averaging procedure, therefore, makes possible to observe weak signals that are comparable to the noise level or even somewhat lower.

After the signal was averaged the fast Fourier transformation (FFT) was carried out. It is possible to do this in two different ways. Either to perform FFT directly from the averaged signal on the intermediate frequency f_B (it means that one should make FFT from a large number of data) or to perform a quadrature detection (electronically or by means of PC simulation from data obtained at f_B , as described below) to reduce a number of data required for FFT.

In order to simulate the quadrature detection (i.e. synchronous detection in two channels having 90^o phase shift) of the spin echo signal the following algorithm is applied. Let us consider a spin echo signal digitalized with time interval t_ν on the carrier frequency with the period T.

The number of intervals t_ν per period T is then $m = T/ t_\nu$. Corresponding amplitudes of the spin echo signal on the carrier frequency are A_i for i=1,…,N-1 , where N is a number of intervals t_ν per echo signal. In the case where $m/2$ is an integer even number the real X_k and imaginary Y_k parts of a signal at time $t_k = k\, m\, t_\nu$ can be written as:

$$X_k = \frac{1}{m}\left[\sum_{i=km}^{(k+1)m/2-1} A_i - \sum_{i=(k+1)m/2}^{(k+1)m-1} A_i\right]$$
$$Y_k = \frac{1}{m}\left[\sum_{i=km}^{(k+1)m/2-1} A_{i+m/4} - \sum_{i=(k+1)m/2}^{(k+1)m-1} A_{i+m/4}\right] \qquad (2.6.3.2)$$

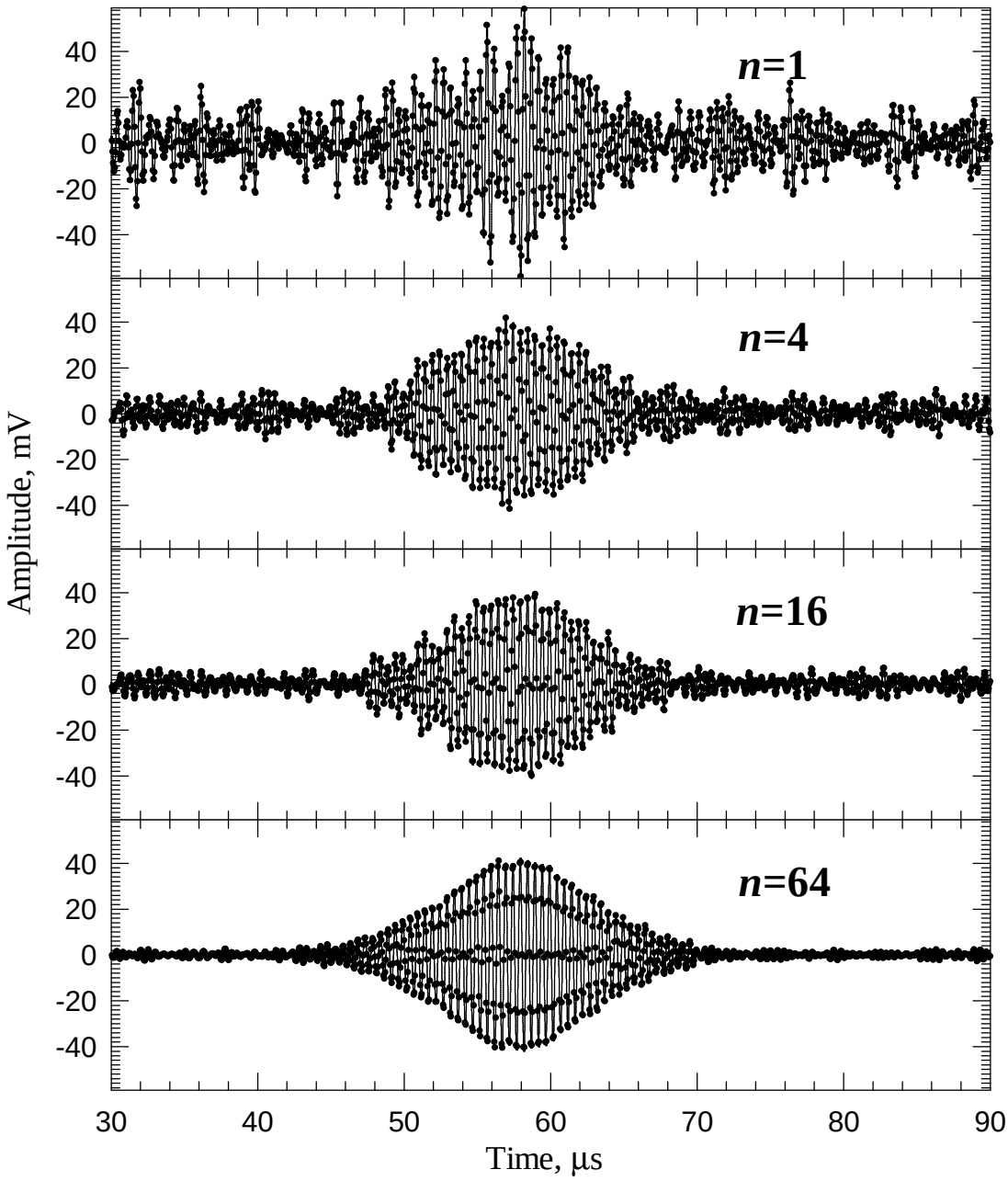

Figure 2.6.3.1. Dependence of the spin echo signal on the number of averages *n* in the hematite sample enriched with the ^{57}Fe isotope; excitation frequency *f*=71.2 MHz, T=295K.

In the case when *m/2* is odd integer and π/2 phase shift does not correspond to the shift at integer number of time intervals t_ν the expressions (2.6.3.2) should be rewritten in the following form:

$$X_k = \frac{1}{m}\left[\sum_{i=km}^{(k+1)m/2-1} A_i - \sum_{i=(k+1)m/2}^{(k+1)m-1} A_i\right]$$
$$Y_k = \frac{1}{2\,m\cos(\pi/m)}\left[\sum_{i=km}^{(k+1)m/2-1}(A_{i+q} + A_{i+q+1}) - \sum_{i=(k+1)m/2}^{(k+1)m-1}(A_{i+q} + A_{i+q+1})\right] \qquad (2.6.3.3)$$

Where $q=(m/2-1)/2$ is an integer number.

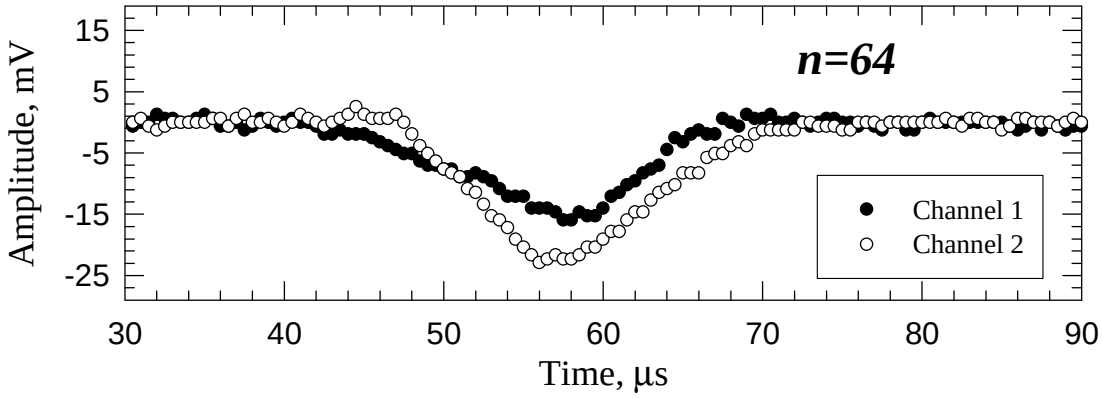

Figure 2.6.3.2. Spin echo signal detected by using the quadrature detection (in hematite sample enriched by ^{57}Fe isotope. T=295K, f=71.2 MHz, number of averages n=64).

In the figure 2.6.3.2 the spin echo signal in hematite sample enriched by ^{57}Fe isotope is displayed as an example of performing procedure of the quadrature detection.

After the quadrature detection had been performed Fast Fourier Transformation could be applied to obtain NMR spectrum of the spin echo signal. In the figure 2.6.3.3 the Fourier transformation of the spin echo signal in hematite sample enriched by ^{57}Fe isotope is plotted.

The spin echo signal contains the frequency components of the NMR spectrum filtered by the bandwidth of the exciting pulses, the bandwidth of the resonance circuit containing the sample and by the bandwidth of the receiver. Thus the Fourier transform of the spin echo signal gives NMR spectrum in limited band. The maximal width of this band is about 0.25 MHz for the lengths of the excitation pulses of τ_1 = 2 μs, τ_2 = 4 μs. In order to obtain complete NMR spectrum in some frequency region (more than 1 MHz for the case of YIG) the excitation frequency should be changed through the spectral frequency region with frequency interval of 0.1 MHz or better less. At each excitation frequency whole described above procedure of averaging, synchronous detection and the fast Fourier transformation of NMR signal should be performed. The individual Fourier transforms should be then overlapped to form a spectrum.

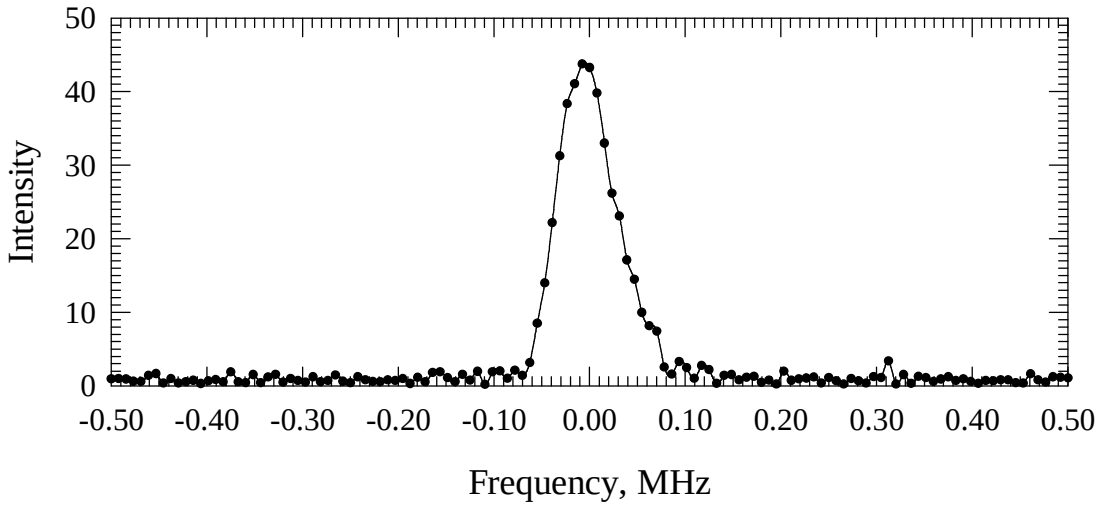

Figure 2.6.3.3. Fourier transformation magnitude of the spin echo signal plotted for hematite sample enriched by ^{57}Fe isotope. *T*=295K, number of averages *n*=64. Zero point at the frequency axis corresponds to the excitation frequency *f*=71.2 MHz.

In the figure 2.6.3.4 the NMR spectrum of hematite enriched by ^{57}Fe isotope is shown. Spectrum in question was obtained by the overlapping of the individual Fourier transforms of the spin echo signal excited by different excitation frequencies, which are also plotted in the figure. Measurements were carried out at room temperature (T=295K). Excitation frequency was changed in the range 71.01 MHz - 71.34 MHz with frequency interval Δ = 30 kHz. Spin echo signals for each frequency were averaged 64 times.

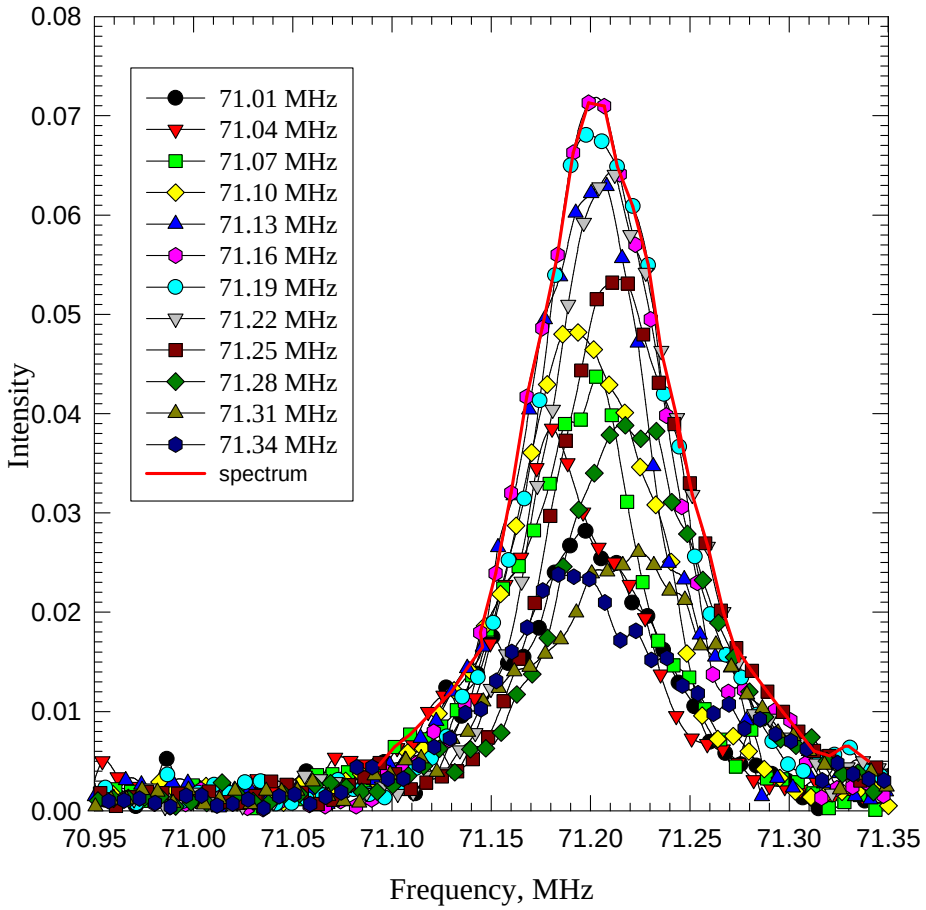

Figure 2.6.3.4. ^{57}Fe NMR spectrum of Fe_2O_3 (red line) obtained by overlapping of individual Fourier transforms (symbols and black lines) of spin echo signal excited by different excitation frequencies. *T*=295K.

2.6.4 Temperature dependence measurements setup.

The temperature dependence measurements were carried out using a continuous flow helium cryostat CF 1200 (Oxford Instruments) with temperature controller ITC4 (Oxford Instruments). In order to control temperature on the sample more precisely additional temperature monitor “Lake Shore” model 218 was used with temperature sensor attached directly to the sample.

3. General properties and NMR investigations of studied magnetic oxides

3.1. General properties and NMR studies of Yttrium Iron Garnet (YIG)

3.1.1. Crystal structure of YIG

Yttrium iron garnet (YIG) is a ferrimagnetic material which is widely used in various microwave and optical-communication devices and other applications - mainly due to its suitable magnetic and magneto-optical properties. The well-known properties of YIG are following: Curie temperature 560 K, saturation magnetization is about 0.2 T (bulk YIG at room temperature), Faraday rotation in doped garnets: -3000-(-4000) degrees/cm for Ce-doped YIG films.

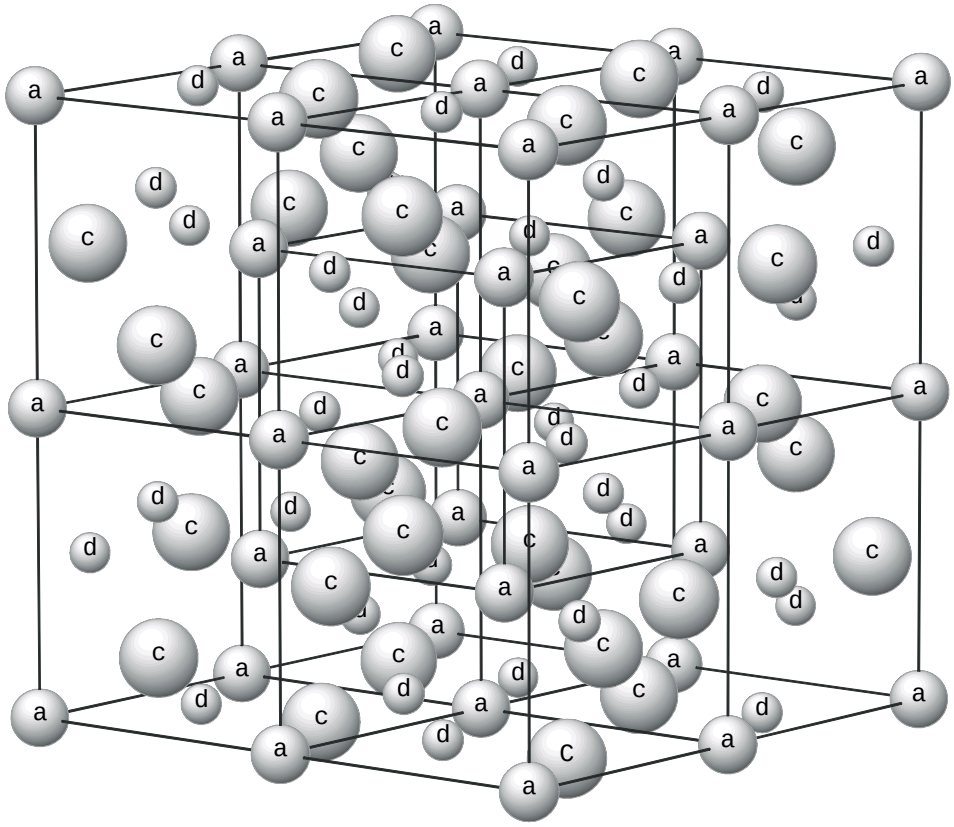

Figure 3.1.1. Cation arrangement in the unit cell of $Y_3Fe_5O_{12}$.

According to a structure analysis [Gell57] yttrium iron garnet belongs to a space symmetry group O_h^{10} (Ia-3d), i.e. it has a body-centered Bravais lattice. Its unit cell contains eight formula units $\{Y_3\}$ $[Fe_2]$ (Fe_3) O_{12}. Different brackets { }, [ ], ( ) are used to denote three different cation sites or types of coordinations to oxygen: { }for 8-fold (i.e. dodecahedron), [ ] for 6- fold (octahedron), ( ) for 4-fold (tetrahedron). The cations are located at the centers of corresponding oxygen polyhedrons. The Y^{3+} ions occupy dodecahedral or {c}-sites, while Fe^{3+} ions occupy octahedral or [a]-sites and tetrahedral or (d)-sites. In fig 3.1.1 a cations arrangement in the unit cell of yttrium iron garnet is demonstrated.

Sublattice	**a**	**c**	**d**	**h**	
Ion	**Fe^{3+}**	**Y^{3+}**	**Fe^{3+}**	**O^{2-}**	
Ionic radius	**0.0645 nm**	**0.1019 nm**	**0.0490 nm**	**0.1400 nm**	
Amount in unit cell	**16**	**24**	**24**	**96**	
Point symmetry	**C_{3i}**	**D_2**	**S_4**	**C_i**	
Coordination to oxygen	**6**	**8**	**4**		
	Coordinates	**Coordinates**	**Coordinates**	**Coordinates**	**Coordinates**
1	**0,0,0**	**⅛,0,¼**	**⅜,0,¼**	**x,y,z**	**-x,y+½,-z+½**
2	**0,½,½**	**¼,⅛,0**	**¼,⅜,0**	**z,x,y**	**-z+½,-x,y+½**
3	**½,0,½**	**0,¼,⅛**	**0,¼,⅜**	**y,z,x**	**y+½,-z+½,-x**
4	**½,½,0**	**⅜,0,¾**	**⅛,0,¾**	**y+¾,x+¼,-z+¼**	**y+¼,-x+¼,z+¾**
5	**¼,¼,¼**	**¾,⅜,0**	**¾,⅛,0**	**x+¾,z+¼,-y+¼**	**-x+¾,-z+¾,-y+¾**
6	**¼,¾,¾**	**0,¾,⅜**	**0,¾,⅛**	**z+¾,y+¼,-x+¼**	**-z+¼,y+¾,x+¼**
7	**¾,¼,¾**	**⅝,0,¼**	**⅞,0,¼**	**-x,-y,-z**	**x,-y+½,z+½**
8	**¾,¾,¼**	**¼,⅝,0**	**¼,⅞,0**	**-z,-x,-y**	**z+½,x,-y+½**
9		**0,¼,⅝**	**0,¼,⅞**	**-y,-z,-x**	**-y+½,z+½,x**
10		**⅞,0,¾**	**⅝,0,¾**	**-y+¼,-x+¾,z+¾**	**-y+¾,x+¾,-z+¼**
11		**¾,⅞,0**	**¾,⅝,0**	**-x+¼,-z+¾,y+¾**	**x+¼,z+¼,y+¼**
12		**0,¾,⅞**	**0,¾,⅝**	**-z+¼,-y+¾,x+¾**	**z+¾,-y+¼,-x+¾**
13				**-x+½,-y,z+½**	**x+½,-y+½,-z**
14				**z+½,-x+½,-y**	**-z,x+½,-y+½**
15				**-y,z+½,-x+½**	**-y+½,-z,x+½**
16				**-y+¾,-x+¾,-z+¾**	**-y+¼,x+¾,z+¼**
17				**-x+¼,z+¾,y+¼**	**x+¼,-z+¼,y+¾**
18				**z+¼,-y+¼,x+¾**	**-z+¾,-y+¾,-x+¾**
19				**x+½,y,-z+½**	**-x+½,y+½,z**
20				**-z+½,x+½,y**	**z,-x+½,y+½**
21				**y,-z+½,x+½**	**y+½,z,-x+½**
22				**y+¼,x+¼,z+¼**	**y+¾,-x+¼,-z+¼**
23				**x+¾,-z+¼,-y+¾**	**-x+¾,z+¾,-y+¼**
24				**-z+¾,y+¾,-x+¼**	**z+¼,y+¼,x+¼**

Table 3.1.1. Crystallographic data of YIG. Lattice constant a=1.2376; 1.2361; 1.2359 nm at the temperatures T=296; 77; 4.2 K [Levi66]. The oxygen parameters are x=-0.027, y=0.057, z=0.149 [Gell57, Eule65, Bonn75]. Remaining part of the ions in the unit cell can be found by translation (½,½,½).

Each oxygen ion belongs simultaneously to two dodecahedrons, one octahedron and one tetrahedron. None of these polyhedrons is regular with respect to an edge length. The deviation from ideal geometry in YIG was first described in the work [Gell57]. The position of the oxygen sites per formula unit is indicated by a set of three parameters x, y, z (expressed in fraction of the lattice constant a). The crystallographic data for YIG are presented in table 3.1.1.

From the viewpoint of NMR study of magnetically ordered materials the nearest environment of a studied ion plays an essential role. Detailed description of a neighborhood of cations belonging to different sublattices is given below.

Octahedral positions

Schematic representation of the arrangement of neighboring ions around Fe cation in *a* position is shown in figure 3.1.2. The figure depicts a fragment of a cluster centered at the Fe atom that is octahedrally coordinated in the crystal.

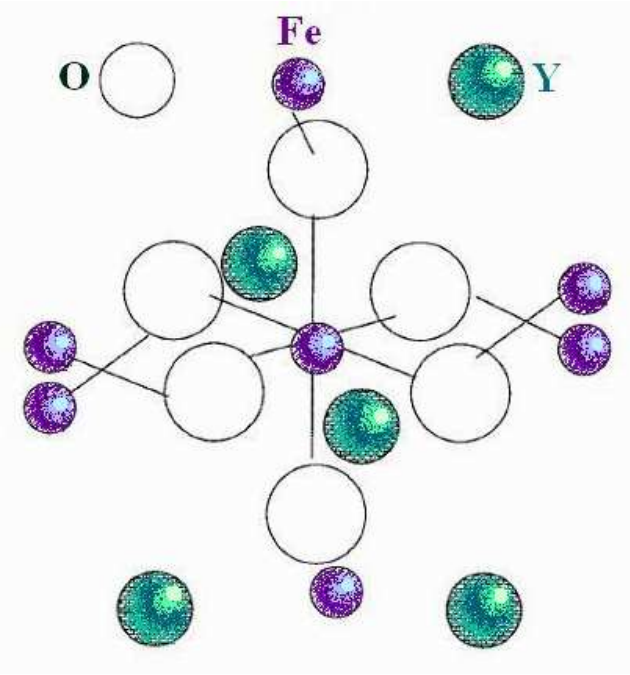

Figure 3.1.2. Schematic representation of the arrangement of neighboring ions around an octahedrally coordinated Fe cation.

Interatomic distances between Fe^{3+} ion in *a*-position and its neighbors from the nearest environment are collected in table 3.1.2:

Ion	Number of nearest neighbors	Distance from Fe^{3+}(a) [nm]
O^{2-}	6	0.2011
Fe^{3+}(d)	6	0.3454
Y^{3+}	2	0.3454

Table 3.1.2. Interatomic distances and amount of nearest neighbors for a Fe^{3+} ion in *a*-position [Wink81].

Octahedral arrangement of oxygen ions around Fe^{3+} ion in *a*-position is given in figure 3.1.3. The local symmetry axis C_{3i} for *a*-positions is along [111] direction.

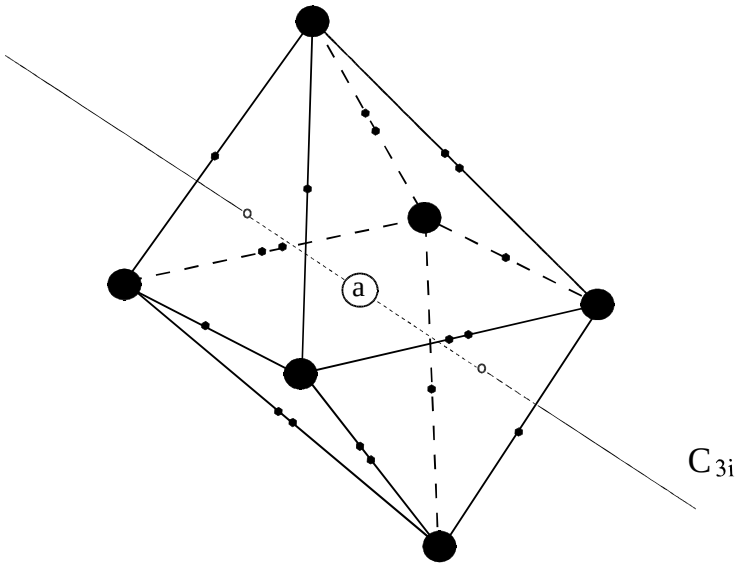

Figure 3.1.3. Coordination octahedron of oxygen ions (•) around Fe^{3+}(a) position (• 0.268nm, • • 0.299nm).

Tetrahedral positions

Schematic representation of the arrangement of neighboring ions around Fe cation in *d* position is shown in figure 3.1.4. The figure depicts a fragment of a cluster centered at the Fe atom that is tetrahedrally coordinated in the crystal.

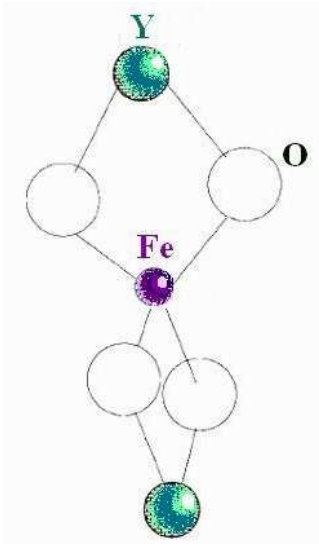

Figure 3.1.4. Schematic representation of the arrangement of neighboring ions around a tetrahedrally coordinated Fe cation.

Interatomic distances between Fe^{3+} ion in *d*-position and its neighbors from the nearest environment are given in table 3.1.3:

Ion	Number of nearest neighbors	Distance from Fe^{3+}(d) [nm]
O^{2-}	4	0.1868
Y^{3+}	2	0.3090
O^{2-}	4	0.3426
Fe^{3+}(a)	4	0.3454
O^{2-}	4	0.3679
Y^{3+}	4	0.3784
Fe^{3+}(d)	4	0.3784

Table 3.1.3. Interatomic distances and the number of nearest neighbors for Fe^{3+} ion in *d*-position.

Tetrahedral arrangement of oxygen ions around Fe^{3+} ion in *a*-position is given in the figure 3.1.5. The local symmetry axis $S_4 = C_{2i}$ for *d*-positions is along [100] direction.

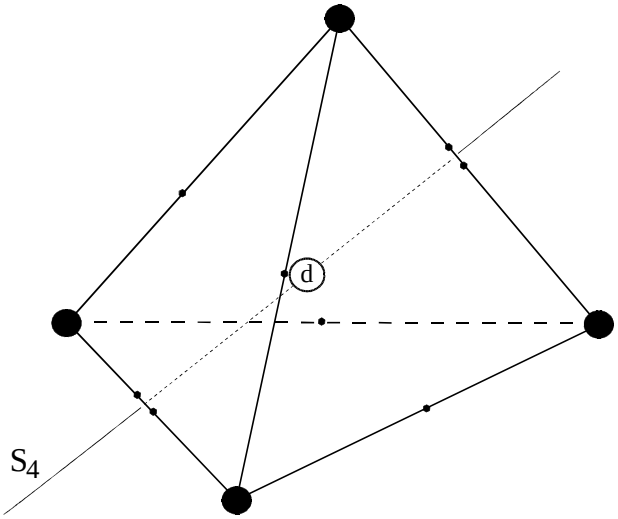

Figure 3.1.5. Coordination tetrahedron of oxygens (•) around Fe^{3+}(d) ion (• 0.316nm, • • 0.287nm).

Dodecahedral positions

Schematic representation of the arrangement of neighboring ions around Y cation in *c* position is shown in figure 3.1.6. The figure depicts a fragment of a cluster centered at the Y atom that is dodecahedrally coordinated in the crystal.

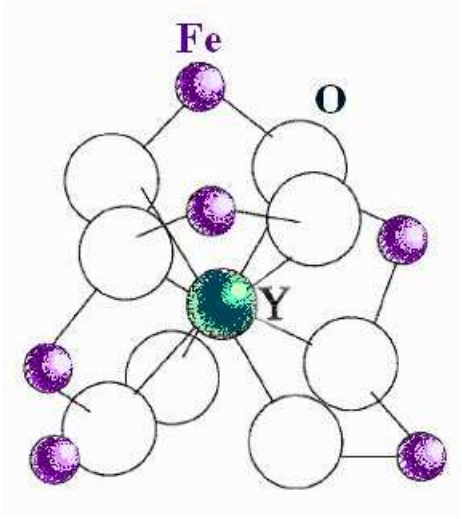

Figure 3.1.6. Schematic representation of the arrangement of neighboring ions around a dodecahedrally coordinated Y cation.

Interatomic distances between Y^{3+} ion in *c*-position and its neighbors from the nearest environment are collected in table 3.1.4:

Ion	Number of nearest neighbors	Distance from Y^{3+}(c) [nm]
O^{2-}	4	0.2356
O^{2-}	4	0.2428
Fe^{3+}(d)	2	0.3090
Fe^{3+}(a)	4	0.3454
Fe^{3+}(d)	4	0.3784
Y^{3+}	4	0.3784

Table 3.1.4. Interatomic distances and numbers of nearest neighbors of Y^{3+} ion in *c*-position.

Dodecahedral arrangement of oxygen ions around Y^{3+} ion in *c*-position is given in the figure 3.1.7.

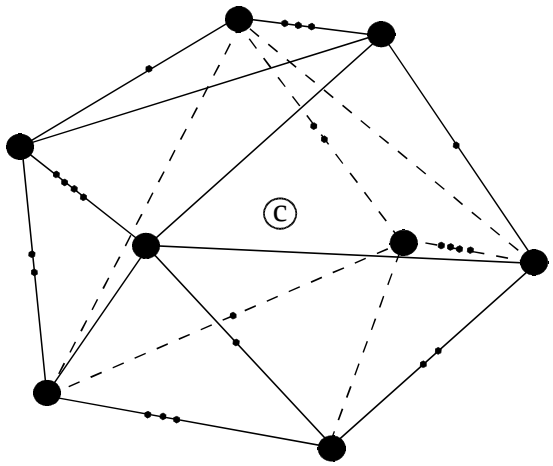

Figure 3.1.7. Coordination dodecahedron of oxygen ions (•) around Y^{3+}(c) ion (• 0.268nm, • • 0.281nm, • • • 0.287nm, • • • • 0.296nm).

3.1.2. Magnetic properties of YIG

The $Y_3Fe_5O_{12}$ belongs to the class of ferrimagnetic oxide compounds. The exchange interaction of Fe^{3+} ions, possessing magnetic moment, takes place through an oxygen ion situated between them (indirect mechanism). In this type of interaction, denoted as superexchange interaction [Ande50, Kram34], spins of magnetic ions are coupled by the interaction via an electron system of oxygen anions. This mechanism corresponds to a so-called configuration interaction, when a ground state configuration and an excited state of this configuration form by superposition a new state with lower energy [Ande63]. The theory predicts maximum superexchange interaction for the angle Fe^{3+}- O^{2-} Fe^{3+} of 180 degrees and small Fe^{3+} - O^{2-} distance. In the case of YIG the strongest interaction occurs between Fe^{3+}(*a*) and Fe^{3+}(*d*) ions for which the Fe^{3+}(*a*) - O^{2-} - Fe^{3+}(*d*) angle is 125.9° [Wink81]. Because interaction of this type is known to be negative in ferrites and because there are $3Fe^{3+}$(*d*) and $2Fe^{3+}$(*a*) ions per formula unit, there should be a net magnetic moment corresponding to one Fe^{3+} ion, i.e. $5\mu_B$. The magnetic moments of Fe^{3+}(*a*) and Fe^{3+}(*d*) ions are antiparallel [Bert56] below Curie temperature Tc=560K [Gell64].

3.1.2.1 Magnetocrystalline properties.

The part of an energy of a magnetic crystal which depends on its magnetic state can be expressed as a sum of four different energies: exchange energy, magnetocrystalline anisotropy energy, magnetoelastic energy and magnetostatic energy. The part corresponding to the exchange energy can be expressed in the form:

$$F_{ex} = -\sum_{i}^{N_K} \sum_{\delta}^{N_B} J_{i,i+\delta}\, S_i\, S_{i+\delta} \qquad (3.1.2.1)$$

where $J_{i,j}$ are exchange integrals, N_K is the number of magnetic ions in the crystal, N_B is the number of magnetic ions from the nearest neighborhood of a magnetic ion under consideration keeping in view the short range of the exchange interaction. This and following formulae are assumed to be applied (or normalized) to a unit volume of a magnetic crystal.

Magnetic properties of YIG are defined by magnitude of the magnetization as well as by orientation of the magnetization vector with respect to the crystallographic axes of the crystal. Because of an anisotropy, the magnetization vector adopts certain preferential directions in the

crystal lattice, the so–called directions of ‘easy’ magnetization (easy axes). For a description of the corresponding free energy F_K a system of coordinates is defined in such a way that its axes coincide with the main directions of the crystal [100], [010], [001]. It is convenient to expand F_K as a power series in directional cosines α_i of the magnetization direction relative to these crystallographic axes:

$$F_K(\vec{\alpha}) = K_1\, s + K_2\, p + K_3\, s^2 + K_4\, s\, p + \ldots \qquad (3.1.2.2)$$

where $s = \alpha_1^2\,\alpha_2^2 + \alpha_2^2\,\alpha_3^2 + \alpha_1^2\,\alpha_3^2$, $p = \alpha_1^2\,\alpha_2^2\,\alpha_3^2$, K_i are anisotropy constants.
Anisotropy constants for YIG can be found in reported tables [Escu75, Pear62, Hans74, Escu75].

When magnetizing garnet, a spontaneous elastic deformation occurs. Due to this deformation which originates from the interaction of the spin system with the lattice, the symmetry of the crystal is slightly disturbed (magnetostriction). Energetically, the appearance of the magnetostriction leads to minimization of the crystal magnetic energy. Corresponding contribution to the free energy can be written in the form:

$$F_{me}(\vec{\alpha},\vec{e}) = b_1 \sum_{i=1}^{3} \alpha_i^2 e_{ii} + b_2 \sum_{i>j}^{3} \alpha_i \alpha_j e_{ij} \qquad (3.1.2.3)$$

where b_i are the magnetoelastic coupling constants, which govern the magnetostrictive effects; and e_{ij} are the components of deformation tensor (i.e. a tensor describing the locations of the points of a body after deformation with respect to their location before deformation. It is a symmetric tensor of the second rank).

The pure elastic contribution to the free energy can be written in the form:

$$F_e(\vec{e}) = \frac{1}{2} \sum_{i=1}^{3} C_{11}\, e_{ii}^2 + \sum_{i>j}^{3} \left(\frac{1}{2} C_{44}\, e_{ij}^2 + C_{12}\, e_{ii}\, e_{jj} \right) \qquad (3.1.2.4)$$

where C_{ij} are the cubic elastic constants.
The equilibrium magnitudes of deformation can be derived from the equilibrium condition of the total energy:

$$\frac{\partial \left(F_{me}(\vec{\alpha},\vec{e}) + F_e(\vec{e}) \right)}{\partial\, e_{ij}} = 0 \qquad (3.1.2.5)$$

In the analysis of experimental data the magnetostriction constants λ are usually used, which denotes the relative changes in length $\delta l/l$ of a single crystal along the principal crystallographic directions. For garnets structures the relative changes in the linear dimension

δl/l of a magnetic crystal along an arbitrary direction **β**(β_1, β_2, β_3) can be described with only two constants, λ_{100} and λ_{111} :

$$\delta l/l = \frac{3}{2}\lambda_{100}\left(\alpha_1^2\beta_1^2 + \alpha_2^2\beta_2^2 + \alpha_3^2\beta_3^2\right) + 3\lambda_{111}\left(\alpha_1\alpha_2\beta_1\beta_2 + \alpha_2\alpha_3\beta_2\beta_3 + \alpha_3\alpha_1\beta_3\beta_1\right) \quad (3.1.2.6)$$

For **α || β**, the relative change in length along [100] and [111] directions can be expressed as:

$$\begin{aligned} \delta l/l_{[100]} &= \lambda_{100} = -\frac{2}{3}b_1/(C_{11} - C_{12}) \\ \delta l/l_{[111]} &= \lambda_{111} = -\frac{1}{3}b_2/C_{44} \end{aligned} \quad (3.1.2.7)$$

The elastic and magnetoelastic constants of YIG could be found in [Haus76, Safa71, Lach69].

Magnetostatic energy means the potential energy of a magnetic body in the magnetic field. It is composed of the magnetostatic interaction of that body with the external field F_H= - ***MB₀*** and with its own demagnetizing energy F_D= - $^1/_2$ ***MB_D***.

The easy directions of magnetization can be derived from the minimization of sum of anisotropic parts of the energy. In the case of yttrium iron garnet corresponding calculation turns out that easy axes of magnetization coincide with [111] direction.

Equilibrium magnetic state of a system should satisfy the condition of total energy minima. From the energetic viewpoint, the more preferable magnetic state in the case of YIG is a state with a splitting into a regions of uniform magnetization, so-called magnetic domains. The direction of magnetization is different from one domain to another.

3.1.2.2 Temperature dependence of saturation magnetization: molecular field and spin wave approaches.

Molecular field approximation.

In the frame of this approximation one has to consider only one magnetic atom and replace its interactions with the remainder of the crystal by an effective field.

$$\begin{aligned} \hat{H} &= -\sum_{i=1}^{N} \boldsymbol{S}_i \sum_{j=1}^{z} J_{ij}\, \boldsymbol{S}_j - g\mu_B \sum_{i=1}^{N} \boldsymbol{S}_i\, \boldsymbol{B}_0 = -g\mu_B \sum_{i=1}^{N} \boldsymbol{S}_i \left(\boldsymbol{B}_0 + \boldsymbol{B}_e\right), \\ \boldsymbol{B}_e &= \frac{1}{g\mu_B} \sum_{j=1}^{z} J_{ij}\, \boldsymbol{S}_j \end{aligned} \quad (3.1.2.8)$$

where J_{ij} are exchange constants, S_i is magnetic spin of the atom *i*, N- number of magnetic atoms in the crystal, z- amount of nearest neighbors, B_e- effective (molecular) field, μ_B is the Bohr magneton.

The next step is an assumption that each S_i can be replaced by its average value $\langle S_i \rangle$. Thus, assuming $J_{ij}=J$

$$\boldsymbol{B}_e = zJ/(g\mu_B)\langle \mathbf{S}_i \rangle = zJ/(N(g\mu_B)^2)\,\mathbf{M} \qquad (3.1.2.9)$$

Here **M** is the total magnetic moment of the crystal ($\mathbf{M}=Ng\mu_B\langle \mathbf{S}_i \rangle$).

Effective field, therefore, could be written as $\boldsymbol{B_e}=\lambda\,\mathbf{M}$.

Taking $\boldsymbol{B_0}$ to be along the z-axis one-particle Hamiltonian is then

$$\hat{H}_1 = -g\mu_B S^z B$$
$$\text{and has eigenvalues} \quad E = -g\mu_B m B, \quad m = S, S-1, \ldots, -S \qquad (3.1.2.10)$$

Where $\boldsymbol{B}$ is a total field acting on the atom: $\boldsymbol{B}=\boldsymbol{B}_0+\boldsymbol{B}_e$.

The corresponding partition function and magnetic moment of the sample can be easily calculated. In particular,

$$M = Ng\mu_B S\, B_S(x) = M(0)\, B_S(x), \qquad x = \frac{g\mu_B B}{k_B T} \qquad (3.1.2.11)$$

Where k_B is the Boltzmann's constant, T is a temperature, $M(0)=Ng\mu_B S$ value of the magnetic moment of the crystal at zero temperature, $B_s(x)$ is the Brrillouin function.

$$B_s(x) = \frac{2S+1}{2S}\coth\left(\frac{2S+1}{2S}x\right) - \frac{1}{2S}\coth\left(\frac{x}{2S}\right) \qquad (3.1.2.12)$$

In the case of yttrium iron garnet there are two different types of crystallographic sites occupied by magnetic atoms (but a single kind of magnetic atom) and, therefore, two different molecular fields acts on the atoms at different sublattices.

$$\boldsymbol{B}_a = \boldsymbol{B}_0 + \lambda_{aa}\,\boldsymbol{M}_a + \lambda_{ad}\,\boldsymbol{M}_d$$
$$\boldsymbol{B}_d = \boldsymbol{B}_0 + \lambda_{ad}\,\boldsymbol{M}_a + \lambda_{dd}\,\boldsymbol{M}_d \qquad (3.1.2.13)$$

Here λ_{ad}, λ_{aa}, λ_{dd} are molecular field coefficients for the interactions *a-d*, *a-a*, *d-d*, respectively.

Let *N* be the total number of magnetic atoms, ν the fraction of magnetic atoms on *a*-sites and $\mu=1-\nu$ the fraction of magnetic atoms on *d*-sites. Let us now introduce the parameters

$$\alpha = \lambda_{aa}/\lambda_{ad}\ , \quad \beta = \lambda_{dd}/\lambda_{ad}$$

$$m_a(\mathrm{T}) = \frac{M_a(\mathrm{T})}{M_a(0)} = M_a(\mathrm{T})/(\nu N g \mu_B S) \qquad (3.1.2.14)$$

and

$$m_d(\mathrm{T}) = \frac{M_d(\mathrm{T})}{M_d(0)} = M_d(\mathrm{T})/(\mu N g \mu_B S)$$

Therefore, the molecular fields can be written in the form:

$$\begin{aligned} \boldsymbol{B}_{\mathrm{a}} &= \boldsymbol{B}_0 + N g \mu_B S \lambda_{\mathrm{ad}} (\nu\, \alpha\, \boldsymbol{m}_{\mathrm{a}} + \mu\, \boldsymbol{m}_{\mathrm{d}}) \\ \boldsymbol{B}_{\mathrm{d}} &= \boldsymbol{B}_0 + N g \mu_B S \lambda_{ad} (\nu\, \boldsymbol{m}_{\mathrm{a}} + \mu\, \beta\, \boldsymbol{m}_{\mathrm{d}}) \end{aligned} \qquad (3.1.2.15)$$

The corresponding molecular field equations are:

$$\begin{aligned} m_a &= B_S(g\mu_B S B_a/(kT)) \\ m_d &= B_S(g\mu_B S B_d/(kT)) \end{aligned} \qquad (3.1.2.16)$$

These equations being applied to YIG with assumption of zero external magnetic fields have the form [Dion70, Nova88]:

$$\begin{aligned} m_a(T) &= B_S(x_a), \qquad x_a = \frac{C}{T}\left(\lambda_{aa} m_a + \frac{3}{2}\lambda_{ad} m_d\right) \\ m_d(T) &= B_S(x_d), \qquad x_d = \frac{C}{T}\left(\lambda_{ad} m_a + \frac{3}{2}\lambda_{dd} m_d\right) \end{aligned} \qquad (3.1.2.17)$$

Where $C = 2N_A(g\mu_B S)^2/k_B$. The experimental values for molecular coefficients of YIG are $\lambda_{ad} = 97$ mol/cm^3, $\lambda_{aa} = -65$ mol/cm^3, $\lambda_{dd} = -30.4$ mol/cm^3 [Dion70].

Equation (3.1.2.16) must be solved simultaneously to give temperature dependence of YIG sublattice magnetization.

Molecular field theory gives rather good description of the experimental results in the region of higher temperatures. Within a low temperature range the spin wave approximation allows better treatment of the temperature behavior of sublattice magnetization.

Spin wave approximation.

At any nonzero temperature there is some probability that individual spins have deviated from the equilibrium. In reality such excitations are distributed over the whole spin system. The precession angle of all spins is slightly increased. The resultant nonuniform magnetization can be described in the form of plane waves of spin deviations, which have

been designated as “spin waves”. Quantized spin wave is called “magnon”. A magnon can be considered in many respects as a free particle governed by Bose - Einstein statistic. For the temperature dependence of sublattice magnetization in ferrimagnetic materials in the region of low temperatures the spin wave approximation gives the so-called “$T^{3/2}$ law” [Bloc30]:

$$\frac{M(T)}{M(0)} = 1 - A_1 T^{3/2} - A_2 T^{5/2} - A_3 T^{7/2} - \ldots \qquad (3.1.2.18)$$

Here A_i are coefficients dependent on type of structures and exchange integrals. For YIG structure above-mentioned values can be found in [Gona67].

3.1.3. NMR in Yttrium Iron Garnet

3.1.3.1. ^{57}Fe NMR in pure Yttrium Iron Garnet

The hyperfine field $\boldsymbol{B}_{hf} \equiv \vec{B}_{hf}$ on the ^{57}Fe nucleus in yttrium iron garnet can be written in the form:

$$\vec{B}_{hf} = \vec{B}_{free} + \vec{B}_c + \vec{B}_{dip} \qquad (3.1.3.1)$$

Here $\boldsymbol{B}_{\text{free}}$ is a field on the nucleus of a free ion Fe^{3+}, $\boldsymbol{B}_{\text{c}}$ is a crystal environment contribution, which arises from the partial covalent bonding of $Fe^{3+} \leftrightarrow O^{2-}$ and from a supertransfer hyperfine field depending on the magnetic moments of surrounding cations and $Fe^{3+} - O^{2-} - Fe^{3+}$ bond angle, $\boldsymbol{B}_{\text{dip}}$ is a dipolar field contribution caused by the surrounding magnetic moments. Contribution of $\boldsymbol{B}_c$ from the crystal environment can be treated in the frame of independent bond model [Engl85] (see the paragraph 3.1.3.5.5). This semiempirical model is based on the assumption that in a solid the ions keep to the first approximation their free ion character, the effect of an environment being a small perturbation. The Hamiltonian of the transition metal ion is then well approximated by the Hamiltonian of corresponding free ion plus contributions from its ligands. Within the superposition model the contributions of the individual ligands to the Hamiltonian are assumed to be mutually independent and axially symmetrical around the cation-ligand bond. Under these assumption the contribution $\boldsymbol{B}_c$ may be written as [Engl85]:

$$B_c = \sum_{i=1}^{N} \left(b_0^i + b^i \cos^2 \phi_i \right) \qquad (3.1.3.2)$$

where the sum is over the N ligands of the Fe^{3+} ion in question, b_o^i and b^i are called isotropic and anisotropic "intrinsic fields", ϕ_i is the angle which the magnetization makes with the bond of the Fe^{3+} to its i^{th} oxygen ligand. The intrinsic fields b_0^i, b^i depend only on the nature of the ligand and on the ligand-Fe^{3+} ion distance.

An essential role for the NMR spectra interpretation plays symmetry of the crystal. The ^{57}Fe nuclei disposed in *d* and *a* sites possess S_4 (C_{4i}) and C_{3i} symmetry respectively. As was shown [Robe62] the hyperfine field on the ^{57}Fe nuclei in yttrium iron garnet can be written in the form:

$$B_{hf} = B_I + B_{AN} \cdot \left(3\cos^2\theta - 1\right) \qquad (3.1.3.3)$$

Here B_I is isotropic and B_{AN} is anisotropic parts of the hyperfine field acting on ^{57}Fe nucleus, θ is an angle between magnetization direction and local symmetry axis. The isotropic part of the hyperfine field includes the hyperfine field of a free ion $\boldsymbol{B}_{\text{free}}$, the supertransfer hyperfine field $\boldsymbol{B}_{\text{st}}$ (the part of $\boldsymbol{B}_{\text{c}}$ depending on the magnetic moments of surrounding cations and Fe^{3+} - O^{2-} - Fe^{3+} bond angle) and the rest of isotropic part of $\boldsymbol{B}_{\text{c}}$. The contributions from dipolar field $\boldsymbol{B}_{dip}$ and from anisotropic part of the crystal field $\boldsymbol{B}_{\text{c}}$ are included in anisotropic part $\boldsymbol{B}_{AN}$.

In the case when magnetization lies along the <111> direction all S_4 symmetry axes of *d*-sites (lying along <100> direction) makes the same angle θ=54.74° with the magnetization direction. Therefore, keeping in view the expression (3.1.3.4), all *d* sites have equal NMR frequency and only one NMR line corresponding to the resonance on the ^{57}Fe nuclei in *d*-positions can be observed for that magnetization direction. In the case of a-sites there are two magnetically inequivalent sets of *a*-positions: a_1 with the local C_3 symmetry axis parallel to the magnetization θ_{a1}=0° and a_2 when the local three-fold symmetry axis and magnetization lie along different body diagonals θ_{a2}=70.53°. The ^{57}Fe NMR spectrum of yttrium iron garnet then consists of three lines with the ratio of intensities *d:* a_1*:* a_2 = 6: 1: 3.

3.1.3.2. Separation of domain wall and domain NMR.

As was already mentioned, the enhancement factor of the radio frequency field can be different for the domain signal and for the signal from the domain walls. This fact can be employed for the separation of domain wall and domain NMR.

For a spin-echo sequence with pulses of the duration τ_1 and $2\tau_1$ the dependence of the NMR echo amplitude B_1 on the *rf* field B_{rf} is given by:

$$B_1 \sim \left|\eta \sin(\varphi)\cos(2\varphi)\right| \qquad (3.1.3.4)$$

where $\varphi = \eta B_{rf} \tau_1 \gamma$ is the angle by which the nuclear spins are turned during the first rf pulse. This leads to maxima of the echo amplitude at

$$\varphi = \pi/2 + n\pi \qquad (3.1.3.5)$$

An example of the dependence of the spin echo amplitude on B_{rf} measured at frequency 76.05 MHz (a_2 line) in the ^{57}Fe NMR spectrum of YIG thin film at 4.2 K is shown in fig.3.1.3.1.

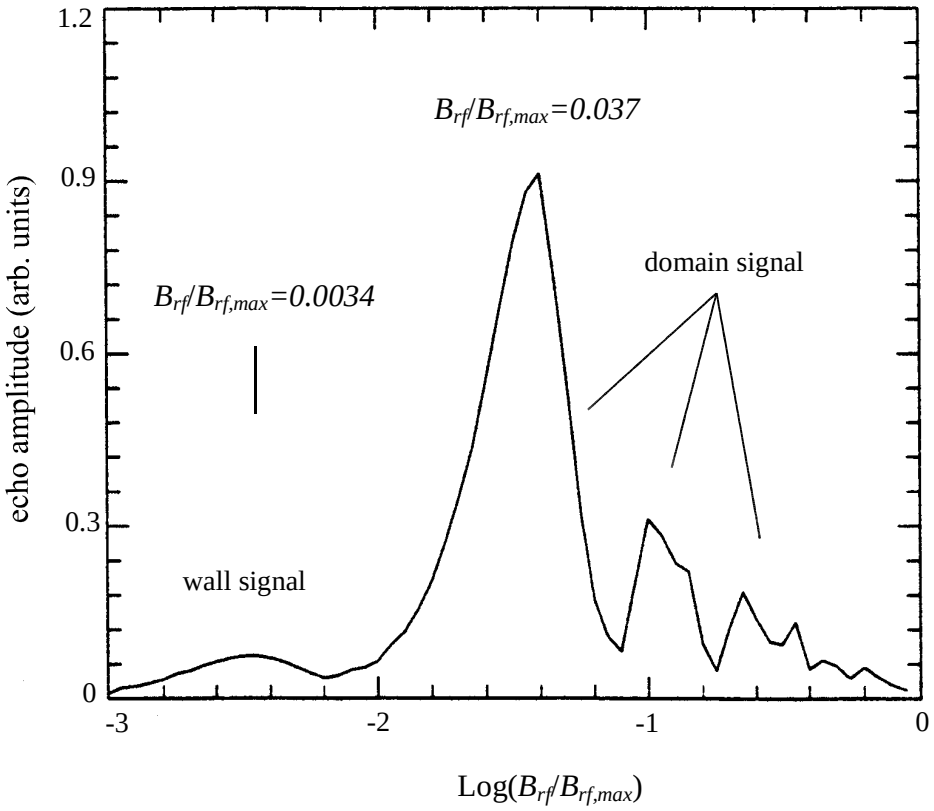

Figure 3.1.3.1. Dependence of the spin echo amplitude on the rf field B_{rf} scaled by its maximum value $B_{rf,\,max}$ (YIG thin film, f=76.05 MHz, T=4.2 K) [Engl98].

Maximum spin echo amplitude at $B_{rf} \sim 0.037\, B_{rf,\,max}$ (where $B_{rf,\,max}$ is the maximum value of B_{rf}) corresponds to $\varphi \sim \pi/2$. The next maximum occurs at higher B_{rf} ($B_{rf} \sim 0.12 B_{rf,\,max}$) that corresponds to n=1 in expression (3.1.3.5). In the region of still higher B_{rf} the inhomogeneity of the B_{rf} in the rf coil and of η leads to the loss of the signal intensity. As a consequence the

maxima for *n=2* and *n=3* are not clearly resolved. The maximum at the lowest $B_{rf} \sim 0.0034 B_{rf,\,max}$ is different in its character and corresponds to the wall signal.

The Fourier transform of the NMR signal excited with the $B_{rf} \sim 0.0034 B_{rf,\,max}$ and $B_{rf} \sim 0.037 B_{rf,\,max}$ was made. Corresponding spectra normalized to the maximum amplitude are shown in Fig. 3.1.3.2. With the high B_{rf} value the narrow domain signal is observed exactly at the frequency of the excitation (76.05 MHz) whereas for low B_{rf} a broad spectrum of the domain wall signal appears with the maximum at 76.1 MHz [Engl98]. The shift of the maximum corresponds to the different values of the hyperfine field for the magnetization along the easy [111] axis in domains and for the magnetization along the direction [110] in the center of the wall.

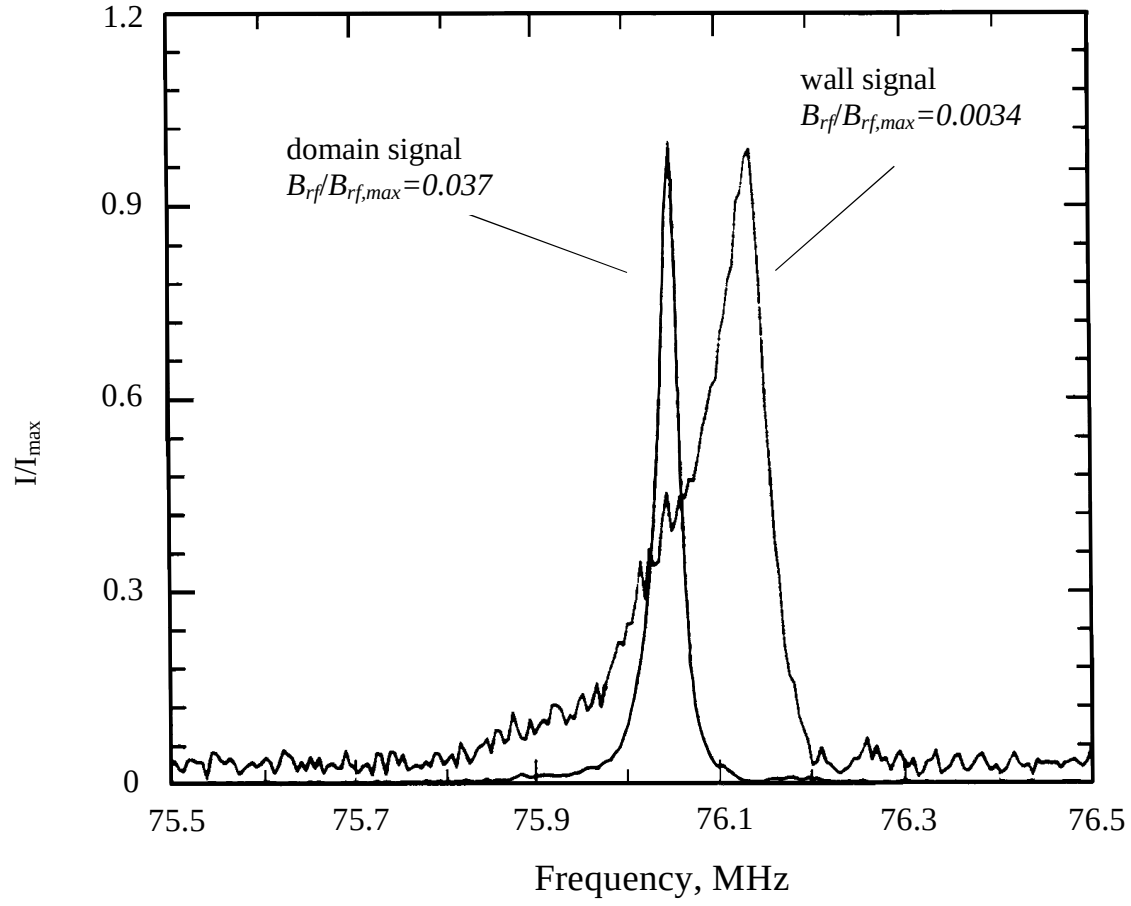

Figure 3.1.3.2. Fourier transform of the spin echo excited with two different B_{rf} amplitudes. (YIG thin film, f=76.05 MHz, T=4.2 K) [Engl98].

Selecting the excitation amplitude of rf field B_{rf} corresponding to the domain signal excitation the ^{57}Fe NMR spectrum (see figure 3.1.3.3) can be obtained where all lines *d*, a_1 and a_2 are well resolved.

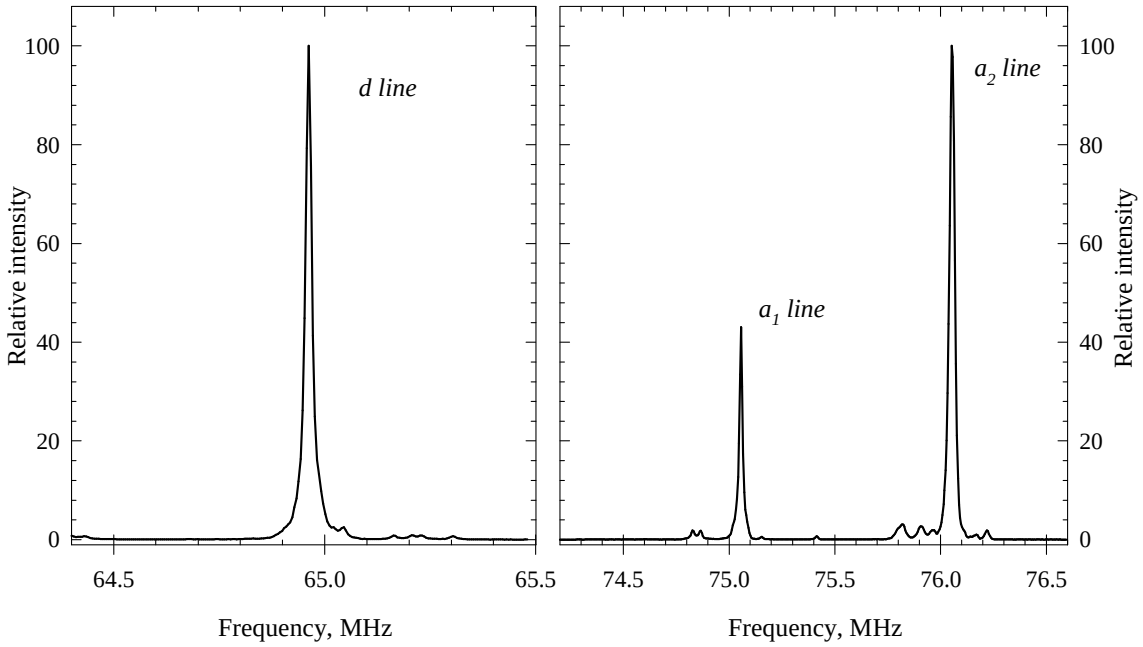

Figure 3.1.3.3. NMR spectrum of ^{57}Fe nuclei in YIG at 4.2 K in zero external magnetic field. Signal from the domains [Engl98].

The expression (3.1.3.3) can be rewritten in terms of frequencies:

$$\nu_j^l = \nu_I^l + \nu_{AN}^l \left(3cos^2\,\theta_j^l - 1\right) \qquad \text{where } l = \text{a , d} \tag{3.1.3.6}$$

Here ν_I^l and ν_{AN}^l are isotropic and anisotropic parts of the resonant frequency accordingly. From the resonant frequencies of the a_1 and a_2 lines the values of the ν_I^l and ν_{AN}^l can be determined unambiguously. In order to determine the corresponding frequency constants for *d* line the magnetization should be rotated to another then <111> direction by applying an external magnetic field. In Table 3.1.3.1 the values of these constants for *a* and *d* positions are displayed:

Position	ν_I^l [MHz]	ν_{AN}^l [MHz]	Paper
a	75.808	-0.366	[Camp92]
	75.809	-0.373	[Koho96]
d	64.958	-0.043	[Camp92]
	64.961	-0.046	[Koho96]

Table 3.1.3.1 Isotropic and anisotropic constants for *a* and *d*-positions in YIG.

Selecting the excitation amplitude of the radio frequency field corresponding to domain walls signal excitation the broad unresolved spectrum is observed (see figure 3.1.3.4) [Camp92].

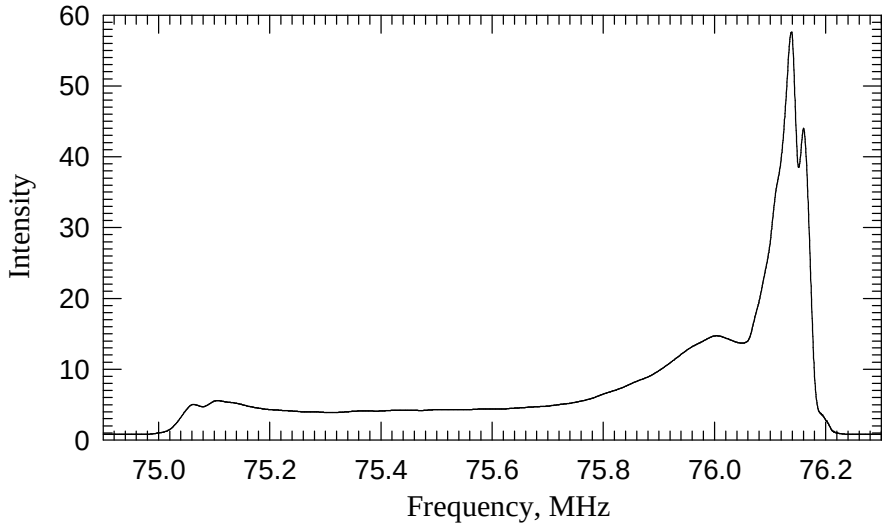

Figure 3.1.3.4. ^{57}Fe NMR spectrum of pure YIG, T=4.2 K. Signal from the domain walls [Engl98].

In some cases the differences between enhancement factors within domain (η_{dom}) and within domain wall (η_{wall}) are not large enough to separate the signal components from the walls and domains. Here the different spin-lattice relaxation rates in the domains and in the domain walls can help to separate the signals. In the domain walls low frequency excitations of the walls open an extra relaxation channel, which decreases the relaxation rates for the nuclei in the walls. If the repetition time of the echo sequence (TR) is longer than the spin lattice relaxation time of the walls ($T_{1\ wall}$), but shorter than the spin-lattice relaxation time of the domains ($T_{1\ dom}$), the domain

signal is severely attenuated and mainly the wall signal is left. The comparison of the spectra determined with fast and slow TR thus allows to separate wall`s and domain`s components of the signal. This is shown in figure 3.1.3.5 where the dependence of the spin echo intensity on B_{rf} is displayed for different values of TR [Engl98].

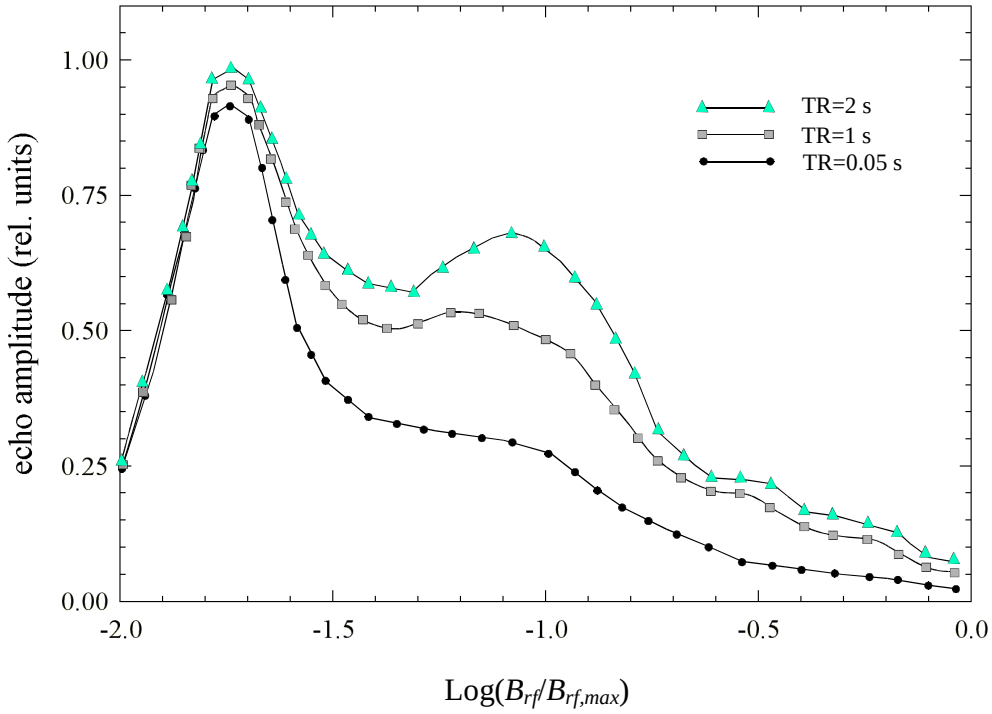

Figure 3.1.3.5. Dependence of the spin echo amplitude on $B_{rf} / B_{rf,\max}$ for three different repetition times TR of the echo sequences. (YIG:Ca, f = 76.05 MHz, T= 4.2 K) [Engl98].

As can be clearly seen from the figure 3.1.3.4, the ^{57}Fe NMR spectrum from the domain wall is much broader than in the case of spectra obtained from domains. The interpretation of corresponding NMR spectra obtained from the domain walls is rather complicated and mostly is used for obtaining information about domain wall parameters and dynamics. Below in this thesis we will be only dealing with ^{57}Fe NMR spectra obtained from the domains.

3.1.3.3. Y^{3+} antisite defects.

In an ideal yttrium iron garnet the octahedral *a*-sites and tetrahedral d-sites are occupied by the Fe^{3+} ions while dodecahedral *c*-positions are completely filled by the Y^{3+} ions. In real YIG system, however, a small amount of the Y^{3+} cations can appear on the Fe *a*-positions (Y antisite defect). Because of relatively large radius of Y^{3+} ion it prefers *a*-positions to relatively small *d*-sites when it replaces Fe^{3+} ion. When the magnetic Fe^{3+} ion is replaced by a nonmagnetic defect, the hyperfine field on the resonating Fe nuclei close to the defect is changed. If the change is larger than the NMR linewidth, satellite lines in the NMR spectra appear. In the figure 3.1.3.6 the rich satellite structure caused by the intrinsic Y antisite defects are displayed. The measurements were performed at liquid helium temperature and zero external magnetic field on the high purity YIG single crystal grown from the BaO/B_2O_3 flux.

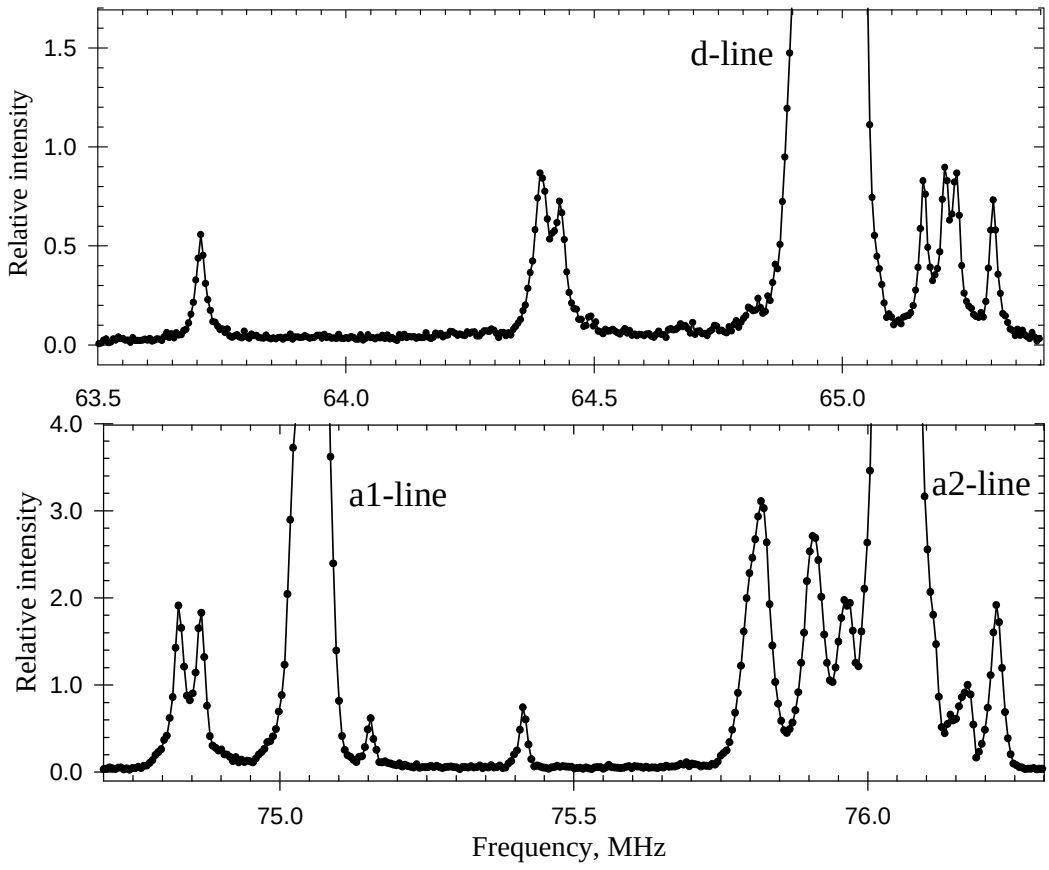

Figure 3.1.3.6. NMR spectrum of ^{57}Fe nuclei in the high purity YIG single crystal at 4.2 K. To see clearly the satellite structure, the spectra were magnified [Engl98].

3.1.3.4. ^{57}Fe NMR in substituted YIG.

A large number of cations exist which can be incorporated into the garnet lattice. From the point of view of valence states and crystallographic positions the YIG formula can be written in the following way:

$$\left\{Y_3^{3+}\right\}^c \left[Fe_3^{3+}\right]^d \left(Fe_2^{3+}\right)^a \; O_{12}$$

(3.1.3.7)

The character of the substitution is defined by its ionic radius and valency state in the corresponding crystallographic position. An important point is charge compensation. If, for example, a trivalent ion Fe^{3+} is substituted, the substituting ion must be trivalent or, if higher valent (ex.: Sn^{4+}, Ge^{4+}), it should be combined with a lower valent cation (ex.: Ca^{2+}, Co^{2+}). If one does not take this measure, the system may react in some sort of "internal compensation" by formation of Fe^{2+} ions (on doping with higher than 3+ valent cations) or Fe^{4+} ions (in the case of doping by lower than 3+ valent cations) or by other types of defects.

On performing substitutions, very often a distribution of the substituting ions on the different cation sites is observed, especially distribution between tetrahedral /octahedral and dodecahedral /octahedral sites. Some preferences, however, take place. Large trivalent cations with ionic radius close to the Y^{3+} ionic radius, as a rule, enter dodecahedral positions. The examples of such cations are Bi^{3+} and rare earth trivalent ions. Ions with spherical symmetry of the electron ground state substitute Fe^{3+} ions in tetrahedral or octahedral positions. Ions with radii smaller than Fe^{3+} ion radius prefer tetrahedral positions (Al^{3+}, Ga^{3+}) while ions greater than Fe^{3+} ion enter preferably octahedral positions (In^{3+}, Sc^{3+}). For small concentrations of substitutions these rules are satisfied with a good accuracy. And thereby for a small concentrations the chemical formula of the substituted garnet can be written in the form:

$$\left\{Y_{3-z}^{3+}\, R_z^{3+}\right\}^c \left[Fe_{3-x}^{3+}\, \left(Al^{3+},\, Ga^{3+}\right)_x\right]^d \left(Fe_{2-y}^{3+}\left(In^{3+},\, Sc^{3+}\right)_z\right)^a \; O_{12} \qquad (3.1.3.8)$$

where R_z^{3+} are trivalent rare earth cations, $x<0.5$ and $y< 0.35$ [Krup69,Wink81].

When a nonmagnetic substitution enters the system the hyperfine field on the resonating ^{57}Fe nuclei close to the substitution is changed. If the change is large enough (the frequency shift

should be larger than NMR linewidth) the satellite lines caused by ^{57}Fe nuclei having substitution in their closest neighborhood in the NMR spectra appear.

Let us consider a small concentration of "noncharged" defects entering the system (when the valency of impurity and substituted ion is the same). Supposing a random distribution of the defects over the sublattice, the probability for a substitution on a certain position is given by the concentration c of the substituent and of the Fe^{3+} ions in the corresponding sublattice. If there are N crystallographically equivalent positions in a certain vicinity of the resonating nucleus and M different satellite lines are generated in the spectrum by single substitution in this vicinity, the intensity ratio σ of a satellite line to its parent line is equals to:

$$\sigma = \frac{I_{sat}}{I_{main}} = \frac{N}{M} \cdot \xi, \qquad \text{where} \quad \xi = \frac{c}{1-c} \tag{3.1.3.9}$$

It should be noted that this relation makes possible to determine the concentration of the defect without using an external standard.

As far as the influence of the defect on the hyperfine field on the resonating nuclei decreases rapidly with the distance between nuclei and the defect, satellite lines caused by the distant defects are covered in most cases by the parent main lines. The only satellite lines are resolved that cause the change of the hyperfine field on the resonating nuclei large than corresponding parent line linewidth. The change of the hyperfine field ΔB_{hf} on the resonating nucleus caused by the presence of nonmagnetic impurity in its vicinity can be written (keeping in view expressions 3.1.3.2 and 3.1.3.3) as:

$$\Delta B_{hf}^{i} = \Delta B_{dip}^{i} + \Delta b_{o}^{i} + \Delta b^{i} \cos^2 \phi_i \tag{3.1.3.10}$$

where term ΔB^{i}_{dip} describes the changes of the dipolar field contribution caused by the substitution. Δb^{i}_{0} and Δb^{i} reflect the corresponding modification of the B_c contribution on the hyperfine field.

An interpretation of the ^{57}Fe NMR spectra in polycrystalline YIG containing nonmagnetic substitutions carried out in the frame of independent bond model (or "superposition model") can be found in [Engl85, Nova88]. Detailed discussion of the model from the point of view of later results is given in 3.1.3.5.5.

In the figure 3.1.3.7 ^{57}Fe NMR spectrum of $Y_3Fe_{3-x}Ga_xFe_2O_{12}$ is displayed. Concentration of the Ga^{3+} substitution is x=0.1 [Engl85, Step98]. Satellite lines denoted as $S^{Ga}_{1,i}$ describe the situation when $Ga^{3+}(d)$ located in the nearest cation neighbourhood of the resonating *Fe* nuclei in *a*-positions. $S^{Ga}_{2,i}$ lines relate to the case of resonating nuclei in *d*-positions having in the $Ga^{3+}(d)$ substitution in the second cation environment (*d*-sites).

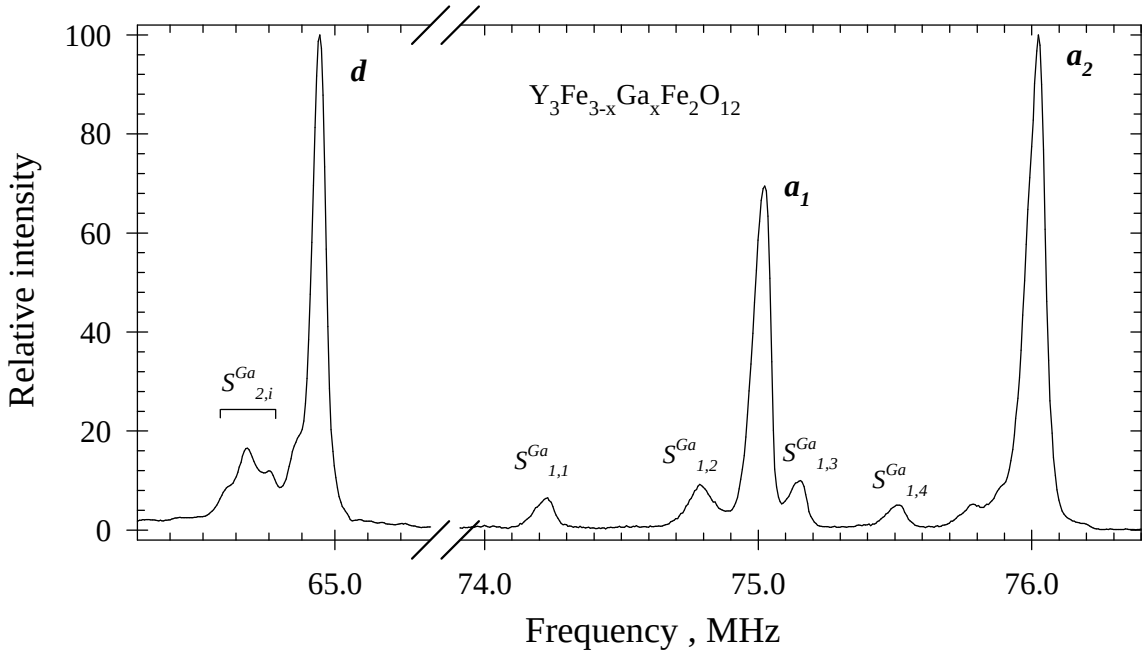

Figure 3.1.3.7. ^{57}Fe NMR spectrum of $Y_3Fe_{3-x}Ga_xFe_2O_{12}$ (x=0.1) at liquid helium temperature and zero external magnetic field.

In the figure 3.1.3.8 ^{57}Fe NMR spectrum of $Y_3Fe_{3-x}Al_xFe_2O_{12}$ is displayed. Concentration of the Al^{3+} substitution is x=0.1 [Step98].

Satellite lines denoted as $S^{Al}_{1,i}$ appear when $Al^{3+}(d)$ located in the nearest cation neighbourhood of the resonating *Fe* nuclei in *a*-positions. $S^{Al}_{2,i}$ lines relate to the case of resonating nuclei in *d*-positions having in the $Al^{3+}(d)$ substitution in the second cation environment (*d*-sites).

From the figure 3.1.3.8 it is clearly seen that the distances between parent (main) lines and corresponding satellite lines are large for *Ga*-substituted sample than for the *Al*-substituted one. That difference is caused by the fact that effect of the diamagnetic substitution on the hyperfine field at neighbouring iron nuclei depends remarkably on the ionic radius of the substituent [Step98] *($r(Ga^{3+})=0.047nm > r(Al^{3+})=0.039nm$)*.

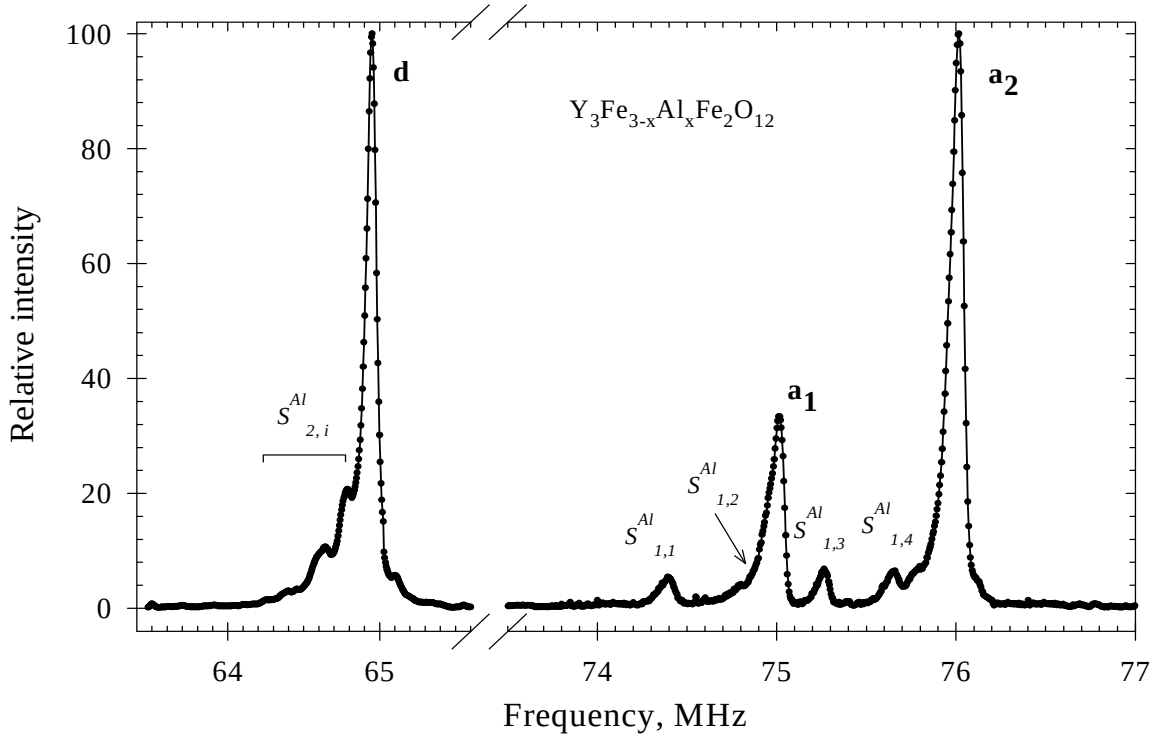

Figure 3.1.3.8. ^{57}Fe NMR spectrum of $Y_3Fe_{3-x}Al_xFe_2O_{12}$ (x=0.1) at T=4.2K and zero external magnetic field.

The ^{57}Fe NMR spectra of In^{3+} and Sc^{3+} substituted samples are displayed in the figure 3.1.3.9 [Koho96, Step98].

In^{3+} and Sc^{3+} ions substitute preferably, as was already mentioned, Fe^{3+} ions in *a*-sublattice of YIG. As far as the influence of the substitution on the resonating *Fe* nuclei decrease rapidly with the distance between resonating nuclei and substitution, it is expected that frequency shifts between satellite lines and corresponding parent line are larger for satellites originating from *d*-positions (denoted in the figure 3.1.3.9 as $d^{In}_{1,i}$ or $d^{Sc}_{1,i}$) because the defect in *a*-position is closer to *d*-position than to the *a* one. Satellite lines designated in the figure 3.1.3.9 as $a^{In}_{1,i}$ and $a^{In}_{2,i}$ ($a^{Sc}_{1,i}$ and $a^{Sc}_{2,i}$) relate to the situation, when *In* (or *Sc*) substituent is located in first (the case of $a^{In}_{1,i}$ and $a^{Sc}_{1,i}$ satellites) and in second ($a^{In}_{2,i}$ and $a^{Sc}_{2,i}$ satellite lines) *a*-cation neighbourhoods of the resonating nuclei. The different frequency distances between satellite lines and corresponding parent lines for *In*-substituted and *Sc*-substituted YIG samples result from the difference in the ionic radii of the substituents [Step98Y]: $r(In^{3+})=0.08nm > r(Sc^{3+})=0.074nm$.

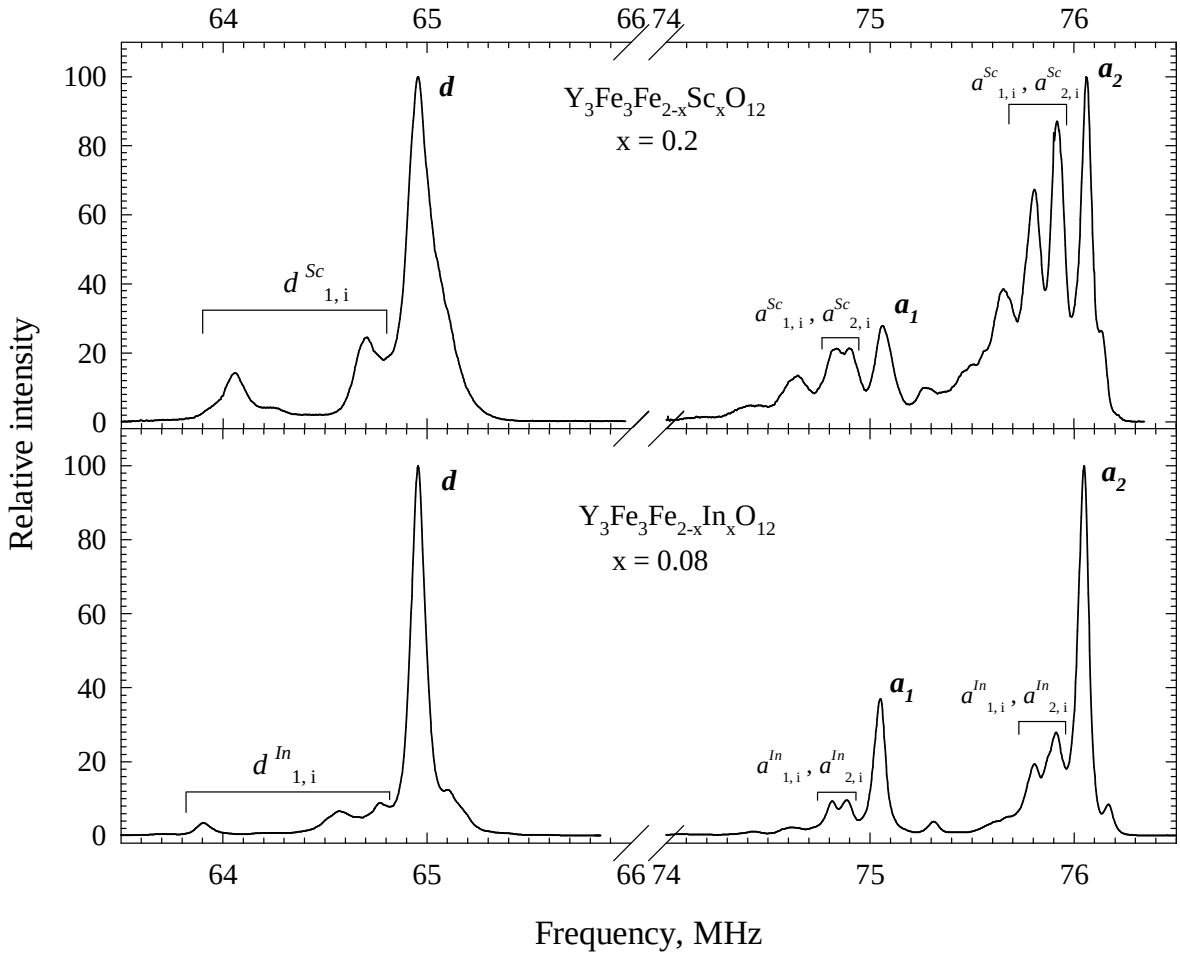

Figure 3.1.3.9. ^{57}Fe NMR spectra of In^{3+} and Sc^{3+} substituted YIG at liquid helium temperature and zero external magnetic field.

In the figure 3.1.3.10 the ^{57}Fe NMR spectrum of $Y_{3-x}Lu_xFe_5O_{12}$ (x=0.1) and spectrum of $Y_{3-x}La_xFe_5O_{12}$ (x=0.1) are displayed [Engl96, Koho96].

La^{3+} and Lu^{3+} substitutions occupy in the YIG system *c*-positions. In the figure 3.1.3.10 satellite lines designated as $d^{Lu}{}_1$ (or $d^{La}{}_1$) relate to the case, when resonating *Fe* nuclei in *d*-site has La^{3+} (or Lu^{3+}) in the nearest *c*-position. Satellites denoted as $a^{Lu}{}_1$ (or $a^{La}{}_1$) originates from the resonating nuclei in *a*-sublattice having in the nearest *c*-neighbourhood La^{3+} (or Lu^{3+}) substituent. Satellite lines $a^{Lu}{}_{1,2}$ (or $a^{La}{}_{1,2}$) correspond to the composite satellites, caused by two or more substitutions in the vicinity of resonating nucleus. Both spectra have similar satellite structure, but distances between satellite lines and corresponding main lines are larger for *La*-substituted sample. In addition, satellite lines caused by the substitutions are on different sides with respect to the parent lines.

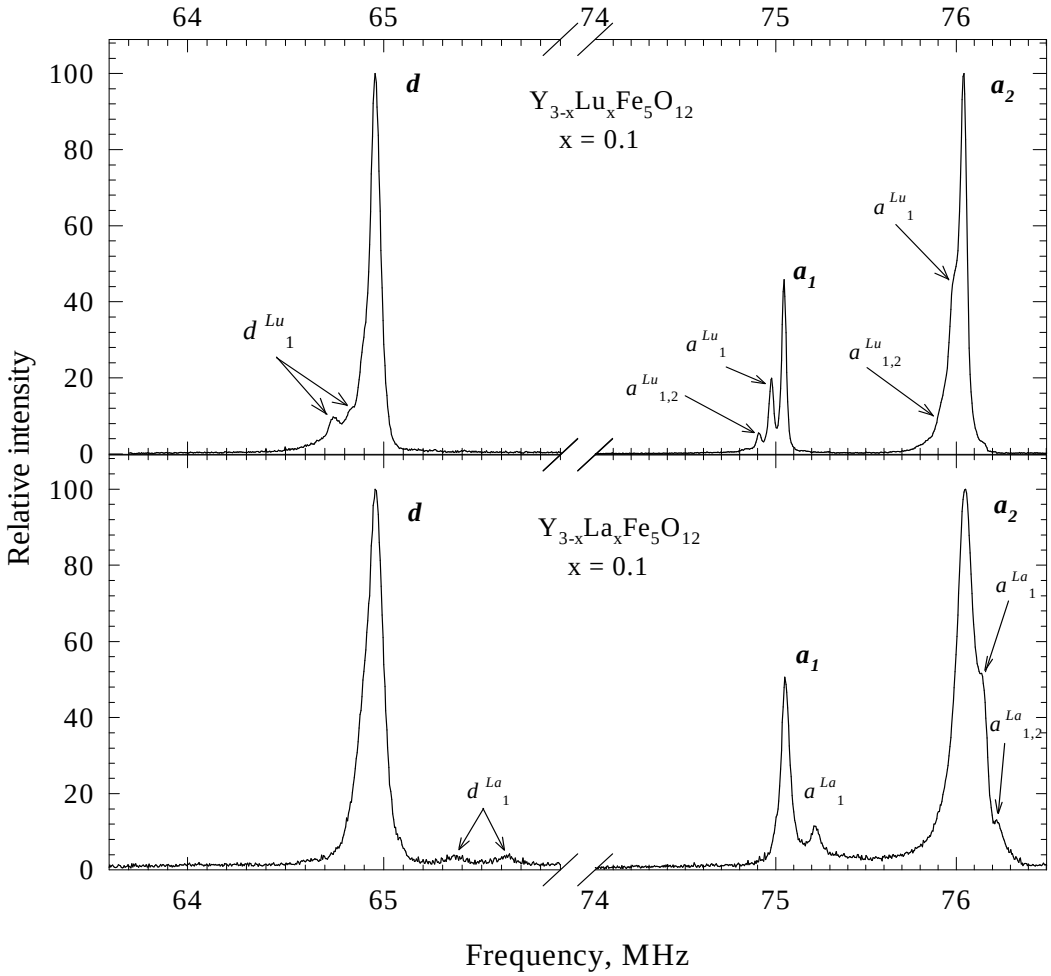

Figure 3.1.3.10. ^{57}Fe NMR spectra of Lu^{3+} and La^{3+} substituted YIG. T=4.2K and zero external magnetic field.

These differences originate from the fact that effect of the substitution on the hyperfine field (see 3.1.3.1) at neighbouring iron nuclei depends remarkably on the ionic radius of the substituent: $r(La^{3+}) = 0.1160\ nm > r(Y^{3+})=0.1019\ nm$, while $r(Lu^{3+}) = 0.0977\ nm < r(Y^{3+})=0.1019\ nm$.

3.1.3.5. Identification of the satellite lines.

3.1.3.5.1. Crystallographic and magnetic equivalence. Application to the garnet structure.

Let *{G}* be the space symmetry group of a crystal structure in question containing n_G operations per unit cell. Unless stated otherwise we use these n_G operations in the following discussion. By applying them to a "reference" site in a general position, a set of n_G crystallographically equivalent sites (CES) is obtained – these sites can always be chosen to lie in a single unit cell. If the reference site is in a special position the CES set contains less than n_G sites. As far as the NMR is concerned, the sites, which are connected by mere translation or by inversion, are fully equivalent and it is sufficient to consider their single representant. In the presence of an external magnetic field or in the presence of a spontaneous magnetization, only those sites in the CES set remain equivalent which are connected by operations which leave the field direction unchanged, or (because of the time inversion) by operations which invert the field direction. The CES set is thus divided into subsets of magnetically equivalent sites (MES). If the sites are occupied by the iron ions, each MES set will give rise to a single NMR line. Relative amplitudes of different NMR lines will be in the same ratio as the numbers of sites in the corresponding MES sets.

The concept of crystallographic and magnetic equivalence may be easily generalized to the pairs of sites, or to any other configuration of points in the lattice. For the pair of sites we define crystallographically equivalent set of configurations (CEC) as a set of all pairs which are obtained from a given pair by n_G symmetry operations of the group *{G}*. In order to be defined unambiguously, one should require that the first partner of the pair always lies in the same unit cell (the second partner may lie beyond the cell). In the presence of a magnetic field or/and spontaneous magnetization the CEC set is decomposed into subsets of magnetically equivalent configurations (MEC) in the same way as the CES set is decomposed into MES sets. Since the presence of the defects causes a shift of NMR frequency, in general each MEC set of the (Fe^{3+}-defect) pairs gives rise to a single satellite line in the NMR spectrum of ^{57}Fe. There exist an infinite number of possible pairs and thus there will be an infinite number of the satellite lines. It is reasonable to assume, however, that the shift of the resonance line decreases with the increasing distance between the defect and the Fe^{3+} ion. Therefore, only a limited number of MEC sets will give rise to the resolved satellites, while the rest of MEC sets will cause a

broadening of the lines. The ratio of amplitudes of the satellite lines is equal to the ratio of the numbers of configurations in the corresponding MEC sets.

Let us now consider the case of yttrium iron garnet. The space symmetry group of the garnet, as was already mentioned, O^h_{10} contains 96 symmetry operations per unit cell. According to the above discussion we get set of 96 CES for oxygen ions, which are located in general positions. They may be generated from an oxygen site at a_o(x, y, z), where a_o and x, y, z are the lattice parameter and oxygen parameters, respectively. For the octahedral site (*a*-site), located at the origin, the procedure leads to 16 crystallographically equivalent sites. 24 crystallographically equivalent sites are obtained for tetrahedral (*d*) and dodecahedral (*c*) sites, with the reference sites located at a_o(3/8,0,1/4) and a_o(1/4,0,3/8), respectively. For magnetization ***M*** along the [111] direction one gets that the CES set of *d* sites is identical with the MES set (i.e. all *d*-sites are magnetically equivalent for this direction of ***M***), while the CES set of the *a*-sites is divided into two MES subsets:a_1 and a_2. The subset a_1 contains four sites (for these sites local trigonal axis is parallel to ***M***), while the subset a_2 contains remaining 12 *a*-sites. It is now easy to see that the NMR spectrum of ^{57}Fe in an ideal YIG for ***M*** $||$ [111] have to consist of three lines with ratio of integral intensities 24 (*d* sites) : 4 (a_1 sites) : 12 (a_2 sites). For a general direction of ***M*** the *d*-sites give rise to 6 NMR lines and the *a*-sites to 8 lines. The sum of intensities of the *d* lines is two times higher than that of the *a* lines. The decomposition of the sites in the cation sublattices into sets of magnetically equivalent sites for several directions of the magnetization is given in Table 3.1.3.2.

Sublattice	Direction of *M*							
	[1, 1, 1]		[0, 0, 1]		[1, 1, 0]		[a, b, c]	
	N_{MES}	n	N_{MES}	n	N_{MES}	n	N_{MES}	n
a	2	4,12	1	16	2	8,8	8	8x2
d	1	24	2	8,16	2	8,16	6	6x4

Table 3.1.3.2. Decomposition of the Fe^{3+} cation sublattices (CES sets) into magnetically equivalent site (MES) subsets for several directions of magnetization. N_{MES} is the number of the MES subsets, n is the number of sites in each MES subset.

Let us now consider the satellite structure of the ^{57}Fe NMR spectrum, which is caused by defects located in one of the cation sublattices. In almost all cases the pairs (Fe^{3+}-defect) have no symmetry left and, as a result, the corresponding CEC sets contain 96 pairs. The O^h_{10} group contains inversion and [(1/2)(1/2)(1/2)] translation and according to the discussion in the previous part, maximum number of the satellite lines corresponding to a given CEC set is then 24. There are only three exceptions when this number is smaller, because the pairs still possess a residual symmetry:

(A) both partners in the pair are on *a*-sites with a common trigonal axis of symmetry (C3 symmetry remains).

(B) first partner is on the *d*-site, second partner is on the *c*-site, which lies on the S4 symmetry axis, which its *d* partner would have in an ideal crystal (C2 symmetry remains)

(C) as (B), but both partners are on *d*-sites.

In Table 3.3.3 the decomposition of the crystallographically configuration (CEC) sets into magnetically equivalent configuration (MEC) sets and the numbers of configurations in the MEC subsets for several directions of the magnetization is displayed. *G* in the table 3.3.3 denotes configuration of the pair with no symmetry left.

CEC Set	Direction of *M*							
	[1, 1, 1]		[0, 0, 1]		[1, 1, 0]		[a, b, c]	
	N_{MEC}	n	N_{MEC}	n	N_{MEC}	n	N_{MEC}	n
G	4	4x 24	3	3x 32	6	6x 16	24	24x 4
A	2	4,12	1	16	2	8,8	8	8x 2
B, C	2	24,24	3	3x 16	4	2x 8,2x 16	12	12x 4

Table 3.3.3. Decomposition of CEC sets into MEC subsets for several magnetization directions. For explanation of N_{MEC}, n see caption to Table 3.1.3.2.

Using the Tables 3.3.2 and 3.3.3 the qualitative form of the NMR spectrum can be obtained. In particular, the number of lines, relative intensities of the main lines as well as relative intensities of the satellite lines and the intensity ratios of a satellite line to its parent line may be directly determined.

In table 3.3.4 the relative intensities of the satellite lines, caused by different types of the substitutions, and corresponding parent lines in terms of substitution concentration *c* are given for the magnetization direction [1,1,1].

CEC	a_0		d_0		A		B,C		G	
Designation	a_0		d_0		${}^{C_3}a_i^a$		${}^{C_2}d_i^c$, ${}^{C_2}d_i^d$		a_i^j, d_i^j	
M	*N*	*Rel. Int*	*N*	*Rel.Int*	*N*	*Rel. Int*	*N*	*Rel. Int*	*N*	*Rel.Int*
[1,1,1]	2	4:12	1	24	2	8ξ:24ξ	2	24ξ	4	24ξ

Table 3.1.3.4. Relative intensities of main lines and satellite lines caused by different types of defects. Magnetization direction is [1,1,1]. ξ is defined by equation (3.1.3.9): $\xi = \frac{c}{1-c}$; *N* designates the number of lines in current CEC.

In this table symbols a_0 and d_0 designate CEC in which there are no defects in the vicinity of the resonating nucleus located on *a* and *d*-position respectively. Symbols ${}^{C_3}a_i^a$ correspond to CEC, where on the C_3 symmetry axis in the i^{th}-neighbourhood of resonating nucleus in *a*-position there is substitution in *a*-sublattice. Symbols ${}^{C_2}d_i^c$, ${}^{C_2}d_i^d$ designate the CEC, where the defect is positioned on the *c*-site or correspondingly d-site on the symmetry axis C_2 in i^{th}-neighbourhood of the resonating nucleus from *d*-sublattice. Symbols a_i^j, d_i^j relate to the CEC, where the defect is positioned on the *j=a,d,c* sublattice in i^{th}-neighbourhood of the resonating nucleus in *a, d*-sublattice respectively when no symmetry is left.

3.1.3.5.2. Different types of defects.

Magnetic ferrites are, as a rule, far from being ideal systems. Usually they contain a number of impurities and intrinsic defects. The impurities may enter the system from not pure enough starting compounds, other impurities enter the system during the preparation. In many cases it is possible to identify the satellites caused by the specific impurity by intentionally increasing the impurity concentration and finding the correlation between the satellite amplitudes and the concentration of the impurity [Engl85]. When this is not possible, comparison of systems prepared in different ways may help [Wagn94].

For cation impurities information on the valency of the impurity may be obtained from the shape of the satellite lines [Wagn95]. If the valency of the impurity and substituted ion is the same (“noncharged" impurities) impurities are distributed randomly as a rule and this leads to pretty identical shapes of satellite and corresponding main lines. On the other hand, because of the Coulomb attraction impurities with valency different from the valency of the substituted cation ("charged" impurities) may tend to be associated with another "charged" defect (for example, in YIG Pb^{2+} may attract Si^{4+} impurity, if both are present in the same system). Then the distribution of such defects is nonrandom. The amplitude of the "composite" satellites is enhanced and at the same time the amplitudes of "simple" satellites caused by a single defect are decreased. If this is the case, relation (3.1.3.10) represents only an upper limit for the actual concentration of the impurity. It is also probable that the preferential pairing enhances not only resolved “composite” satellites, but also unresolved ones. Therefore, the satellite lines caused by a "charged" impurity will be broader than corresponding main line. Thus, the line shape of the satellite can be used to distinguish "charged" and "noncharged" impurities. Some caution is necessary, however, as the distribution of the “noncharged" impurities might not be entirely random too. The correlation between the impurities, which leads to the nonrandom distribution, may be caused not only by the Coulomb interaction but also by an elastic energy. Thus, the shape of the satellite line may deviate from the shape of the main line also for the “noncharged” impurities. Nonrandom distribution of the cations may also be induced during the growth of a thin fi1m [Wink81].

3.1.3.5.3. Sets of crystallographically equivalent configurations.

When the satellites caused by a specific defect are identified the next task is to find out a correspondence between a given satellite line and a particular CEC set. It should be noticed that usually the change of resonant frequency caused by the presence of the defect is substantially smaller compared to the difference of resonant frequency of Fe^{3+} ions in different oxygen coordinations. For example, f_{res} of *a* and *d* site Fe^{3+} ions differ by more than 10MHz. Splittings between the main and satellite lines are much smaller, being less than 2MHz. This allows differentiating between the CEC sets in which the resonating nuclei are on the sites with different oxygen coordination.

The presence of the defect often modifies the exchange interactions. This is certainly the case when a nonmagnetic impurity is substituted for a Fe^{3+} ion and several exchange bonds are thus broken. It is generally accepted that the temperature dependence of the hyperfine field on

the nuclei of a magnetic ion follows the temperature dependence of the average value of the electron spin $<S_z>$ of the ion. $<S_z>$ is in turn determined by the exchange field acting on the magnetic ion. If this field is isotropic $<S_z>$ should be the same for all members of the same CEC set. Because Fe^{3+} ion is in the *S* electronic ground state, any anisotropy of the exchange is expected to be very small [Wink81]. As a consequence the temperature dependence of the splittings (satellite - main line) is expected to be the same for all configurations belonging to the same CEC set.

The modification of the hyperfine field by the defect in principle decreases with increasing distance between the defect and the resonating nuclei and that fact can be used for identification of the satellite line. Caution is needed, however, when applying this argument - an important part of the change is connected with the change of the transfer and supertransfer of the electrons. Here often the angles between the bonds, rather than distances decide which interaction is stronger. A similar situation arises in the superexchange interaction. An example relevant to this problem is provided by the $Ca_3Fe_2Ge_30_{12}$ garnet, where the superexchange interactions between the nearest and second nearest Fe^{3+}(a) neighbours are of the same magnitude [Brue88].

3.1.3.5.4. Sets of magnetically equivalent configurations.

The only possibility to make an unambiguous correspondence between a given satellite line and a particular MEC set is if the pairs (defect-Fe^{3+} ion) still retain some symmetry (in the garnet structure pairs A, B, C in the Table 3.1.3.3). The correspondence may be then established by measurements of the angular dependence of the spectra together with the symmetry analysis. If pairs (defect-Fe^{3+} ion) have no symmetry left (general pairs in Table 3.1.3.3), the identification, based on the experimental results only, is not possible and a microscopic model is needed. In some cases a semiempirical “superposition” (or “independent bond” model) can help.

3.1.3.5.5. Superposition model.

The superposition model is based on a picture that in compounds of ionic character the ions keep in a first approximation their free ion character having the effect of an environment as a small perturbation. The Hamiltonian of the transition metal ion is then approximated by the Hamiltonian of corresponding free ion plus contributions from its ligands. Within the superposition model the contributions of the individual ligands to the Hamiltonian are assumed to be (1) mutually independent (additive) and (2) axially symmetrical around the cation-ligand

bond. The contribution of the oxygen ligands (including the supertransfer contributions in the Fe-O-Fe or Fe-O-Y triads) to the hyperfine field of the Fe^{3+} ion may be written as

$$B_C = \sum_{i=1}^{N} (b_0^i + b^i \cos^2 \varphi_i) \qquad (3.1.3.11)$$

where the sum is over N ligands of the Fe^{3+} ion in question, b_0^i and b^i are called isotropic and anisotropic "intrinsic fields", φ_i is the angle which the magnetic moment of Fe^{3+} ion makes with the bond of the ion and its i^{th} oxygen ligand. The intrinsic fields b_0^i and b^i depend only on the nature of the ligand and on the Fe^{3+}ion-ligand distance.

When there is an impurity on a cation site near the resonating nucleus the electron structure of the oxygen in a triad Fe^{3+}-O^{2-}- impurity is modified by the presence of impurity. Then one should expect a modification of B_C. Neglecting the change of geometry caused by the impurity and taking into account relation (3.1.3.12), the corresponding change of B_C will have the form:

$$\Delta B_C^i = \Delta b_0^i + \Delta b^i \cos^2 \varphi_i \qquad (3.1.3.12)$$

where Δb_0 and Δb are the changes in corresponding intrinsic fields.

As the angles φ_i are known from the geometry of the compound in question, only two parameters are needed to characterize the splitting between satellite and the main line caused by the change of an electron transfer in bonds with neighbouring oxygen ions (including oxygen mediated supertransfer in triads Fe^{3+}-O^{2-}-impurity). Moreover, the superposition model allows to establish an unambiguous correspondence between the satellite line and the MEC set. Several drawbacks of the model should be noticed. One might be a deviation from its prediction connected with the fact that the assumptions on which it is based are fulfilled only partly. The path for the electron transfer may be more complicated than the simple triad considered above. For example, the c site of the garnet is bonded to the nearest *a* or *d* site through two oxygen ligands.

The superposition model for magnetic garnets was tested in [Step99]. For the testing of the superposition of independent contributions of single bonds between the central iron cation (with resonating nucleus) and ions in its surroundings the composed satellites were investigated and then the results were taken into account for comparison of frequencies of main lines in YIG and GdIG and satellite lines in $Y_{3-x}Gd_xFe_5O_{12}$. The composed satellites, induced by a simultaneous presence of substitution in two iron positions (i.e. the presence of two substitutions in a given surroundings of resonating nucleus) would have, according to the additive principle, a

frequency shift (with respect to a corresponding main line) equal to a sum of frequency shifts of simple satellites (i.e. satellites induced by the presence of one substitution in a given surroundings only). The results of the investigation of composed satellites at 4.2 K for resonating nuclei in *a* and *d* positions and trivalent substitutions in *a* positions (In, Sc, Y) and in *d* positions (Ga, Al) have revealed that the difference between shifts predicted by the additive principle (superposition model) and real shifts in spectra are small. The maximal deviation from the additive principle was detected for Y^{3+} substitution in *a* position closest to a resonating nucleus in *d* position and equal ~15%.

Besides the superposition of independent contributions the independent bond model has also a suggestion of the axial symmetry of the anisotropy part of contribution (i.e. the part depending on the direction of the magnetic moment of the central iron ion) with the axis of symmetry along the bond between the central Fe cation and oxygen ligand in triad Fe-O-cation. This suggestion was tested by studying of difference between tensors of anisotropy of hyperfine field defined for main lines and for satellite lines. That difference should be (according to the independent bond model) an axial symmetric tensor with one main axis along the bond Fe-O. If an iron cation is substituted by another cation (substituent) then the contribution to anisotropy tensor given by that iron cation is replaced by the substituent`s contribution. The foregoing difference is then the difference between the effect of the iron cation and the substituent. Because according to the superposition model both interactions are given by axial symmetric tensors with the same axis, their difference should be axial symmetric too. The possible influence of deformations of local surroundings induced by substituent with ionic radius different from the ionic radius of Fe^{3+}, deviating an oxygen ion from its original position, was studied by a comparison of results for different substitutions having similar electronic structure of their valent shells, but different in their ionic radii. The results have touched on the central iron cation in *d* position and the substituent Y^{3+} in the closest *a* position and the central iron cation in *a* position and substituents Ga^{3+} and Ge^{4+} in the closest *d* position. Experimental data were treated assuming anisotropy of resonant frequency described by second rank tensors (A) consisting of hyperfine (A^{hf}) and dipolar (A^{dip}) parts: $A = A^{hf} + A^{dip}$ (see paragraph 3.1.4 for details). In the case of the central iron cation in *d* position and the substituent Y^{3+} in *a* position thorough investigations revealed that no one of the resulting 24 tensors $\Delta A^{hf} = \Delta A - \Delta A^{dip}$ was axial symmetric and no one of its main axis pointed along the link between the positions of the resonating nucleus and the oxygen ion. So the conclusion was that the independent bond model in the form of its second suggestion is not an appropriate approximation for the case of the ion

with resonating nucleus in *d* position and substituent in the closest *a* position. For the case of the resonating nucleus in *a* position and the substituent Ga^{3+} in the closest *d* position the same procedure of the elimination of dipolar contribution for all the possibilities (in this case the number of those is reduced to 6 ones) has led to an agreement with the independent bond model in just one case. The tensor ΔA^{hf}, reflecting changes of anisotropy of the hyperfine field by the presence of Ga had one of the main axes pointed along the link between the ion with resonating nucleus and oxygen in the bond Fe-O-Ga (a deviation amounted to 2.8° only) and was approximately axial. By the same way the isotropic part and tensors A for the main and satellite lines were calculated for the case of the substituent Ge^{4+} in *d* position. The comparison of the results for two substituents pointed out that Ge^{4+} induced larger changes of the isotropic part, but it less affects anisotropy component. Tensor ΔA^{hf} for Ge^{4+} is more deviated from the axial symmetry: the main axis corresponding to the maximal main value lies 11° away from the link Fe-O in triad Fe-O-Ge (Table 3.1.6.1).

3.1.4. Anisotropy of the hyperfine field on ^{57}Fe nucleus in YIG with defects.

3.1.4.1. General description.

Free Fe^{3+} ion has an electronic configuration $3d^5$ in a ground state $^6S_{5/2}$, i.e. the hyperfine field on a nucleus of a free ion is isotropic. The hyperfine field on the nucleus of that ion could become anisotropic being incorporated into a crystal lattice. The hyperfine field on a nucleus in a crystal lattice reflects the symmetry of the lattice. The field is anisotropic in general, i.e. it depends on the direction of a magnetization with respect to the crystallographic axes, so one can write $\boldsymbol{B}_{hf}(\boldsymbol{n})$, where $\boldsymbol{n}$ is the unit vector in the direction of the magnetization. In real crystal lattices with defects the symmetry of an infinite crystal lattice is disturbed by the presence of defects. Then, to describe the hyperfine field on Fe nuclei one can use an idea of crystallographic equivalent configurations (CEC) as local crystallographic surroundings of a nucleus under consideration which can be superimposed with themselves under symmetry operations of a space group of the crystal. Under local surrounding of a nucleus one understands all atoms (including defects) of the crystal lattice within the sphere, drawn around the Fe ion.

The radius of the sphere should be chosen so, that the influence of the crystal lattice beyond the sphere could be neglected. Then NMR resonance frequency $f_s(\boldsymbol{n})$, depending on the value of the hyperfine field as:

$$f_s(\boldsymbol{n}) = \frac{\gamma}{2\pi} B_{hf}^s(\boldsymbol{n}) \qquad (3.1.4.1)$$

(where *s* designates a given CEC), can be used for the description of the anisotropy of the hyperfine field. Expanding $f_s(\boldsymbol{n})$ in series on $\boldsymbol{n}=(n_1,n_2,n_3)$ and supposing that $f_s(\boldsymbol{n}) = f_s(-\boldsymbol{n})$ one will obtain:

$$f_s(\boldsymbol{n}) = \sum_{i=0}^{N} \frac{1}{(2i)!} \left(n_1 \frac{\partial}{\partial n_1} + n_2 \frac{\partial}{\partial n_2} + n_3 \frac{\partial}{\partial n_3} \right)^{2i} f_s(\boldsymbol{n})\Big|_{n_0} \qquad (3.1.4.2)$$

Limiting ourselves to the first three terms of the expansion and supposing that the derivation does not depend on the order of variables, one can write:

$$\mathrm{f_s}(\mathbf{n}) = \mathrm{I^s} + \sum_{i,j=1}^{3} \mathrm{A_{ij}^s n_i n_j} + \sum_{\mathrm{i,j,k,l=1}}^{3} \mathrm{B_{ijkl}^s n_i n_j n_k n_l} + \ldots \qquad (3.1.4.3)$$

where for i,j,k=1,...,3 is fulfilled:

$$A_{ij}^s = A_{ji}^s, \quad B_{iiij}^s = B_{iiji}^s = B_{ijii}^s = B_{jiii}^s, \quad B_{iijj}^s = B_{ijij}^s = B_{ijji}^s = B_{jiij}^s = B_{jiji}^s = B_{jjii}^s,$$
$$B_{iijk}^s = B_{iikj}^s = B_{ijik}^s = B_{ijki}^s = B_{ikij}^s = B_{ikji}^s = B_{jiik}^s = B_{jiki}^s = B_{jkii}^s = B_{kiij}^s = B_{kiji}^s = B_{kjii}^s \qquad (3.1.4.4)$$

Taking into account that $n_1^2 + n_2^2 + n_3^2 = 1$, the components of the tensor are not more independent, i.e.

$$B_{1111}^s n_1^4 = B_{1111}^s \left(n_1^2 - n_1^2 n_2^2 - n_1^2 n_3^2 \right) \Rightarrow B_{1111}^s = 0 \qquad B_{2222}^s n_2^4 = B_{2222}^s \left(n_2^2 - n_1^2 n_2^2 - n_2^2 n_3^2 \right) \Rightarrow B_{2222}^s = 0$$
$$B_{3333}^s n_3^4 = B_{3333}^s \left(n_3^2 - n_1^2 n_3^2 - n_2^2 n_3^2 \right) \Rightarrow B_{3333}^s = 0$$
$$B_{1123}^s n_1^2 n_2 n_3 = B_{1123}^s \left(n_2 n_3 - n_2^3 n_3 - n_3^3 n_2 \right) \Rightarrow B_{1123}^s = 0$$
$$B_{2213}^s n_2^2 n_1 n_3 = B_{2213}^s \left(n_1 n_3 - n_1^3 n_3 - n_3^3 n_1 \right) \Rightarrow B_{2213}^s = 0$$
$$B_{3312}^s n_3^2 n_1 n_2 = B_{3312}^s \left(n_1 n_2 - n_1^3 n_2 - n_2^3 n_1 \right) \Rightarrow B_{3312}^s = 0 \qquad (3.1.4.5)$$

Having an isotropic term I_z^s in the expansion, one can accept a zero trace of the tensor A_{ij}^s, i.e. $A_{11}^s + A_{22}^s + A_{33}^s = 0$ and then the expansion will have the only following nonzero terms:

$$f_s(\mathbf{n}) = I^s + A^s_{11}n_1^2 + A^s_{22}n_2^2 + \left(-A^s_{11} - A^s_{22}\right)n_3^2 + 2A^s_{12}n_1n_2 + 2A^s_{13}n_1n_3 + 2A^s_{23}n_2n_3 +$$
$$4B^s_{2221}n_2^3n_1 + 4B^s_{2223}n_2^3n_3 + 4B^s_{3331}n_3^3n_1 + 4B^s_{3332}n_3^3n_2 + 4B^s_{1112}n_1^3n_2 + 4B^s_{1113}n_1^3n_3 +$$
$$6B^s_{1122}n_1^2n_2^2 + 6B^s_{1133}n_1^2n_3^2 + 6B^s_{2233}n_2^2n_3^2 \qquad (3.1.4.6)$$

Then for a general description of the anisotropy of resonance frequencies one will obtain 15 independent constants. Having the isotropic term I^s and tensors A^s_{ij} and B^s_{ijkl} for a given crystallografic equivalent configuration, one can define all the resonance frequencies of that configuration considering $f_s^{\,w}(\boldsymbol{n})$ as an invariant with respect to translation from the relation:

$$f_s^{\,w}(\mathbf{n}) = I^s + \sum_{i,j,k,l=1}^{3} A^s_{ij}G^w_{ki}G^w_{lj}n_kn_l + \sum_{\substack{i,j,k,l=1\\o,p,q,r=1}}^{3} B^s_{ijkl}G^w_{oi}G^w_{pj}G^w_{qk}G^w_{rl}n_on_pn_qn_r \qquad (3.1.4.7)$$

where the terms of higher orders are neglected provided that I^s is dominating, G^w_{ij} (i,j=1,...,3; w=1,...,m; m is a number of symmetry elements of a point group) is a vector representation of a point symmetry of a given crystal ($(\boldsymbol{G}^w)^{-1}=(\boldsymbol{G}^w)^{\mathrm{T}}$, $\boldsymbol{G}^w\,.(\boldsymbol{G}^w)^{\mathrm{T}}=\boldsymbol{I}$, where $\boldsymbol{I}$ is a unit matrix). A sum of resonance frequencies for s`s crystallografic equivalent configuration over all symmetry elements of the point group of the garnet crystal will give us an invariant Inv_s of that CEC under condition that the contributions from B^s_{ijkl} can be neglected:

$$Inv_s = \frac{1}{m}\sum_{w=1}^{m} f_s^{\,w}(\boldsymbol{n}) \qquad (3.1.4.8)$$

where m is the number of symmetry operations of the point group.
Otherwise (if the right part of the equation depends on n_1 and n_2 (n_3 is dependable in the sense that n=1)) then it will depend on n_1 and n_2 (see formula 3.1.4.9).

3.1.4.2. Intensities and a number of main and satellite lines in YIG.

Crystal lattice of YIG belongs to the space symmetry group $O_h^{10}(Ia\bar{3}d)$ and the point group $O_h(m\bar{3}m)$. The invariant Inv_s for s`s crystallographic equivalent configuration for that point group is the following expression:

$$Inv_s = \frac{1}{m}\sum_{w=1}^{m} f_s^{\,w}(\boldsymbol{n}) = I_z^s + \left(B^s_{1122} + B^s_{1133} + B^s_{2233}\right)\cdot\left(2n_1^2n_2^2 + 2n_1^2n_3^2 + 2n_2^2n_3^2\right) \qquad (3.1.4.9)$$

Following tables demonstrate how the local symmetry of particular CEC of YIG reduces the number of independent components of tensors A^s_{ij} and B^s_{ijkl}. For those tensors the relation

$$A^s_{ij} = \sum_{k,l=1}^{3} A^s_{ij} G^{w_p}_{ki} G^{w_p}_{lj},\ B^s_{ijkl} = \sum_{o,p,g,r=1}^{3} B^s_{ijkl} G^{w_p}_{oi} G^{w_p}_{pj} G^{w_p}_{qk} G^{w_p}_{rl} \qquad (3.1.4.10)$$

should be fulfilled. $G^{w_p}_{ki}$ are vector representations of all elements of local symmetry for a given CEC.

Local symmetry	$\bullet\bar{3}\bullet$, e.g. $S_3^c \parallel [111]$					
Multiplicity of CEC	8					
Symmetry elements	S_3^c	$(S_3^c)^2$	$(S_3^c)^3$	$(S_3^c)^4$	$(S_3^c)^5$	E
Vector reprezentation	$\begin{pmatrix} 0 & 0 & -1 \\ -1 & 0 & 0 \\ 0 & -1 & 0 \end{pmatrix}$	$\begin{pmatrix} 0 & 1 & 0 \\ 0 & 0 & 1 \\ 1 & 0 & 0 \end{pmatrix}$	$\begin{pmatrix} -1 & 0 & 0 \\ 0 & -1 & 0 \\ 0 & 0 & -1 \end{pmatrix}$	$\begin{pmatrix} 0 & 0 & 1 \\ 1 & 0 & 0 \\ 0 & 1 & 0 \end{pmatrix}$	$\begin{pmatrix} 0 & -1 & 0 \\ 0 & 0 & -1 \\ -1 & 0 & 0 \end{pmatrix}$	$\begin{pmatrix} 1 & 0 & 0 \\ 0 & 1 & 0 \\ 0 & 0 & 1 \end{pmatrix}$
Conditions for components of tensors A^s_{ij} and B^s_{ijkl}	$A^s_{11} = A^s_{22} = 0,\quad A^s_{12} = A^s_{13} = A^s_{23},\quad B^s_{1122} = B^s_{1133} = B^s_{2233},$ $B^s_{1112} = B^s_{2223} = B^s_{3331},\quad B^s_{1113} = B^s_{2221} = B^s_{3332}$					
Expansion of resonance frequency	$f_s(\boldsymbol{n}) = I^s_z + 2A^s_{12}(n_1n_2 + n_1n_3 + n_2n_3) +$ $4B^s_{1112}(n_1^3n_2 + n_2^3n_3 + n_3^3n_1) + 4B^s_{1113}(n_1^3n_3 + n_2^3n_1 + n_3^3n_2) +$ $6B^s_{1122}(n_1^2n_2^2 + n_1^2n_3^2 + n_2^2n_3^2)$					

Table 3.1.4.1. – An influence of local symmetry of a given CEC on anisotropy of a resonance frequency.

Local symmetry	$\bullet 32$, e.g. $(C_3^c \parallel [1,1,1]) \perp (C_2^1 \parallel [-1,1,0])$					
Multiplicity of CEC	8					
Symmetry elements	C_3^c	$(C_3^c)^2$	E	C_2^1	C_2^3	C_2^5
Vector reprezentation	$\begin{pmatrix} 0 & 0 & 1 \\ 1 & 0 & 0 \\ 0 & 1 & 0 \end{pmatrix}$	$\begin{pmatrix} 0 & 1 & 0 \\ 0 & 0 & 1 \\ 1 & 0 & 0 \end{pmatrix}$	$\begin{pmatrix} 1 & 0 & 0 \\ 0 & 1 & 0 \\ 0 & 0 & 1 \end{pmatrix}$	$\begin{pmatrix} 0 & -1 & 0 \\ -1 & 0 & 0 \\ 0 & 0 & -1 \end{pmatrix}$	$\begin{pmatrix} 0 & 0 & -1 \\ 0 & -1 & 0 \\ -1 & 0 & 0 \end{pmatrix}$	$\begin{pmatrix} -1 & 0 & 0 \\ 0 & 0 & -1 \\ 0 & -1 & 0 \end{pmatrix}$
Conditions for components of tensors A^s_{ij} and B^s_{ijkl}	$A^s_{11} = A^s_{22} = 0,\quad A^s_{12} = A^s_{13} = A^s_{23},\quad B^s_{1122} = B^s_{1133} = B^s_{2233},$ $B^s_{1112} = B^s_{2223} = B^s_{3331} = B^s_{1113} = B^s_{2221} = B^s_{3332}$					
Expansion of resonance frequency	$f_s(\boldsymbol{n}) = I^s_z + 2A^s_{12}(n_1n_2 + n_1n_3 + n_2n_3) +$ $4B^s_{1112}(n_1^3n_2 + n_2^3n_3 + n_3^3n_1 + n_1^3n_3 + n_2^3n_1 + n_3^3n_2) +$ $6B^s_{1122}(n_1^2n_2^2 + n_1^2n_3^2 + n_2^2n_3^2)$					

Table 3.1.4.2. – An influence of local symmetry of a given CEC on anisotropy of a resonance frequency.

Local symmetry	$2 \bullet 22$, e.g. $(C_2^x \square [1,0,0]) \perp (C_2^6 \square [0,1,1]) \perp (C_2^5 \square [0,-1,1])$			
Multiplicity of CEC	12			
Symmetry elements	C_2^x	C_2^6	C_2^5	E
Vector reprezentation	$\begin{pmatrix} 1 & 0 & 0 \\ 0 & -1 & 0 \\ 0 & 0 & -1 \end{pmatrix}$	$\begin{pmatrix} -1 & 0 & 0 \\ 0 & 0 & 1 \\ 0 & 1 & 0 \end{pmatrix}$	$\begin{pmatrix} -1 & 0 & 0 \\ 0 & 0 & -1 \\ 0 & -1 & 0 \end{pmatrix}$	$\begin{pmatrix} 1 & 0 & 0 \\ 0 & 1 & 0 \\ 0 & 0 & 1 \end{pmatrix}$
Conditions for components of tensors A_{ij}^s and B_{ijkl}^s	$A_{11}^s = -2A_{22}^s, \quad A_{12}^s = A_{13}^s = 0, \quad B_{1122}^s = B_{1133}^s, \quad B_{2223}^s = B_{3332}^s,$ $B_{1112}^s = B_{3331}^s = B_{1113}^s = B_{2221}^s = 0$			
Expansion of resonance frequency	$f_s(\boldsymbol{n}) = I_z^s + A_{22}^s(-2n_1^2 + n_2^2 + n_3^2) + 2A_{23}^s n_2 n_3 + 6B_{2233}^s n_2^2 n_3^2 +$ $6B_{1122}^s(n_1^2 n_2^2 + n_1^2 n_3^2) + 4B_{2223}^s(n_2^3 n_3 + n_3^3 n_2)$			

Table 3.1.4.3. – An influence of local symmetry of a given CEC on anisotropy of a resonance frequency.

Local symmetry	$\bar{4} \bullet \bullet$, e.g. $S_4^z \square [0,0,1]$			
Multiplicity of CEC	12			
Symmetry elements	S_4^z	$(S_4^z)^2$	$(S_4^z)^3$	E
Vector reprezentation	$\begin{pmatrix} 0 & 1 & 0 \\ -1 & 0 & 0 \\ 0 & 0 & 1 \end{pmatrix}$	$\begin{pmatrix} -1 & 0 & 0 \\ 0 & -1 & 0 \\ 0 & 0 & 1 \end{pmatrix}$	$\begin{pmatrix} 0 & -1 & 0 \\ 1 & 0 & 0 \\ 0 & 0 & 1 \end{pmatrix}$	$\begin{pmatrix} 1 & 0 & 0 \\ 0 & 1 & 0 \\ 0 & 0 & 1 \end{pmatrix}$
Conditions for components of tensors A_{ij}^s and B_{ijkl}^s	$A_{11}^s = A_{22}^s, \quad A_{12}^s = A_{13}^s = A_{23}^s = 0, \quad B_{1133}^s = B_{2233}^s,$ $B_{1112}^s = -B_{2221}^s, \quad B_{2223}^s = B_{3331}^s = B_{1113}^s = B_{3332}^s = 0$			
Expansion of resonance frequency	$f_s(\boldsymbol{n}) = I_z^s + A_{11}^s(n_1^2 + n_2^2 - 2n_3^2) + 6B_{1122}^s n_1^2 n_2^2 +$ $6B_{1133}^s(n_1^2 n_3^2 + n_2^2 n_3^2) + 4B_{1112}^s(n_1^3 n_2 - n_2^3 n_1)$			

Table 3.1.4.4. – An influence of local symmetry of a given CEC on anisotropy of a resonance frequency.

Local symmetry	•3• , e.g. $C_3^c \square [1,1,1]$		
Multiplicity of CEC	16		
Symmetry elements	C_3^c	$(C_3^c)^2$	E
Vector reprezentation	$\begin{pmatrix} 0 & 0 & 1 \\ 1 & 0 & 0 \\ 0 & 1 & 0 \end{pmatrix}$	$\begin{pmatrix} 0 & 1 & 0 \\ 0 & 0 & 1 \\ 1 & 0 & 0 \end{pmatrix}$	$\begin{pmatrix} 1 & 0 & 0 \\ 0 & 1 & 0 \\ 0 & 0 & 1 \end{pmatrix}$
Conditions for components of tensors A_{ij}^s and B_{ijkl}^s	$A_{11}^s = A_{22}^s = 0, \quad A_{12}^s = A_{13}^s = A_{23}^s, \quad B_{1122}^s = B_{1133}^s = B_{2233}^s,$ $B_{1112}^s = B_{2223}^s = B_{3331}^s, \quad B_{1113}^s = B_{2221}^s = B_{3332}^s$		
Expansion of resonance frequency	$f_s(\boldsymbol{n}) = I_z^s + 2A_{12}^s(n_1n_2 + n_1n_3 + n_2n_3) + 6B_{1122}^s(n_1^2n_2^2 + n_1^2n_3^2 + n_2^2n_3^2)$ $+4B_{1112}^s(n_1^3n_2 + n_2^3n_3 + n_3^3n_1) + 4B_{1113}^s(n_1^3n_3 + n_2^3n_1 + n_3^3n_2)$		

Table 3.1.4.5. – An influence of local symmetry of a given CEC on anisotropy of a resonance frequency.

Local symmetry	2 •• , e.g. $C_2^x \| (1,0,0)$	
Multiplicity of CEC	24	
Symmetry elements	C_2^x	E
Vector reprezentation	$\begin{pmatrix} 1 & 0 & 0 \\ 0 & -1 & 0 \\ 0 & 0 & -1 \end{pmatrix}$	$\begin{pmatrix} 1 & 0 & 0 \\ 0 & 1 & 0 \\ 0 & 0 & 1 \end{pmatrix}$
Conditions for components of tensors A_{ij}^s and B_{ijkl}^s	$A_{12}^s = A_{13}^s = 0, \quad B_{1112}^s = B_{3331}^s = B_{1113}^s = B_{2221}^s = 0$	
Expansion of resonance frequency	$f_s(\boldsymbol{n}) = I_z^s + A_{11}^s n_1^2 + A_{22}^s n_2^2 + (-A_{11}^s - A_{22}^s) n_3^2 + 2A_{23}^s n_2 n_3 +$ $6B_{1122}^s n_1^2 n_2^2 + 6B_{1133}^s n_1^2 n_3^2 + 6B_{2233}^s n_2^2 n_3^2 + 4B_{2223}^s n_2^3 n_3 + 4B_{3332}^s n_3^3 n_2$	

Table 3.1.4.6. – An influence of local symmetry of a given CEC on anisotropy of a resonance frequency.

Local symmetry	$\bullet\bullet 2$, e.g. $C_2^2 \square [1,1,0]$	
Multiplicity of CEC	24	
Symmetry elements	C_2^2	E
Vector reprezentation	$\begin{pmatrix} 0 & 1 & 0 \\ 1 & 0 & 0 \\ 0 & 0 & -1 \end{pmatrix}$	$\begin{pmatrix} 1 & 0 & 0 \\ 0 & 1 & 0 \\ 0 & 0 & 1 \end{pmatrix}$
Conditions for components of tensors A_{ij}^s and B_{ijkl}^s	$A_{11}^s = A_{22}^s$, $A_{12}^s = -A_{13}^s$, $B_{1133}^s = B_{2233}^s$, $B_{1112}^s = B_{2221}^s$, $B_{1113}^s = -B_{2223}^s$, $B_{3331}^s = -B_{3332}^s$	
Expansion of resonance frequency	$f_s(\boldsymbol{n}) = I_z^s + A_{11}^s(n_1^2 + n_2^2 - 2n_3^2) + 2A_{13}^s(n_1 n_3 - n_2 n_3) + 2A_{12}^s n_1 n_2 + 4B_{1112}^s(n_1^3 n_2 + n_2^3 n_1) + 4B_{1113}^s(n_1^3 n_3 - n_2^3 n_3) + 4B_{3331}^s(n_3^3 n_1 - n_3^3 n_2) + 6B_{1122}^s n_1^2 n_2^2 + 6B_{1133}^s(n_1^2 n_3^2 + n_2^2 n_3^2)$	

Table 3.1.4.7. – An influence of local symmetry of a given CEC on anisotropy of a resonance frequency.

Local symmetry	1
Multiplicity of CEC	48
Symmetry elements	E
Vector reprezentation	$\begin{pmatrix} 1 & 0 & 0 \\ 0 & 1 & 0 \\ 0 & 0 & 1 \end{pmatrix}$
Conditions for components of tensors A_{ij}^s and B_{ijkl}^s	
Expansion of resonance frequency	$f_s(\boldsymbol{n}) = I_z^s + A_{11}^s n_1^2 + A_{22}^s n_2^2 + (-A_{11}^s - A_{22}^s) n_3^2 + 2A_{12}^s n_1 n_2 + 2A_{13}^s n_1 n_3 + 2A_{23}^s n_2 n_3 + 4B_{1112}^s n_1^3 n_2 + 4B_{2221}^s n_2^3 n_1 + 4B_{1113}^s n_1^3 n_3 + 4B_{2223}^s n_2^3 n_3 + 4B_{3331}^s n_3^3 n_1 + 4B_{3332}^s n_3^3 n_2 + 6B_{1122}^s n_1^2 n_2^2 + 6B_{1133}^s n_1^2 n_3^2 + 6B_{2233}^s n_2^2 n_3^2$

Table 3.1.4.8. – An influence of local symmetry of a given CEC on anisotropy of a resonance frequency.

Reducing the local symmetry elements of CEC from the symmetry elements of point group in the formula (3.1.4.7) and considering that relation as being an invariant to inversion one will have the maximal number of main lines and their satellites in ^{57}Fe NMR spectra. Designating $G_{ki}^{w_s}$ (where w_s=1,...,m_s and m_s stands for the number of residual symmetry elements) as a vector

representation of elements of point symmetry group without the reducted elements of local symmetry of CEC one will obtain:

$$f_s^w(\mathbf{n}) = I^s + \sum_{i,j,k,l=1}^{3} A_{ij}^s G_{ki}^{w_s} G_{lj}^{w_s} n_k n_l + \sum_{\substack{i,j,k,l=1 \\ o,p,q,r=1}}^{3} B_{ijkl}^s G_{oi}^{w_s} G_{pj}^{w_s} G_{qk}^{w_s} G_{rl}^{w_s} n_o n_p n_q n_r \qquad (3.1.4.11)$$

where m_s depends on the local symmery of a given CEC.

Supposing statistically random occupation of defects of each type and their small concentration in the crystal lattice, the integral intensities of the main lines and satellites will obey the binominal law describing the probability to find defects in *K* positions from *N*::

$$P_K^N(c) = \frac{N!}{K! \cdot (N-K)!} \cdot c^K \cdot (1-c)^{N-K} \qquad (3.1.4.12)$$

where *N* is the number of positions in a given surrounding of resonating nucleus of an Fe^{3+} ion where a defect of the crystal lattice could occur (i.e. N is the number of neighbours). The probability to find the defect in a particular position is $P_1^1(c) = c$ (concentration of defects in a given sublattice) and the probability that in that position there is no defect is $P_0^1(c) = (1-c)$. Provided that the concentration of defects is low ($c \langle\langle 1$) the probabilitities of a finding of two or more defects in the surrounding of a resonating nucleus of an Fe^{3+} ion are negligible.

The next table 3.1.4.9 collects data on local symmetries, intensities, number and designations of the lines of different CEC which could occur in YIG. In this table the „order“ means the order of expansion in the relaions (3.1.4.7)- (3.1.4.11) taken into consideration. Symbols a_0 and d_0 mean CEC without any defects in neighborhoods of, correspondingly, *a* and *d* positioned resonating nuclei, symbols ${}^{C_3}a_i^a$ mean CEC having defect in *a*-position on the symmetry axis C_3 in i-surrounding of resonating nucleus which is in *a* position as well. Symbols ${}^{C_2}d_i^c$ mean CEC having defects in *c*-position on the symmetry axis C_2 in i-surrounding of resonating nucleus that is in *d* position. a_i^j and d_i^j are CEC with defects in i-surrounding of resonating nuclei in *a* (or *d*) position and indexes *j=a,d,c* mean the sublattice in which the defect is located.

Symmetry of CEC		$\bullet\bar{3}\bullet$		$\bar{4}\bullet\bullet$		$\bullet 3\bullet$		$2\bullet\bullet$		1	
Multiplicity of CEC		8		12		16		24		48	
Designation of CEC		a_0		d_0		$^{C_3}a_i^a$		$^{C_2}d_i^c$		a_i^j , d_i^j	
n	Order	N of lines	Inten. *[1-c]*	N of lines	Inten. *[1-c]*	N of lines	Inten. *[c]*	N of lines	Inten. *[c]*	N of lines	Inten. *[c]*
(n_1,n_2,n_3)	0	1	8	1	12	1	16	1	24	1	48
(n_1,n_2,n_3)	4	8	1	6	2	8	2	12	2	24	2
(n_1,n_2,n_3)	2	4	2	3	4	4	4	12	2	24	2
(1,1,0)	4	4	2	3	4	4	4	6	4	12	4
(1,1,0)	2	3	2:2:4	2	4:8	3	4:4:8	6	4	12	4
[1,1,1]	4, 2	2	2:6	1	12	2	4:12	2	12	4	12
[1,1,0]	4, 2	2	4	2	4:8	2	8	4	8:8:4:4	6	8
[1,0,0]	4, 2	1	8	2	4:8	1	16	3	8	3	16

Table 3.1.4.9. Local symmetry, intensities, number and designations of the lines of different CEC in NMR spectra of YIG with small concentrations of defects. Here N is the number of lines in a spectrum.

Usually, experimental data of Fe^{57} in trivalent cation states in magnetic oxides are analyzed in approximation of the second rank tensor, the influence of further members of the expansion could be neglected.

3.1.5. Methods of YIG preparation.

Technologies of crystalline inorganic materials generally comprise three main areas: ceramic materials, bulk single crystals and epitaxial layers on single crystal substrates. Yttrium iron garnets in this respect behave quite normally and are processed technologically in all three categories. However, one serious handicap has to be overcame: magnetic garnets do not melt without decomposition. Thus, special techniques have to be developed for crystallization from solvents at elevated temperatures, mostly molten oxide mixtures, which commonly are called “fluxes”. Below the preparation of polycrystalline materials by the classical ceramic technology will be described, and the basis for the garnet flux growth technology will be considered.

3.1.5.1 Preparation of the polycrystalline material.

The starting material in ceramic technology is a powder of Y_2O_3 and Fe_2O_3, which has to be converted into a solid body. This is accomplished by shaping and final sintering at a temperature below melting temperature (1470°C). In the standard procedure the ceramic technology of garnets starts with mixing of the constituent oxides. After that the oxide mixture is subjected to a prefiring step (several hours at 1000-1200 °C) which mainly aims at the formation of the garnet phase.

$$3Y_2O_3 + 5Fe_2O_3 \rightarrow 2Y_3Fe_5O_{12} \qquad (3.1.5.1)$$

During this reaction, at the relatively higher temperature, however, sintering also takes place and results in “baking” of the powder. To homogenize the reaction product and to make it once more reactive enough for the following final sintering step (the particle size should be generally below 1μm), this prefired product has to be grinded. Without addition of any binder the powder is shaped and hydrostatically pressed with about 100 bar and finally sintered for several hours at 1250-1450 °C in an oxygen atmosphere [Wink81].

YIG materials prepared by this method contain contaminations entered the system from the starting oxide mixture and from the material of the mill used for the grinding.

3.1.5.2 Preparation of single crystals and epitaxial single crystal films.

Standard flux technology of YIG single crystals growth consists of several steps. First of all the starting mixture of Y_2O_3, Fe_2O_3 and solvent hearted for melting in a platinum crucible to about 1350 °C. As solvents are used following many-component mixtures:

a) $PbO – PbF_2 – B_2O_3$
b) $BaO – B_2O_3$
c) $BaO – BaF_2 – B_2O_3$

The melt is held at this (around 1350 °C) constant temperature a few hours and then cooled slowly at a rate 0.5 to 5 °C/hour to the desired withdrawal temperature. With an appropriate temperature profile (top of the crucible 8 to 10 degrees hotter than the bottom) nucleation on the surface of the melt is prevented and a great increase in both size and quality of the crystals results. The crystals normally stick to the walls and bottom of the crucible, so that they can be picked up from the empty crucible after the run.

In the liquid phase epitaxy of garnets, thin films of high perfection are grown most often from a PbO – B_2O_3 flux on nonmagnetic garnet substrates. One of the methods is so-called "tipping" technique. In this technique YIG crystals (or components forming the YIG compound), a suitable solvent/flux for the YIG and a substrate are placed in a platinum crucible. The crucible is heated to 1000 to 1100 °C for a time sufficient to ensure saturation of the solvent. The boat is then tipped so that the solvent runs over the substrate. When the film has grown to the desired thickness the boat is tilted back and the temperature lowered to room temperature.

Disadvantage of the flux technology is contamination of the prepared YIG by the Pb from the flux and by Pt from the crucible. Comparison of NMR spectra of YIG samples prepared in different fluxes could be found in [Step99].

3.1.5.3. Synthesis of bismuth iron garnet (BIG) and bismuth-yttrium iron garnet (BiYIG) films.

BIG as well as YIG is a synthetic material. The completely Bi-substituted iron garnet bulk crystals are not a thermodynamic phase at high temperatures (because of the considerable difference in ionic radii of Y^{3+} and Bi^{3+}) and so, only thin film material can be obtained. The use of the Liquid Phase Epitaxy (LPE) technique is practically impossible in view of the following reasons. The amount of Bi which can be incorporated into the garnet lattice increases with increase of the Bi concentration in the melt (Bi_m) and of degree of supercooling of the melt (ΔT) and with decrease of growth temperature (T_g). As Bi_m and ΔT increase and T_g decreases, the melt becomes highly viscous and the metastable supercooled state approaches the lability point. This results in the lowering of diffusion rate of solute and precipitation of microcrystallines. Finally, the crystal growth will not proceed any more. Difficulties associated with LPE growth of BIG will be avoided by separating the material source from the substrate and by transporting the material via vapor phase (epitaxial growth from vapour phase). Such conditions one can satisfy creating the BIG as a single crystal film using a reactive Ion Beam Sputtering (IBS) technique [Okud89], [Sato90], [Okud87], [Okud87MAG], [Okud90]. The IBS process is essentially a non-thermal equilibrium one. Since sputtered particles have energy of several eV which corresponds to thermal energy of several thousand degrees, reaction for crystallization may occur at lower temperatures comparing with those required for purely thermal reaction.

As far as the bismuth has large ionic radius (0.117 nm) compared to ionic radius of Y^{3+} (0.1019 nm), its substitution for yttrium is problematic in view of a strong lattice expansion. The nucleation and growth of BIG film become favorable if during the deposition the single crystal garnet substrate with sufficiently high lattice parameter is kept at appropriate temperature in a proper oxidizing atmosphere. Substrate for the deposition should be a material with lattice constant being close to BIG lattice constant which equals 1.2624 nm. As a result of testing of different substrate materials it was found that the garnet phase of BIG could not be obtained on substrates other than garnet. The good results were reached using $Nd_3Ga_5O_{12}$ garnet with lattice constant 1.2509 nm and $Gd_3(ScGa)_5O_{12}$ garnet with the 1.2569 nm lattice constant.

The target preparation. For deposition of film of multi-component material with high uniformity in thickness and composition the flux of sputtered particles is required to have spatial homogeneity in composition and density. Such flux may be obtained from a target with a microscopically homogeneous structure and composition. From this point of view a ceramic target composed of the garnet phase is the best for this work. The procedure is as follows: mixing of Bi_2O_3 and Fe_2O_3 powders in the molar ratio of 3:5. A mixed powder of constituent oxides then should be cold-pressed at 600 kg/cm^2 and then sintered at the temperature 900-1100 ° C for 6 to 9 hours. A target size of 5 cm in diameter is determined by taking into consideration the divergence of a beam diameter during transportation from a beam source to a target surface.

The IBS process consists of the following three steps: 1) generation of inert gas ion beam for sputtering, 2) sputtering of target, and 3) deposition of sputtered particles in reactive atmosphere. Both of the ion sources for target sputtering and for substrate cleaning are Kaufman type which is suitable for producing homogeneous beam with a broad profile. Argon ion beam is neutralized before bombarding the target to prevent the charge accumulation on insulating target.

The BIG phase is obtainable if the substrate temperature is held between 470 and 550 ° C. Substrate temperature required for crystallization during deposition lowers as the bismuth content of target decreases. The deposition rate is about 0.06 micron/hour.

In the frame of investigations of the thesis were used BIG single crystal film and bismuth-yttrium iron garnet single crystal film of high Bi concentration, prepared by IBS. Characteristics of these samples are given in Table 3.1.5.1.

x	3	2.75
Target composition	$Bi_3Fe_5O_{12}$	$(Y_{0.25}Bi_{2.75})_{2.44/3}Fe_{4.56}O_{12}$
Substrate ((111) plane)	$Nd_3Ga_5O_{12}$	$(GdCa)_3(GaMgZr)_5O_{12}$
Substrate lattice constant (nm)	1.2509	1.2499
Thickness (μm)	2.75	1.75
Lattice constant (nm)	1.2629	1.2638
Faraday rotation (°/μm) at 635 nm, room temperature	−5.35	−5.1

Table 3.1.5.1 Characterization of iron garnet films prepared by IBS.

Three comparative samples with low x were used: pure single crystal YIG film grown onto gadolinium galium garnet substrate by liquid phase epitaxy (LPE), bulk single crystal (x = 0.02) grown from flux and polycrystalline sample (x = 0.15) prepared by ceramic technique.

3.2. General properties and NMR studies of magnetites

The general chemical formula of spinel ferrites is $M^{(2+)}Fe_{2-x}^{(3+)}M_x^{(3+)}O_4$, where x is a composition parameter, $M^{(2+)}$ represents a divalent cation or a combination of cations with an average valency of two, $M^{(3+)}$ represents a trivalent cation or a combination of cations with an average valency of three. Among these oxides, magnetite Fe_3O_4 is an important compound, from which the spinel ferrites can be derived by partial substitution of the iron ions by other cations. Despite it is the earliest discovered magnet (~1500 B.C.) and one of the best known magnetic compounds, this mixed-valence system hitherto is not completely understood and the investigation of the physical properties of magnetite is still an intriguing field of research, especially, the properties in relation to the electronic ordering of the Fe^{2+} and Fe^{3+} ions on octahedral sites below and above the Verwey transition, and the phase transition itself.

Magnetite exhibits a variety of properties, depending on its temperature. There are three main regions of temperatures where magnetite behaves differently: first region- between 0K and the Verwey transition temperature T_V (of about 120-125K, depending on purity and internal stresses), second region - from T_V up to T_C (the Curie temperature, which is of about 840K) and the third one - above T_C. In the last region magnetite behaves as a paramagnet. At T_C magnetite turns from paramagnetic to ferrimagnetic phase, in temperature region 0K – T_C it is a collinear ferrimagnet. At the Verwey temperature T_V, Fe_3O_4 undergoes a metal-insulator transition, accompanied by a structure transition from cubic to monoclinic. This the so-called Verwey transition is characterized by a large decrease in conductivity (of about two orders of magnitude) and a drop of the magnetization as well as by a heat capacity anomaly at the transition temperature. Just above the Verwey temperature T_V magnetite undergoes another transition – the so-called spin-reorientation transition, when the easy direction of magnetization is changing. In pure Fe_3O_4 this transition occurs at T_{SR} ~ 130 K.

The conductivity of Fe_3O_4 at room temperature is relatively high (about $2x10^4$ $(\Omega m)^{-1}$) compared to the rather low values ($\sim 10^{-5}(\Omega m)^{-1}$) of “normal” spinels such as Co_3O_4 and Mn_3O_4 [Walz02]. From this striking difference Verwey et al. deduced an inverse spinel structure of magnetite.

3.2.1. Crystal structure of magnetite

Magnetite crystallizes into the cubic spinel structure (space symmetry group Fd3m-O_h^7) above the Verwey transition temperature (~120-125K). Magnetite is an inverse spinel and its formula unit is written as $Fe^{3+}[Fe^{2+}Fe^{3+}]O_4$ to distinguish the first A-type tetrahedrally coordinated Fe^{3+} ions from the bracketed Fe^{2+} and Fe^{3+} ions in B-type octahedral sites. The cubic unit cell corresponds to eight formula units ($Fe_{24}O_{32}$). Oxygen ions are cubic closest packed, so there are 32 octahedral and 64 tetrahedral holes in the structure. 1/8 of the tetrahedral holes are filled with ferric ions Fe^{3+} (8 ions per unit cell) while 1/2 of octahedral holes are nominally filled by both ferric and ferrous ions (16 ions per unit cell).

The coordinates of the equivalent positions of the space group $Fd\bar{3}m - O_h^7$ are given in Table 3.2.1.

The first column in Table 3.2.1 gives the number of the equivalent positions in the set, which is denoted by a letter in the second column. The third one gives the point symmetry of the position of each set and the fourth one represents different types of sites occupied in the magnetite unit cell. The next columns present the coordinates of all the equivalent positions in fractions of the lattice parameter. In real spinels the closed cubic packing of the oxygen ions is deformed by the cations. The tetrahedral sites are usually too small to contain the metal ions and the oxygen ions will be displaced from their ideal position into a <111> direction away from the central tetrahedral ion. A quantitative measure of this displacement is the oxygen parameter μ, which determines the exact positions *e* of the oxygen lattice sites as indicated in Table 3.2.1. If there is no enlargement of the tetrahedrons, the oxygen parameter μ equals 3/8 (μ=0.375) in the spinel structure. The cubic unit cell of magnetite can be divided into 8 octants (cubes). All octants have the same occupation for the oxygen ions, but there are two types of octants (with adjacent faces) having different positions for the metal cations. They can be surrounded by four oxygen anions (tetrahedral or A-positions) and by six oxygen anions (octahedral or B-positions), as shown in figures 3.2.1, 3.2.2 and 3.2.3.

In fact the oxygen ions of magnetite unit cell form the close-packed face-centered-cubic (fcc) lattices with an edge of 1/2*a*, where a = 8.398Å is a lattice parameter of magnetite [Brab95] The tetrahedral sites form two interpenetrating fcc lattices shifted with respect to each

Num-ber	Site	Site symmetry	Sites occupied in magnetite	Coordinates			
48	f	mm		μ,0,0; 0, μ,0; 0,0, μ;	$\underline{\mu}$,0,0; 0, $\underline{\mu}$,0; 0,0, $\underline{\mu}$;	1/4+μ,1/4,1/4; 1/4,1/4+μ,1/4; 1/4,1/4,1/4+μ;	1/4-μ,1/4,1/4; 1/4,1/4-μ,1/4; 1/4,1/4,1/4-μ;
32	e	3m	oxygen sites	$\underline{\mu}$, $\underline{\mu}$, $\underline{\mu}$; $\underline{\mu}$, μ, $\underline{\mu}$; $\underline{\mu}$, $\underline{\mu}$, μ; μ, μ, μ;	1/4 -μ, 1/4 - μ, 1/4 - μ; 1/4 - μ, 1/4 + μ, 1/4+ μ; 1/4 + μ, 1/4 - μ, 1/4+μ; 1/4 + μ, 1/4+ μ, 1/4 - μ;		
16	d	$\underline{3}$m	iron B-sites	5/8,5/8,5/8;	5/8,7/8,7/8;	7/8,5/8,7/8;	7/8,7/8,5/8;
16	c	$\underline{3}$m		1/8,1/8,1/8;	1/8,3/8,3/8;	3/8,1/8,3/8;	3/8,3/8,1/8;
8	b	$\underline{4}$3m		1/2,1/2,1/2;	3/4,3/4,3/4;		
8	a	$\underline{4}$3m	iron A-sites	0,0,0;	1/4,1/4,1/4;		

Table 3.2.1. The sets of the equivalent symmetry points of the space group $Fd\bar{3}m - O_h^7$ and their occupation in the spinel structure and magnetite unit cell. The origin is taken at a tetrahedral site and the value of an oxygen parameter μ is approximately 3/8 [Brab95]. The coordinates of additional positions can be found by translations (0,1/2,1/2), (1/2,0,1/2) and (1/2,1/2,0). The unit cell of magnetite contains 8 "cubes" of $Fe^{3+}[Fe^{2+}Fe^{3+}]O^{2-}{}_4$ (see fig.3.2.1): 32 O^{2-}ions occupies the positions e, 16 Fe-ions are in d positions in the centers of oxygen octahedrons (B-sites), and 8 Fe-ions are in a positions in the centers of oxygen tetrahedrons (A-sites).

other over a distance $1/2\sqrt{3}\,a$ in the direction of one body diagonal of the cube; the octahedral sites form four fcc lattices that are shifted over a distance $1/2\sqrt{2}\,a$ in the direction of the face diagonals of the cube. The oxygen parameter of magnetite equals μ=0.379 [Brab95].

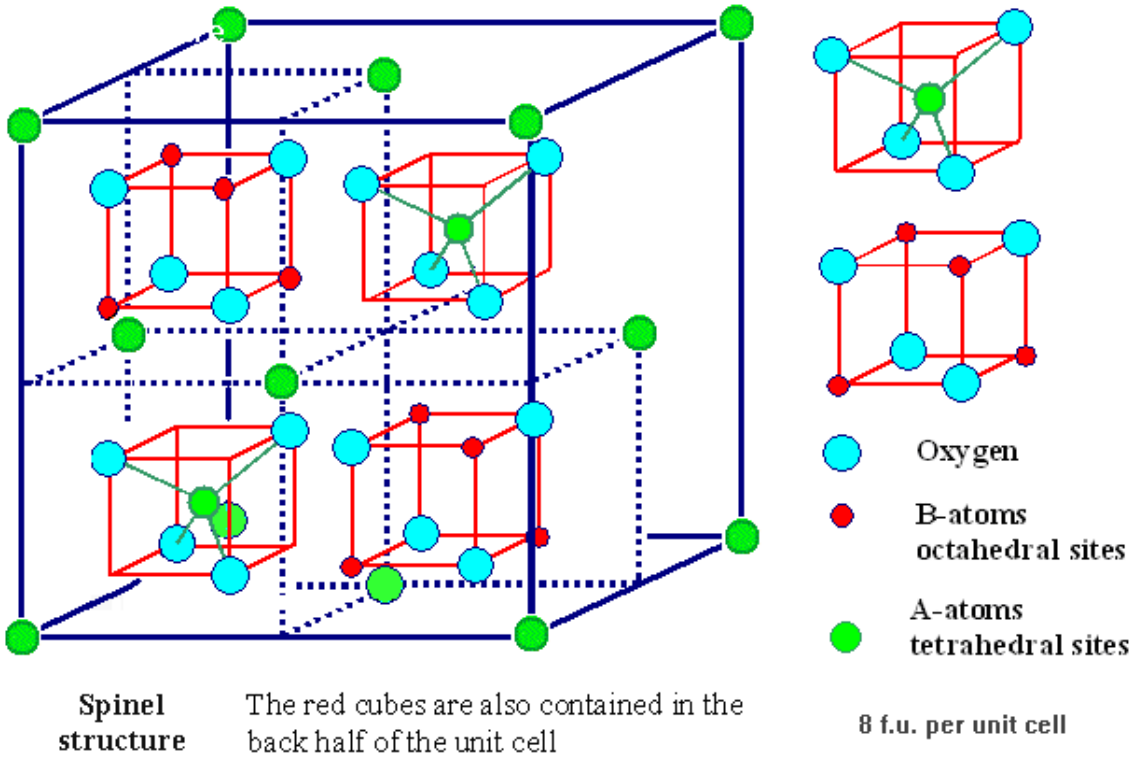

Figure 3.2.1. Unit cell of magnetite Fe_3O_4 above the Verwey transition temperature.

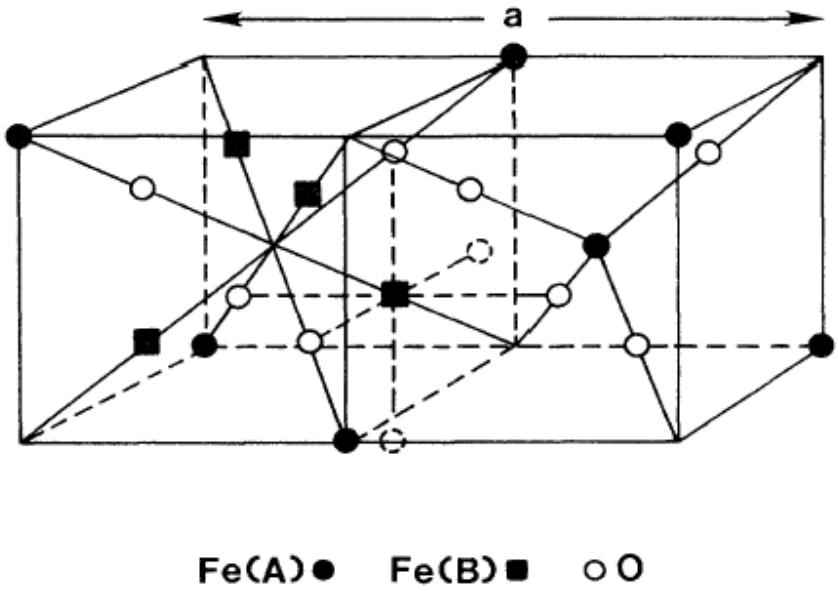

Figure 3.2.2. Neighborhood of tetrahedral A and octahedral B iron ions in magnetite. The crystal is made up of alternate stacking of the two cubes which form the basis in a face-centered cubic lattice [Zhan91].

It is convenient to present crystal structural of magnetite above the Verwey transition in terms of a layer sequence displayed below in the fig. 3.2.3:

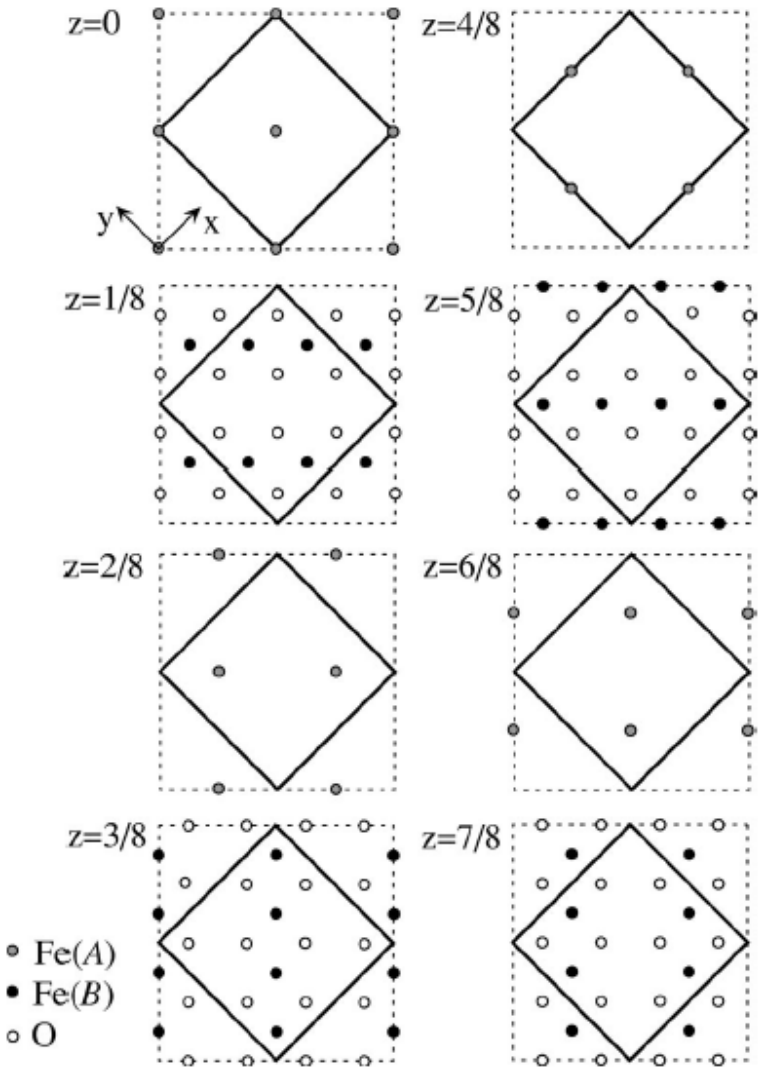

Figure 3.2.3. The layer sequence representing the structure of magnetite above the Verwey transition. The thick squares show the cubic unit cell with a lattice constant *a* in the xy plane, while the z coordinates are indicated by the fraction of *a*. The unit cell at xy plane is shown by dotted lines for $T<T_V$ [Seo02].

Below the Verwey transition the space symmetry group of magnetite was confirmed to be C_C (monoclinic crystal structure), in contrast to the cubic O_h^7 $Fd\bar{3}m$ -structured high-temperature ($T > T_V$) phase [Iizu82]. The distortion from the orthorhombic symmetry is small [Wrig02]. The

unit cell of the monoclinic structure contains four rhombohedrally distorted cubic cells (Fig. 3.2.4).

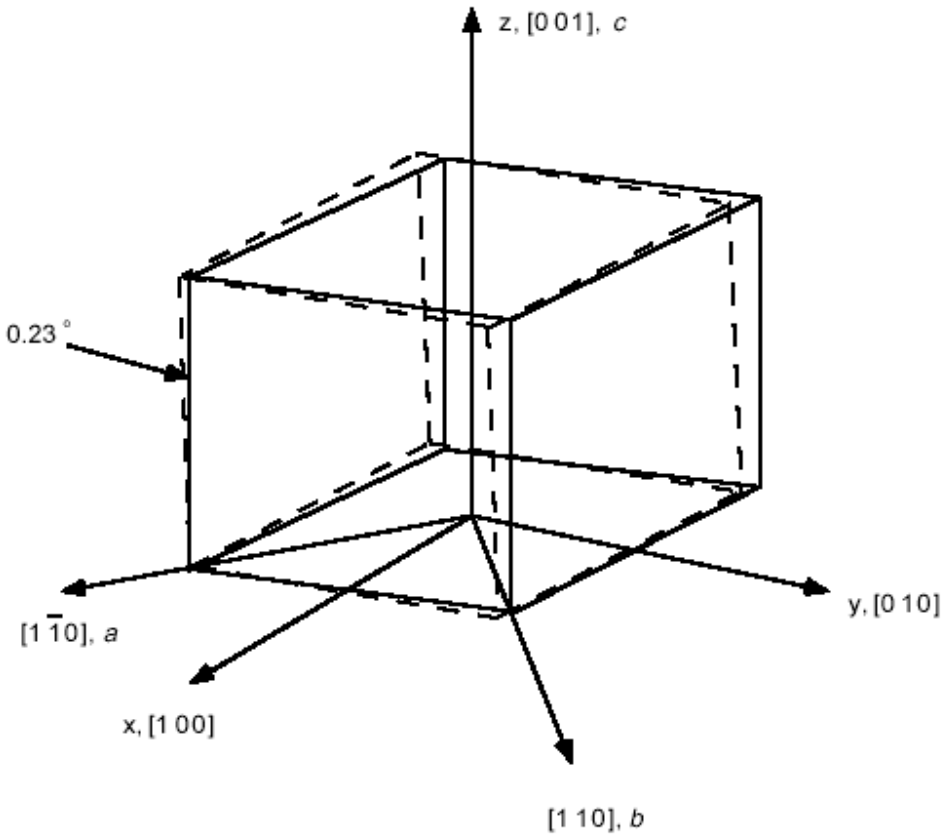

Figure 3.2.4. Relationship between the low-temperature monoclinic axes (a, b and c), the rhombohedrally distorted cell (solid line), and the high-temperature cubic unit cell (dashed line). Each monoclinic unit cell consists of four rhombohedrally distorted cells [Muxw00].

The reported lattice parameters of the monoclinic phase at 10K are *a*=11.868 Å, *b*= 11.851 Å, *c*=16.752 Å and β= 90.20°, with 32 formula unit per unit cell [Iizu82].

C_c group has the following symmetry operations: C = translation (1/2,1/2,0); *c* = reflection in (*ac*) plane + (0,0,1/2) translation. While all the A-sites and all the B sites are crystallographically equivalent in the cubic phase, there are 8 nonequivalent A-sites and 16 nonequivalent B-sites in the Cc structure.

3.2.2. Magnetic properties of magnetite.

Magnetite is a ferrimagnet with magnetic moments on A-site antiparallel to moments on B-sites. The cubic unit cell contains 32 oxygen anions O^{2-} and 24 iron cations, one-third of which (i.e. 8 cations) are in tetrahedral sites, and the rest (i.e.16 cations) are in octahedral sites, see fig 3.2.5.

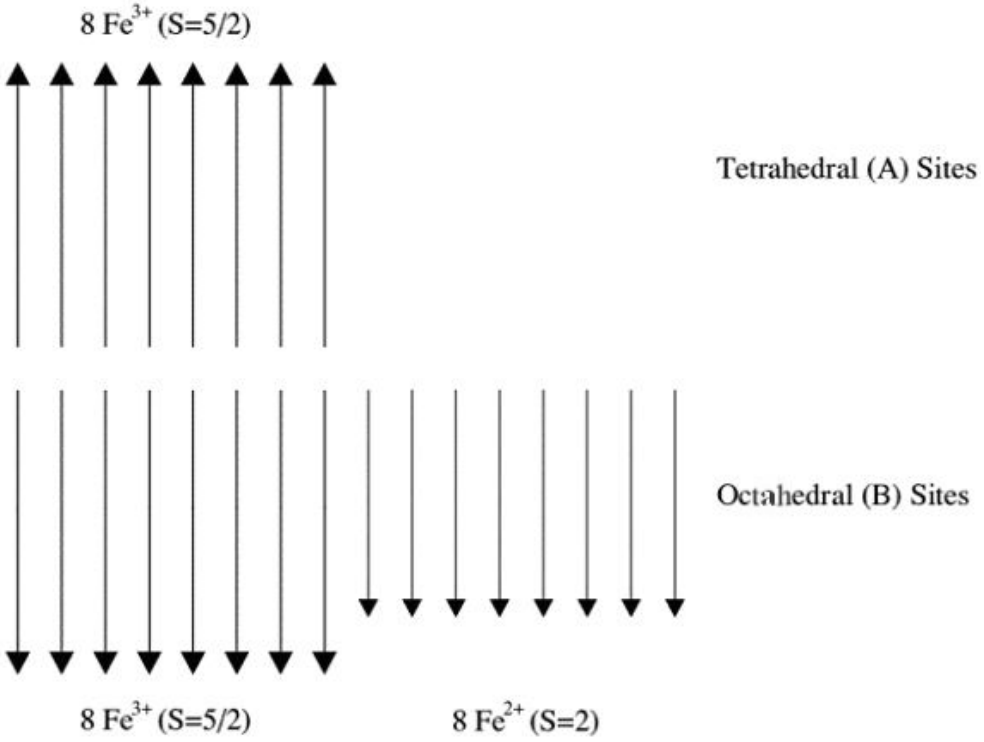

Figure 3.2.5. A scheme of ferrimagnetic ordering of electron spins in a cubic unit cell of magnetite, supposing ferric ions in A-sites and ferric and ferrous ions in B-sites.

From figure 3.2.5 can be seen that the Fe^{3+} ions on the A and B sites are aligned anti-parallel so that the magnetic moment of the unit cell only comes from the Fe^{2+} ions, with a magnetic moment of $2S = 2 \cdot 2 = 4\ \mu_B$ per formula unit, giving $32\mu_B$ per unit cell.

Fe^{3+} ion has half-filled 3d electron shell (electron configuration $3d^5$) and zero angular momentum in the ground state. On the other hand, the ground state of the free Fe^{2+} ion (electron

configuration $3d^6$) is ^5D and considerable orbital momentum remains even when this term is split by the crystal field. Fe^{3+} and Fe^{2+} ions in octahedral sites are ferromagnetically coupled via a double-exchange mechanism associated with inter-ion electron transfer [Cox92], [Elli98]. The lone electron whose spin is pointed opposite to the spins of other electrons—is easily exchanged between equivalently B-sited, closely spaced Fe^{2+} and Fe^{3+} ions, according to the relation:

$$Fe^{2+} - e^{-} \Leftrightarrow \quad Fe^{3+}$$

In contrast, the Fe^{3+} ions in tetrahedral and octahedral sites are antiferromagnetically coupled through the intervening oxygen atom.

Above T_V (~120K) the crystal structure of magnetite is cubic. Close to this temperature the easy direction of magnetization is [001], changing to [111] at the spin-reorientation transition. In pure Fe_3O_4 this transition occurs at T_{SR} ~ 130 K.

For M || [001] in the cubic phase ($T_V<T<T_{SR}$) all Fe ions on octahedral (B) sites are magnetically equivalent.

Above T_{SR} (M || [111]) there are two magnetically non-equivalent B sites. The sites B_1 have the axis of local trigonal distortion parallel to the magnetization (i.e. parallel to [111] direction), while for sites B_2 trigonal distortion and magnetization point along different body diagonals (i.e. local trigonal axis points along one of the remaining three diagonals [-1,1,1], [1,-1,1] or [1,1,-1]).

All tetrahedral (A) sites are magnetically equivalent for both M || [001] and M || [111].

Below the Verwey transition the space symmetry group of magnetite is C_C and magnetization is along the easy [001] direction [Mats77, Ozde99]. The number of magnetically nonequivalent sites then equals to the number of crystallographically nonequivalent sites, i.e. 16 for B sites and 8 for A sites.

3.2.2.1. Temperature dependence of saturation magnetization.

The temperature dependences of saturation magnetization $M_S(T)$ measured parallel to [001], [1 $\bar{1}$ 0], and [110] on cooling from 300 K to 10 K in an external field H= 2T are shown in Figs. 3.2.6, 3.2.7 and 3.2.8 [Mats77, Ozde99, Muxw00]. In all three crystallographic orientations, M_S increases with decreasing T according to a $(T_C - T)^{0.4}$ relation between 300 K and T_V=119K. Below T_V, the $M_S(T)$ curves are significantly different for different crystallographic directions (Figs. 3.2.6 and 3.2.8). These results show that the magnetocrystalline anisotropy of monoclinic magnetite below T_V is much greater than the anisotropy of cubic magnetite above T_V.

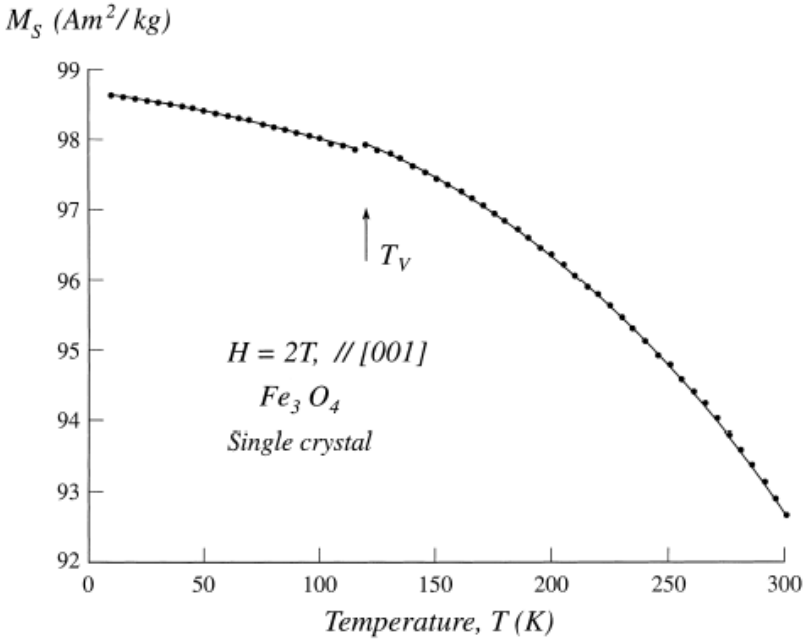

Figure 3.2.6. M_S–T curve along the cubic [001] direction (monoclinic *c* axis) of the crystal during cooling from 300 K to 10 K in a field H=2T [Ozde99].

Another the most immediately obvious feature (Figs. 3.2.6, 3.2.7, 3.2.8) is the sharp jump in M_S at the Verwey transition by 0.1%, 1.6% and 1.2% for fields applied along [001], [1 $\bar{1}$ 0] and [110], respectively [Mats77, Ozde99, Muxw00]. Increasing the applied field from 0.5 to 0.8 T increases the measured magnetization below T_V, which decreases the size of the sharp anomaly at T_V (Fig.3.2.6).

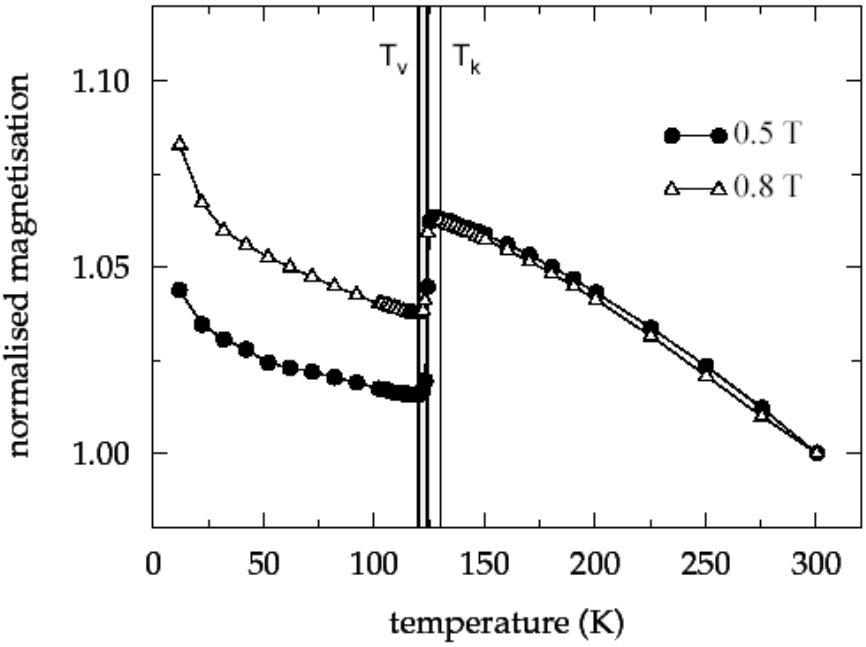

Figure 3.2.7. Magnetization of magnetite sample as a function of temperature in the presence of two different applied fields [Muxw00].

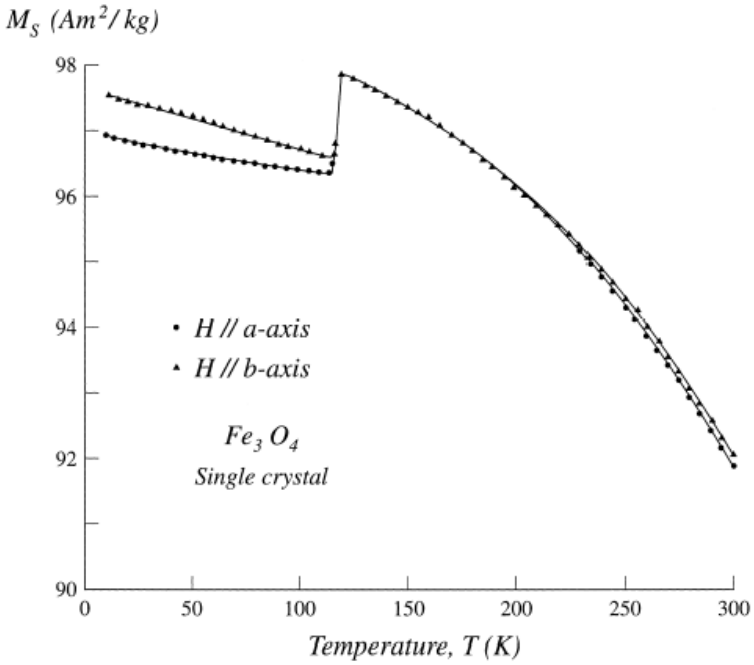

Figure 3.2.8. Temperature dependence of saturation magnetization M_S parallel to $[1\,\bar{1}\,0]$ and [110] (*a* and *b* axes, respectively) during cooling from 300 K to 10 K in a field H=2T [Ozde99].

These effects have been suggested to be caused by a change in the magnetic structure on passing the Verwey transition [Mats77, Ozde99]. Another approach to explain these effects as well as other magnetic properties of magnetite is the magneto-electronic theory of Belov [Belo93] which incorporates the paraprocess [Belo94, Belo96] for interaction of a weak magnetic e-sublattice (i.e. the magnetically ordered subsystem of hopping electrons) with an external saturating magnetic field (see paragraph 3.2.3).

3.2.2.2. Magnetocrystalline properties of magnetite.

The total anisotropy energy E_{anis} of magnetite is the sum of the magnetocrystalline anisotropy energy E_{MC} , the magnetostrictive anisotropy energy E_{stric} and the magnetoelastic anisotropy $E_{elastic}$:

$$E_{anis} = E_{MC} + E_{stric} + E_{elastic} \qquad (3.2.2.1)$$

As in the case of yttrium iron garnet in section 3.1.2 we will dwell upon the magnetocrystalline anisotropy energy of magnetite. The cubic magnetocrystalline anisotropy is given by (Kittel 1949):

$$E_{MC}^{cubic} = K_1(\alpha_1^2\alpha_2^2 + \alpha_2^2\alpha_3^2 + \alpha_3^2\alpha_1^2) + K_2\alpha_1^2\alpha_2^2\alpha_3^2 + ..., \qquad (3.2.2.2)$$

where K_1 and K_2 are the first two cubic anisotropy constants, respectively, and α_I are the directional cosines of the magnetization vector with respect to the cubic axes. The behaviour of the magnetocrystalline anisotropy energy at low temperatures is still under debate (Fig. 3.2.9) [Muxw00]. The two most complete sets of low-temperature magnetocrystalline anisotropy data [Bick57] and [Syon65] (Fig. 3.2.9) are for $K_1^{'}$ and $K_2^{'}$, that is, K_i plus a magnetostrictive contribution. In theory, it is possible to obtain K_i by either direct measurement using ferromagnetic resonance (FMR) as suggested by Ye et al. [Ye94], or by simply removing the experimentally measured magnetostrictive term from $K_i^{'}$ [Kako91], [Sahu95]. With regard to FMR, however, the data sets are rather sparse [Bick49, Bick50]. The second method of

calculating $K_i^{'}$ is fraught with errors, because for magnetite the values of the magnetostrictive constants are often smaller than the error in the measurement of K_i.

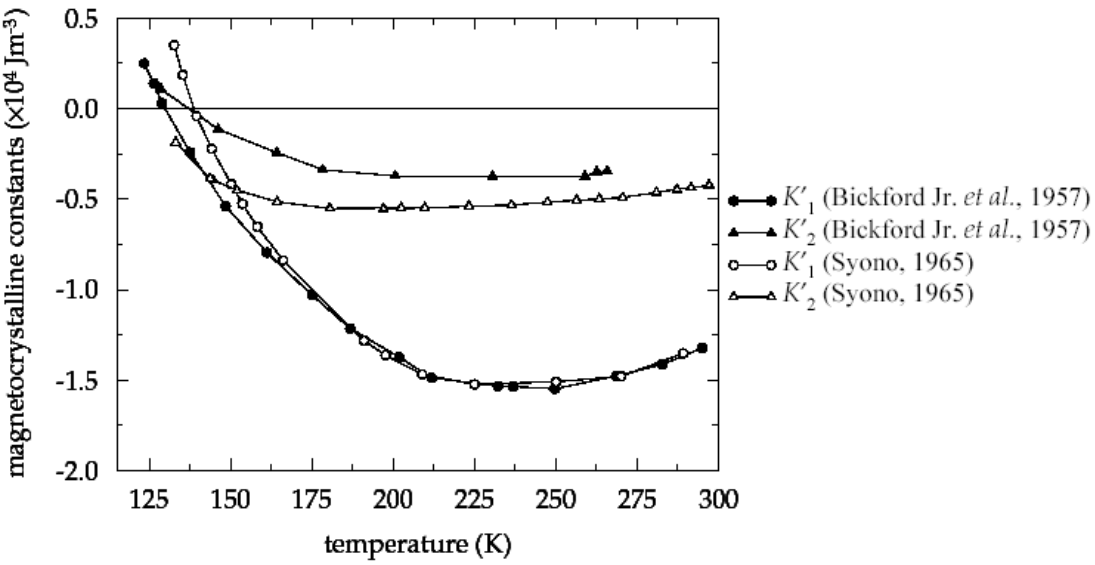

Figure 3.2.9. Magnetocrystalline anisotropy constants $K_1^{'}$ and $K_2^{'}$ as functions of temperature showing the large difference in the values of [Bick57] and [Syon65].

For the monoclinic low-temperature structure, the magnetocrystalline energy $E_{MC}^{monoclinic}$ is expressed by [Abe76]:

$$E_{MC}^{monoclinic} = k_a + \alpha_a^2 k_b \alpha_b^2 + k_{aa}\alpha_a^4 + k_{bb}\alpha_b^4 + k_{ab}\alpha_a^2\alpha_b^2 - k_u\alpha_{111}^2, \qquad (3.2.2.3)$$

where α_a, α_b *and* α_{111} are the directional cosines of the magnetization with respect to the monoclinic *a*-, *b*- and cubic [111] axes respectively (see Fig.3.2.4 for coordinate system). The temperature-dependent behaviour of magnetocrystalline constants for both cubic and monoclinic phase is shown in Fig. 3.2.10. Again the magnetocrystalline anisotropy `constants` in Fig.3.2.10 are not k_i but $k_i^{'}$, i.e. k_i plus a magnetostrictive contribution [Muxw00]. The magnetocrystalline anisotropy constants are considerably larger than the cubic magnetocrystalline constants (Fig.3.2.10). The monoclinic constant $k_a^{'}$ is approximately 10 times greater than $K_1^{'}$. Consequently, the relative importance of the monoclinic magnetocrystalline anisotropy to the domain structure is far greater than the cubic one: $E_{MC}^{monoclinic} >> E_{MC}^{cubic}$. The abrupt jump in the

magnetocrystalline anisotropy on cooling through T_V is expected, because the magnetocrystalline anisotropy is controlled by the mobility of the hopping electrons [Flet74], [Belo93]. As the mobility decreases, the magnetocrystalline anisotropy increases [Belo93].

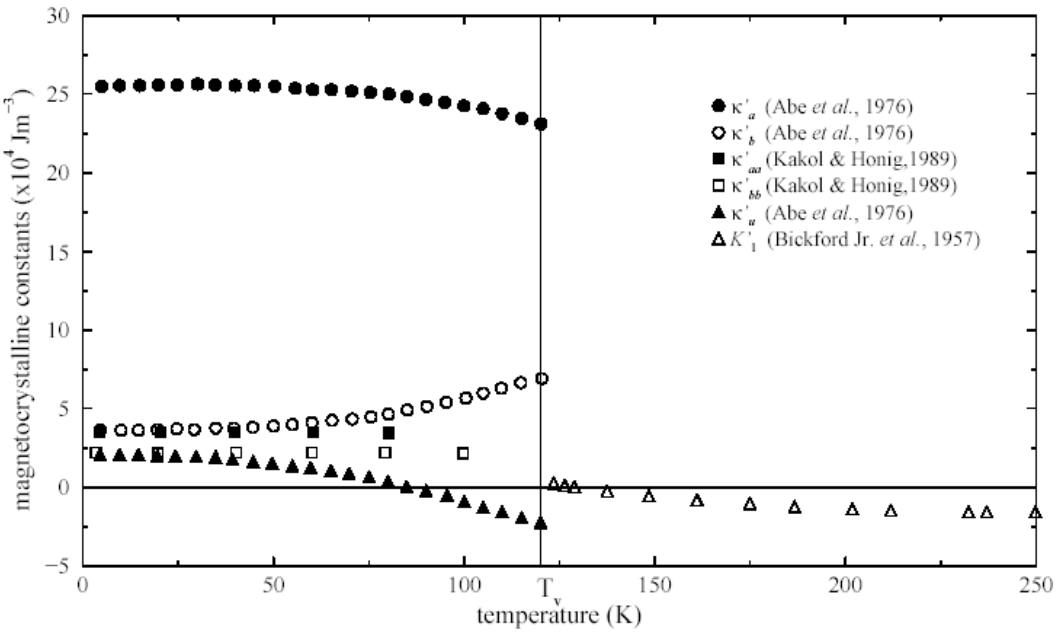

Figure 3.2.10. Temperature dependence of the cubic and monoclinic magnetocrystalline constants. $K_1^{'}$ is the first cubic magnetocrystalline anisotropy constant (eq. 3.2.2.2) and $k_i^{'}$ are the low-temperature monoclinic constants (eq.3.2.2.3).

There is also a significant reduction in the symmetry of the magnetocrystalline anisotropy field. In next figures the magnetocrystalline energy fields for T=290, 126 and 110K are depicted [Muxw00]. In the cubic phase, for T>130K the easy-axis is the [111] (Fig.3.2.11), and for T_V<T<130K, $K_1^{'}$ is positive (Fig.3.2.8), and switches the easy-axis from [111] to [001] (Fig.3.2.12). The monoclinic magnetocrystalline anisotropy has a lower order of symmetry than the cubic phase, the easy-axis is the c-axis. However, the b-axis is also relatively easy compared to the a-axis (Fig.3.2.13).

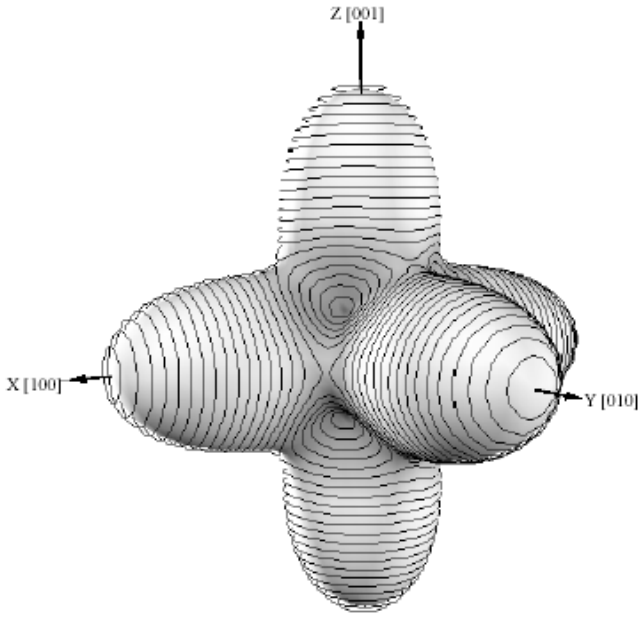

Figure 3.2.11. The cubic magnetocrystalline anisotropy of magnetite at 290 K [Muxw00]. The hard axes are in the [100], [010] and [001] directions.

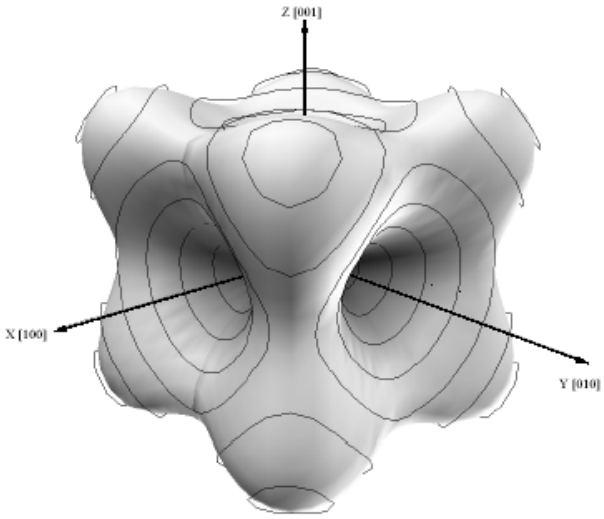

Figure 3.2.12. The cubic magnetocrys-talline anisotropy of magnetite at 126 K [Muxw00]. The hard axis is in the [111] direction.

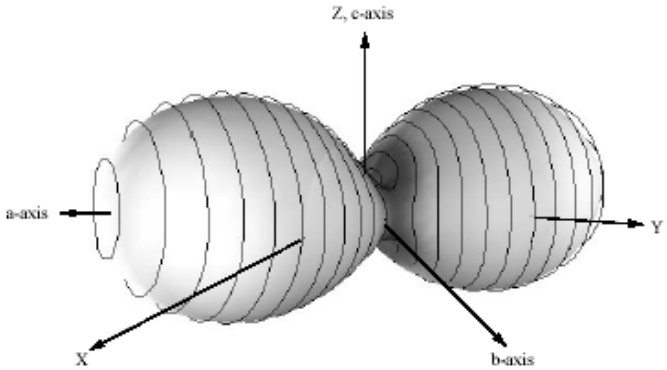

Figure 3.2.13. The monoclinic magnetocrystalline anisotropy of magnetite at 110 K [Muxw00]. The hard axis is the a-axis.

3.2.3. Review of previous experimental results and theoretical approaches.

The history of interest in magnetite, covering more than 60 years of intensive experimental and theoretical investigations of its electro-magnetic properties and the Verwey transition, discloses an uncommon example of a variety of sometimes puzzling results, because of their incompatibility. During the last two decades some progress in understanding of the magnetite system has been achieved, but despite of considerable efforts many basic questions are still not answered.

In order to touch a modern view of the magnetite problem it seems desirable to dwell on some previous experimental results and theoretical approaches on this issue.

The first report that magnetite exhibits a low-temperature transition was made by Millar (1929) [Mill29], who discovered an anomaly in the heat capacity near 120K. However, it was Verwey and co-workers (Haayman, Heilmann et al.) who carried out much of the initial research into the anomalies in both the structure and electrical properties (fig.3.2.14) at the transition. They explained it as a structural transformation caused by a charge ordering of iron cations of different valency (Fe^{2+} and Fe^{3+} in lattice octahedrons) in alternating (001) layers [Verw39]. The ordering process involves electron hopping between the cations. At $T>T_V$ this ordering is broken down by the thermal excitations.

Many refinements of this model were subsequently introduced and later some experimental facts were obtained, pointing out that this picture is inadequate. There is no consensus so far about the ordering of Fe^{2+} and Fe^{3+} in the octahedral sites below the Verwey transition.

Subsequent experimental facts such as 1) the small value of the magnetic anisotropy energy accompanying the magneto-electric effect [Kita79], 2) the small change of the saturation magnetization (0.1%) at the transition temperature [Iida76] (see Fig.3.2.6), and 3) the absence of anomalies of the magnetic anisotropy constants on passing the critical non-stoichiometry parameter δ_c for $Fe_{3-\delta}O_4$, above which the transition disappears [Kako89], allowed to conclude, that the driving mechanism of the ordering at low temperatures could be not primarily induced by magnetic interactions, but could probably be related to the Coulomb interactions.

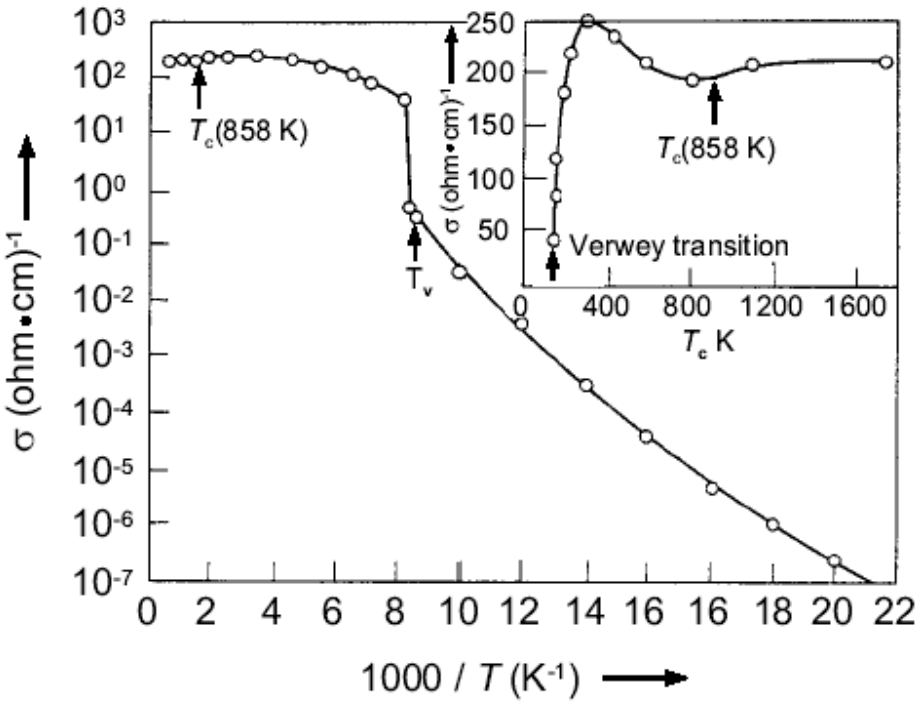

Figure 3.2.14. Typical temperature dependence of the electrical conductivity in Fe_3O_4 [Walz02].

If the ordering mechanism would be related to the nearest-neighbour Coulomb interaction, the transition temperature above 10^4K would be expected, as was pointed out by Anderson [Ande56],whereas the real transition is at about 120K.

To clear this apparent contradiction Anderson assumed that the actual transition is not so drastic and occurs only between two alternate ordered states, long-range ordered state (LRO) below the Verwey transition and short-range ordered state (SRO) above the transition, that is he interpreted the Verwey transition as a loss of LRO upon heating through the transition. The assumed residual SRO state above T_V was besides in agreement with another experimental results: 1) the thermal activation of conduction, persisting within the temperature range above T_V ($Q \approx 0.05$eV) –despite a relatively high conductivity [Adle68], [Broe68], and 2) the concordance between the observed transition-induced molar entropy variation of about 0.3R with the predicted value of 0.2R for a LRO-SRO transition, as opposed to $\triangle S = 0.69R$, expected for a complete order-disorder transition at T_V [Ande56], [Ihle86].

Anderson proposed to take into account the particular geometry of the spinel lattice. Proposed SRO is characterized as a state of minimum lattice energy, realized by a maximum number of adjacent, B-sited Fe^{2+} - Fe^{3+} pairs. The octahedral sites in the spinel structure are

arranged in tetrahedrons B_4 with each site belonging to two tetrahedrons. In this arrangement of octahedral sites it is possible to keep strong short-range order, imposed by the so-called *Anderson condition*: the charge of the individual tetrahedron, formed by nearest-neighbour B sites, must be constant. It means for stoichiometric magnetite two Fe^{2+} ions and two Fe^{3+} ions in octahedral positions (i.e. an effective charge of 10+) per particular tetrahedron. In a magnetite crystal it is possible to keep this short range order and the number of ionic distributions which fulfills Anderson`s condition is very large (is minimized by $\sim(3/2)^{N_B/2}$ different configurations , where N_B is the number of B sites). The energy differences between the various states with short-range order will be very small, moreover if the interaction leading to the Verwey transition is restricted to nearest neighbour pairs, the energies of all configurations fulfilling Anderson`s condition will be identical and no transition will occur. It means, that if the LRO exists below the Verwey transition, it would not be achieved by nearest neighbour interactions alone but, possibly, in the presence of additional interactions, like next nearest neighbors Coulomb interactions.

Since then many other models have been proposed to account for new experimental data, like for the structural change, magnetic relaxation processes [Walz02], the magnetocaloric effect [Belo93], magnetoresistance [Belo94], spontaneous magnetization [Belo93], magnetocrystalline anisotropy [Bick49], [Abe76] and many others (below in this paragraph). It has also been found that variations in stoichiometry [Arag85], [Arag88], [Honi95] and pressure [Roze96] strongly affects the Verwey transition. Although many theories exist none of them has been able to explain all the experimental data. The various models can be roughly split into several camps [Muxw00], including structural-electronic models (like Verwey&Naayman`s , Anderson`s) and magneto-electronic models (Belov`s model).

To the *structural-electronic models* belong such conceptual extensions of the Verwey model like:

-*Polaron-based models*: Haubenreisser [Haub61] used a model of non-interacting polarons to treat quantitatively the problem of high-temperature conductivity in magnetite (the correct location of high-temperature conductivity maximum was missed by a factor of 2 (600K instead of 300K) (fig.3.2.14). Simsa calculated the room temperature conductivity in terms of non-interacting small polarons (SP) model, obtained a value smaller by a factor of 5, of only $55\Omega^{-1}cm^{-1}$ (fig. 3.2.14) [Sims79]. Chakraverty [Chak74] suggested to attribute the low-temperature Verwey ordering to a cooperative Jahn-Teller transition, associating the low-temperature

conductivity with localization and high-temperature conductivity with hopping of polarons. As a mode of polaron transport, accounting for polaron-polaron interaction, the formation of bipolarons has been suggested. The here assumed Jahn-Teller distortion, however, remained without experimental verification [Walz02].

-*Band-based models:* Cullen and Callen [Cull70] proposed band conductivity to be the dominant charge transport mechanism in magnetite by assuming the two B-sited Fe-ions (per formula unit) to distribute their 11 d-electrons, as a function of the spin-state, on two distinctly separated bands. In this picture, according to Camphausen *et al* [Camp72], the lower-energy band is completely filled by ten electrons of, e.g. spin-down orientation, whereas the eleventh, spin-up electron solely occupies the higher-energy band, thus initiating metallic conductivity above *T*v. Due to restriction on Coulomb-interactions only—thereby disregarding any type of electron–phonon coupling- self-consistent Hartree calculations are not able to account for any of the experimentally suggested ionic ordering schemes deviating from the Verwey order.

Another band model has been conceived by Ihle and Lorenz [Lore75] on the basis of the original Cullen–Callen conception by accounting additionally for both the Anderson condition and the electron–phonon interactions. Ihle and Lorenz were able to exactly reproduce the temperature dependence of the electrical conductivity over the range 65 K < T < 500 K. As a necessary condition for the setting-in of low-temperature carrier localization and ordering—due to gap formation by band splitting - they deduced the relation upon which the conduction process is restricted to small-polaron (SP) inter-band hopping. Just above T_V—after gap-shrinkage by about a factor of two, due to formation of sub-bands—the charge transport, up to about 300 K, is mainly supported by band conduction. The observed increase of the conductivity within this temperature range is explained by a corresponding increase of the density of states in addition to a thermally activated destruction of the SR order [Lore75], [Ihle86]. For higher temperatures, T >350 K, the SP conductivity is decreasing owing to a temperature dependent exponential reduction of the polaronic overlapping integral, so that in this temperature range hopping becomes the leading transport mechanism in their model. In addition they were able to quantitatively describe the shift of T_V as a function of pressure and the problem of high-temperature optical conductivity in terms of their spinless small-polaron model [Ihle86].

Another band structure calculations have been performed by Yanase [Yana84] using Augmented Plane Wave approximations, by Zhang [Zhan91] using Local Spin Density

Approximation (LSDA) in combination with Density Functional Technique (DFT), by Anisimov [Anis97] (LDA+U method), and others.

From the last articles on that issue one should note the articles of Jeng et al. [Jeng04] and Madsen et al. [Mads05]. The first one reports the electronic structure calculations within LDA with generalized gradient correction (GGA) plus on-site Coulomb interaction U (LDA+U) using the refined structure data of Wright et al [Wrig02]. These calculations point out that magnetite forms an insulating charge-orbital-ordered state below the Verwey transition temperature. As an explanation of why this charge-(orbital) ordering pattern does not satisfy Anderson`s criterion was pointed out that in Anderson`s calculations, the charges in ferrites are treated as the point charges and thus the electrostatic energy depends only on the number of divalent-trivalent cation-pairs. Minimization of the number of those pairs per tetrahedron would give rise to the lowest energy. The second mentioned article of Madsen et al. presents the electronic structure calculations on the refined structure data of Wright et al. by using LDA+U calculations with fixing the U within the linearized augmented plane wave (LAPW) method. They obtained a periodic charge disproportion along the c-axis in the monoclinic structure of Fe_3O_4. The proposed charge order is in good agreement with experiment.

-*Ionic low-temperature ordering models* (like Yamada`s model [Yama75], Iida`s [Iida76], Mizoguchi`s [Mizo78], Ihle and Lorenz [Ihle86], Wright et al. [Wrig02] and others). All these ordering models reflect the indefiniteness of the underlying experimental data which sometimes have been obtained on imperfect magnetite crystals [Walz02].

The *magneto-electronic model* was developed by Belov [Belo93] in response to two discrepancies between the structural-electronic models and experimental data, namely, the extremely low mobility of the conduction electrons above T_V, which is not explained by other models, and an unexplained anomaly in magnetization M_S (Fig.3.2.6) at the transition. The number of available hopping electrons in magnetite above T_V is $1.35 \times 10^{22} cm^{-3}$ [Belo93], which is comparable with that in metals, and is much greater that the value in ordinary semiconductors. However, the actual conductivity of magnetite is akin to that in semiconductors [Belo93], and so the conduction electrons should have very low mobility. Neither hopping mechanism of electrical conduction in magnetite (like in Verwey`s model) or band theory of the conduction (like in Cullen&Callen`s model [Cull71] and others) explains the extremely low mobility of the conduction electrons in magnetite above the Verwey transition. Instead, Belov points out that in semiconductors there is another mechanism that causes localization of conduction electrons – the Vonsovskii exchange interaction [Vons46], [Naga71]. This is the exchange interaction

between valence and inner electrons in ferromagnetic materials. The spin of valence electrons is acted upon by the magnetic field exerted by the internal electrons [Vons46]. According to the theory, on cooling through the Verwey transition, the hopping (valence) electrons are magnetically ordered under the influence of the Vonsovskii exchange interaction with magnetic cations, to form an e-sublattice. Because the Vonsovskii exchange interaction between the hopping electrons and iron cations is negative (antiferromagnetic), this leads not only to localization of the conduction electrons but also to a partial screening of the total magnetic moment (Abrikosov 1968) [Abri68]; that is, the e-sublattice electrons align antiparallel to the net magnetic moment of the A- and B-sublattices, and hence antiparallel to the B-sublattice (Fig.3.2.5). Consequently, there is a small decrease in M_S for $T<T_V$. At $T>T_V$, the thermal motion destroys the magnetization of the e-sublattice, which results in small experimentally detected anomaly in M_S (fig.3.2.6). The interaction of a strong sublattice (A- and B-sublattices) with a weak sublattice (e-sublattice) retards the Verwey transition so, that it is spread over a certain temperature interval. Above T_V, the Vonsovskii exchange interaction is insufficient to cause LRO of the hopping electrons; however, it is large enough to affect the orientation of the hopping electrons. Because the Vonsovskii exchange interaction in magnetite is antiferromagnetic, the hopping electrons periodically reverse (flip) their spins during hopping from A- to B- cations, which requires an additional activation energy and results in a reduction of the electron mobility [Belo96].

The discussion on the electronic structure of magnetite is intensively continuing and other ideas concerning the electronic structure of magnetite and the nature of the Verwey transition are suggesting, examining and discussing. For instance, if it is correct at all to talk about the charge ordering in the magnetite system [Subi04], what character could it have [Wrig02], if it is more correct to talk about itinerant model or about localized model of fluctuating mixed valence (for example [Huan04], what is the role of an orbital moment [Huan04], what is the role of electron-phonon (electron-lattice) interaction [Gupt02], and so on.

Turning to the experimental investigations of magnetite one should start from the investigation of *crystallographic structure* of magnetite below the Verwey transition, which has remained a subject of continued efforts by means of various techniques. Below the Verwey transition the space symmetry group of magnetite reported by Iizumi et al. from neutron diffraction measurements, was confirmed to be C_C (monoclinic crystal structure). The lattice parameters of the monoclinic phase at 10K are a=11.868 Å, b= 11.851 Å, c=16.752 Å and β=

90.20°, with 32 formula unit per unit cell [Iizu82]. Similar results were reported from X-ray measurements for temperatures between 80K and T_V [Yosh77, 79]. And the same conclusion was drawn from high-resolution electron microscopy experiments [Otsu86] and previous magneto-electric [Rado75,77], [Sira79] and electron-diffraction [Zuo90] studies. Recent NMR measurements of magnetite below Tv [Nova00, NovaICF00] are in good agreement with proposed space symmetry group C_C, since they observed predicted for the symmetry 8 Fe(A) lines and 16 Fe(B) lines in the spectra.

Concerning the *low-temperature ($T<T_V$) charge ordering*, a number of experimental data indicate that the low-temperature state could be an ordered localized charge phase [Mott74], [Rose96]. However, recent resonant x-ray scattering [Garc01] and high pressure conductivity [Todo01] results did not find charge ordering in the low-temperature phase. In the latter case of NMR results in [Nova00] the authors on the basis of their high-resolution NMR studies on high-quality single crystals pointed out that below T_V the charge carriers remain localized, or at least they move with the characteristic time much longer compared to the characteristic time of the NMR measurements (10^{-8} s), since in agreement with C_C crystal symmetry they were able to resolve, over the temperature range 4.2 K < T < T_v, eight A-type and 16 B-type lines. But because of the doubling of the lowest frequency Fe(A) line, which is not broadened when the temperature is increased, they concluded that trivalent iron ions of two types, giving rise to that line, have nearly the same oxygen environment and also their effective exchange fields are equal (difference larger than 2% would lead to a detectable splitting of the line). The latter means that also a cation environment of the two sites in question should be similar, requiring the same number of nearest Fe^{3+}(B) and Fe^{2+}(B) neighbours and very close geometry of Fe(B)-O^2-Fe^{3+}(A) triads. This provided a stringent condition for the arrangement of iron valencies on B sublattice, which being supplemented by a relaxation and bond-length analysis, led them to the conclusion, that below T_V the states of iron ions on the B sublattice are mixed strongly and the notion of 2+ and 3+ valencies may lose their meaning. NMR measurements of magnetite are discussed in more details in corresponding section below.

The next important question is whether a short-range order exists *above the Verwey transition ($T>T_V$).* Photoemission spectroscopy experiments on (100) surface of Fe_3O_4 [Park97, Chai95] provided evidence of short-range order while recent NMR measurements [Nova00] gives the contradictive results. The analysis of the NMR spectra above the Verwey transition

give rise to the conclusion that if the short-range order exists for $T>T_V$ it must fluctuate rapidly comparing to the characteristic time of NMR measurements (10^{-8}s).

*Another interesting issue regarding magnetite is low-temperature conductivity at T < T*v. As reported by Drabble et al [Drab71], the conductivity is found to be thermally activated in the temperature range from below Tv to about 50 K, thereby following a $T^{1/4}$ temperature dependence as derived by Mott [Mott74] for the case of variable range hopping (VRH). This temperature interval (50 K< T < 125 K) coincides with the occurrence of an extended plateau-like magnetic after-effect (MAE) spectrum which also has been associated with small-polaron hopping [Walz79]. Two additional intervals of MAE spectra with different conductivity activation were observed within 4 K< T < 25 K, and 25 K< T < 40 K [Leng84]. These low-temperature processes have been identified as thermally activated, incoherent electron tunneling and intra-ionic electronic excitation respectively.

Influence of pressure on the Verwey transition (T_v) and on low-temperature conductivity of Fe_3O_4 was reported by Rozenberg et al [Rose96] for temperatures $T_V > T > 30$ K and pressures below 16 GPa. The VRH-specific $T^{1/4}$ law fails for temperatures below 30 K. Different results have been obtained by Todo et al [Todo01]. They have found nonlinear decrease of T_V up to pressures of $P \leq 8$ GPa. above which the transition is completely suppressed. In the range $7.5 < P < 8$ GPa below Tv the temperature dependence of conductivity is 'metallic' type i.e. $\sigma(T)$ decreases with temperature instead of increase as expected for electron hopping and actually observed in stress-released Fe_3O_4 (see figure 6). In the transition-suppressed range, $P \geq 8$ GPa, this type of conduction dominates the whole temperature range (3 K < T < 300 K).

High-temperature conductivity (*T > T*v) has been recently studied by means of various techniques yielding results which have been differently interpreted by their authors in terms of either polaron hopping or band conduction. Todo et al [Todo95], from conductivity and Hall effect measurements on synthetic single crystal (SSC, 123K), deduced charge transport of possibly large-type polarons within the range Tv < T < 250 K, with rather small stoichiometry dependence (Fe_3O_{4+x}) within the range $0.002 \leq x \leq 0.035$. Similarly, Nakamura et al [Naka97] interpreted their Mossbauer spectra, obtained at temperatures T≤300 K on crystals of comparable quality, in terms of large polaron conduction. Boekema et al [Boek86] concluded

from their muon-spin-relaxation data, for T > Tv, that the carriers formed a *Wigner-glass phase*, supporting conduction in the form of *phonon-assisted electron hopping within a narrow polaron band* as suggested by Mott [Mott74]. In terms of similar arguments, Siratori et al [Sira98] and Degiorgi et al [Degi87] described their data obtained from, respectively, neutron diffuse scattering [SSC, 122.5 K] and optical- combined with direct-current (dc)-conductivity [NSC, ~120 K] studies. The optical results were deduced from low-energetic spectra (0.001eV< E < 0.6 eV) and analyzed in terms of the Ihle–Lorenz model, combining the small-polaron (SP) concept with Anderson's short-range order. On this basis, dc-conductivity within 100K < T < 450K can be well described by a superposition of SP band and hopping conductivity [Ihle86, Ihle83].

The old problem concerning the Verwey transition being of metal–insulator or rather semiconductor–insulator type (the more correct notation could be ′semiconductor–semiconductor transition between two states of different conductivity′) stood in the focus of recent photo-emission studies. Chainani et al [Chai95] deduced a metal–semiconductor transition from their observation [SSC, 122 K] of a gap of 0.07 eV, separating the low- and high-temperature phase, which closes upon heating above Tv. Park et al [Park97] countered with further experiments [SSC, 121 K], pointing to a semiconductor–insulator transition at T_V. They found a gap (of about 0.14 eV) between the two phases which, however, instead of becoming closed above T_v was only narrowed by about 0.05 eV. Consequently they associated this narrowing with the loss of long-range order above T_v giving rise to the observed conductivity jump. Gasparov et al [Gasp00] found their infrared and Raman data [SSC, 120 K] best explained in terms of polaronic pictures. Below T_v they deduced strong polaron localization, as expressed by an approximately *hundred-fold increased effective mass indicating the role of lattice dynamic*. The increased conductivity above T_v they explained by partial delocalization of carriers in agreement with Park et al's conceptions.

Substituted magnetite

The *Verwey transition temperature* is very sensitive to the ***impurity content and non-stoichiometry***. In perfect stoichiometric Fe_3O_4 samples this transition occurs at temperatures

close to 125K while in non-stoichiometric and substituted compounds it occurs at lower temperatures, decreasing to about 80K for impurity levels of a few percent [Brab95].

Since the Verwey ordering mechanism is believed to originate from the Coulomb interactions, the effects of substitutions that alter the Fe^{2+}/Fe^{3+} ratio on the octahedral sites is of a great interest. Many authors [Brab98], [Kozl96], [Miya72], [Arag85], [Arag88] investigated the shift of the transition temperature T_V as a function of the concentration for a number of impurities , like Ni^{2+}, Co^{2+}, Mg^{2+}, Ga^{3+}, Zn^{2+}, Al^{3+}, Ti^{4+}, and oxygen nonstoichiometry (see fig.3.2.15). The Verwey phase transition changes its order from first to second with an increased degree of oxygen-metal non-stoichiometry δ in $Fe_{3-\delta}O_4$, or Al content x in $Fe_{3-x}Al_xO_4$. Similar changes occur upon substitution of iron by other substituents [Brab98]. Aragon et al. reported two regimes on the non-stoichiometry dependence of the transition temperature on either side of a critical composition δ_c=0.0117 for $Fe_{3-\delta}O_4$, with a first-order transition for $\delta<\delta_c$ and a second-order transition for $\delta>\delta_c$. Similar results were reported for stoichiometric magnetite single crystals doped with Zn^{2+} and Ti^{4+}, $Fe_{3-z}Zn_zO_4$ and $Fe_{3-y}Ti_yO_4$.

The transition in *Al^{3+} doped magnetite* switches from first to second order for critical Al concentration lying between $0.01< x < 0.02$ [Brab98] (x>0.012 according to [Kozl96]), comparable with the value of about 0.012 for the Zn^{2+} or Ti^{4+} substitutions.

Brabers et al. [Brab98] reported the effect of a large number of impurities on the shifting of T_V. A study of stoichiometric magnetite single crystals doped with Ni^{2+}, Co^{2+} or Mg^{2+} showed a T_V shift which is about of a half of the effect of Ti or Al substitution and is about three times as large as for Ga-substitution (fig.3.2.15 is taken from their article).

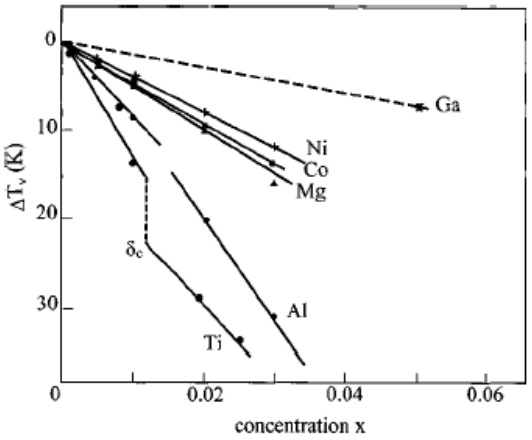

Figure 3.2.15. The shift of the Verwey transition temperature for substituted stoichiometric magnetites $Fe_{3-x}M_xO_4$, with *M*=Ga, Ni, Co, Mg, Al, and Ti [Brab98].

The small influence of the Ga^{3+}-impurities they explained by the position of the most of Ga ions in tetrahedral sites, which obviously does not act on the octahedral ordering, since Ga is trivalent. In the article of Rosenberg [Rose85] authors point to the possibility of a distribution of Ga ions on B and A sites in a ratio 1:2.

Ti-ions enter octahedral sites (curved brackets {} stand for octahedral positions further below) with a simultaneous appearance of additional Fe^{2+} -ions:

$$Fe_{3-y}Ti_yO_4 \equiv (Fe^{3+})\{Fe^{3+}{}_{1-2y}Fe^{2+}{}_{1+y}Ti^{4+}{}_{y}\}O_4$$

That could be a possible explanation of the twice larger effect for Ti compared to the two-valent Ni, Co and Mg.

Doping magnetite with Ni, Co, or Mg yields a transition temperature shift that is in between that of Ga and Al (as can be seen from the fig. 3.2.15). For all the measured Ni, Co and Mg concentrations, sharp transitions were observed (fig.3.2.15), thus suggesting that for all these samples the transition is still of the first order. Ni, Co, and Mg are all bivalent ionic substituents in magnetite. All three metals give similar shifts for T_v, slightly increasing from Ni to Mg. This small increase was explained by taking into consideration that 5–20% of the Mg or Co ions are located on A sites, whereas Ni will remain at the B sites. Since these cations are divalent, the ratio of B-sited di- and trivalent cations is for Ni exactly 2, which is a condition for perfect Verwey ordering, whereas for Co and Mg this ratio deviates weakly from 2. Another interesting moment is that if magnetic interactions were primarily involved in the mechanism of the Verwey ordering, one would expect a substantial difference between the doping with magnetic (Ni^{2+}, Co^{2+}) and nonmagnetic (Mg^{2+}) ions, which was not observed.

Honig [Honi95] reported the concentration dependence of the Tv shift in Zn-substituted magnetite to be about two times larger, as was observed for the Ni^{2+} magnetites and comparable to the Ti^{4+} effect. Zn^{2+} is known to occupy A sites, thereby changing the Fe^{2+}/Fe^{3+} ratio on the B sites (since Zn is bivalent):

$$Fe_{3-z}Zn_zO_4 \equiv (Fe^{3+}{}_{1-z}Zn^{2+}{}_{z})\{Fe^{3+}{}_{1+z}Fe^{2+}{}_{1-z}\}O_4$$

The order-disturbing effect of Zn^{2+} substitutions, as was explained in [Brab98], results from the fact that an equal amount of octahedral Fe^{2+} has to be replaced by Fe^{3}. That is why Zn, though not entering the B sublattice, has a larger effect upon T_v than the two-valent substitutions on the octahedral lattice, which -in contrast to Fe^{2+} sites- are immobile and thereby may even contribute to a stabilization of the ordered phase.

Let`s now consider the Al substituted magnetite in details, since this composition has a direct relation to investigations of the present thesis.

There are different reports concerning the cation distribution in $Fe_{3-x}Al_xO_4$. Based on Mossbauer measurements, Dehe et al. [Dehe75] have reported, that both Al^{3+} and Fe^{2+} ions enter tetrahedral as well as octahedral positions, leading to the following distribution over the crystal positions:

$$Fe_{3-x}Al_xO_4 \equiv (Fe^{3+}_{1-0.5x}Fe^{2+}_{0.385x}Al^{3+}_{0.115x})\{Fe^{3+}_{1-0.5x}Fe^{2+}_{1-0.385x}Al^{3+}_{0.885x}\}O_4$$

One can see that Al^{3+} ions mainly contribute on octahedral sites at the rough ratio 8:1 to their tetrahedral occupancy.

On the other hand, Rosenberg et al. [Rose85], Gillot and Jemmali [Gill83] and Mason and Bowen [Maso81] reported that, for low concentrations, aluminum cations occupy only octahedral sites:

$$Fe_{3-x}Al_xO_4 \equiv (Fe^{3+})\{Fe^{3+}_{1-x}Fe^{2+}Al^{3+}_{x}\}O_4$$

The first of the mentioned reports - a Mössbauer study of $Fe_{3-x}Al_xO_4$ of Rosenberg et al. claimed, that Al substituent even up to x=1.4 shows a strong preference for B sites, giving rise to a normalization of the spinel structure with Fe^{2+} located mainly on tetrahedral sites. Therefore, the problem of cation distribution for small Al concentrations is still not resolved unambiguously and requires a further study. Nevertheless authors agree that *aluminum* in small concentrations *preferentially* occupies *octahedral* sites in magnetite.

In fig. 3.2.16 the electrical resistivity of Al-doped magnetite samples is plotted as function of the temperature, as was reported by Brabers et al [Brab98]. They found a strong dependence of the transition temperature upon the concentration x. For x=0.005 and x=0.01 a sharp first-order transition was observed, whereas for x=0.02 and 0.03 a gradual change was observed pointing out to a second-order transition. The maximum in the derivative of the ln ρ-T plot of these compositions was taken as the transition temperature. From these data one can see that the critical Al concentration for the transition from first to second order lies between 0.01

and 0.02, comparable with the value of 0.012 for the Zn or Ti substitutions, as was mentioned above.

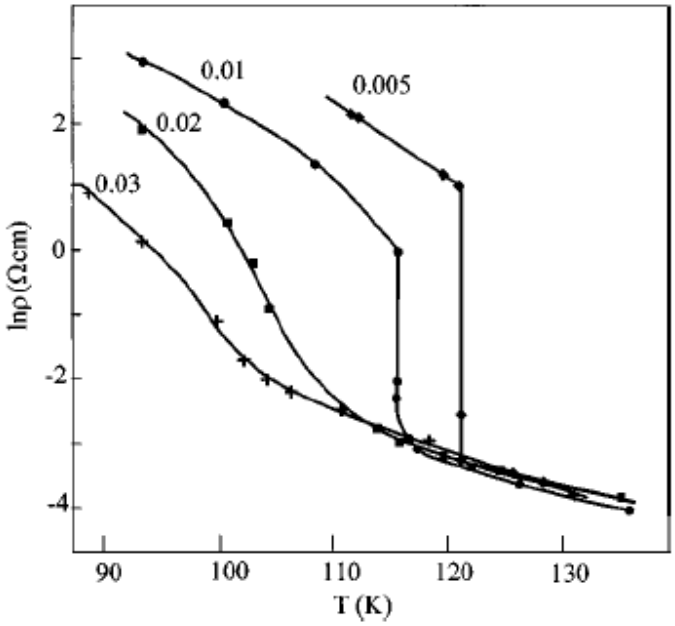

Figure 3.2.16. The resistivity of stoichiometric $Fe_{3-x}Al_xO_4$ single crystals with x=0.005, 0.01, 0.02, and 0.03 as function of temperature [Brab98].

The strong effect of Al substitution they explained in terms of the ionic radii of Al^{3+} =0.535 Å (see Table 3.2.2). The geometry of a B_4 unit containing one small Al^{3+} ion will be more deformed, resulting in a variation of the Coulomb energy and, consequently, a larger effect on the Verwey ordering.

The ionic radii of the bivalent ions Ni^{2+}, Co^{2+}, Mg^{2+} are larger than one of Al^{3+} being in the range between the radii of Fe^{3+} and Fe^{2+} ions. Thus, they are disturbing to a smaller extent the ionic packing that governs the Verwey transition.

Ion	Electronic configuration	Coordination number	Effective Ionic Radius (Å)
Al^{3+}	$2p^6$	IV	0.39
		VI	0.535
Co^{2+}	$3d^7$	IV	0.58
		VI	0.65
			0.745*
Fe^{2+}	$3d^6$	IV	0.63

		VI	0.61
			0.78*
Fe^{3+}	$3d^5$	IV	0.49
		VI	0.55
			0.645*
Mg^{2+}	$2p^6$	IV	0.57
		VI	0.72
Ni^{2+}	$3d^8$	IV	0.55
		VI	0.69
Ti^{4+}	$3p^6$	IV	0.42
		VI	0.605

Table 3.2.2. Effective ionic radii of some ions, used as magnetite substituents [Shan76]. * is used for effective ionic radii obtained as most reliable from r^3 vs V plots [Shan76].

In view of the foregoing facts concerning the Al substituted magnetite it is still an open question how the substitution affects the electronic structure of magnetite below and above the Verwey transition. This is one of the central questions studied in the frame of the present thesis.

3.2.4. NMR investigations of magnetite

NMR measurements of magnetite and, in particular, the temperature dependence of the ^{57}Fe NMR lines in magnetite have been reported starting earlier 70s. However only in recent NMR research [StepHT99, Nova00, NovaICF00] the authors succeeded in identification of all NMR lines detected at the liquid He temperature also at higher temperatures. The spectra were compatible with the space group C_c. Besides the temperature dependences of ^{57}Fe NMR spectra in high-purity ($T \geq 121.5K$) magnetite below, around and above the Verwey transition in temperature range $4.2K < T < 430K$, they also found the temperature dependences of the spin-spin (T_2) and spin-lattice (T_1) relaxation times below the transition to be qualitatively the same for all lines, with $T_2(T)$ exhibiting a sharp minimum at about 40K. One would expect the Fe^{2+} ions to relax with a considerable shorter T_1 due to their stronger coupling to the lattice via their non-zero spin–orbital interaction. The authors interpreted their results in terms of strongly intermixed, localized Fe^{2+} (B) and Fe^{3+} (B) configurations, allowing fast electron exchange on a timescale of $\tau < 10^{-8}$ s even at lowest temperatures, which would explain the closeness of T_1 for all ions and also confirm the assumed conception of the absence of a stable low-temperature

ionic ordering. T_2-relaxation on B-sites was found to be by an order of magnitude faster than one on the A-sites with the exception of two lines, T_2 of which were comparable to T_2 of the A-lines. For temperatures above T_V the temperature dependence of the linewidths was studied. The widths of the NMR lines close to the temperature of the spin-reorientation transition were found to be dominating because of the corresponding disorder in the spin system.
Since half of B sites of magnetite are occupied by Fe^{3+} ions and the other half by Fe^{2+} ions, eight of the B lines could correspond to Fe^{3+} and eight to Fe^{2+} ions. Mizoguchi [Mizo78] divided the B-subspectrum into 2 groups of B-lines, corresponding to Fe^{2+} and Fe^{3+} ions, resonating in B sites. But as it was pointed out recently [StepHT99], spin-lattice relaxation times T_1, measured for all lines of the spectrum at 4.2K , did not show an expected for Fe^{2+} and Fe^{3+} difference (the maximum ratio is ~2), raising a doubt about the unambiguous consideration of integer valences of iron ions in magnetite and their reflection in NMR spectra.

Recent NMR investigations of pure magnetite in an external magnetic field at 4.2K were performed by M.Mizoguchi [Mizo00], [Mizo01] and concerned the studying of an anisotropy of the hyperfine field of all observed A and B sites determined from the angular dependence of the resonance frequencies on an external magnetic field. On a basis of these experimental results the author proposed a charge and orbital ordering structure in the low temperature phase of magnetite and a model of charge density waves above the metal-insulator transition temperature [Mizo01].

There are almost no publications regarding NMR measurements on substituted magnetite samples with the exception of [Miya71], where reported spectra of Ga substituted magnetite have no good-quality resolution.

Detailed information on results of ^{57}Fe NMR measurements in zero external magnetic field in pure magnetite is presented in the following chapter 3.2.4.1.

3.2.4.1. ^{57}Fe NMR in pure magnetite

As it was mentioned above the Fe ions in magnetite are present in different crystallographic positions (sites): tetrahedral or A- positions and octahedral or B-positions. The local fields (and the corresponding resonance frequencies) on nuclei of differently positioned iron ions can be different, so each site in fact has its own subspectrum, which can be divided into several lines, distant up to several MHz. The structure of subspectrum (the number of lines, their relative intensities and splitting) is given by a symmetry of the corresponding crystallographic position

and crystal structure, magnetic structure and anisotropy of local field on nuclei (i.e. its dependence on direction of a magnetic moment of an ion).

According to a character of a change of NMR spectra of magnetite in temperature range $4.2K \leq T \leq 430K$ (how it was measured and reported in [StepHT99]) one can mark out three different regions:

1) $4.2K \leq T < T_V$

As was already mentioned, the monoclinic cell of Fe_3O_4 contains 32 formula units with 32 A-positioned and 64 B-positioned iron ions. However, the number of crystallographically inequivalent sites is reduced by C_C symmetry to 8 of A-type and 16 of B-type sites. Easy direction of magnetization at low temperatures is [001] and it does not reduce the symmetry, so there are 8 and 16 magnetically inequivalent iron ions on A and B sites respectively. As a consequence, 8 Fe(A) lines and 16 Fe(B) lines are predicted in the NMR spectrum below T_V.

In fig. 3.2.17 the ^{57}Fe NMR spectrum of magnetite single crystal of high purity (T_V=123.9K), measured at T = 4.2K at zero external magnetic field, is displayed [StepHT99].

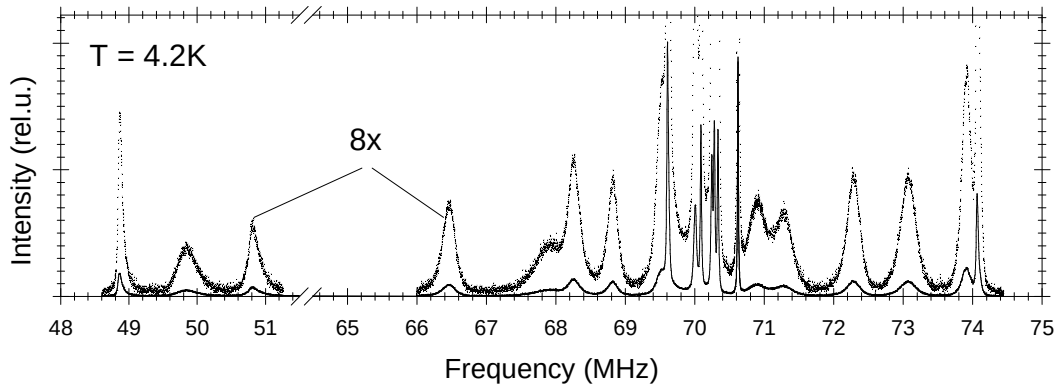

Figure 3.2.17. ^{57}Fe NMR spectrum of magnetite single crystal measured at T=4.2K (T_V=123.9K) [StepHT99].The upper spectrum is 8 times magnified.

The spectrum occupies the broad frequency interval (48-75 MHz) and consists of a superposition of A- and B- subspectra: 7 narrow resonance lines (6 of those are simple and the 7th is doubled) of A-positioned iron ions (A- subspectrum) within the frequency interval 69-71 MHz (see fig.3.2.18) and the rest are B-lines (B subspectrum, fig.3.2.19) [StepHT99, Nova00, NovaICF00].

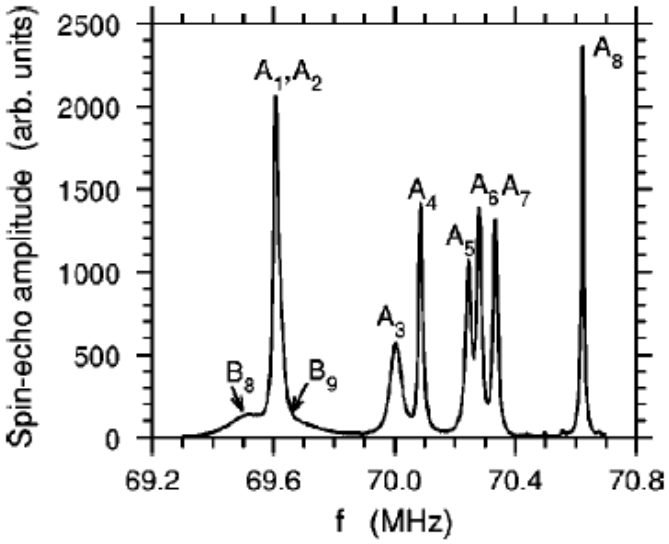

Figure 3.2.18. *A*-subspectrum of a high-purity magnetite single crystal measured at 4.2 K [Nova00]. A_1 and A_2 lines are superimposed.

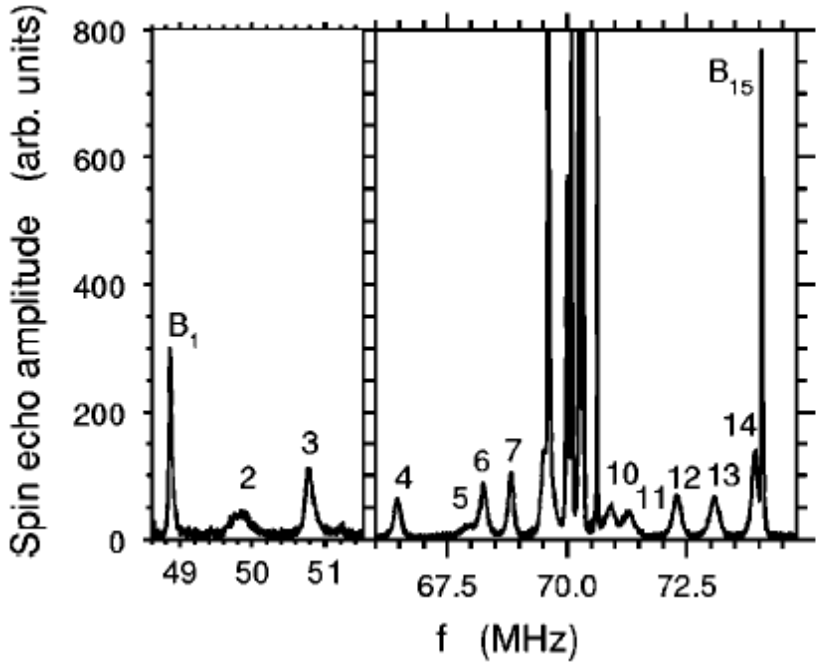

Figure 3.2.19. NMR spectrum of a magnetite single crystal at T=4.2K pointing B-subspectrum out [Nova00]. The line B_9 and partially the line B_8 are hidden behind the intensive lines A_1, A_2 (fig.3.2.18), as well as the line B_{16} is hidden by the line A_3 at helium temperature [NovaICF00].

The temperature region in question is characterized by following temperature dependences of spin-lattice (T_1) and spin-spin (T_2) relaxation times. At the liquid He temperature the spin-lattice relaxation times (T_1) of A- and B- lines are considerably long, as a consequence of a ″stiffness″ of the electronic spin system. As the temperature is increased, the electronic spin excitations appear and T_1 decreases rapidly, having on average the same order of magnitudes (fig. 3.2.20):

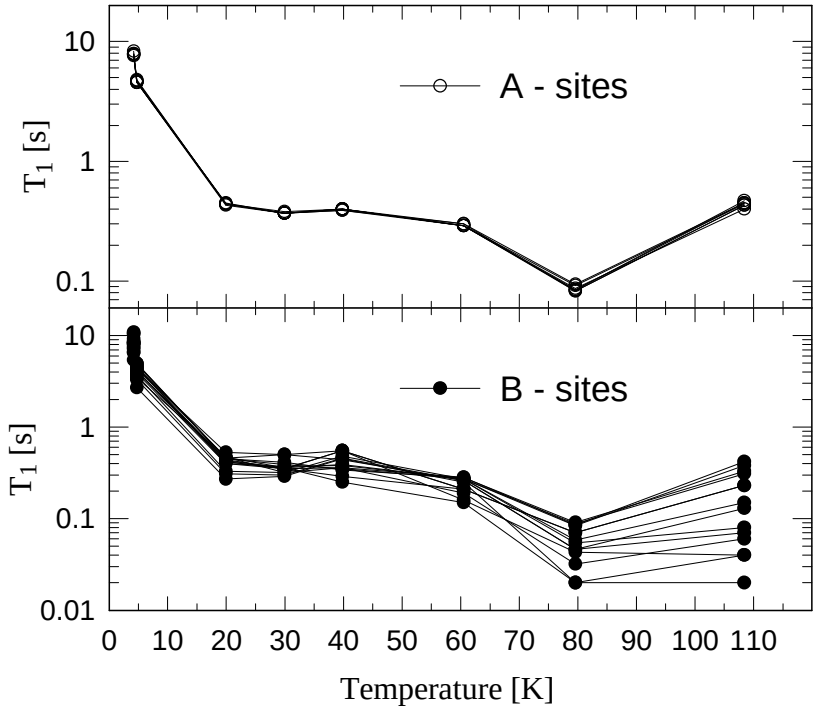

Figure 3.2.20. Temperature dependences of the spin-lattice relaxation times T_1 for the sets of A and B lines of magnetite [NovaICF00].

Temperature dependence of the spin-spin relaxation times T_2 is displayed in fig.3.2.21. The behavior of $T_2(T)$ is similar for all A and B lines, exhibiting the minimum for $T \approx 40$ K. Around this temperature T_2 for several of the B lines was too small to be determined with any accuracy. Relaxations on B sites are by an order of magnitude faster than on A sites with the exception of the B_{15} and B_{14} lines where T_2 are comparable to ones of A lines.

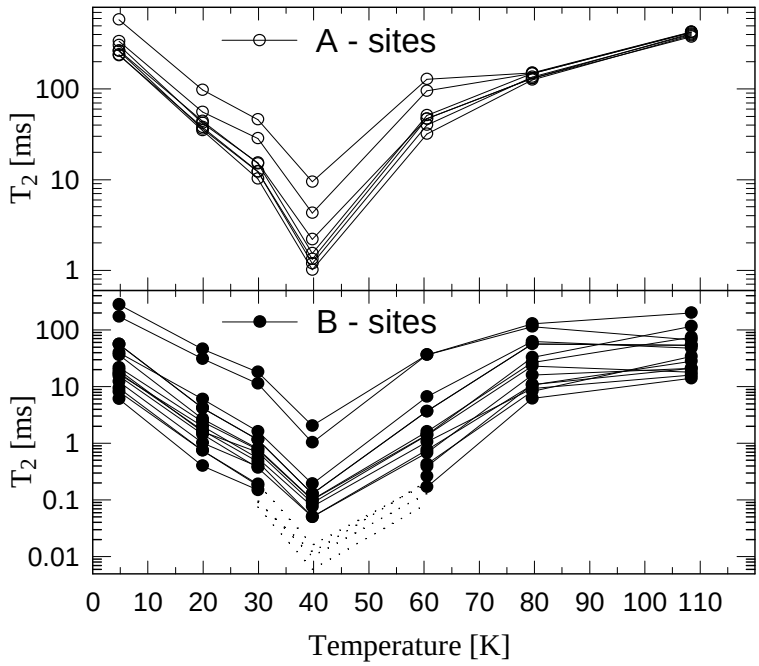

Figure 3.2.21. Temperature dependences of the spin-spin relaxation times T_2 for the sets of A and B lines of magnetite [NovaICF00].

2) $T_V < T < T_{SR}$

Above T_V and close to this temperature the spectrum is drastically simplified, being reduced to two lines, as expected for the cubic symmetry and magnetization direction along the <001> direction (in absence of an external magnetic field) leading to the unification of the iron ions on B-sites. For M || [001] all Fe ions on octahedral (B) sites are magnetically equivalent. All tetrahedral (A) sites are magnetically equivalent for M || [001] too. So the spectrum consists of a single Fe(A) line (very narrow line at 69.590 MHz) and single Fe(B) line (66.297 MHz) (fig.3.2.22) [StepHT99], [Nova00].

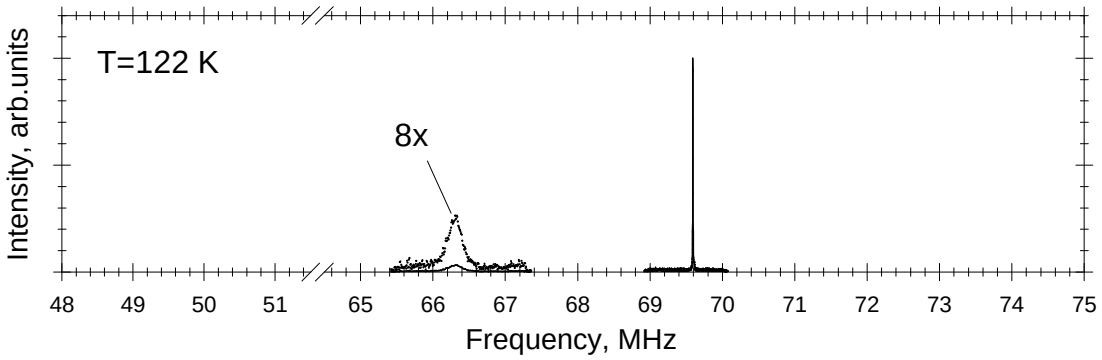

Figure 3.2.22. ^{57}Fe NMR spectrum of magnetite single crystal (T_V=121.5K) at 122K [StepHT99].

3) $T_{SR} < T < 430K$

Between 125 and 131K magnetite undergoes the spin-reorientation transition: magnetization changes its direction from <001> to <111>. Then above T_{SR} there are two magnetically non-equivalent B sites: for the sites B_1 the axis of local trigonal distortion is parallel to the magnetization, while for sites B_2 trigonal distortion and magnetization point along different body diagonals (i.e. the local trigonal axis is along one of the three remaining diagonals [-1,1,1], [1,-1,1], [1,1,-1]). It leads to the splitting of the Fe(B) line to two lines (B_1 and B_2) with the ideal intensity ratio 1:3 (in terms of atoms per unit cell it means 4 ions of B_1 type to 12 ions of B_2 type, or 16 ions of B-type together). The line at lower frequency corresponds to B_1 sites, while the higher frequency line to B_2 sites [StepHT99], [Nova00]. All tetrahedral (A) sites are magnetically equivalent for M || <111> (8 atoms of A-type per unit cell). Then the spectrum of magnetite above the spin-reorientation transition is expected to consist of 3 lines: two B and one A lines with the ideal ratio of integral intensities $I(B_1):I(B_2):I(A) = 1:3:2$ (fig.3.2.23) [StepHT99].

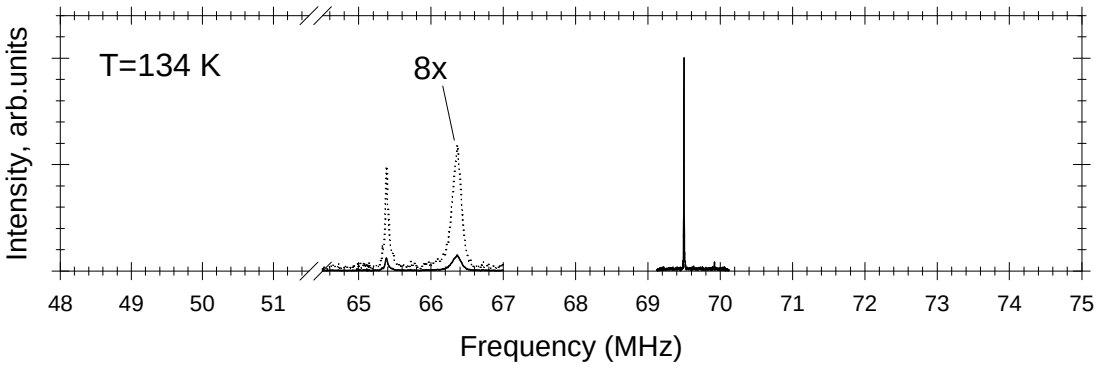

Figure 3.2.23. ^{57}Fe NMR spectrum of magnetite single crystal (T_V=121.5K) at 134K [StepHT99].

The next figure 3.2.24 shows temperature dependences of linewidths and splitting (a frequency distance) between B_1 and B_2 lines [NovaICF00], characterizing the temperature interval in question of relatively pure magnetite (T_V=121.5K).

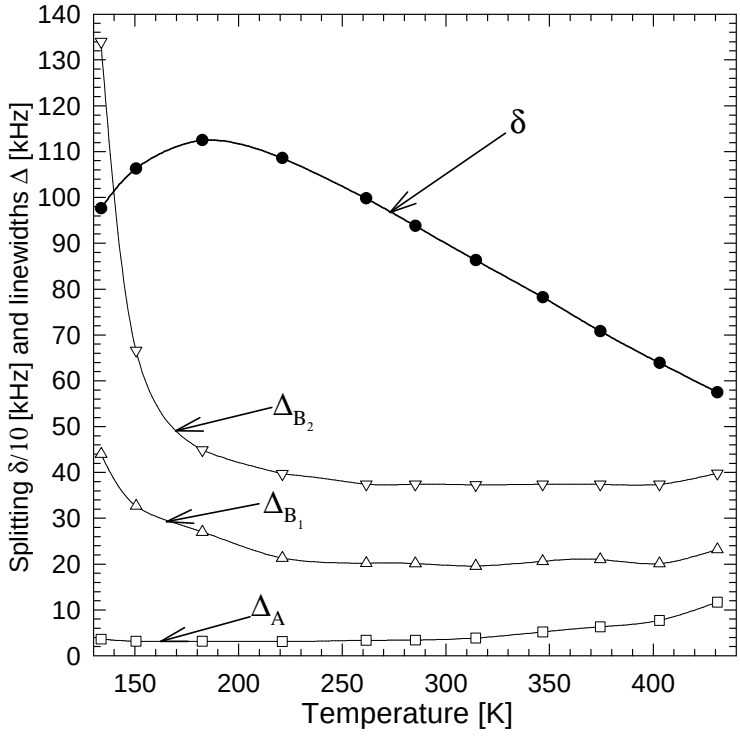

Figure 3.2.24. Temperature dependences of a splitting δ and linewidths Δ of NMR lines of relatively pure magnetite (T_V=121.5K) [NovaICF00].

The widths Δ of the NMR lines close to the temperature of spin-reorientation transition are dominated by corresponding disorder in the spin system. For higher temperatures they decrease rapidly and for B lines they level out above 180K. The width of A line reaches a shallow minimum at about 260K and increases at higher temperatures [NovaICF00].

The splitting δ between lines B1 and B2 reflects the anisotropy of the hyperfine field, depending on the angle between magnetization and the local trigonal axis. It increases with increasing temperature, attaining maximum at about 180K and then monotonically decreases [NovaICF00].

The temperature dependence of resonance frequencies of magnetite within the temperature range $4.2\text{K} \leq \text{T} \leq 430\text{K}$ is shown in fig.3.2.25.

Below the Verwey transition all resonance frequencies change smoothly with increasing temperature, reflecting tangly a dependence of crystal, electron and magnetic structure parameters on temperature. Temperature dependence of all A-lines has the same character. The behavior of B-lines is somewhat unusual because of the frequency increase for some of them with temperature, reflecting that besides the change of the magnetic moment the temperature variations of other order parameters are important [Nova00]. The NMR frequency *f* is connected with the effective magnetic field $\vec{B}$ by the relation

$$f = \frac{\gamma \left| \vec{B} \right|}{2\pi} \qquad (3.2.4.1)$$

where γ is the gyromagnetic ratio and the dominating part of $\vec{B}$ is given by the hyperfine contribution $\vec{B}_{hf}$

$$\vec{B}_{hf} = \hat{A}\vec{\mu} \qquad (3.2.4.2)$$

Here $\hat{A}$ is the hyperfine coupling tensor and $\vec{\mu}$ is the electronic magnetic moment. The temperature dependence of *f* below the Verwey transition is given by the change of both $\hat{A}$ and $\vec{\mu}$. While $\left|\vec{\mu}\right|$ decreases monotonically with the increasing temperature, $\hat{A}(\text{T})$ reflects the temperature dependence of an ordering parameter (or parameters) *p* and for nonequivalent sites it may have different character. Above T_V p=0 and there is only one Fe(B) line at T_V. So for B

lines with f<53 MHz $\hat{A}(T)$ dependence could dominate and the frequencies of these lines increase with increasing temperatures.

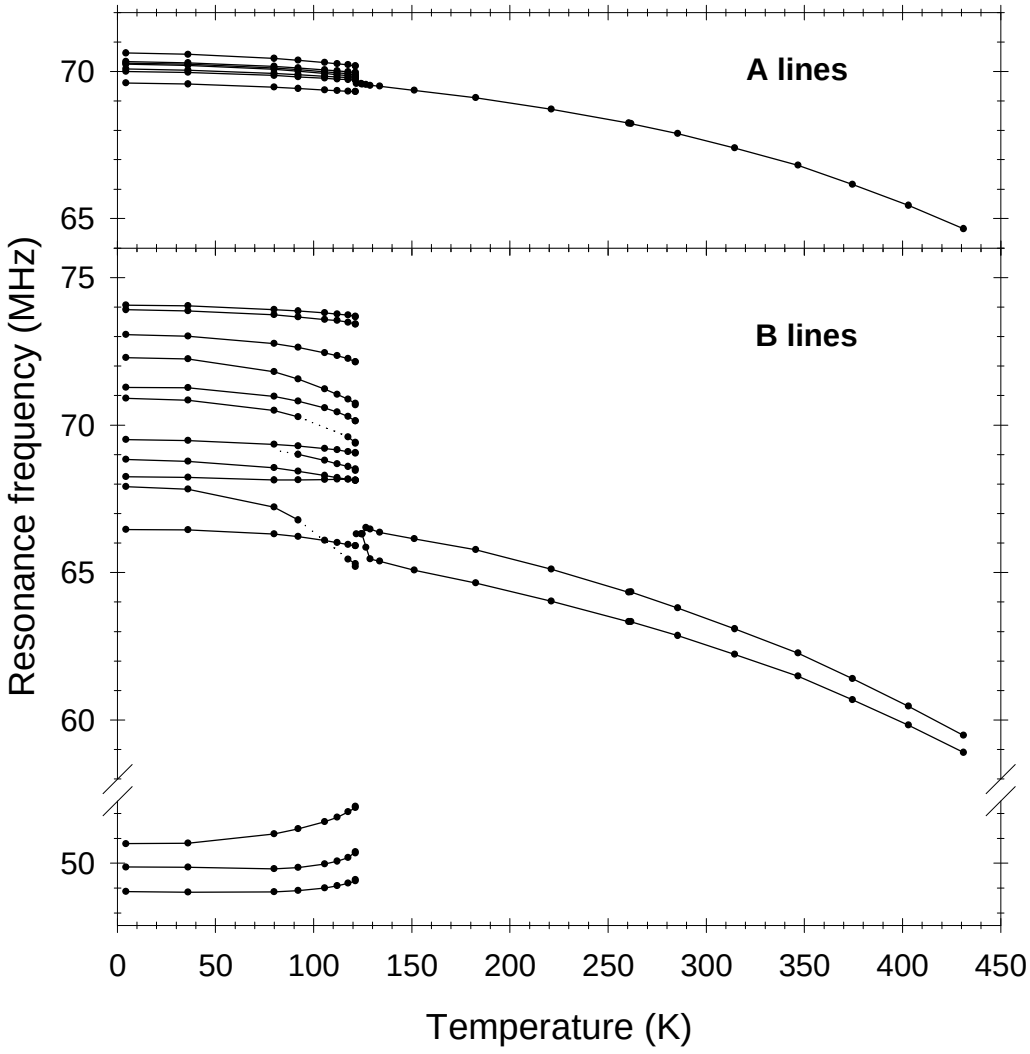

Figure 3.2.25. Temperature dependence of ^{57}Fe NMR resonance frequencies in magnetite single crystal (T_V=121.5K) [StepHT99].

On passing the Verwey temperature T_V to higher temperatures the frequency dependences in Fig.3.2.25 reflect a drastic simplification of NMR spectra, caused by an above mentioned unification of iron ions in B positions leading to a high symmetry of local surroundings of resonating nucleus.

4. Experimental results, calculations and discussions

4.1. Experimental results on studied garnets

In following paragraphs, the results of the study of hyperfine interactions and relaxation parameters in substituted YIG (YIG:Al, YIG:In, YIG:La, YIG:Ca, YIG:Bi) and BIG are presented.

4.1.1. Effect of aluminum substitution in YIG on ^{57}Fe hyperfine field anisotropy

Fe^{3+} cations occupy octahedral (a) and tetrahedral (d) sites in the yttrium iron garnet. Previously [Koho99, Koho00] Ga^{3+} and Ge^{4+} substitutions on the tetrahedral sites of YIG have been studied. The present studying deals with the aluminum substituted YIG. The Al^{3+} ions also enter preferentially the tetrahedral sites and they have almost the same ionic radii as Ge^{4+} but differ in their valency. It enables us to study besides the effect of Al substitution on the iron hyperfine field anisotropy also the influence of (i) different ionic radii of trivalent nonmagnetic substitution, (ii) replacement of the magnetic Fe^{3+} ion by a nonmagnetic one, and (iii) the influence of different valencies of the nonmagnetic substituents.

A series of $Y_3Al_xFe_{5-x}O_{12}$ single crystal films with increasing content of Al substitution was prepared from Fe_2O_3 and Al_2O_3 oxides in $BaO/B_2O_3/BaF_2$ flux by an epitaxial growth on the gadolinium gallium garnet substrates of (111) and (110) orientations. Samples were prepared by M.Kucera and K. Nitsch. The thickness of the films was typically of several micrometers.
^{57}Fe NMR spectra were measured at 4.2K using spin-echo technique with coherent data accumulation in time domain and subsequent Fourier transform (for experimental details see paragraph 2.6). The amplitude of radiofrequency field was set to excite the signal originated from the nuclei inside magnetic domains only.

^{57}Fe NMR spectra of the a-sites in the samples with (111) substrate orientation are shown in Figure 4.1.1.1. For the magnetization in <111> direction the spectrum of a-sites of a pure sample consists of two main lines with the integral intensity ratio 1:3. This splitting reflects the magnetic nonequivalency of the a-sites with respect to the magnetization direction. The

assignment of the satellites induced by the Al^{3+} substitution is based on their intensity dependence on the amount of Al_2O_3 in the flux assuming that the substitution into the d-site influences predominately the resonant frequency of the nuclei in the nearest a-sites. The amount of Al in the YIG samples given in Fig. 4.1.1.1 was determined from the relative integral intensities of the satellites and the main lines. Satellites caused by the intrinsic 'antisite' defects (Y^{3+} on a-sites) identified previously [Step98] in YIG samples are also pronounced in the spectra.

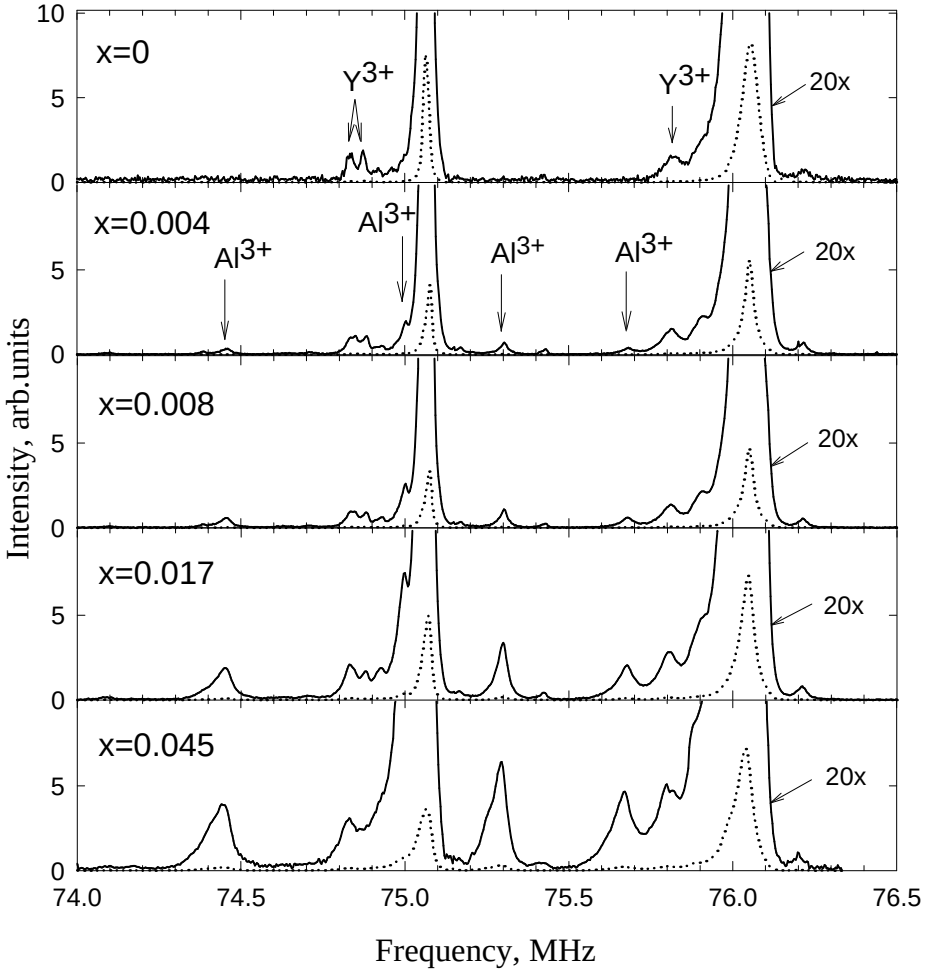

Figure 4.1.1.1. ^{57}Fe NMR spectra (a-sites) of $Y_3Fe_{5-x}Al_xO_{12}$ epitaxial films measured at zero external field at 4.2 K. Satellites induced by the Al substituents and Y antisite defects are denoted.

For the reason of a good resolution of a satellite structure in spectra one need a low concentration of substitution. On the other hand, the concentration of studied defects should be

high enough from the point of view of the method sensitivity and in comparison with other present defects to measure and resolve studied satellites good enough. Following these criteria, the film with the x=0.017 (fig.4.1.1.1) and (110) substrate orientation was then picked out for the studying of changes of the hyperfine field tensor induced by the presence of Al. This film (12 μm thickness) was measured at 4.2K in the external magnetic field of 0.1T applied consecutively in 16 different directions parallel to the plane (110) of the film. The dependence of resonant frequencies of main and satellite lines on the angle between magnetization direction and the direction [001] was studied.

Spectra of *a*-main lines and satellite lines induced by Al^{3+} nearest *d*-neighbors and others nearby at different angles ϑ are displayed in figure 4.1.1.2.

The angles ϑ were identified according to the known angular dependence of the main *a* and *d* lines. The satellites induced by the presence of Al^{3+} ions in the nearest *d*-neighborhood of *a* sites were identified after elimination of the Y^{3+} antisite defects satellites with known angular dependences.

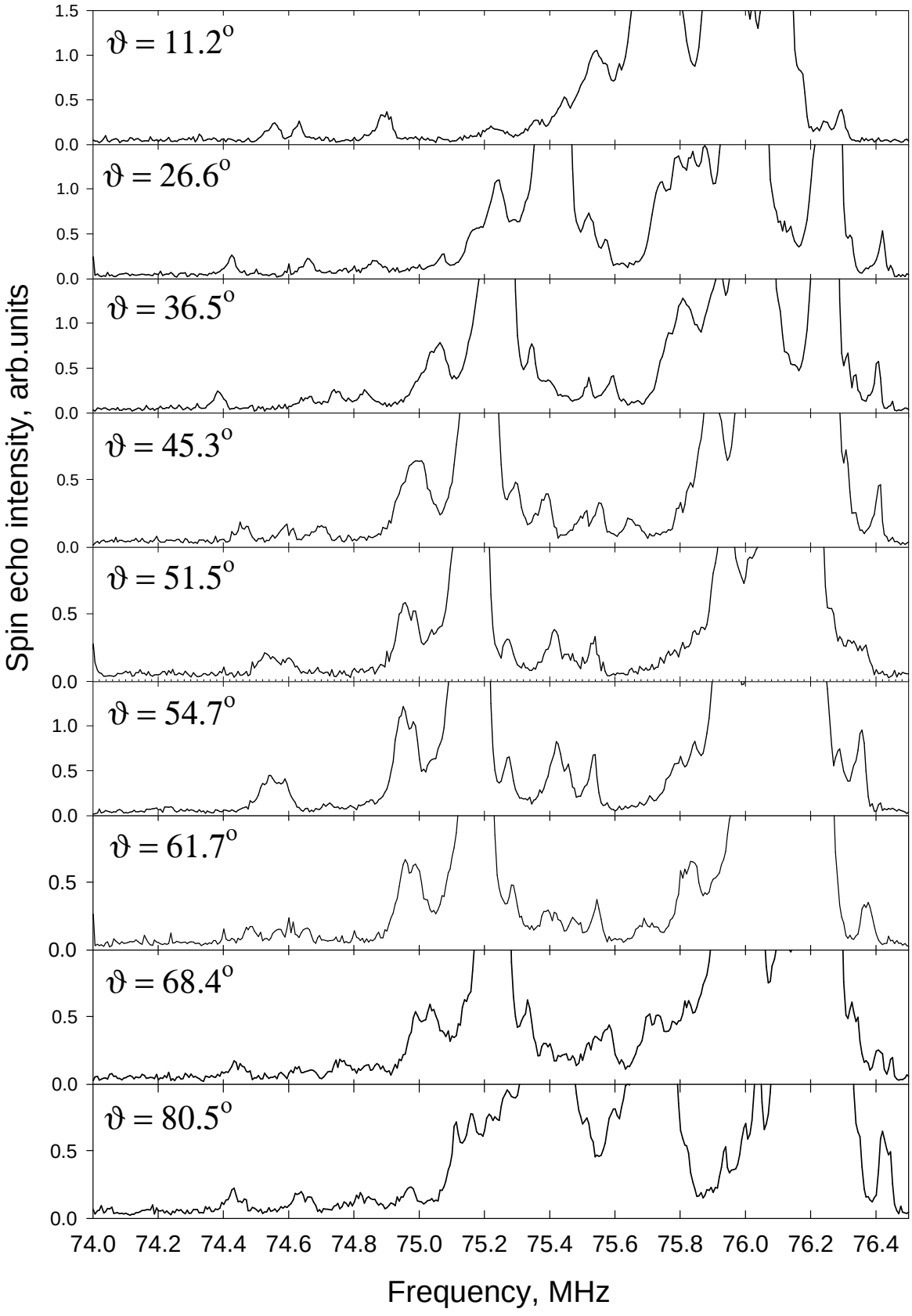
ϑ = 11.2°
ϑ = 26.6°
ϑ = 36.5°
ϑ = 45.3°
ϑ = 51.5°
ϑ = 54.7°
ϑ = 61.7°
ϑ = 68.4°
ϑ = 80.5°
Spin echo intensity, arb.units
Frequency, MHz
74.0 74.2 74.4 74.6 74.8 75.0 75.2 75.4 75.6 75.8 76.0 76.2 76.4

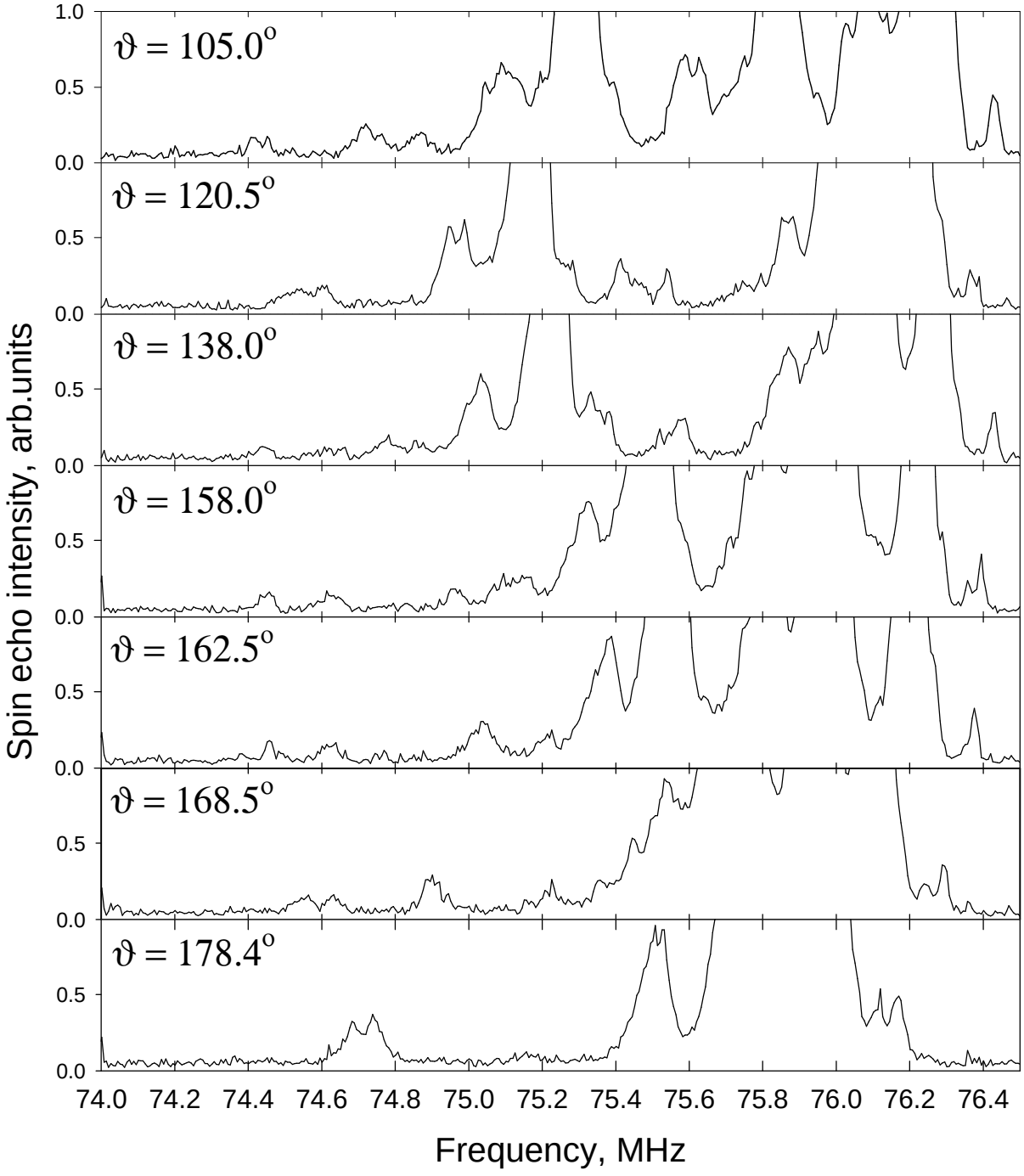

Figure 4.1.1.2. Spectra of *a*-main lines and satellites nearby (including Al-induced and "antisite" defects satellites) at different angles ϑ measured at 4.2K in external field 0.1T applied in the plane (110) of the film.

The angular dependences of the resonant frequencies corresponding to the main *a* and *d* lines are shown in Fig. 4.1.1.3.

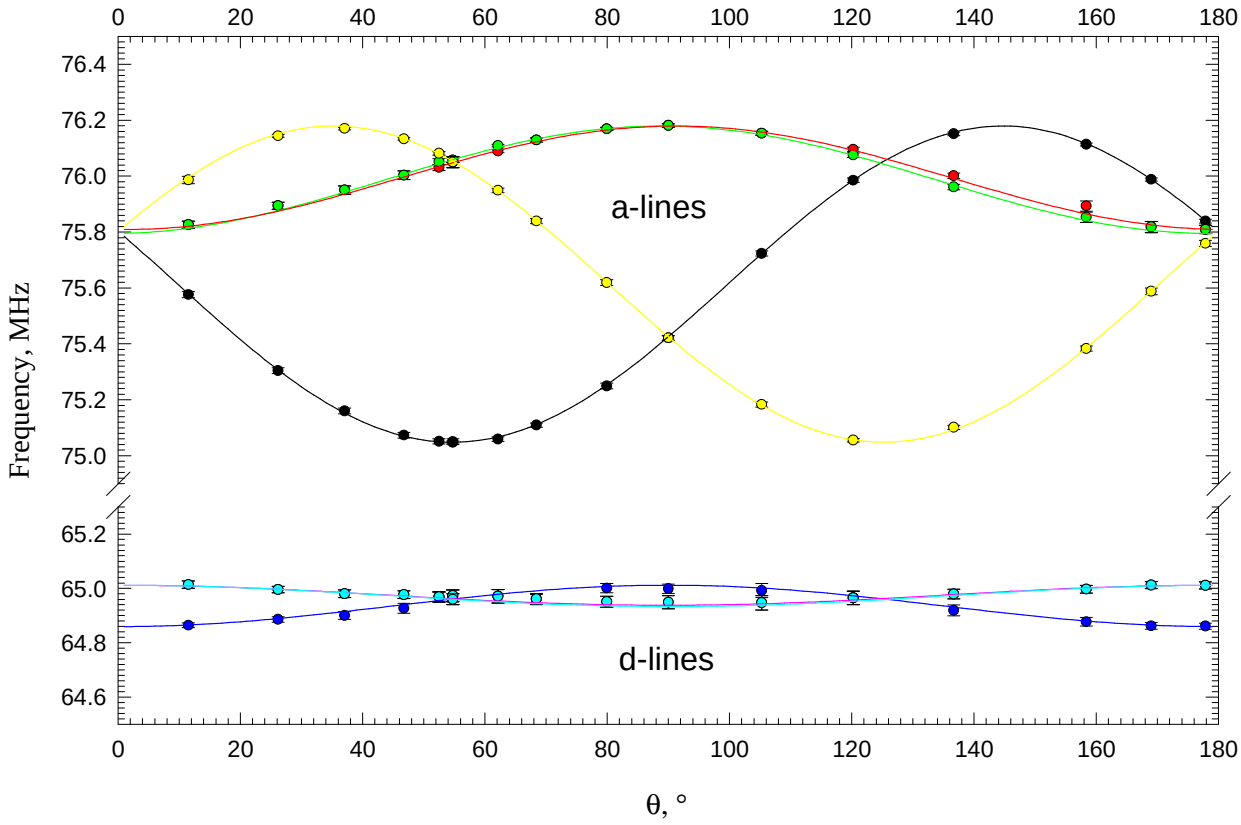

Figure 4.1.1.3. The angular dependences of the resonant frequencies of the main *a* and *d* lines measured at 4.2K in the external field of 0.1T on the sample $Y_3Al_xFe_{5-x}O_{12}$ with x=0.017.

The angular dependence of the resonant frequencies corresponding to the *a*-main lines and to the Al^{3+} induced satellite lines is shown in Fig. 4.1.1.4.

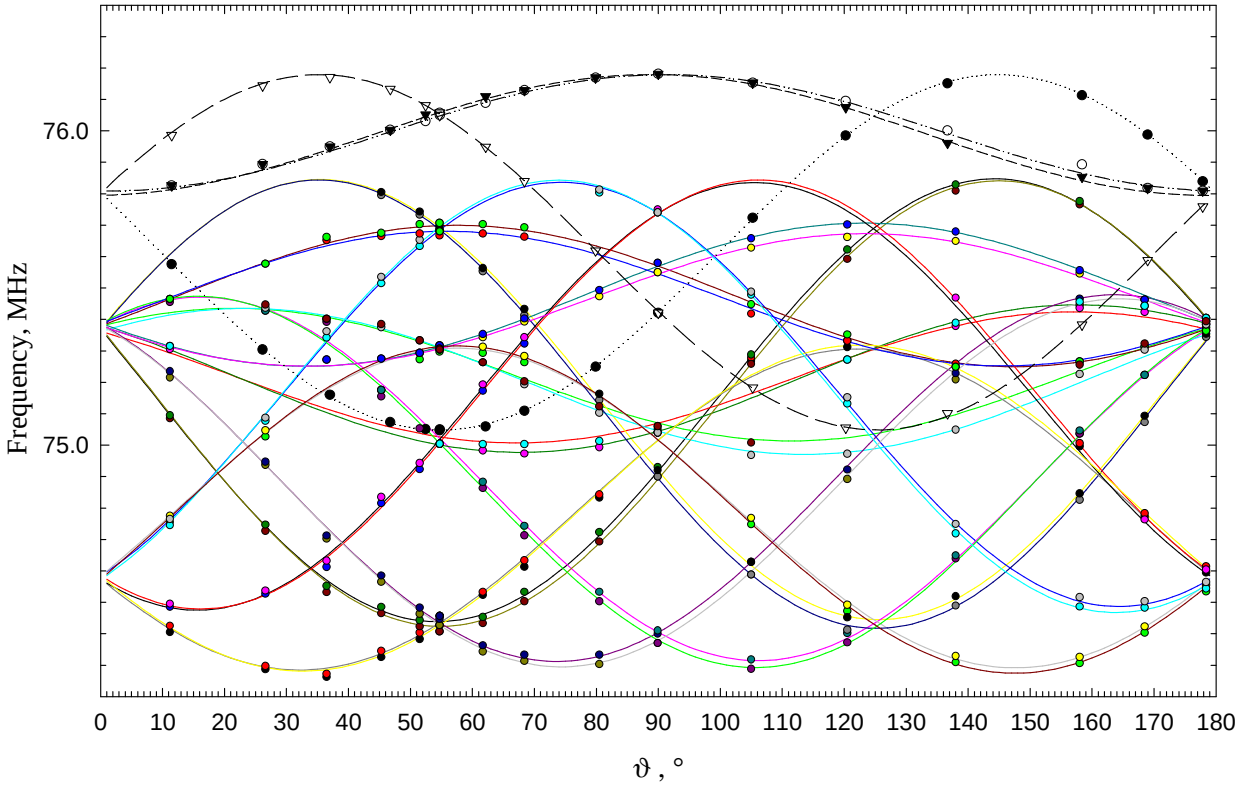

Figure 4.1.1.4. The angular dependences of the ^{57}Fe (a-sites) NMR frequencies of $Y_3Al_xFe_{5-x}O_{12}$ with x=0.017. ϑ is the angle between magnetization direction and [001]. Experimental points (open circles correspond to the main lines, full circles – to satellites) and fitted curves. The fit has shown that the plane of the film is slightly declined (~0.6 °) from (110).

Analysis of the angular dependences was performed for the sets of main lines (of both *d* and *a* iron sites) and for the complete set of the satellites corresponding to all crystallographically equivalent configurations of the resonating iron on the *a*-site and the Al^{3+} substituent on one of its nearest *d*-sites. Resonant frequencies within a particular set (f_w) depend on the magnetization direction $\boldsymbol{n}$ according to the formula (3.1.4.7):

$$f_{(w)} = I + \boldsymbol{n}\boldsymbol{A}_{(w)}\boldsymbol{n} = I + \boldsymbol{n}\boldsymbol{G}_{(w)}^{-1}\boldsymbol{A}\boldsymbol{G}_{(w)}\boldsymbol{n} \qquad (4.1.1)$$

neglecting terms with higher powers of $\boldsymbol{n}$. I is the isotropic term and $\boldsymbol{A}$ is the second-order traceless symmetric tensor describing the hyperfine field anisotropy for the reference configuration (w=1) of the set. The matrices $\boldsymbol{G}_{(w)}$ represent point-symmetry operations

transforming the reference configuration to the other configurations of the set. Considering the $Ia\bar{3}d$ space group of the YIG crystal structure, local symmetries of the sites with the resonating irons and general direction of ***n***, equation (4.1.1) predicts three main *d*-lines, four main *a*-lines and 24 satellite lines of *a*-sites having one Al^{3+} ion on the nearest *d*-site, and for ***n*** in (110) plane it predicts two main *d*-lines, three main *a*-lines and 12 satellite lines of *a*-sites having one Al^{3+} ion on the nearest *d*-site (see paragraph 3.1.4.2 and the table 3.1.4.9 within).

A number of main and satellite lines higher than expected for magnetization in (110) plane were observed in our spectra (fig. 4.1.1.2), indicating that the plane of the film, in which the external field was applied, was slightly declined from the (110) plane.

The values of *I* and components of ***A*** were obtained by a least-square fit of Eq. (4.1.1) to the experimental data (see figures 4.1.1.3 and 4.1.1.4). The declination parameters, taking into account a discrepancy between the plane of the film and the (110) plane, were used as additional free parameters in a least-squares fit of the satellites and main line frequencies in that equation. The fit has shown that the plane of the film is declined ~$0.6°$ from (110).

The results of the fitting procedure for the main lines:

$$I^{d,main} = 64.966 MHz, A^{d,main} = \begin{pmatrix} 51 & 0 & 0 \\ 0 & 51 & 0 \\ 0 & 0 & -102 \end{pmatrix} kHz, \qquad (4.1.2)$$

$$I^{a,main} = 75.798 MHz, A^{a,main} = \begin{pmatrix} 0 & -375 & -375 \\ -375 & 0 & -375 \\ -375 & -375 & 0 \end{pmatrix} kHz \qquad (4.1.3)$$

are very close to those found previously for the nominally pure YIG single crystal [Koho97, Step98] and Ga:YIG film [Koho99]. The tensors are given in the coordinate system of an elementary cell and correspond to the d-sites having its S_4 local symmetry axis along $\pm[0,0,1]$ direction and to the a-sites with their local symmetry axis S_6 along $\pm[1,1,1]$.

For a-sites with Al in their nearest neighbourhood one has been obtained:

$$I^{a,sat} = 75.111 MHz, A^{a,sat} = \begin{pmatrix} 273 & -76 & -361 \\ -76 & -533 & -583 \\ -361 & -583 & 260 \end{pmatrix} kHz \qquad (4.1.4)$$

While the isotropic term is supposed to be modified predominately by the change of electron transfer to the 4 s levels of the Fe^{3+} ion, the anisotropic part depends on the transfer to 3d and 4p levels but contains also a contribution of a dipolar magnetic field of iron magnetic moments. To obtain the only contribution of the electron transfer modification, the change $\Delta A^{a,dip}$ of the dipolar field connected with the replacement of the neighbour iron with a nonmagnetic ion should be eliminated. The dipolar field for any position of the resonating iron nucleus and the replaced neighbouring Fe^{3+} can be calculated using the crystallographic data [Step00]. Unfortunately it is not possible to choose unambiguously the corresponding tensor from the set of

$$\boldsymbol{A}_{(w)}^{a,sat} = \boldsymbol{G}_{(w)}^{-1} \boldsymbol{A}^{a,sat} \boldsymbol{G}_{(w)} \qquad (4.1.5)$$

tensors (to decide to which of 24 possibilities it corresponds) without an additional assumption.

To solve this problem we have used the superposition model [Engl85,Engl90] (see paragraph 3.1.3.5.5). This model predicts that the resulting hyperfine field on the iron nucleus (after a subtraction of a dipolar field) is a sum of contributions of the individual bonds from the central iron to the neighbour cations via connecting oxygens; and each of the contributions is given by a uniaxial tensor with the axis along the Fe–O direction of the Fe-O-Al triad. The experimental data do not yield these individual contributions of course, but only their sum. Supposing that the model is valid with the precision up to the difference for an iron with and without substitution in its neighbourhood, the tensor

$$\Delta \boldsymbol{A}^{a,hf} = \boldsymbol{A}^{a,main} - \boldsymbol{A}^{a,sat} - \Delta \boldsymbol{A}^{a,dip} \qquad (4.1.6)$$

should be also uniaxial with the axis in the Fe–O direction.

The all 24 possibilities were tested and, similarly as in the cases with Ge and Ga substitutions, only one of them was close to the prediction of the superposition model. After its diagonalization, the principal values 421, -246, -175 kHz were obtained. The first one

corresponds to the principal axis deviated by only 1.1° from the Fe-O direction. The second principal value differs only slightly from the third one. The tensor is therefore nearly (however not exactly) uniaxial. The principal values (eigenvalues) of $\Delta A^{a,hf}$ tensor following from its diagonalization and the deviation of the first principal axis are given in Table 4.1.1, together with the summarized data for Ge and Ga.

We can conclude that the situation studied (resonating iron nucleus on *a* site, substituent (Al) on the nearest *d* site) (together with analogous cases of Ga and Ge substitutions) complies with the "independent bond" model, while a contradiction was found for the complementary case (resonating iron on *d* site, substituent on the nearest *a* site) (see paragraph 3.1.3.5.5).

Substitution	Ionic radius (nm) [a)]	$I^{a,main} - I^{a,sat}$ (MHz)	Eigenvalues of $\Delta A^{a,hf}$ (kHz)	Q [b)] $(MHz)^2$	α (°) [c)]
Ge^{4+}	0.039	1.135	(224; -152; -72)	0.078	11
Al^{3+}	0.039	0.687	(421; -246; -175)	0.027	1.1
Ga^{3+}	0.047	0.852	(451; -254; -197)	0.037	2.8

Table 4.1.1. Modification of the hyperfine parameters in substituted YIG.

$\Delta \boldsymbol{A}^{a,hf} = \boldsymbol{A}^{a,main} - \boldsymbol{A}^{a,sat} - \Delta \boldsymbol{A}^{a,dip}$

a) Ionic radius of Fe^{3+} in tetrahedral coordination is 0.049 nm.

b) Anisotropy invariant of $\Delta \boldsymbol{A}^{a,hf}$ defined as $Q = \frac{1}{3}\left[\left(\Delta A_{xx}^{a,hf} - \Delta A_{yy}^{a,hf}\right)^2 + cyclic.\right]$.

c) Deviation of the 1st principal axis from the Fe(a)-O direction.

These results together with those previously obtained for Ga^{3+} [Koho99] and Ge^{4+} [Koho00] substitutions form a basic set of hyperfine parameters enabling us to consider the influence of (i) different ionic radii of trivalent nonmagnetic substitution, (ii) replacement of the magnetic ion Fe^{3+} by a nonmagnetic one, and (iii) the influence of different valencies of the nonmagnetic substituents. All the three nonmagnetic substituents decrease the isotropic term for iron nuclei in their nearest a-sites (see Table 4.1.1). The effect of the valence change is somewhat smaller but comparable to that due to the replacement of iron by a nonmagnetic trivalent cation with similar ionic radius. Angular dependences of the a-main lines and the

satellites resonant frequencies for Ge, Ga, and Al substitution show at first glance the increase of the hyperfine field anisotropy induced by the substitution, weaker for Ge than for Ga or Al.

We can then conclude that the major change of the hyperfine field anisotropy is caused by the replacement of the magnetic moment on the neighbour cation site. It remains important for the a-sites even after elimination of the dipolar field contribution. The change of valency has weaker but comparable impact. The influence of the ionic radii difference seems to be less important.

The results concerning ^{57}Fe NMR in Al substituted YIG have been published [Gama02-1], together with the analysis and comparison of hyperfine fields modifications induced by Al, Ga and Ge cation substitutions.

4.1.2. Nuclear magnetic relaxation in YIG films with nonmagnetic trivalent substitutions

Effects of cation substitutions and impurities on nuclear magnetic resonance (NMR) of ^{57}Fe in magnetic iron oxides are usually observed directly in spectra where they reveal themselves as additional weak lines (satellites) arising from the modification of the hyperfine field at the nuclei in the nearest neighbourhood of substituents. Another, but less explored effect of impurities is their influence on the nuclear magnetic spin–lattice and spin–spin relaxations. For instance, paramagnetic substitutions by rare earths cations enhance the relaxation rates in YIG significantly [Genn61, Robe61]. However, relaxation studies on magnetic oxides meet difficulties in both the theoretical analysis of the relaxation mechanisms [Beem68] and in an experimental verification. The only systematically studied changes of the relaxation rates in YIG epitaxial films were carried out on YIG with nonmagnetic non-trivalent (charged) cation substitutions (silicon, calcium, lead) [Wagn96]. While for increasing content of Si^{4+} the spin–lattice rates increase, they are reduced for Ca^{2+}. In the case of lead which can be either di- or tetravalent, the spin–lattice relaxation rates sharply decrease up to a certain Pb concentration. These results were interpreted as due to the modification of the number of charge compensating intrinsic defects, namely a formation of Fe^{2+} ions, by the charged substitution. In comparison with that mechanism the direct influence of the charged substitutions was supposed to be negligible.

The aim of the present study is to estimate the direct impact of the substitution. It should be then investigated in systems where the valence of the substituent is the same as that of the replaced cation. Three sets of samples were studied. Our choice covers all cation sites of the garnet structure, i.e. the nonmagnetic Al^{3+} that prefers tetrahedral sites of ferric ions, In^{3+} occupying octahedral sites, and La^{3+} that replaces yttrium in dodecahedral sites.

Epitaxial films were grown from $BaO/B_2O_3/ BaF_2$ flux on a GGG substrate with (111) orientation. In comparison with the PbO flux used in [Wagn96], the barium flux excludes the presence of lead in the samples and minimizes platinum impurities from the crucible. The preparation technique allows to increase gradually the content of the substituent in the flux and to prepare well-defined concentration series of samples. Our samples were prepared by M. Kucera and K. Nitsch.

YIG spectra measured in zero external field consist of a single main line of d-sites (resonant frequency ~64.95MHz at 4.2 K) and two main lines *a1* and *a2* (resonant frequencies ~75.06 and ~76.06 MHz at 4.2K) assigned to a-sites divided due to the magnetic nonequivalency. In the spectra of the substituted samples we have detected a satellite structure characteristic of the particular substitution. Its concentration in the sample has been calculated using the relative integral intensities of satellites and main lines (according to the formula 3.1.4.12). Beside the satellites corresponding to a given substitution, satellites corresponding to the intrinsic defects as yttrium occupying a-sites and silicon impurities on d-sites also appear in the spectra. Their intensities do not vary notably with the increasing amount of the aimed substitution.

Relaxation rates were measured in zero external magnetic field at 4.2K on the signal within magnetic domains only for all the three main lines, i.e. *d*; *a1* and *a2*. The spin– lattice relaxation rate T_1^{-1} was determined from the dependence of NMR signal on the repetition time of the two-pulse spin echo pulse sequence. The spin–spin relaxation rate T_2^{-1} was measured by two techniques:

(1) from the signal intensity dependence of the two-pulse spin echo on the delay between pulses and (2) from the decay of the individual echoes in the multiple pulse Carr-Purcell-Meiboom-Gill (CPMG) sequence.

Analyses of the time dependences were made by a least square fit assuming a single-exponential behaviour. The time intervals, within which the fits were carried out, were kept constant.

An effect of substitution was characterized by the induced change of the relaxation rate:

$$\Delta\frac{1}{T_i}=\frac{1}{T_i^{subst}}-\frac{1}{T_i^{pure}},\qquad i=1,2. \tag{4.1.7}$$

The changes of the spin–lattice relaxation rate obtained are shown in Fig. 4.1.2.1. All the three types of impurities influence ΔT_1^{-1} within the studied concentration range in a similar way, i.e. the increase of their concentrations leads to the reduction of the relaxation rate. The decrease seems to stop when the concentration of about x= 0.1 is reached.

The ΔT_1^{-1} values obtained for the same amount of the substituent per formula unit are quite comparable, although the substitutions concern magnetic (Al, In replacing ferric ions) as well as nonmagnetic (La replacing yttrium) sublattices. The only common feature then seems to be an increased perturbation of the crystal structure periodicity caused by the presence of cations with different ionic radii.

The nuclear magnetic spin–lattice relaxation mechanisms proposed for magnetic oxides [Beem68] assume that the energy dissipation is enabled by the hyperfine and dipole–dipole coupling between nuclear and electron magnetic moments. Our results might relate to the influence of the disturbed crystal and electron structure periodicity on the electron spin dynamics. The principal role of other effects of the substitution, like possible influence on the domain wall properties or magnetic dilution in iron sublattices by In and Al, cannot however be excluded.

Detailed comparison reveals that in cases of Al and In substitutions the decrease of the relaxation rate is rather more pronounced for the octahedral than the tetrahedral sites.

Fig. 4.1.2.2 displays the results obtained for the spin–spin relaxation rates. In certain cases significantly different values were obtained from the two techniques used - the two-pulse spin echo and the multiple pulse Carr-Purcell sequence. For this reason we refer $T_2^{-1}(1)$ to the former and $T_2^{-1}(2)$ to the latter method.

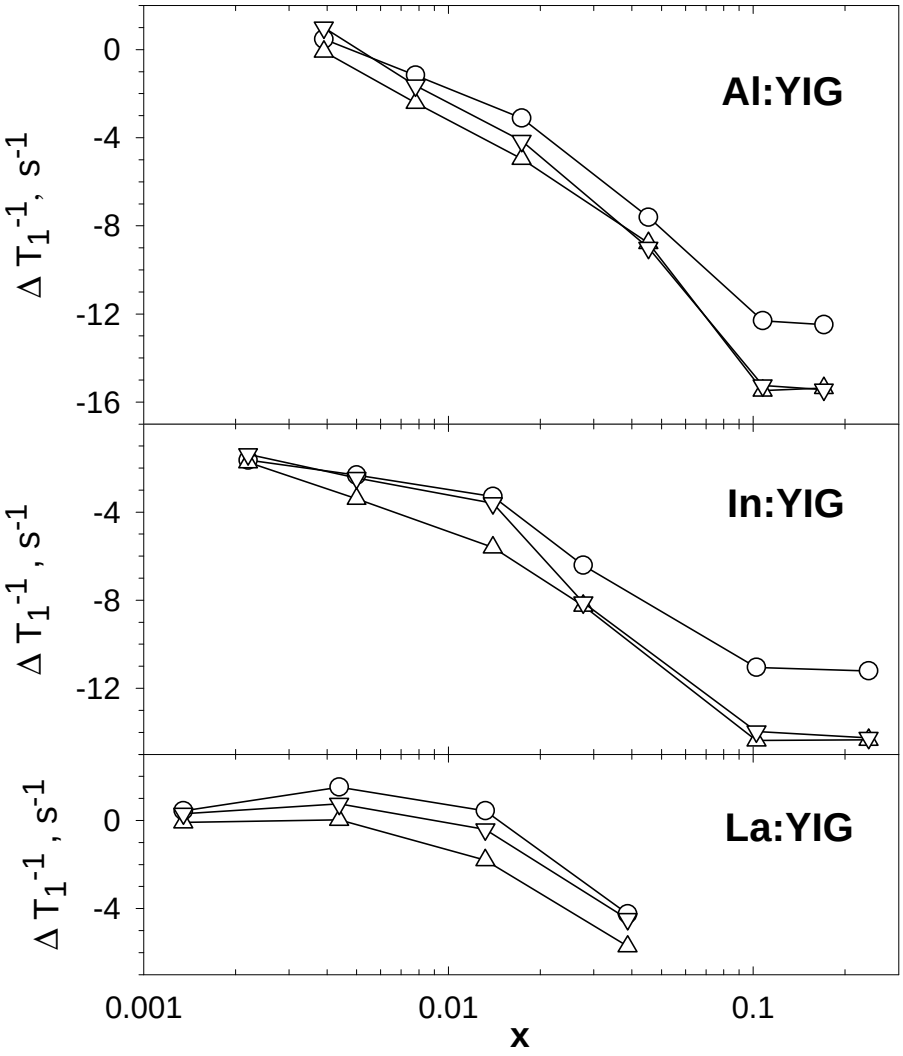

Figure 4.1.2.1. Dependence of ^{57}Fe nuclear relaxation rates T_1^{-1} of main lines for $Y_3Fe_{5-x}Al_xO_{12}$, $Y_3Fe_{5-x}In_xO_{12}$ and $Y_{3-x}La_xFe_5O_{12}$ on x-axis, plotted as differences between the values of the substituted and the pure sample. Symbols: circle=d-site, triangle up=a1-site, triangle down=a2-site. Relaxation rates T_{1pure}^{-1} of the pure sample for d; a1; a2 main lines are respectively 16, 20, 20 s^{-1}.

The $T_2^{-1}(2)$ relaxation rates are comparable to the T_1^{-1} values of the same samples and also exhibit similar dependence on the amount of substitution.

The $T_2^{-1}(1)$ for the Al and La substitutions follow more or less the $T_2^{-1}(2)$ values, but a substantial difference is seen for the In substitution where after reaching x~0.05 the $T_2^{-1}(1)$ sharply increases.

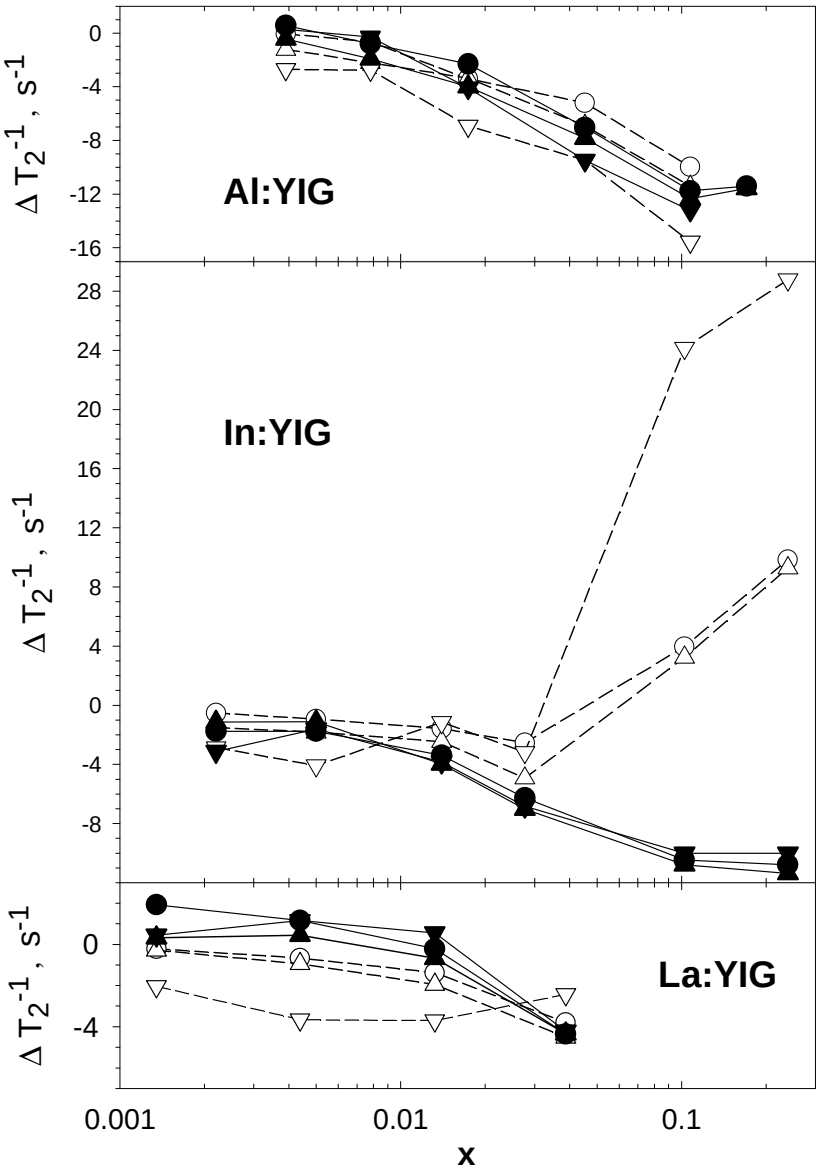

Figure 4.1.2.2. Dependence of ^{57}Fe nuclear relaxation rates T_2^{-1} of main lines for $Y_3Fe_{5-x}Al_xO_{12}$, $Y_3Fe_{5-x}In_xO_{12}$ and $Y_{3-x}La_xFe_5O_{12}$ on x-axis, plotted as differences between the values of the substituted and the pure sample. Open symbols correspond to the $T_2^{-1}(1)$, full to the $T_2^{-1}(2)$; circle=d-site, triangle up=a1-site, triangle down=a2-site. Relaxation rates $T_{2,pure}^{-1}(1)$ of the pure sample for d; a1; a2 main lines are respectively 15, 16, 24 s^{-1}, relaxation rates $T_{2,pure}^{-1}(2)$ are 16, 16, 19 s^{-1}.

Following Ref. [Ghos71, Klau62], the time dependences of the signal intensities obtained by the two methods in solids may differ by a diffusion-like terms as a consequence of a

different reflection of frequency fluctuations in the methods used for relaxation measurements. The fluctuations give rise to an extra decay of the spin-echo signals apart from their usual exponential relaxation decay. The resultant decay is, in general, nonexponential in character and depends on the peculiar nature of the experiment. Also, it is worth to point out the anisotropy pronounced for the octahedral sites by a significant difference between the $T_2^{-1}(1)$ values of a1 and a2 main lines.

In conclusion, the effect of trivalent substitutions on the spin–lattice and spin–spin relaxation rates has been studied. Although the changes are more subtle than in the case of substituents with different valencies, they are well detectable. All the trivalent substitutions studied decrease the spin–lattice relaxation rate with increased concentration. Similar dependence was found for the spin–spin relaxation rate except $T_2^{-1}(1)$ for the In substitutions above x~0.05.

These results have been published [Gama02-2].

4.1.3. NMR spectra and relaxations of ^{57}Fe in calcium-doped yttrium iron garnet films

Various impurities can enter the cation sites in YIG. If their charge is different from 3+, compensation is needed to balance the extra charge. These impurities are therefore called charged impurities, in contrast with trivalent ones. If the charge cannot be balanced by the present impurities, the formation of charged intrinsic defects like Fe^{2+} and Fe^{4+} takes place. It has been shown [Donn94] that these intrinsic defects will be created only if other impurities cannot balance the charge. Since the presence of a small quantity of nontrivalent Fe ions is difficult to detect directly in presence of a large number of Fe^{3+}, only indirect methods can be used to prove their existence.

Ca^{2+} is supposed to replace Y^{3+} in c-sites. Charge compensation can be reached by paired substitutions (e.g. Ca^{2+}-Ge^{4+}, Ca^{2+}-Si^{4+}). On the other hand, $Y_{3-x}Ca_xFe_5O_{12}$ samples without charge compensation doping can also be prepared. ^{57}Fe NMR was employed to trace an effect of Ca^{2+} substitution in YIG films prepared by liquid-phase epitaxy on GGG substrates. The following series of samples were used for our study: YIG:Ca prepared from lead oxide flux, YIG:Ca–Ge, YIG:Ca–Si and YIG:Ca prepared from barium oxide flux. Samples were prepared

by M. Kucera and K. Nitsch. NMR spectra and for YIG:Ca samples prepared from barium oxide flux also relaxation rates were measured at 4.2K in zero external magnetic field. The spin echo technique with coherent data accumulation in time domain and subsequent Fourier transform was used.

Comparing the ^{57}Fe NMR spectra of various series of Ca substituted samples (YIG:Ca, YIG:Ca–Ge and YIG:Ca–Si) and considering their changes with the increasing Ca content in a flux, a pronounced satellite line induced by Ca was identified at 65.6 MHz in the d-site spectral region. Examples of spectra are in Fig. 4.1.3.1.

The analysis based on the YIG crystal and magnetic structure predicts two satellite lines corresponding to those resonating iron nuclei in d-sites which have one of their nearest c-sites occupied by the substituent. Provided the Ca cations are randomly distributed on c-sites, the satellites should be of equal integral intensities $I_{sat} = I_{main} \cdot x/3$, where I_{main} is the intensity of the main d-line and *x* means Ca content per formula unit. The second satellite line was not observed being presumably hidden by the main d-line. The content of Ca per formula unit (x_{NMR}) was estimated from the ratio of the Ca-induced satellite and the main d-line integral intensities.

The impact of the Ca substitution in YIG:Ca samples on relaxation rates was also studied. A well-defined series of YIG:Ca epitaxial films grown from the flux $BaO/B_2O_3/BaF_2$ on a substrate

orientation (110) with gradually increased content of $CaCO_3$ in the flux was measured. Lead-free $BaO/B_2O_3/BaF_2$ flux, in comparison with a flux based on PbO, yielded samples without lead impurities and with a minimal Pt content [Step99]—see Fig. 4.1.3.1.

Relaxation parameters were measured for main d-lines at 4.2 K. The spin–lattice relaxation rate T_1^{-1} was determined from the dependence of a two-pulse spin echo on a repetition time. Spin-spin relaxation rate T_2^{-1} was measured from the dependence of a two-pulse spin echo on a time delay between pulses and alternatively from the decay of individual echoes in a Carr–Purcell- Meiboom-Gill multiple pulse sequence. As the time dependences may differ probably due to the diffusion-like term we refer $T_2^{-1}(1)$ to the former and $T_2^{-1}(2)$ to the latter method.

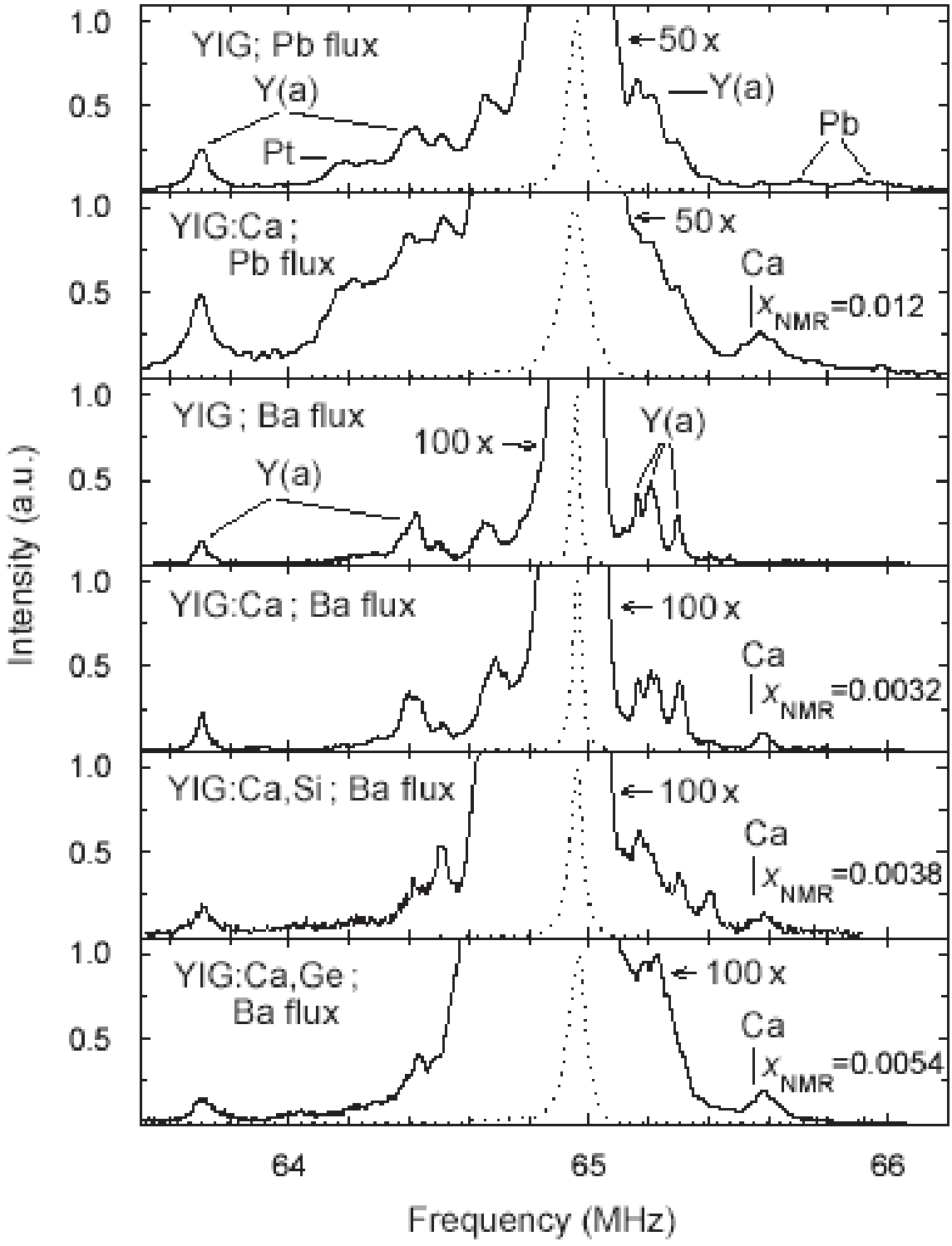

Figure 4.1.3.1. d-site regions of ^{57}Fe NMR spectra of YIG films prepared by liquid phase epitaxy on GGG substrate of (111) orientation, T = 4:2K. Assigned are Ca-induced satellites and the previously identified [Step99, Nova95, Step00] satellites induced by yttrium antisite defects Y(a) and by Pb and Pt impurities.

The results are plotted in Fig. 4.1.3.2. The divalent calcium ions could be charge compensated by charged impurities, vacancies, and also by an induced decrease of the Fe^{2+} ions in a sample (needed for charge compensation of tetravalent impurities like Pt^{4+} if not enough divalent impurities are present). With increasing Ca^{2+} concentration, the formation of Fe^{2+} should be then more and more suppressed. The NMR satellite lines assigned to Fe^{2+} ions have not been identified till now, but the relaxations offer a possibility to monitor Fe^{2+} indirectly. Fe^{2+} is a strong NMR relaxation centre and the diminution of its concentration should rapidly decrease the spin–lattice relaxation rates [Wagn96]. The decrease was really observed (see Fig. 4.1.3.2) in our series of YIG:Ca films prepared from barium flux, but only for x_{NMR} higher than ~0.002. It indicates that for lower content of Ca when the relaxation rates remain approximately constant, the charge compensation is reached by other mechanisms.

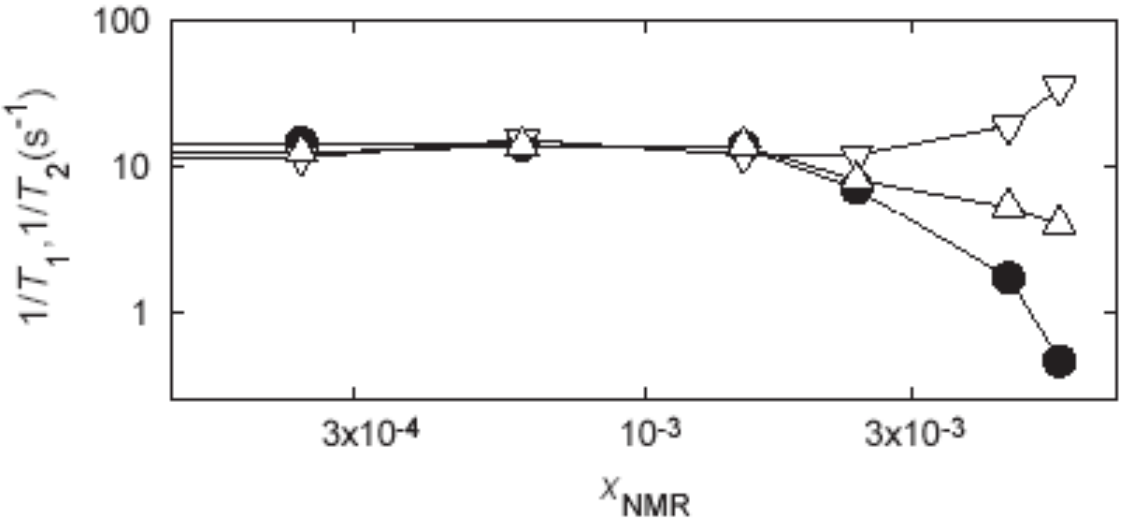

Figure 4.1.3.2. Dependence of ^{57}Fe NMR relaxation rates on Ca content for the main d-line in a series of YIG:Ca films prepared from Ba flux on GGG substrate, (110) orientation, T = 4:2K. Circles= T_1^{-1}, triangles down = $T_2^{-1}(1)$, triangles up = $T_2^{-1}(2)$.

In conclusion one can summarize: the effect of Ca^{2+} substitution on the ^{57}Fe NMR spectra and relaxations was measured in YIG epitaxial films. A satellite line caused by the presence of Ca^{2+} was identified in the spectra of d-sites of YIG:Ca, Ca–Ge and Ca–Si films. In a YIG:Ca series, after an initial constant region the decrease of a spin–lattice relaxation rate was observed in a dependence on the increasing Ca^{2+} content. The changes in relaxation rates are much more pronounced compared to trivalent substitutions studied in the previous paragraph

4.1.2. The onset of the relaxation rate decrease in YIG:Ca series is supposed to correspond to the induced decrease of an amount of Fe^{2+} ions, while charge compensation is reached by other mechanisms for lower calcium content.

These results have been published [Step04].

4.1.4. NMR of ^{57}Fe in bismuth-yttrium iron garnets

In previous paragraphs a modification of hyperfine magnetic field at nuclei in a vicinity of cationic substitution was discussed. Low concentration of substitution gives rise to characteristic satellite lines which appear in a spectrum besides the main lines (corresponding to the nuclei with no substituent in their vicinity) supposing that the induced change of frequency exceeds the linewidth. In case of a complete replacement of Y^{3+} in dodecahedral (c) cation sites the pattern of the spectrum is expected to be analogous to that of YIG (provided magnetization direction remains parallel to [111]), with possible shifts of the resonant frequencies. In the present paragraph we dwell upon ^{57}Fe NMR spectra dependence on the replacement of Y^{3+} in dodecahedral sites by Bi^{3+}. The Bi^{3+} substitution is well known to modify iron garnets magnetic properties and especially to enhance magneto-optical effects. Because of the considerable difference in ionic radii of Y^{3+} (0.1019 nm) and Bi^{3+} (0.117 nm) [Shan76] a bulk sample of bismuth iron garnet (BIG) cannot be synthesized. Nevertheless, techniques of film preparation by direct epitaxial growth from vapour phase proved to be successful [Okud01] (see paragraph 3.1.5.3).

BIG single crystal film and bismuth–yttrium iron garnet single crystal film of high Bi concentration (x=2.75) were prepared by ion beam sputtering (IBS) (paragraph 3.1.5.3) by T.Okuda et al. Characteristics of these samples are given in Table 3.1.5.1. Three comparative samples with low x were used: pure single crystal YIG film grown onto gadolinium gallium garnet substrate by liquid phase epitaxy (LPE), bulk single crystal (x = 0.02) grown from flux and polycrystalline sample (x = 0.15) prepared by ceramic technique. NMR spectra were measured at 4.2 K in zero external magnetic field. Spin echo pulse sequence with coherent data summation and Fourier transformation was employed.

Spectra of $Bi_xY_{3-x}Fe_5O_{12}$ (x = 0, 0.02, 0.15, 2.75 and 3) are plotted in Fig.4.1.4.1. The spectrum of BIG consists of a single line centered at 66.46 MHz which corresponds to iron nuclei in d-sites and of two lines at 74.00 MHz and 75.06 MHz (with relative integral intensities

~1:3) assigned to iron ions in a-sites. This scheme of a spectrum is characteristic for an iron garnet having magnetization direction along ~ [111].

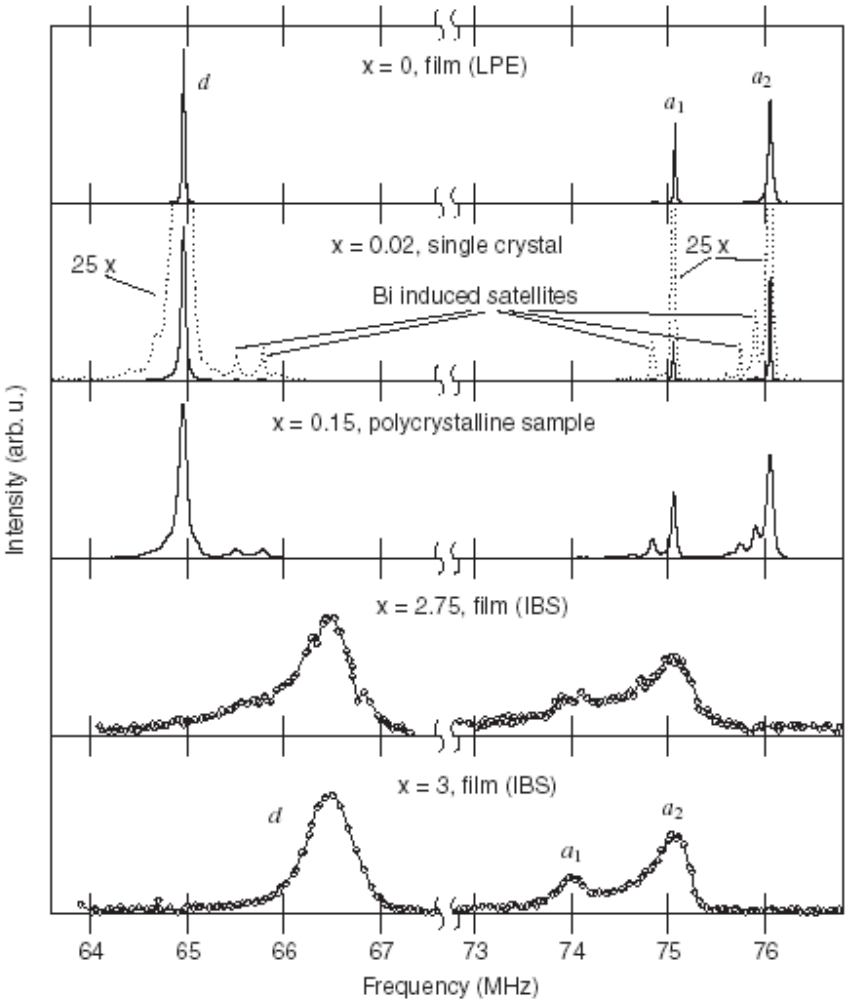

Figure 4.1.4.1. ^{57}Fe NMR spectra of bismuth-yttrium iron garnets $Bi_xY_{3-x}Fe_5O_{12}$ with x = 0, 0.02, 0.15, 2.75 and 3 measured at 4.2K in zero external magnetic field.

Comparison of resonant frequencies of BIG and YIG films is given in Table 4.1.4.1.

	f_d (MHz)	Δ_d (MHz)	f_{a1} (MHz)	Δ_{a1} (MHz)	f_{a2} (MHz)	Δ_{a2} (MHz)	I_a (MHz)	δ_a (MHz)
BIG	66.46	0.57	74.00	~0.40	75.05	0.50	74.79	1.05
YIG	64.96	0.025	75.06	0.023	76.06	0.041	75.81	1.00

(f_d, f_{a1}, f_{a2} ... resonant frequencies of d, a_1 and a_2 lines; Δ_d, Δ_{a1}, Δ_{a2} ... linewidths;
$I_a = (f_{a1} + 3 f_{a2})/4$, $\delta_a = f_{a2} - f_{a1}$)

Table 4.1.4.1. Comparison of ^{57}Fe NMR spectral parameters of BIG and YIG films

The spectral lines of BIG sample exhibit more than an order higher inhomogeneous broadening in comparison with YIG epitaxial films and the lines shape is asymmetric with the slower decrease towards lower frequencies. The most probable reason for the line broadening is a higher amount of intrinsic defects, nevertheless a distribution of magnetization directions close to [111] or distribution of demagnetizing fields cannot be excluded.

Keeping in mind that NMR yields more precise values of the hyperfine fields, a good agreement is found between the hyperfine field on iron nuclei in BIG as well as in YIG obtained from our NMR spectra at 4.2 K and by Mössbauer conversion electron spectroscopy at 6 K [Fuji90].

Resonant frequency of a given iron crystallographic site can be described as a sum of two contributions: a dominating isotropic part *I* and a small anisotropic part, i.e. a contribution dependent on the magnetization direction with respect to the local coordinate system of the site (see paragraph 3.1.4.1). For magnetization parallel to [111] the resonant frequency of d-spectrum equals directly to the isotropic part and a parameter characterizing the anisotropy cannot be determined from this spectrum. In the case of a-spectrum the isotropic part is a weighted average of the *a1* and *a2* resonant frequencies and the anisotropy can be expressed by means of a splitting δ_a between *a1* and *a2* lines. Comparison of BIG and YIG given in Table 4.1.4.1 shows that in BIG the isotropic part is higher for d-sites, while it is smaller for a-sites. The splitting of a-lines does not change considerably.

X-ray diffraction performed for yttrium-bismuth [Gell74] and bismuth iron garnets [Tora95] indicates that replacement of Y^{3+} by Bi^{3+} leads to a shortening of Fe–O^{2-} distances in the tetrahedron while in the octahedron they lengthen. In this respect the comparison of iron hyperfine fields in BIG and YIG is interesting since the higher covalency related to the shorter interatomic distances is believed to lower resonant frequencies. The found spectral shifts of BIG in respect to the YIG reveal, however, just an opposite tendency, i.e., decrease in resonant frequency with increasing size of the octahedron, and increasing frequency in case of the decreasing tetrahedron. This indicates a substantial impact of the bismuth electron structure on electron transfer in Fe–O-cation triads.

In samples with x = 0.02 and 0.15 we have detected resolved satellites in spectra induced by the presence of Bi substituent in the nearest c-neighbourhood of the resonating iron (fig.4.1.4.1). Two satellite lines are pronounced in the *d*-spectrum (shifted by 0.54 and 0.81 MHz from the main d-line). *a*-spectrum contains one satellite line close to a1-main line (shifted

by –0.215 MHz), and three satellite lines near a2, two of them overlap (shifted by –0.16 MHz and, for the double satellite, by –0.31 MHz).

For high values of x (close to 3) a mirror structure of spectra is expected. It means that the spectra contain satellites corresponding to the resonating irons with a single Y^{3+} cation in their nearest *c*-neighbourhood regularly occupied (in BIG) by Bi^{3+}. These satellite lines should be shifted from the BIG main lines in an opposite direction than satellites in YIG with small concentration of Bi. The inhomogeneous line broadening in the spectrum of the film with x ~ 2.75 disables detailed analysis, however the mirror position of satellite lines is still evident at least in the spectrum of d-sites.

Assuming that the additivity principle is valid for a contribution of individual Bi → Y substitutions in the neighbor c-site of the resonating iron nucleus to its resonant frequency, the NMR frequencies for BIG can be predicted on the basis of the YIG main lines frequencies and the shifts of Bi^{3+} induced satellites observed in spectra of the yttrium-bismuth iron garnets with low Bi content. Considering numbers of the nearest c-neighbours of the *d* and *a* iron sites and neglecting small differences in dipolar and Lorentz magnetic fields one obtains for BIG (in MHz):

$f_d \equiv I_d = 66.31,\ f_{a1} = 73.76,\ f_{a2} = 74.79,\ I_a = 74.53,\ \delta_a = 1.03.$

These values differ somewhat from those obtained from the experiment (see Table 4.1.4.1) predominately in the isotropic parts for which the estimated values are systematically lower.

To summarize the results of the present study it should be noted that the hyperfine magnetic interaction at iron nuclei in a bismuth–yttrium iron garnet system $Bi_xY_{3-x}Fe_5O_{12}$ with $0 \leq x \leq 3$ was studied using nuclear magnetic resonance. ^{57}Fe NMR spectra were measured by spin echo technique at 4.2 K in zero external magnetic field. The spectrum measured in a single crystal film of BIG ($Bi_3Fe_5O_{12}$) prepared by IBS reflects the garnet crystal structure having magnetization along ~[111] direction. The resonant frequencies are slightly shifted in comparison with yttrium iron garnet $Y_3Fe_5O_{12}$. Satellite lines and line broadening appear in spectra of partially substituted samples due to a distribution of Y^{3+} and Bi^{3+} cations in dodecahedral sites. The modification of a hyperfine interaction induced by replacement of Y^{3+} with Bi^{3+} was found. It evidences a considerable difference in the electronic structure of these cations.

These results have been published [Step03].

4.1.5. Conclusions on studied garnets.

In the frame of the present thesis the following problems concerning the NMR investigations of *substituted yttrium iron garnets* have been studied:

1. ***The effect of Al substitution in YIG on iron hyperfine field anisotropy.***

   It was found that the presence of Al substitution in the nearest cation site in YIG modifies the hyperfine filed on iron nuclei and gives rise to a satellite structure of spectra. The corresponding Al^{3+}-caused satellites were identified for series of five substituted samples and the angular dependences of the resonant frequencies for main and satellite lines were measured for 16 different magnetization directions. In fact, the isotropic parts and the anisotropic tensors for the main and satellite lines were calculated and compared to those previously obtained for Ga^{3+} and Ge^{4+} substituted YIG, enabling to consider the influence of (i) different ionic radii of trivalent nonmagnetic substitution, (ii) replacement of the magnetic ion Fe^{3+} by a nonmagnetic one, and (iii) the influence of different valencies of the nonmagnetic substituents. It was concluded, that all the three nonmagnetic substituents decrease the isotropic term for iron nuclei in their nearest a-sites (Table 4.1.1). The effect of the valence change is somewhat smaller but comparable to that due to the replacement of iron by a nonmagnetic trivalent cation with similar ionic radius. Angular dependences of the a-main lines and the satellites resonant frequencies for Ge, Ga, and Al substitution show at first glance the increase of the hyperfine field anisotropy induced by the substitution, weaker for Ge than for Ga or Al. One can then conclude that the major change of the hyperfine field anisotropy is caused by the replacement of the magnetic moment on the neighbour cation site. It remains important for the a-sites even after elimination of the dipolar field contribution. The change of valency has weaker but comparable impact. The influence of the ionic radii difference seems to be less important.

2. *The effect of nonmagnetic trivalent substitutions (Al, In, La) in YIG on nuclear magnetic relaxation.*

The aim of this study was to estimate the direct impact of the substitutions to changes of nuclear relaxation rates in YIG. Three sets of samples were studied. The choice covered all the cation sites of the garnet structure, i.e. the nonmagnetic Al^{3+} that prefers tetrahedral sites, In^{3+} occupying octahedral sites, and La^{3+} that replaces yttrium in dodecahedral sites.

In the spectra of the substituted samples one was detected a satellite structure characteristic of the particular substitution. The spin–lattice relaxation rate T_1^{-1} was determined from the dependence of NMR signal on the repetition time of the two-pulse spin echo pulse sequence. The spin–spin relaxation rate T_2^{-1} was measured by two techniques: (1) from the signal intensity dependence of the two-pulse spin echo on the delay between pulses $T_2^{-1}(1)$ and (2) from the decay of the individual echoes in the multiple pulse Carr-Purcell sequence $T_2^{-1}(2)$.

The changes of the spin–lattice relaxation rate obtained have shown that all the three types of impurities influence ΔT_1^{-1} within the studied concentration range in a similar way, i.e. the increase of their concentrations lead to the reduction of the relaxation rate. The decrease seems to stop when the concentration of about x= 0.1 is reached (fig.4.1.2.1). The ΔT_1^{-1} values obtained for the same amount of the substituent per formula unit were quite comparable, although the substitutions concerned magnetic (Al, In replacing ferric ions) as well as nonmagnetic (La replacing yttrium) sublattices. The only common feature then seems to be an increased perturbation of the crystal structure periodicity caused by the presence of cations with different ionic radii and then the results might be related to the influence of the disturbed crystal and electron structure periodicity on the electron spin dynamics. The principal role of other effects of the substitution, like possible influence on the domain wall properties or magnetic dilution in iron sublattices by In and Al, cannot however be excluded. Detailed comparison revealed that in cases of Al and In substitutions the decrease of the relaxation rate is more pronounced for the octahedral than for the tetrahedral sites (fig.4.1.2.1).

The results obtained for the spin–spin relaxation rates (fig.4.1.2.2) demonstrate in certain case significantly different values from the two techniques used. The $T_2^{-1}(2)$ relaxation rates are comparable to the T_1^{-1} values of the same samples and also exhibit similar

dependence on the amount of substitution. The $T_2^{-1}(1)$ for the Al and La substitutions follow more or less the $T_2^{-1}(2)$ values, but a substantial difference was obtained for In substitution where after reaching x~0.05 the $T_2^{-1}(1)$ sharply increases. Also the anisotropy is clearly pronounced for the octahedral sites by a significant difference between the $T_2^{-1}(1)$ values of a1 and a2 main lines. Following Ref. [Ghos71, Klau62], the time dependences of the signal intensities obtained by the two methods in solids may differ by a diffusion-like terms as a consequence of a different reflection of frequency fluctuations in the methods used. The resultant decay is, in general, nonexponential in character and depends on the peculiar nature of the experiment.

3. The effect of Ca^{2+} substitution in YIG on ^{57}Fe NMR spectra and relaxations.

Ca^{2+} is a charged substitution for YIG, in contrast to trivalent Al, In and La, and replaces Y^{3+} in c-sites. Comparing ^{57}Fe NMR spectra of various series of Ca substituted samples (YIG:Ca, YIG:Ca–Ge and YIG:Ca–Si) and considering their changes with the increasing Ca content in a flux, a pronounced satellite line induced by Ca was identified at 65.6 MHz in the d-site spectral region. (Fig. 4.1.3.1). The second satellite line was not observed being presumably hidden by the main d-line. The impact of the Ca substitution in YIG:Ca samples on relaxation rates was also studied. The spin–lattice and spin-spin relaxation rates were measured by the same way as in the case of trivalent substitutions. The divalent calcium ions could be charge compensated by charged impurities, vacancies, and also by an induced decrease of the Fe^{2+} ions in a sample (needed for charge compensation of tetravalent impurities like Pt^{4+} if not enough divalent impurities are present). With increasing Ca^{2+} concentration, the formation of Fe^{2+} should be then more and more suppressed. The NMR satellite lines assigned to Fe^{2+} ions have not been identified till now, but the relaxations offer a possibility to monitor Fe^{2+} indirectly. Fe^{2+} is a strong NMR relaxation centre and the diminution of its concentration should rapidly decrease the spin–lattice relaxation rates [Wagn96]. The decrease was really observed (see Fig. 4.1.3.2), but only for x_{NMR} higher than ~0.002. It indicates that for lower content of Ca when the relaxation rates remain approximately constant, the charge compensation is reached by other mechanisms.

4. NMR of ^{57}Fe in bismuth-yttrium iron garnets.

This study concerned the dependence of ^{57}Fe NMR spectra on the replacement of Y^{3+} in dodecahedral sites by Bi^{3+}. Samples of $Bi_xY_{3-x}Fe_5O_{12}$ with x = 0, 0.02, 0.15, 2.75 and 3 were measured and their spectra were analyzed. It was found that the spectrum measured on a single crystal film of BIG ($Bi_3Fe_5O_{12}$) prepared by IBS reflected the garnet crystal structure having magnetization along ~[111] direction. The resonant frequencies were slightly shifted in comparison with yttrium iron garnet $Y_3Fe_5O_{12}$. The spectral lines of BIG sample exhibited more than an order higher inhomogeneous broadening in comparison with YIG epitaxial films and the line shapes were asymmetric with the slower decrease towards lower frequencies. The most probable reason for the line broadening is a higher amount of intrinsic defects, nevertheless a distribution of magnetization directions close to [111] or distribution of demagnetizing fields cannot be excluded.

A good agreement was found between the hyperfine field on iron nuclei in BIG as well as in YIG obtained from our NMR spectra at 4.2 K and by Mössbauer conversion electron spectroscopy at 6 K [Fuji90].

Comparison of isotropic and anisotropic parameters of BIG and YIG have shown that in BIG the isotropic part is higher for d-sites, while it is smaller for a-sites. The splitting of a-lines did not change considerably.

X-ray diffraction performed for yttrium-bismuth [Gell74] and bismuth iron garnets [Tora95] indicates that replacement of Y^{3+} by Bi^{3+} leads to a shortening of $Fe–O^{2-}$ distances in the tetrahedron while in the octahedron they lengthen. In this respect the comparison of iron hyperfine fields in BIG and YIG is interesting since the higher covalency related to the shorter interatomic distances is believed to lower resonant frequencies. The found spectral shifts of BIG in respect to the YIG revealed, however, just an opposite tendency, i.e., decrease in resonant frequency with increasing size of the octahedron, and increasing frequency in case of the decreasing tetrahedron. This indicates a substantial impact of the bismuth electron structure on electron transfer in Fe–O-cation triads.

In samples with x = 0.02 and 0.15 the resolved satellites have been detected in spectra induced by the presence of Bi substituent in the nearest c-neighbourhood of the resonating iron (fig.4.1.4.1). Two satellite lines were pronounced in the *d*-spectrum (shifted by 0.54 and 0.81 MHz from the main d-line). *a*-spectrum contained one satellite line close to a1-

main line (shifted by –0.215 MHz), and three satellite lines near a2, two of them overlap (shifted by –0.16 MHz and, for the double satellite, by –0.31 MHz).

For higher values of x (close to 3) a mirror structure of spectra was expected. The inhomogeneous line broadening in the spectrum of the film with x ~ 2.75 disabled detailed analysis, however the mirror position of satellite lines was still evident at least in the spectrum of d-sites.

Assuming that the additivity principle is valid for a contribution of individual Bi $\rightarrow$ Y substitutions in the neighbor c-site of the resonating iron nucleus to its resonant frequency, the NMR frequencies for BIG were estimated on the basis of the YIG main lines frequencies and the shifts of Bi^{3+} induced satellites observed in spectra of the yttrium-bismuth iron garnets with low Bi content. The values differed somewhat from those obtained from the experiment (Table 4.1.4.1) predominately in the isotropic parts for which the estimated values were systematically lower.

4.2. Experimental results on studied magnetites.

In the frame of the thesis, the modification of the electronic structure of magnetite by Al and Ga substitutions is studied by means of NMR on ^{57}Fe nuclei.

A partial substitution of iron ions in magnetite by Al^{3+} cations affects strongly NMR spectra of magnetite, despite the trivalent state of these ions, As it was discussed earlier, it was surprising that Al^{3+}-substitution lowers T_V much stronger than Ga^{3+}-substitution. This fact was explained by the assumption that Al ions occupy preferentially B-sites while Ga ions occupy preferentially A-sites. If it is so, we should expect that NMR spectra of Al-substituted magnetite will have the most pronounced satellite structure in the vicinity of A-lines, and Ga-substituted magnetite spectra will have the most pronounced satellite structure in the vicinity of B-lines.

To analyze the NMR spectra, the prediction of number and intensities of lines of ^{57}Fe in the spectra has been performed. We have been focused on the analysis of satellite structure of simplified (due to higher symmetry of local surroundings) spectra above the Verwey transition. Below T_V the lower symmetry is expected to result in a high number of irresolvable weak satellite lines.

4.2.1. ^{57}Fe NMR in substituted magnetite – symmetry consideration

As it was mentioned in paragraph 3.2.3, a large number of cations exist which can be incorporated into the magnetite lattice. Substitution of iron ions in magnetite by other cations lowers the Verwey temperature T_V. The reduction of the temperature is particularly large for divalent and tetravalent substitutions, indicating that their presence hinders the valence ordering of iron ions on octahedral sites, which is believed to occur below T_V.

On performing substitutions, very often a distribution of the substituting ions on the different cation sites is observed, as it was discussed in paragraph 3.2.3 for different substituents of magnetite. The presence of a substitution (including a nonmagnetic one) modifies a hyperfine field **B** on the nuclei of those iron ions (sites) which are situated in a neighborhood of a substituted ion, giving rise to a modification of their resonance frequencies and, as a consequence, satellites appear in NMR spectra in addition to main lines (if a frequency shift is

larger than the linewidth of the corresponding main line). Amplitudes of satellite lines are proportional to a concentration of an impurity. As far as an influence of a defect on the hyperfine field of the resonating nuclei decreases rapidly with the distance between nuclei and the defect, satellite lines caused by the distant defects are covered in most cases by the parent main lines because of the smallness of their frequency shifts. The only satellite lines are resolved that cause the change of the hyperfine field on the resonating nuclei larger than corresponding parent line linewidth.

To predict the number of satellite lines in ^{57}Fe spectra and their intensities for magnetite structure above the Verwey temperature, we have considered the local symmetries of iron sites with resonating nuclei and the symmetry disturbance when the defect/substituent appears in their vicinity. We have employed a concept of crystallographic and magnetic equivalency in a similar way as it was done for the garnet structure (paragraph 3.1.3.5). The results of the analysis are given in the next table 4.2.1. The prediction of satellite patterns for both resonating iron sites without and with substitutions in their neighbouring A or B sites is presented together with the anisotropic term $\sum_{i,j=1}^{3} A_{ij}^{s} n_i n_j$ in the expansion of Eq.3.1.4.1 up to its second order term (see Eq.3.1.4.3).

Notation	Position of a resonating nucleus	Position of a substitution	Fe surrounding (within 5Å)
a)	8*a*=A	16*d*=B	12 x 3.453 Å
b)		8*a*=A	4 x 3.607 Å
c)	16*d*=B	16*d*=B	6 x 2.945 Å
d)		8*a*=A	6 x 3.453 Å

Magnetization direction	$\sum_{i,j=1}^{3} A_{ij}^{s} n_i n_j$	Notation from the upper table	Number of satellites	Relative ratio of intensities of the satellites	Positions of the satellites (in order of the previous column)
[100]	A_{xx}	a),c),d)	2	2 : 1	I+α; I-2α;

		b)	1	-	I
[110]	$A_{xx}+A_{yy}+2A_{xy}$	a),c),d)	4	1 : 1 : 2 : 2	I+2α+2β; I+2α-2β; I-α+2γ; I-α-2γ;
		b)	2	1 : 1	I+2γ; I-2γ;
[111]	$2A_{xy}+2A_{xz}+2A_{yz}$	a),c),d)	3	1 : 2 : 1	I+2β+4γ; I-2β; I+2β-4γ;
		b)	2	1 : 3	I+6γ; I-2γ;

Table 4.2.1. Surrounding of an iron ion in magnetite above the Verwey transition and corresponding satellite structure of spectra.

Notations in the table:

a) - substitution is positioned in the plane of the symmetry for the position of a resonationg nucleus ($x\rightarrow y$, $y\rightarrow x$, $z\rightarrow z$) . Then tensor A has 3 independent terms, designated as α, β, γ:

$$\begin{pmatrix} \alpha & \beta & \gamma \\ \beta & \alpha & \gamma \\ \gamma & \gamma & -2\alpha \end{pmatrix}$$

Another terms GAG^{-1} one can obtain by 24 operations of the symmetry group, where G are the same as for garnets (paragraph 3.1.3.5, Eg. 3.1.4.7). There will be 12 different results.

b) - substitution is positioned in the plane of the symmetry and on the 3 fold axis:

1. rotation $x\rightarrow z$, $z\rightarrow y$, $y\rightarrow x$

2. rotation $x\rightarrow y$, $y\rightarrow z$, $z\rightarrow x$

symmetry plane $x\rightarrow y$, $y\rightarrow x$, $z\rightarrow z$

Tensor A has 1 independent term, designated as gama:

$$\begin{pmatrix} 0 & \gamma & \gamma \\ \gamma & 0 & \gamma \\ \gamma & \gamma & 0 \end{pmatrix}$$

Another terms GAG^{-1} one can obtain by 24 operations of the symmetry group, where G are the same as for garnets (Eq. 3.1.4.7). There will be 4 different results.

c) - substitution is positioned in the plane of the symmetry for the position of a resonating nucleus, as for a) .

d) - substitution is positioned in the plane of the symmetry for the position of a resonating nucleus, as for a).

4.2.2. ^{57}Fe NMR of Al^{3+} substituted magnetite below the Verwey transition.

To study the effect of Al-impurities on the electronic structure of magnetite several synthetic single crystals of $Fe_{3-x}Al_xO_4$ were used with aluminum contents x = 0.005, 0.01, 0.02, 0.03. The compounds with x = 0.005 and x = 0.01 exhibit the first order Verwey transition, while the other two compounds exhibit the second order Verwey transition (fig.3.2.16).

Single crystals were prepared from α-Fe_2O_3 (99.9% purity) by means of a floating zone technique by V. Brabers and coworkers. After a crystallization, the single crystals were additionally annealed for at least 48 hr at temperatures between 1150 and 1300°C in adjusted mixtures of CO_2 and H_2 to obtain the highest oxygen stoichiometry [Brab98]. With this technique, homogeneous and stoichiometric single crystals with a predetermined impurity composition can be prepared.

High-sensitivity magnetic disaccommodation technique was used for analysis of the oxygen stoichiometry. This technique allows resolving deviations in the oxygen stoichiometry smaller than 1 ppm, in order to ascertain a high oxygen stoichiometry of the samples [Brab98]. In all the substituted samples the relaxations due to electronic processes were distinctly present in the temperature range below 150 K, whereas the vacancy induced peaks at about 300K were completely absent, thus indicating a vacancy concentration of lower than 10^{-6} [Brab98].

The Verwey temperatures T_V of the samples were determined from the temperature dependence of the electrical conductivity measured by a four-probe technique [Brab98]. T_V's of the substituted samples were then independently estimated by means of NMR technique in our research. They were found decreasing with increasing Al content in agreement with [Brab98]: $T_V(x=0.005)\leq 121K$, $T_V(x=0.01)\leq 117K$, $T_V(x=0.02)<105K$, $T_V(x=0.03)<100K$.

NMR spectra were measured by the spin-echo method using the phase-coherent spectrometer with an averaging technique and the Fast Fourier Transformation. The measurements were performed at zero external magnetic field. The high radiofrequency power was used to excite the signal from nuclei in domains only. The signal-to noise ratio was significantly improved by using the Carr-Purcell pulse sequence.

We also have taken into account the fact that T_2 relaxation times are different for different resonance lines and reconstructed the spectrum in the limit $\tau \to 0$, where τ is the time interval between the exciting and refocusing radio frequency pulses.

4.2.2.1. ^{57}Fe NMR spectrum of Al-substituted magnetite at T=4.2K.

In fig.4.2.1 the NMR spectra of pure magnetite (according to [Nova00]) and Al-substituted magnetite with x=0.005, measured at helium temperature, are compared. Line notations are taken the same as it was for pure magnetite spectrum.

The spectrum structure and positions of all lines of A and B-type are exactly the same for both spectra: all lines visible on the pure magnetite spectrum (having notations over them) are present in the substituted spectrum and the lines did not change their positions under the aluminum substitution of such content. The differences are that the bottom spectrum has lines of A and B-type visually broadened. Also new weak lines (designated as an additional spectrum in the figure 4.2.1) were found within the frequency range 35-48 MHz.

The character of magnetite spectrum having superimposed many of B and all A-lines within the frequency range 68-72MHz (see fig.3.2.18 and fig.3.2.19 for details) and additional lines broadening caused by the presence of Al^{3+} ions makes impossible to reveal satellites in the vicinity of A-lines, caused by the substitution of nearest neighbor Fe ions of B-type by Al^{3+} ions at such content.

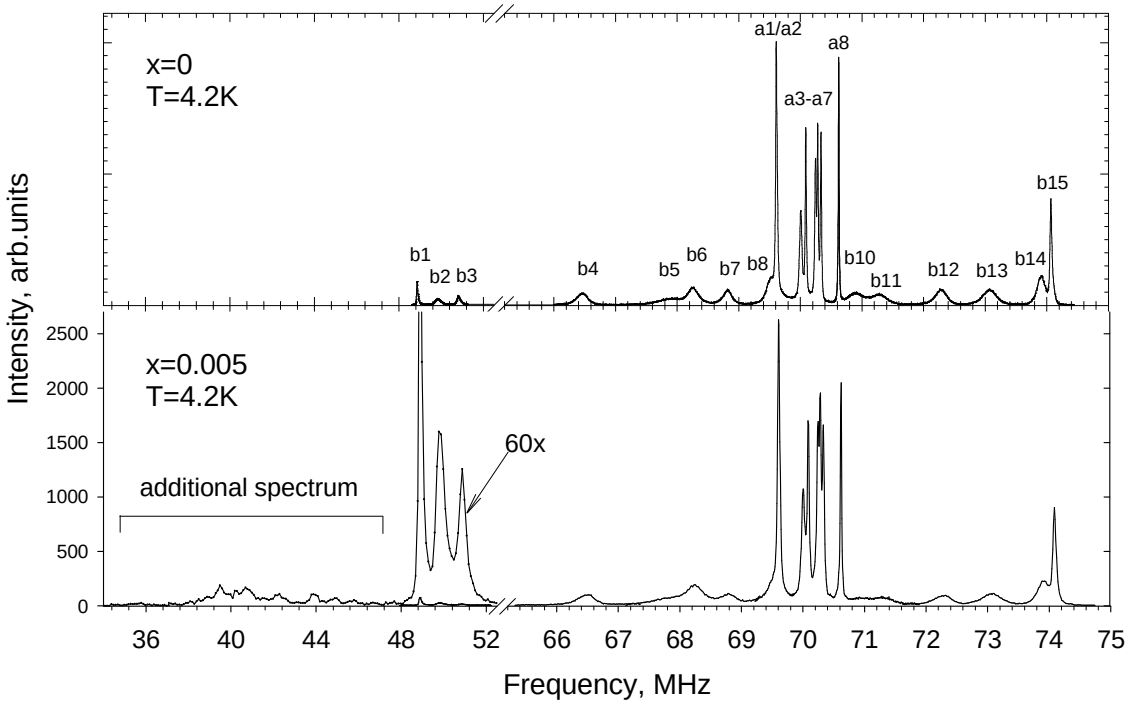

Figure 4.2.1. Comparison of ^{57}Fe NMR spectra of pure magnetite Fe_3O_4 (according to [Nova00]) and Al-substituted magnetite $Fe_{3-x}Al_xO_4$ with x=0.005 at T=4.2K. The bottom spectrum has 60 times-magnified low-frequency part within the frequency range 35-52MHz.

4.2.2.2. Dependence of linewidths on aluminum content.

In fig.4.2.2 NMR spectra measured at liquid helium temperature of Al-substituted magnetite are presented for different aluminum contents, namely x=0; 0.005, 0.01, and 0.03.

The positions of all lines of A and B-type in all spectra of figure 4.2.2 are the same (the lines did not change their positions under the aluminum substitution up to x=0.03 at T=4.2K).

The differences of the spectra are similar to those observed in fig.4.2.1: the substituted spectra have all the lines (of A and B-type) broadened. The broadening depends on aluminum content: the more substitutions - the broader NMR lines are.

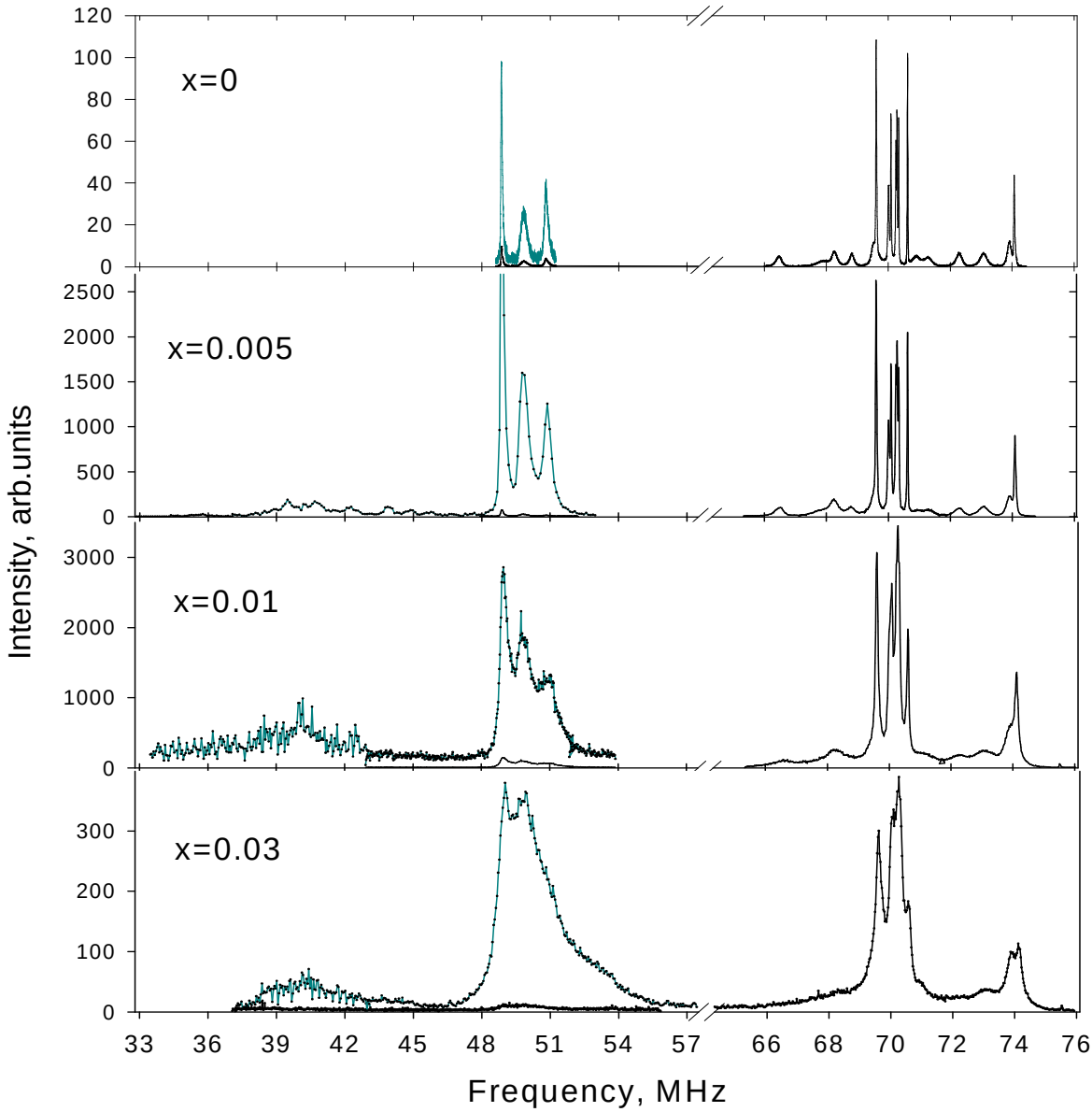

Figure 4.2.2. ^{57}Fe NMR spectra of pure magnetite Fe_3O_4 (according to [Nova00]) and Al-substituted magnetite $Fe_{3-x}Al_xO_4$ with increasing aluminum content x measured at T=4.2K. In the frequency region 33-57 MHz, the spectra are drown also magnified (in cyan) for clearness.

Figures 4.2.3 and 4.2.4 demonstrate this tendency in details.

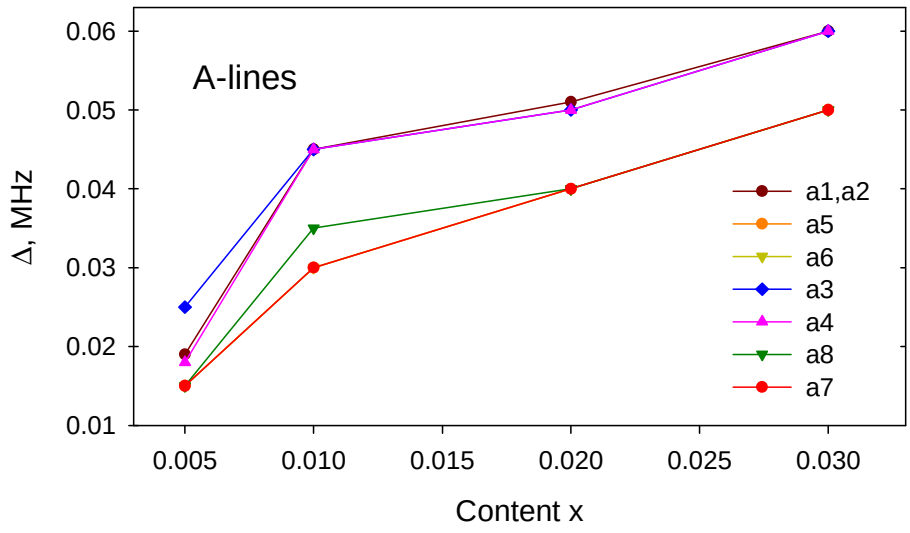

Figure 4.2.3. Dependence of the widths Δ for A-lines taken at a half of their amplitudes on aluminum content (T=4.2K). (Lines are to guide eye).

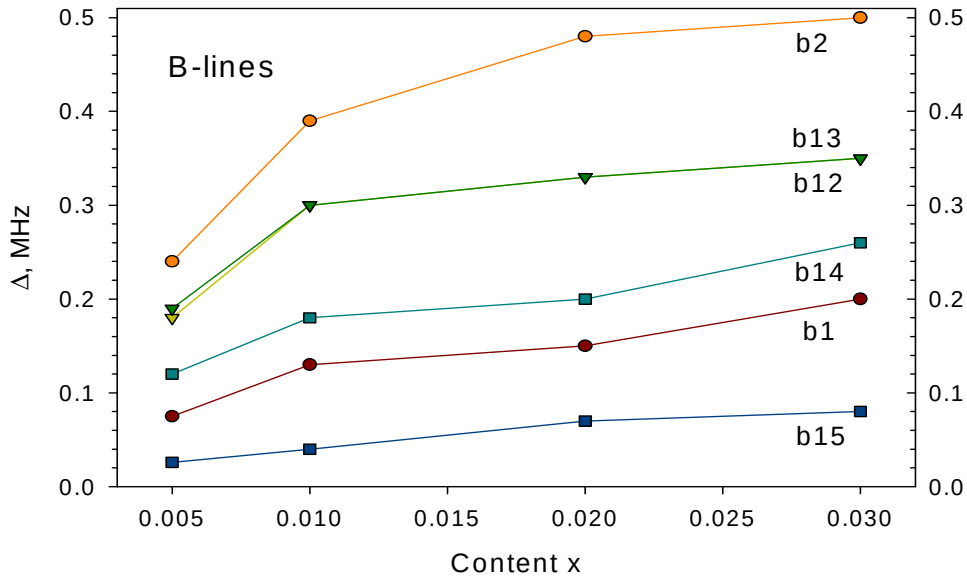

Figure 4.2.4. Dependence of the widths Δ for several B-lines taken at a half of their amplitudes on aluminum content (T=4.2K). (Corresponding symbols are connected to guide eye).

In the figure 4.2.4 data for B-lines which are well-resolved at all aluminum contents studied are presented. Data for corresponding linewidths for pure magnetite first reported in [Nova00] are collected in the table 4.2.2:

A-lines	Δ, MHz	B-lines	Δ, MHz
A1+A2	0.019	B1	0.044
A3	0.040	B2	0.340
A4	0.015	B12	0.188
A5	0.028	B13	0.215
A6	0.017	B14	0.065
A7	0.015	B15	0.031
A8	0.009		

Table 4.2.2. Widths of some NMR lines of pure magnetite at T=4.2K [Nova00].

In view of these data the broadening of lines could be attributed to the influence of Al substitution. Systematic broadening can be the explanation of visual missing of satellites in the vicinity of A-lines for higher aluminum contents.

New sets of weak lines (similar to that observed in fig.4.2.1) appears within the frequency range 35-48 MHz in all substituted spectra. These new sets of weak and broad lines could be assigned either to the resonance of ^{27}Al nuclei (nuclei of ^{27}Al have quadrupole moment $0.15*10^{-24}$ cm^2 and magnetogyric ratio $\approx 6.98*10^7$ rad$\cdot$T$^{-1}\cdot$s^{-1}, which are known to produce wide spectrum with large line broadening at zero external magnetic field) or to some defects in magnetite structure. Further careful inspection has revealed that traces of NMR signal are also present in the spectra of nominally pure sample within this frequency region. Thus the origin of these lines is not clear at present and an additional study of various nominally pure magnetite samples would be necessary to proceed to clarify this issue. However, long spin-lattice relaxation times T_1 of pure magnetite samples would lead to enormously time consuming measurements of weak signals within this frequency region.

Some of Al-substituted spectra studied revealed other weak lines the origin of which was attributed to the sample preparation process. For example, well enough distinguished narrow

weak line at 46.63MHz is presented in x=0.03 spectrum only (Fig.4.2.2) and was recognized as the line of powdered iron at helium temperature [Turo69].

4.2.2.3. Temperature behavior of resonance frequencies of the main lines below the Verwey transition

In this paragraph we will consider the temperature behavior of ^{57}Fe resonance frequencies of Al-substituted magnetite below the Verwey transition in details.

Resonance frequencies of tetrahedral (A) iron sites for aluminum substituted samples with x=0, 0.005, 0.01, 0.02 and 0.03 are plotted in figure 4.2.5 as functions of temperature.

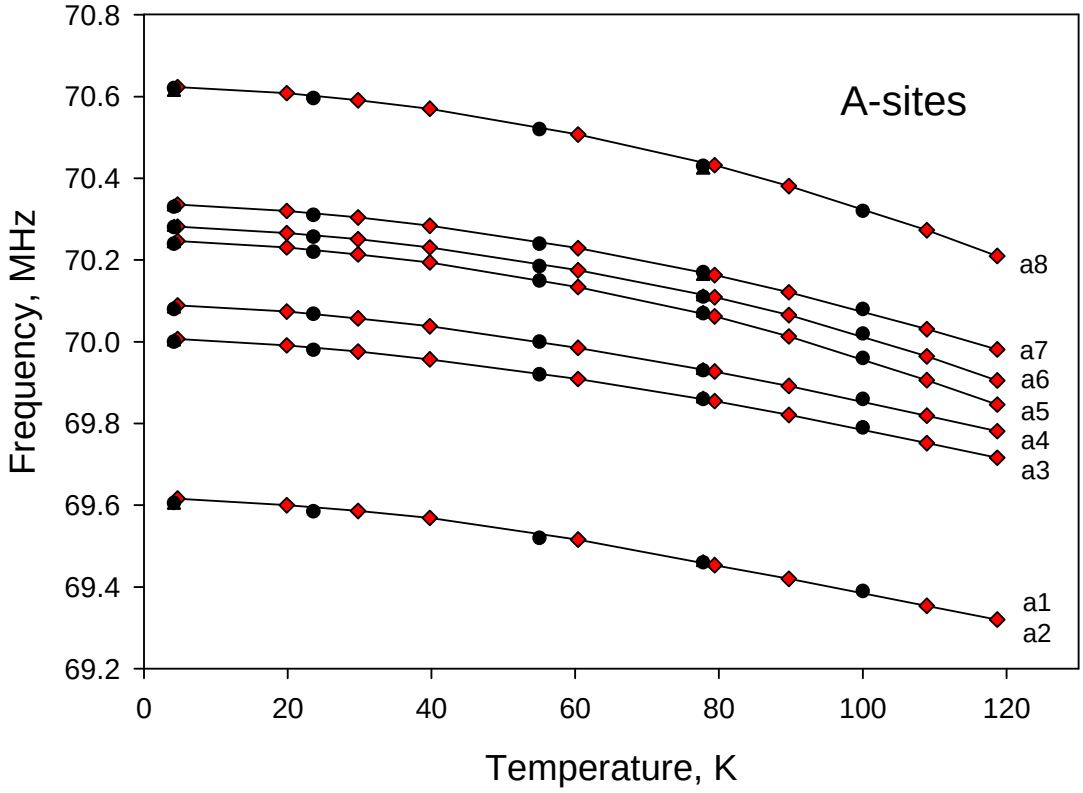

Figure 4.2.5 Temperature dependence of resonance frequencies of the main lines for tetrahedral (A) iron sites below the Verwey transition. Data for pure magnetite (x=0) are taken from [Nova00] and are plotted in red. Black circles, triangles, diamonds and squares designate the resonance frequencies of the samples with aluminum content 0.005, 0.01, 0.02 and 0.03 respectively.

Apparently positions of the main lines of tetrahedral iron sites at a given temperature do not depend on Al concentration and are the same as those of the pure samples reported in [NovaICF00, Nova00] (see fig.3.2.25).

In figure 4.2.6 the temperature dependences of resonance frequencies of octahedral (B) iron sites for the samples with aluminum contents x=0, 0.005, 0.01, 0.02 and 0.03 are presented. Notations of the lines to the right of the curves correspond to designations of B-lines in figures 3.2.18, 3.2.19 and 4.2.1.

Since some of B-lines are not always well resolved in spectra the fitting procedure is not reliable enough for them. As a consequence, only those B-lines were taken into consideration, which were reliably fitted. The most problematic spectra in that sense were ones at approximately 23K and 55K because of the behavior of spin-spin relaxation times within the region close to those temperatures. It will be discussed in one of the next paragraphs.

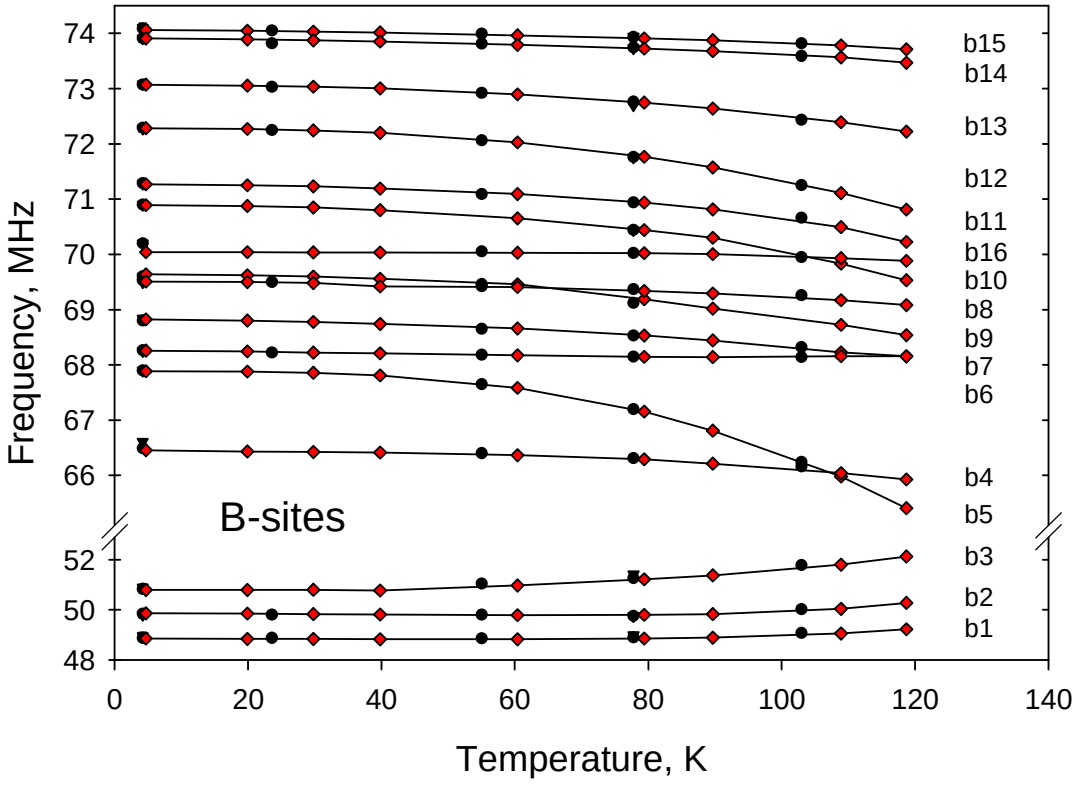

Figure 4.2.6. Temperature dependence of resonance frequencies of the main lines of octahedral (B) iron sites below the Verwey transition. Data for pure magnetite (x=0) are taken from [NovaICF00] and are plotted in red. Black circles, triangles, diamonds and squares designate

the resonance frequencies of the samples with aluminum content x=0.005, 0.01, 0.02 and 0.03 respectively.

As in the case of A-lines, positions of the main lines of octahedral iron sites at a given temperature do not depend on Al concentration and are the same as those of the pure samples.

The temperature dependences in question did not reveal any changes in the values of hyperfine fields on iron sites, giving rise to main lines of magnetite below T_V, in the presence of Al substitution up to x=0.03.

These results together with ^{57}Fe NMR spectra of Al-substituted magnetite with increasing aluminum content have been published [Koho04].

4.2.2.4. Temperature behavior of linewidths of main lines below the Verwey transition.

The temperature dependence of linewidths of the main lines of $Fe_{3-x}Al_xO_4$ below the Verwey transition was studied on the sample with x=0.005 that has more lines resolved than the other samples have.

In figure 4.2.7 the A-spectra of the sample measured at 3 different temperatures are shown. Visually, the lines a3-a8, being a little broadened at liquid nitrogen temperature become narrower at higher temperature. The presence of satellites under A-spectrum was undoubtedly seen when the fitting procedure had been performed. However, taking into account that Al satellites with unknown positions and temperature redistribution under A-spectrum could affect the linewidths noticeably, the quantitative data of linewidths for A-lines are not presented here because of their unreliability. In addition, line b16 (fig.3.2.18, 3.2.19, 3.2.25) which is within the whole measured temperature interval covered with lines a3-a8 and, as a consequence, has unknown linewidth and intensity, affects results as well.

The only exception is the line a1+a2, the fitting procedure of which seems to be reliable enough. The halfwidth of the line is 0.017 ± 0.002 MHz within the whole temperature region below the Verwey transition.

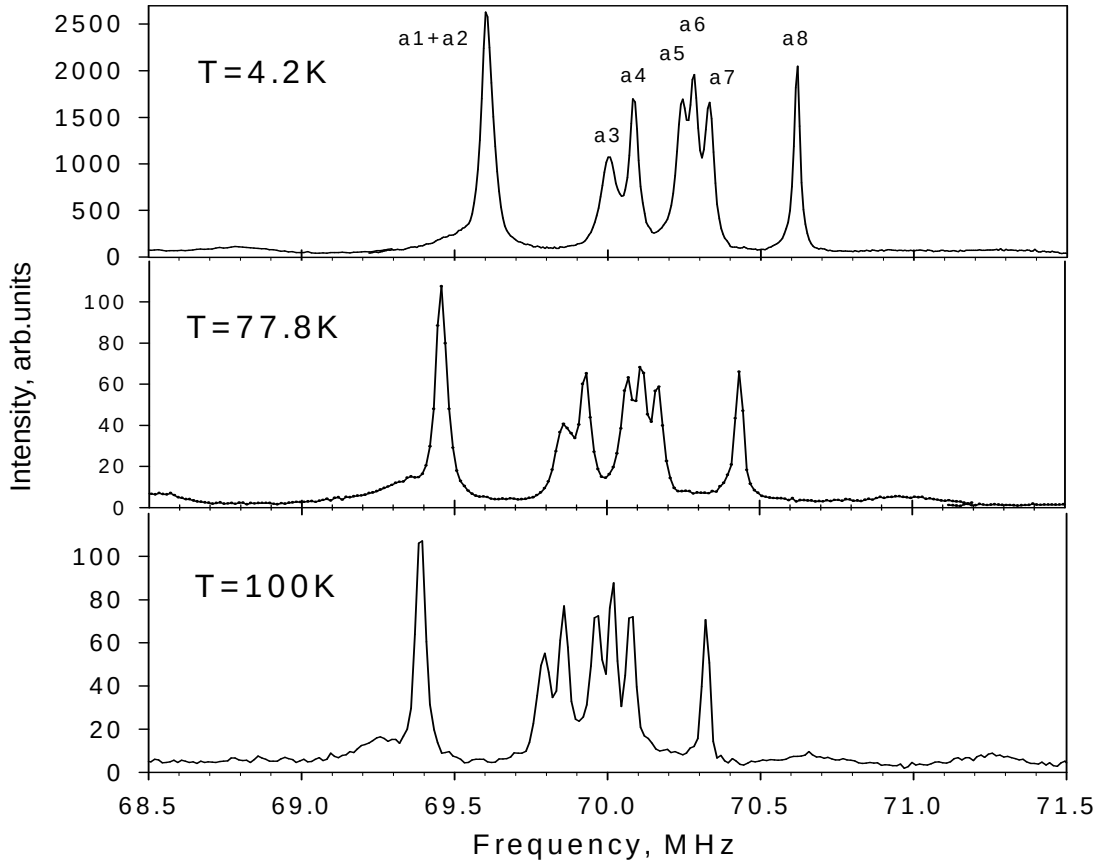

Figure 4.2.7. A-spectra of $Fe_{3-x}Al_xO_4$ with x=0.005 at temperatures of liquid helium, liquid nitrogen and 100K.

The behavior of the linewidth of a1+a2 line below the Verwey transition was reported for pure magnetite in [Nova00]. It was found no broadening of this line with increasing temperature up to T_V (the reported value of linewidth was 0.019 MHz). The conclusion was that two formally inequivalent Fe^{3+}-sites, giving rise to this line, have nearly the same oxygen environment and also their effective exchange fields are equal. In other words, the sites should have the same arrangement of nearest iron cation neighbors and very close geometry of Fe(B)-O^{2-}—Fe^{3+}(A) triads. Presence of aluminum substitution of the content x=0.005 does not change the situation for the linewidth of a1+a2 line.

In figure 4.2.8 the halfwidths of several B-lines are displayed. The lines were chosen under condition of a good resolution at all measured temperatures. There is no significant and systematic change in the temperature behavior of B-lines` linewidths. However, a slight

tendency to decrease the linewidth with increasing temperature is observed in some cases. Nearest neighbor lines (b1 and b2, b12 and b13, b14 and b15) seem to have similar temperature behavior of their linewidths.

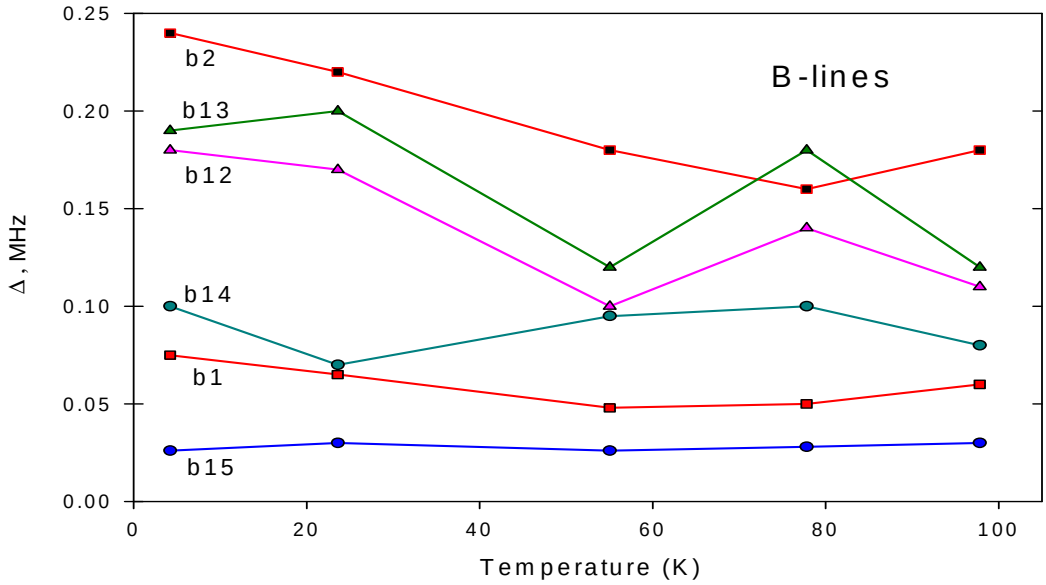

Figure 4.2.8. Temperature dependence of halfwidths for several octahedral (B) lines of $Fe_{3-x}Al_xO_4$ with x=0.005 below the Verwey transition.

4.2.2.5. Relaxation times of $Fe_{3-x}Al_xO_4$ below the Verwey transition.

Measurements of Al-substituted magnetite samples below the Verwey transition revealed that the temperature behavior of relaxation times of substituted magnetite is in rough outline similar to that of the pure magnetite (reported first in [Mizo66] and then more carefully in [NovaICF00]), however some significant differences occur. To compare the temperature behavior of relaxations for substituted sample with those for the pure sample the most intensive lines from low-frequency interval (i.e. b1 line), middle- and high –frequency intervals (a1+a2 and b15 lines correspondingly) of $Fe_{3-x}Al_xO_4$ with x=0.005 were chosen. The spin-lattice relaxation time T_1 was determined from the dependence of a maximum of an amplitude for a line in question on repetition time of two-impulse spin echo. Spin-spin relaxation time T_2 was determined from a decrease of spin-echo amplitude in Carr-Purcell echo series. Taken into account that in [Mizo66] the relaxations below the Verwey transition have been measured only

for a1+a2 line and not for b lines, we compared our relaxation data of substituted magnetite with corresponding data of the pure magnetite taken from [NovaICF00], where they are presented for as a- and b-lines below the Verwey transition.

In figures 4.2.9 and 4.2.10 relaxation times T_1 and T_2 for various Al contents are shown.

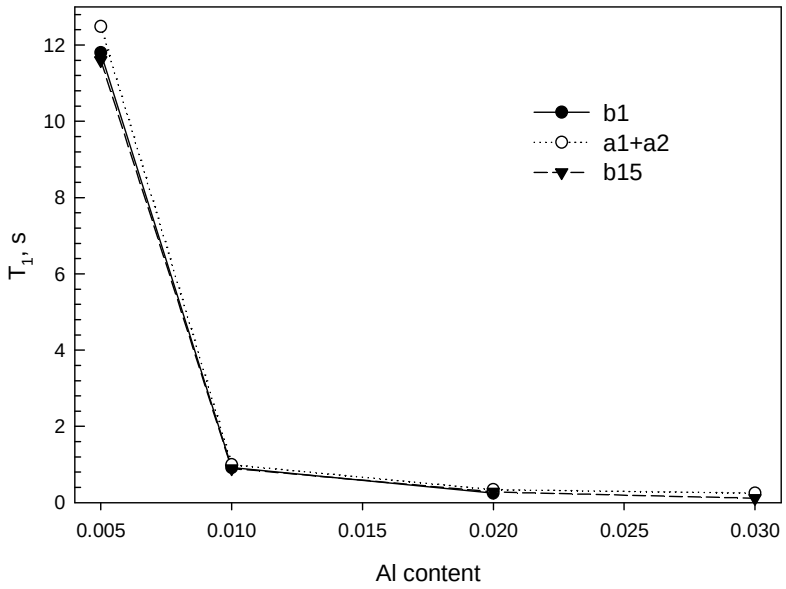

Figure 4.2.9. Spin-lattice (T_1) relaxation times of b1, b15 and a1+a2 lines for Al substituted magnetite samples at T=4.2K. (Lines are to guide eye only).

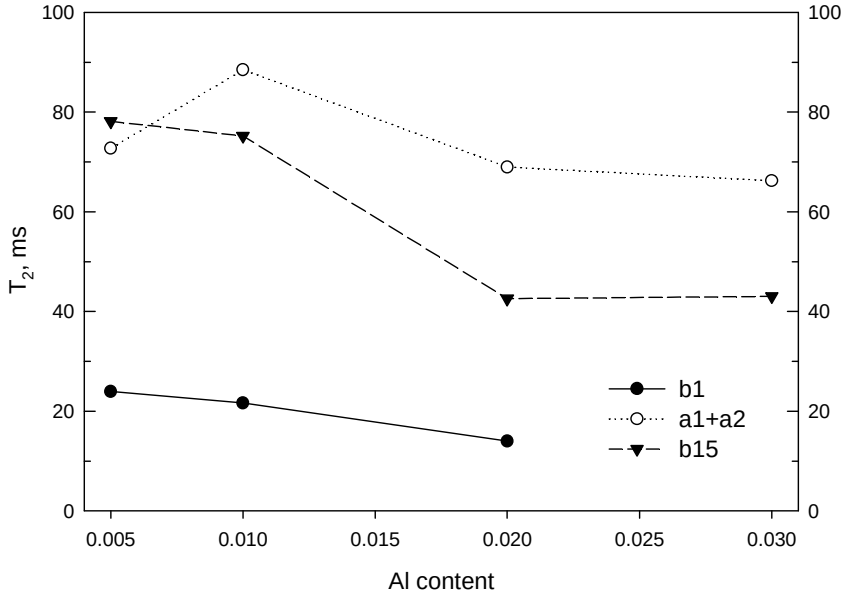

Figure 4.2.10. Spin-spin (T_2) relaxation times of b1, b15 and a1+a2 lines for Al substituted magnetite samples at T=4.2K. (Lines are to guide eye).

The errors of the fitting procedure for T_2 relaxation data do not exceed 7%.

Data of T_1 and T_2 relaxation times at T=4.2K for corresponding lines of pure magnetite reported in [Nova00] and data for aluminum substituted sample with x=0.005 are collected in the table 4.2.3.

Line	T_1(s) , x=0	T_1(s) , x=0.005	T_2(ms), x=0	T_2(ms), x=0.005
B1	6.6	11.8	59.2	23.9
B15	6.5	11.6	220.9	78.1
A1+A2	7.9	12.5	197	72.7

Table 4.2.3. T_1 and T_2 relaxation times for some lines of pure magnetite [Nova00], and corresponding data for aluminum substituted sample with x=0.005 at 4.2K.

Comparing data for pure and substituted samples in the Table 4.2.3, one can see that the spin-spin relaxation times T_2 for the smallest concentration of impurity (x=0.005) are more than twice lower than those for the pure sample, while the spin-lattice relaxation times T_1 are about twice increased as for A and for B lines compared with the pure sample data.

The effect of increasing Al content at liquid helium temperature revealed itself the most in lowering by more than 10 times of spin-lattice relaxation times T_1 as for A and for B lines (Fig. 4.2.9).

In figures 4.2.11 and 4.2.12 temperature dependences of T_1 relaxation times for a1+a2, b1 and b15 lines of Al substituted magnetite sample with x=0.005 below the Verwey transition are presented. The corresponding temperature dependences of T_1 relaxation times for pure magnetite are displayed in red.

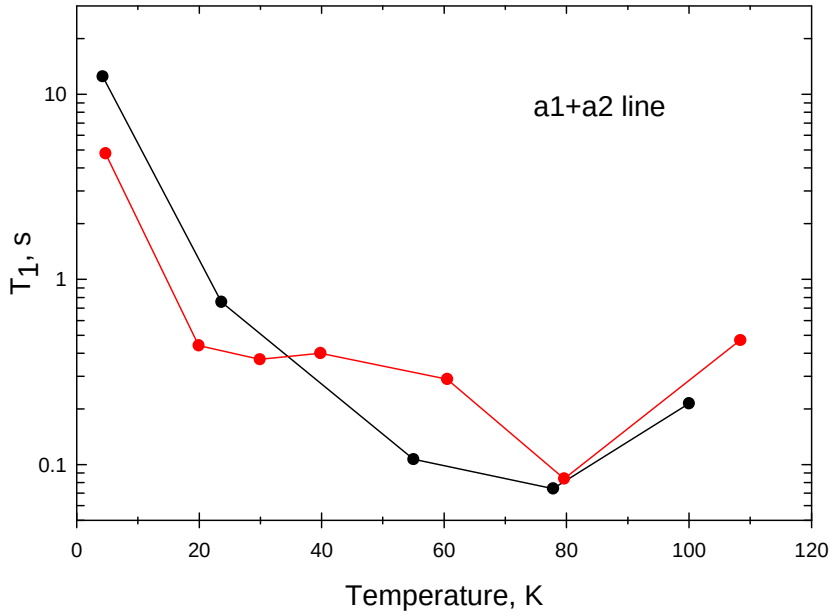

Figure 4.2.11. Temperature dependence of spin-lattice relaxation time for a1+a2 line below the Verwey transition for $Fe_{3-x}Al_xO_4$ with x=0.005. Temperature dependence for the line of pure magnetite is shown in red [NovaICF00].

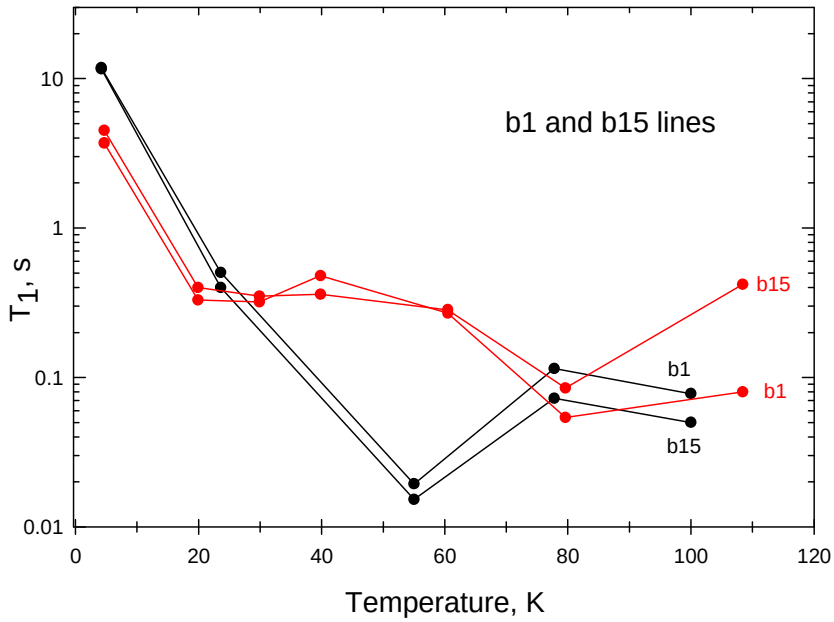

Figure 4.2.12. Temperature dependences of spin-lattice relaxation times for b1 and b15 lines below the Verwey transition for $Fe_{3-x}Al_xO_4$ with x=0.005. Temperature dependences for the same lines of pure magnetite are shown in red.

Comparing data of pure and substituted magnetite, one can see a noticeable difference in behavior of T_1 relaxations of a1+a2 and b-lines of the substituted sample. The main difference in temperature behavior as for A and for B lines is observed in the temperature interval 30K - 80K where T_1 relaxations of A and B lines have a tendency to be faster (especially relaxations of b-lines) than those of the pure sample. For the B-lines the minima of the relaxations are shifted to lower temperatures. Another significant change in relaxation behavior can be noticed for B lines above 80K where T_1 relaxations decrease instead of increasing ones for the pure sample. In addition, T_1 relaxation times of A and B ions of substituted samples below 20K are approximately twice more than ones of the pure sample reported in [NovaICF00].

In figures 4.2.13 and 4.2.14 temperature dependences of T_2 relaxation times for a1+a2, b1 and b15 lines below the Verwey transition are presented. The corresponding temperature dependences of T_2 relaxation times for pure magnetite are displayed in red.

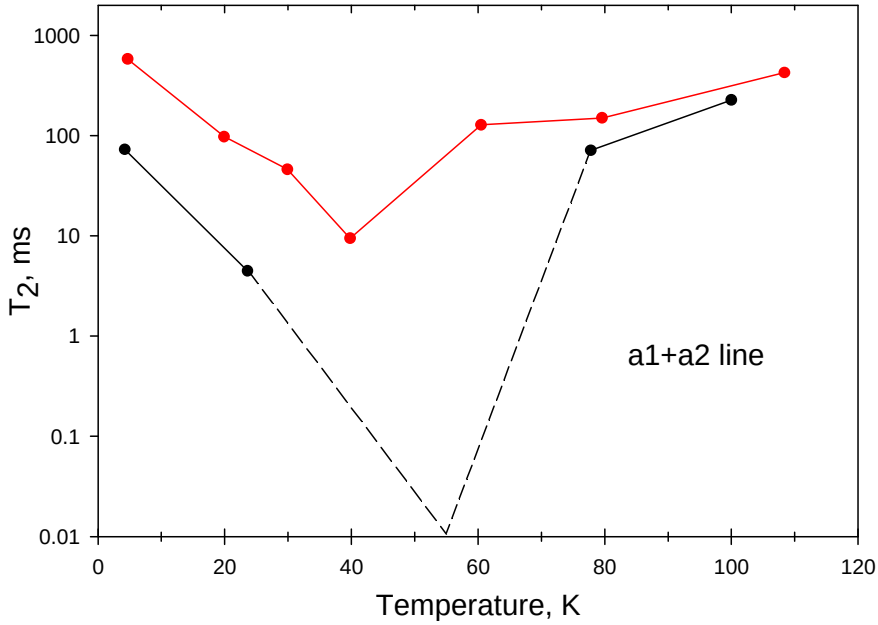

Figure 4.2.13. Temperature dependence of spin-spin relaxation time for a1+a2 line below the Verwey transition for $Fe_{3-x}Al_xO_4$ with x=0.005. Temperature dependence for the line of pure magnetite is shown in red.

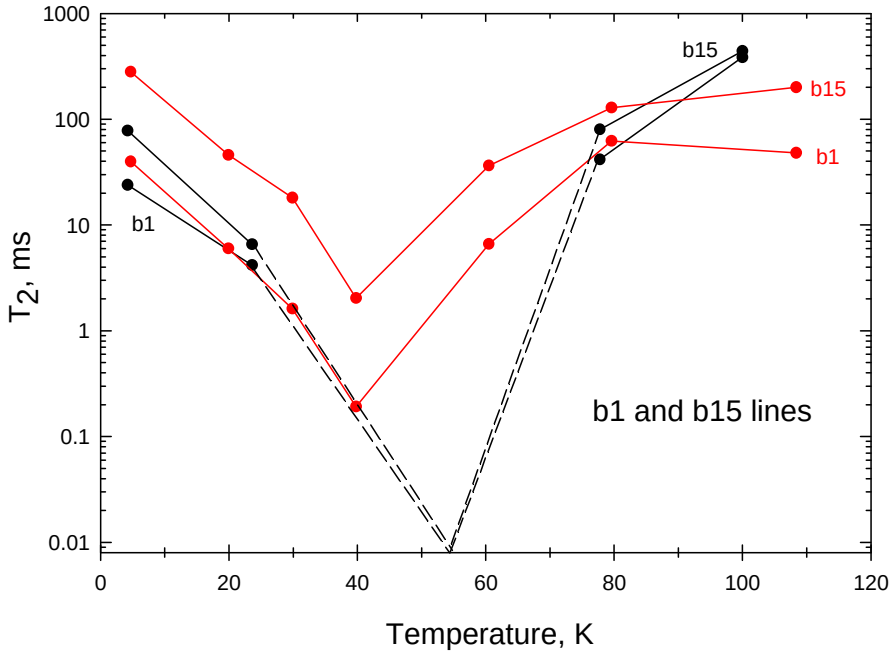

Figure 4.2.14. Temperature dependences of spin-spin relaxation times for b1 and b15 lines below the Verwey transition for $Fe_{3-x}Al_xO_4$ with x=0.005. Temperature dependences for the same lines of pure magnetite are shown in red [NovaICF00].

At 55K it was too fast for the lines to be measured for change of their amplitudes in Carr-Purcell sequence, so their T_2-relaxations could not be determined with any accuracy. In fact, T_2-relaxation times around 55K are ≤0.01ms that is the lowest value we can reliably measure. As a consequence, most of B-lines are not resolved in this temperature region. That is why it is not possible to study thoroughly temperature region around that temperature, as it was done for the pure magnetite.

From figures 4.2.13 and 4.2.14 one can see that the presence of Al impurity intensifies processes leading to minima of T_2 relaxations. As in the case of spin-lattice relaxation times T_1, the spin-spin relaxations are much faster in the temperature region of approximately 30-80 K. In addition, as in the case of T_1 relaxations, there is a difference in behavior of T_2 relaxation times for B lines above 80K: they increase more intensively than those of the pure sample. In the low temperature region T_2 relaxations of A line are by an order of magnitude lower than those of the pure sample, while relaxations of B lines remain comparable to the pure sample relaxations.

Taking into account that our measurements of NMR spectra have revealed that the smallest Al concentration we have studied (x=0.005) gives only a small effect on the electronic structure of magnetite below the Verwey transition, one can accept that the estimations of main contributions to relaxation mechanisms performed for pure magnetite in [Mizo66] could be applied in outline to this substituted sample too.

The relaxation mechanisms of ^{57}Fe which has the nuclear spin I=1/2 can be solely attributed to the fluctuations of the local magnetic fields. The behaviour of the temperature dependences of T_1 and T_2 relaxations in pure magnetite [Mizo66] was in outline explained semi-quantitatively by the effect of the electron migration in B sites. There were pointed out two possible relaxation mechanisms for the nuclear spin on tetrahedral A site due to the electron migration in B sites. The first mechanism arises through the dipolar interaction of the nuclear spin with the migrating electrons, and the second mechanism - through the hyperfine interaction of the A ion modulated via the A-B exchange coupling. On this basis, the minima in temperature behavior of T_1 and T_2 relaxations of ^{57}Fe in tetrahedral (A) positions for pure magnetite below the Verwey transition were explained.

It was estimated in [Mizo66] that the relaxation mechanism through the dipolar interaction is more significant at T<80K, while the relaxation through the hyperfine interaction modulated via A-B-exchange was estimated to be significant at T>80K and is not negligible in this temperature region compared with that from the dipolar interaction.

The relaxation of the nuclear spin on B site was suggested to be arisen mainly from the direct fluctuation of the hyperfine field caused by the own electronic spins (due to the electron migration).

The magnon contribution to the relaxation mechanism was found to be insignificant in temperature range about 77-300 K compared to the electron migration. However, below 20K the low frequency excitations due to the mixing of magnons and phonons contributions were mentioned to become important for the nuclear relaxation processes [Mizo66].

The introduction of Al substitution into magnetite sublattice can lead to different effects on relaxation times and their temperature behaviour. However, finding out the quantitative contributions of those effects is still unfeasible. Nevertheless, one can point out some reasons of possible effects on the magnetite relaxation times under Al substitution. The low temperature structure of magnetite below the Verwey transition is monoclinic. Considerable lattice deformations are expected to arise upon continued Al doping into B sublattice, since the radii of participating ions differ noticeably: $r(Fe^{2+})$=0.77Å, $r(Fe^{3+})$=0.645Å, $r(Al^{3+})$=0.535Å [Shan76].

As a possible consequence of a local stress reduction accompanied by a redistribution of energy affecting the nuclear spin system, additional effects on relaxation times of substituted magnetite are expected. From the point of view of the lattice mobility, which is important at low temperatures, the introduction of Al impurity could lead to the increase of a phonon frequency, and as a consequence to a possible influence on an average lifetime of nuclei in the higher energy states, i.e. to additional influence on T_1 relaxation times with increasing Al content at liquid helium temperature.

Concerning the influence of defects on the relaxation processes and their temperature dependences, it is interesting to mention the comparative results of numerous studies of pure magnetite by the Magnetic After-Effect (MAE) spectroscopy [Walz02] presented in the next Fig.4.2.15. The comparison of MAE results with the results of other experimental methods went Walz and coworkers to make following conclusions on the temperature dependence of electron transport mechanisms in pure magnetite.

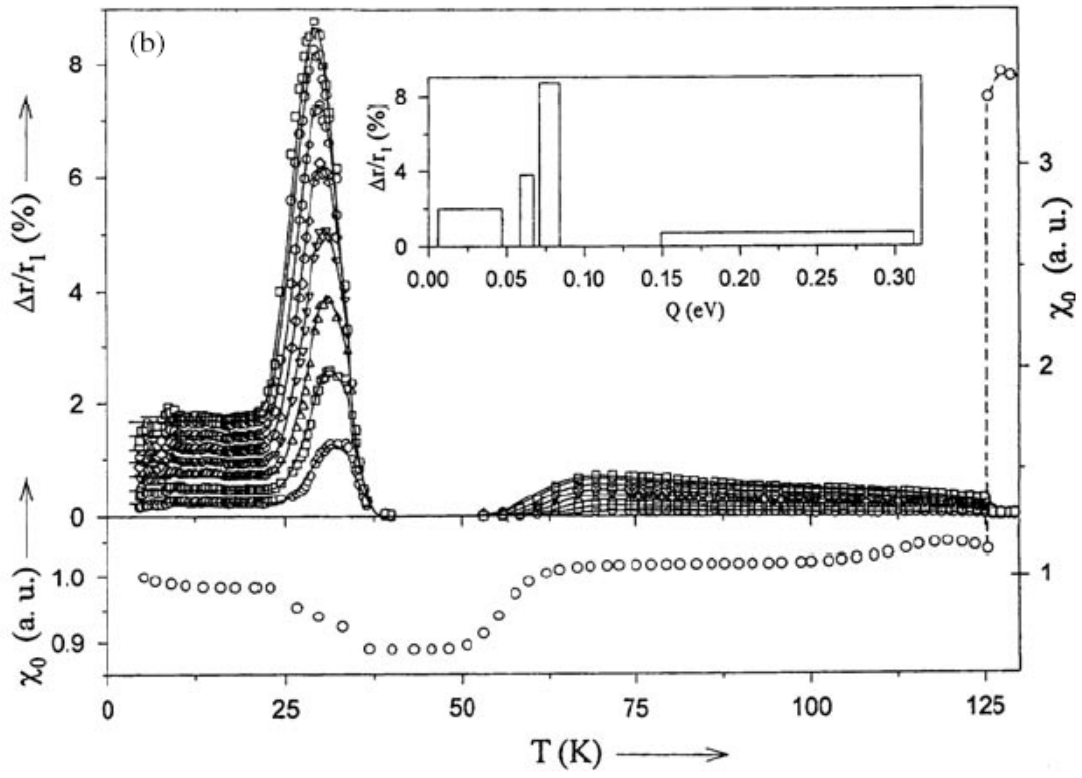

Figure 4.2.15. Low-temperature MAE spectrum of perfect (BRA-type) single-crystalline magnetite, as reported in [Walz02]. The isochronal relaxation of the initial reluctivity, *r(t)*, was measured—beginning at *t*1 = 1s after sample demagnetization—over the times *t*2 = 2

s*(1)*, 4 s(2), 8 s(3), 16 s(4), 32 s(5), 64 s(6), 128 s(7), 180 s(8) and plotted in the form $\Delta r/r(t1) = [r(t2) - r(t1)]/r(t1)$ [Walz02]; the initial permeability $\mu 0$, like $\mu(t)$, depends on the susceptibility, $\chi(t)$, and the reluctivity, $r(t)$ via: $\mu - 1 \sqcup \chi = 1/r$ (SI-system). The inset shows the energy distributions of participating processes—as determined from numerical fitting (continuous curves) of the experimental data (symbols).

The spectrum of pure magnetite is composed of three parts [Walz02]:

(1) a low-temperature plateau, already activated below T= 4.2 K and culminating into a pronounced relaxation peak near 30 K; (2) a second, similar plateau-like relaxation extending between 50 K < T < T_V (≈125 K), being separated from the former one by (3) a distinct relaxation-free gap located between 35 K < T < 50 K. Of these processes, the two plateaus have been associated with different mechanisms of electron transfer, i.e. (1a) interatomic, *incoherent* electron tunneling (T < 25 K), (1b) intra-atomic electron excitation within the crystal-field split levels (30 K); (2) thermally activated small-polaron hopping (50 K < T < 125 K); (3) the gap between the two relaxation plateaus marks a temperature span within which thermal activation, on the one hand, is intense enough to equilibrate the low-temperature processes prior to minimum observation time of MAE (t < 1 s) but, on the other hand, is still too weak to initiate the second, higher-temperature plateau process. In other words, the occurrence of a relaxation gap between 35 and 50 K was explained as a result of a suppression of band motion due to the destruction of the periodic lattice potential by thermal phonons [Walz82]. It is also known from numerous experiments on differently impurity-charged magnetite poly- and single crystals ([Walz03] and cited references within), that the electronic tunneling processes, which are expected to be significant at 4K < T < 35 K due to formation by small polarons of narrow bands of temperature-dependent width [Walz02], are strongly affected by the smallest deviations from stoichiometry, and at doping rates of x≤0.05 are nearly completely suppressed. Corresponding observations have been made after doping with Ba^{2+}, Mn^{2+}, Ni^{2+}, Co^{2+}, Mg^{2+}, Zn^{2+}, Ga^{3+}, Ti^{4+}, and in the presence of B-site (octahedral) vacancies [Kron74], [Walz82], as described and referred to in [Walz03]. The suppression of the electron tunneling in Al-substituted magnetite at temperatures below 35 K would lead to the increase of an average lifetime of nuclei in higher energy states and in fact to the increase of T_1 relaxation times on both A and B sites below 35K with respect to the pure magnetite relaxations. This situation could be a possible explanation of

somewhat higher values and the corresponding temperature behaviour of our relaxation data presented in figures 4.2.11 and 4.2.12 below 35K.

In contrast to the electronic tunneling processes, variable-range electron hopping – which is believed to occur typically in the temperature interval 50K < T < 125 K in pure magnetite [Walz02] – proves to be more resistant against various types of lattice perturbations [Walz03], thus remaining observable up to somewhat higher doping rates. For Al substituted magnetite, that would mean smaller differences in relaxations with those of the pure magnetite above 80K. Considering our data, it could especially work for T_1 and T_2 relaxations of a1+a2 line above 80K (Fig.4.2.11 and 4.2.13). The corresponding data of T_1 and T_2 relaxations of B-sited nuclei (Fig. 4.2.12 and 4.2.14) also show undoubtedly close to pure magnetite values at temperatures above 80K, changing somewhat in the vicinity of the Verwey transition which occurs for this sample at T<120K.

The values of the minima of T_1 and T_2 relaxations in pure magnetite were estimated in [Mizo66] in satisfactorily agreement with the experiment, assuming the presence of 2% disorder in the B sites at 80K (for the explanation of T_1 relaxation minimum), and correspondingly assuming the presence of 0.1% disorder in the B sites at 40K (for the explanation of T_2 relaxation minimum) for a1+a2 line. The mentioned disorders were intended to be caused by the electron migration in B sites. In this outline, our data showing much deeper minima of T_2 relaxations would assume larger disorder in the B sites within 30-80K. It would assume the intensification of adiabatic as well as non-adiabatic relaxation processes (see chapter 2.5) in this temperature region.

4.2.3. ^{57}Fe NMR of Al^{3+} substituted magnetite above the Verwey transition.

As was mentioned, above T_V the crystal structure of magnetite is cubic, close to this temperature, the easy direction of magnetization is [001], which changes to [111] at the spin-reorientation transition. In pure Fe_3O_4 this transition occurs at $T_{SR} \approx 130$ K. For M□[001] all Fe ions on octahedral (B) sites are magnetically equivalent, giving rise to a single Fe (B) NMR line. Above T_{SR} there are two magnetically inequivalent B sites: for sites B1, the axis of local trigonal distortion is parallel to the magnetization, while for sites B2, trigonal distortion and magnetization point along different body diagonals. There are thus two Fe (B) NMR lines with

the intensity ratio B1:B2=1:3. All tetrahedral (A) sites are magnetically equivalent both for M□[001] and M□[111], hence a single A line exists in the NMR spectrum for all temperatures above T_V.

The modification of the electronic structure of magnetite by Al substitution above the Verwey transition was studied on three $Fe_{3-x}Al_xO_4$ (x = 0; 0.005, 0.03) single crystals. They were investigated in the temperature range of T≈120-340 K. The measurements were carried out at zero external magnetic field. The high RF power was used in order to excite the signal from the nuclei in domains only.

4.2.3.1. ^{57}Fe NMR spectra of Al^{3+} substituted magnetite above the Verwey transition.

In fig.4.2.15 ^{57}Fe NMR spectra for three studied compounds, taken at temperatures close to 240K (well above the Verwey transition) are displayed.

In the present case, only for Fe (A) ions with an Al (B) nearest neighbor, the modification of B_{hf} is strong enough to yield the resolved satellite lines. As an example, in the spectra of x= 0.005 and x= 0.03 compounds the satellite lines are clearly seen, their amplitudes increase with the nominal concentration of Al. Symmetry analysis of this situation shows that the A line has two satellites with an amplitude ratio 1:2 for M□[001] ($T_V < T < T_{SR}$), while for M□[111] ($T > T_{SR}$) three satellite lines exist in the ratio 1:1:2 (see table 4.2.1).

As in the case of NMR spectra of Al substituted magnetite below the Verwey transition, Al doping leads to broadening of main (and satellite) lines. The difference of the spectra of x= 0.005 crystal and the pure magnetite is small, indicating that Al doping at low concentration has only a small effect on the electronic structure of magnetite. Eventual larger differences, which might exist close to T_V, are obscured by the presence of the spin-reorientation transition, what can be seen in fig.4.2.16 for x=0.005 compound. Close to this transition (T_{SR}≈128K), the lines are additionally broadened and considerable information is lost, in particular, the satellites caused by Al are no longer resolved. However, for the x=0.005 compound, the satellites reappear below T_{SR}.

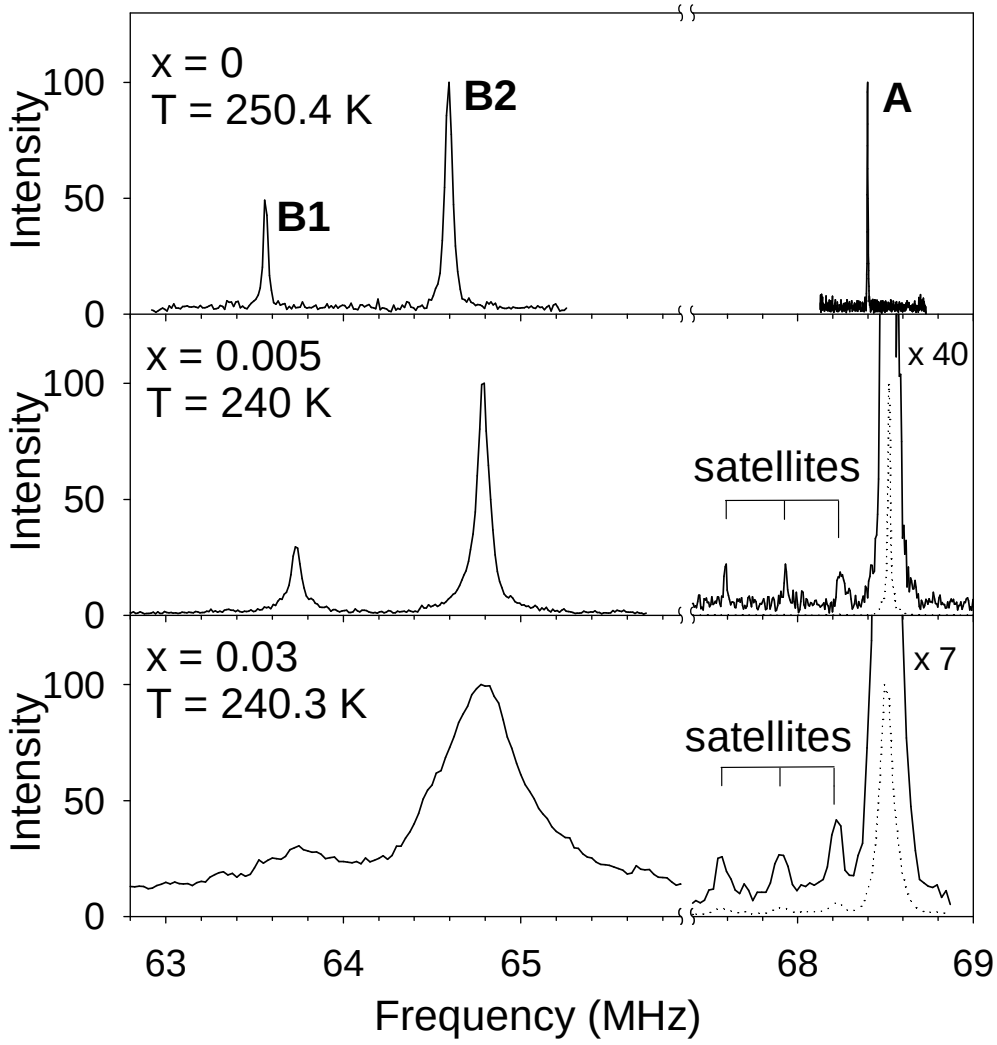

Figure 4.2.15. ^{57}Fe NMR spectra of Fe_3O_4 (T = 250.4 K), $Fe_{2.995}Al_{0.005}O_4$ (T j= 240 K) and $Fe_{2.97}Al_{0.03}O_4$ (T = 240.3 K) single crystals.

In agreement with the symmetry analysis, two satellites below T_{SR} and three satellites above T_{SR} to the left of A line are clearly resolved.

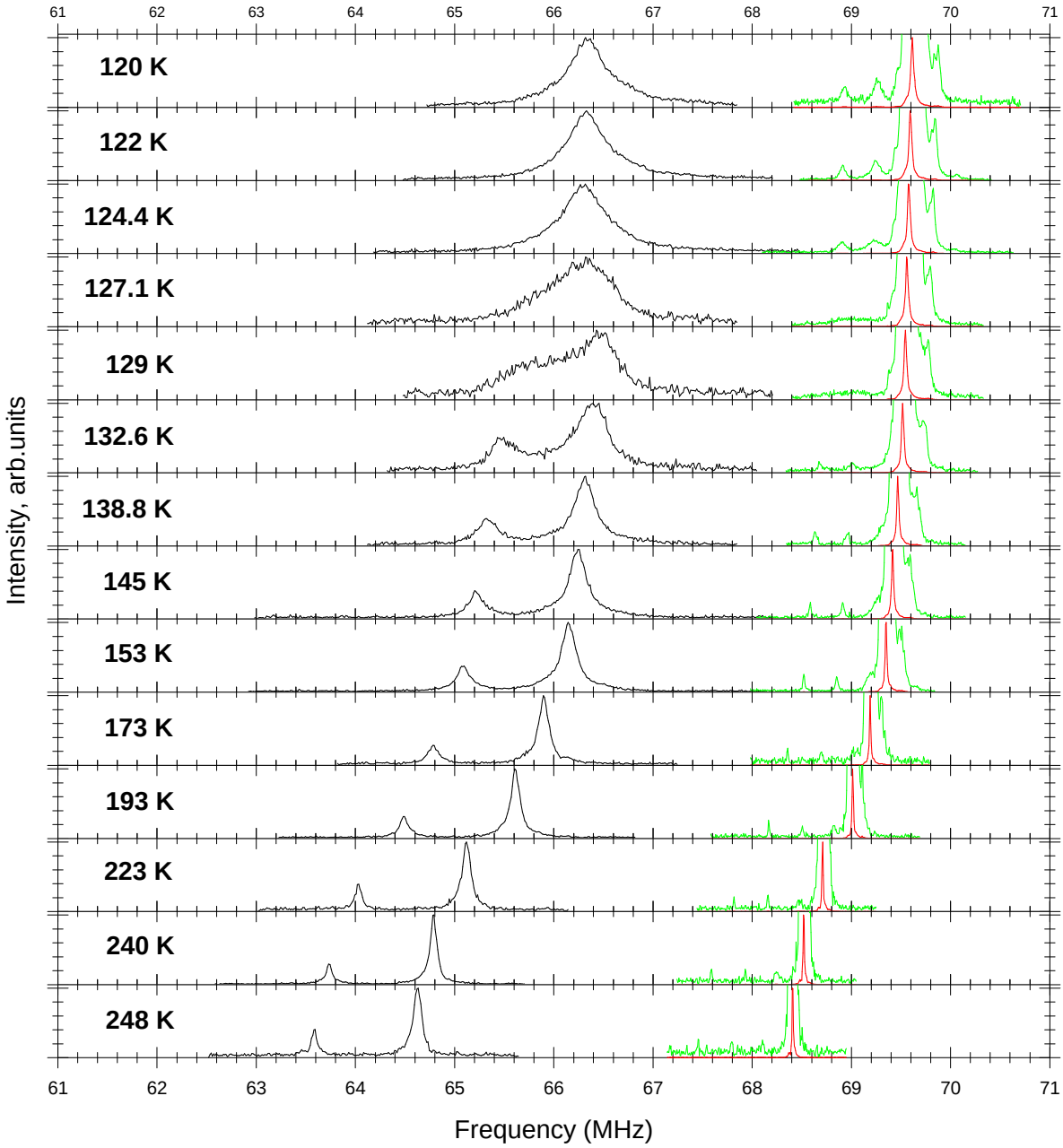

Figure 4.2.16. ^{57}NMR spectra of Al substituted magnetite with x=0.005, measured at different temperatures above the Verwey transition with specific attention to the region of the spin-reorientation transition T_{SR}≈128K. Black curves display octahedral (B) lines, red curves – tetrahedral (A) lines, green curves display magnified tetrahedral lines and satellites.

These results have been published [Gama02].

4.2.3.2. Temperature behavior of resonance frequencies of main and satellite lines above the Verwey transition.

The temperature dependences of NMR frequencies of the main and corresponding satellite lines of tetrahedral Fe^{3+} ions for pure and substituted samples are shown in fig. 4.2.17.

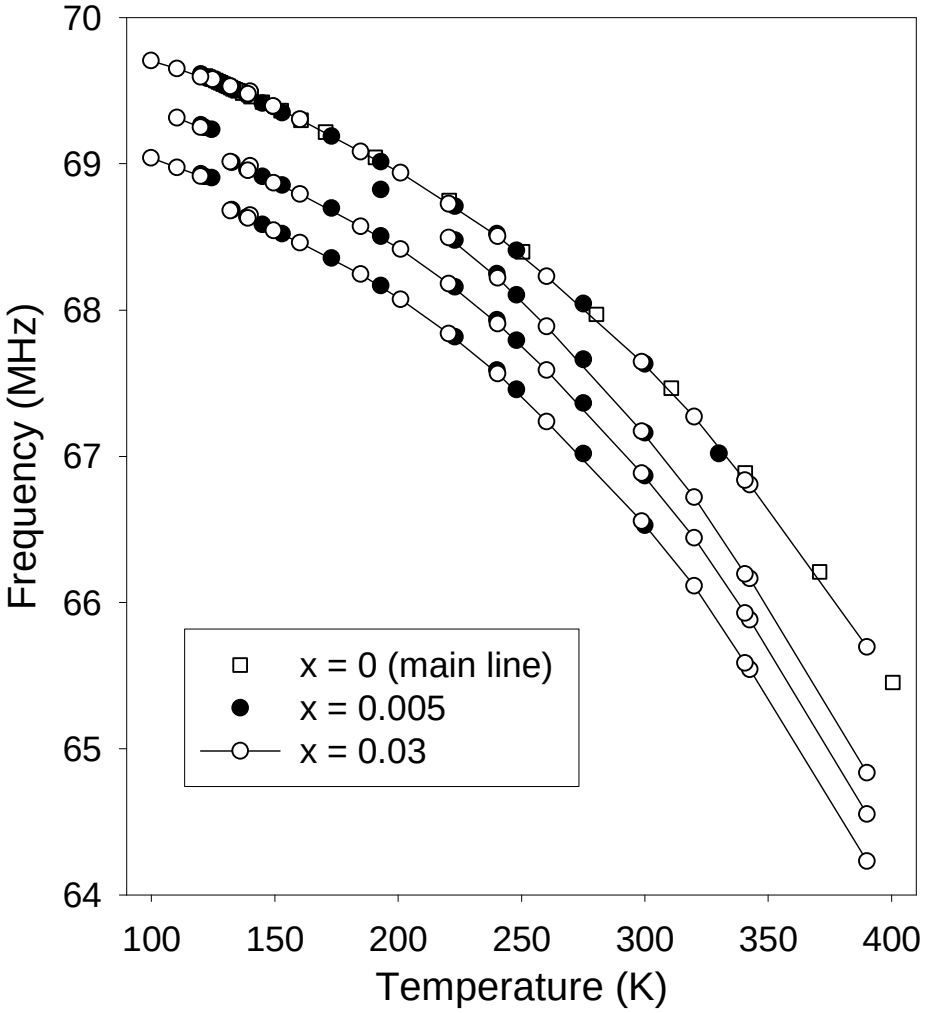

Figure 4.2.17. Temperature dependence of the resonance frequencies of the main line and satellite lines of tetrahedral Fe^{3+} ions for $Fe_{3-x}Al_xO_4$ with x=0; 0.005 and 0.03 above the Verwey transition. The line with the highest frequency corresponds to Fe (A) with only Fe-nearest neighbors on the B sublattice. Remaining lines are satellites (one Fe substituted by Al).

The decrease of the resonance frequencies of the satellite lines with increasing T is slightly faster compared to the corresponding main line. This is expected, as for the Fe (A) with a nearest Al neighbor, one of the Fe (A)–oxygen–Fe (B) superexchange interactions is missing (there are 12 such interactions in an ideal environment).

The next figure 4.2.18 presents temperature dependence of NMR frequencies for octahedral B lines above the Verwey transition. As in the case of tetrahedral lines, one can see no difference in temperature dependencies of the frequencies of octahedral lines for pure and substituted samples, i.e. aluminum content up to x=0.03 does not affect the temperature behavior of NMR frequencies of the main lines of magnetite.

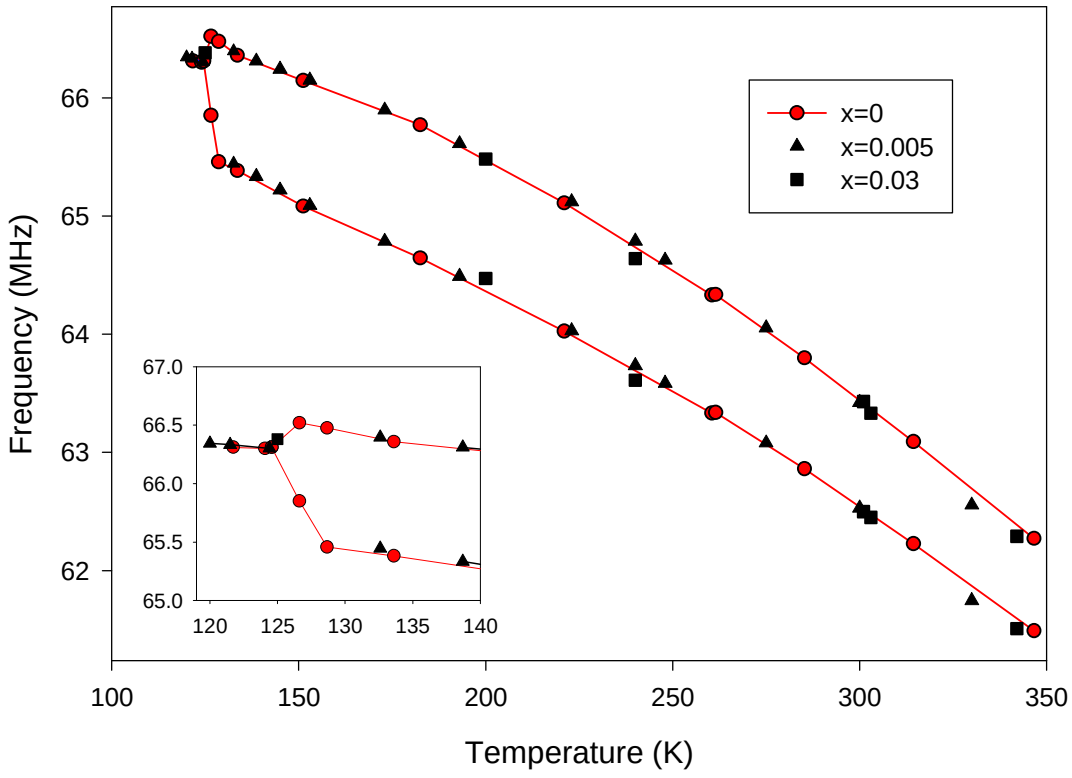

Figure 4.2.18. Temperature dependence of the resonance frequencies of the main lines of octahedral (B) iron ions for $Fe_{3-x}Al_xO_4$ with x=0; 0.005 and 0.03 above the Verwey transition.

As a result of unchanged temperature dependences of NMR frequencies of B_1 and B_2 lines, the temperature behavior of the splitting δ of the lines is not affected by the aluminum substitutions too. Under the splitting δ one understands a difference in the frequencies of the lines, as is shown in the figure 4.2.19 on the spectrum of pure magnetite.

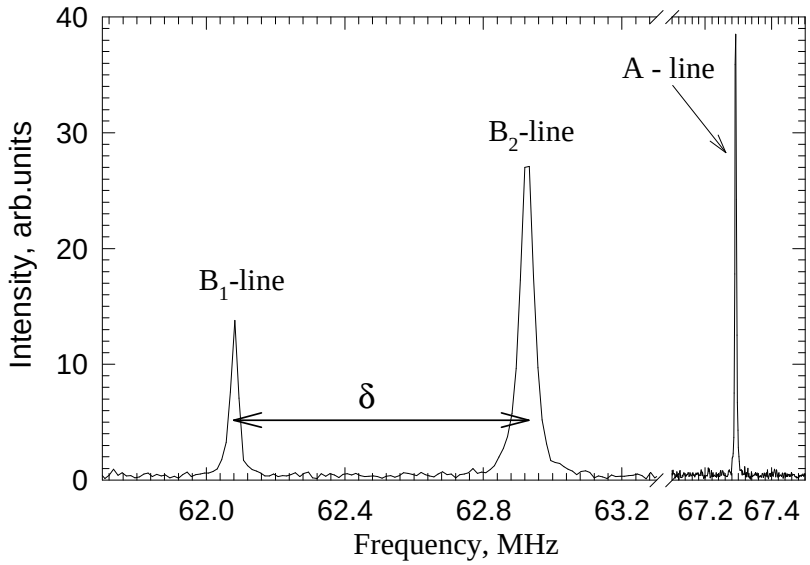

Figure 4.2.19. NMR spectrum of pure magnetite at T=320K. The splitting δ is shown as a difference of the frequencies of the B-lines maxima.

In the next figure 4.2.20 the temperature dependence of the splitting δ between B_1 and B_2 lines above the Verwey transition for pure and substituted samples is presented.

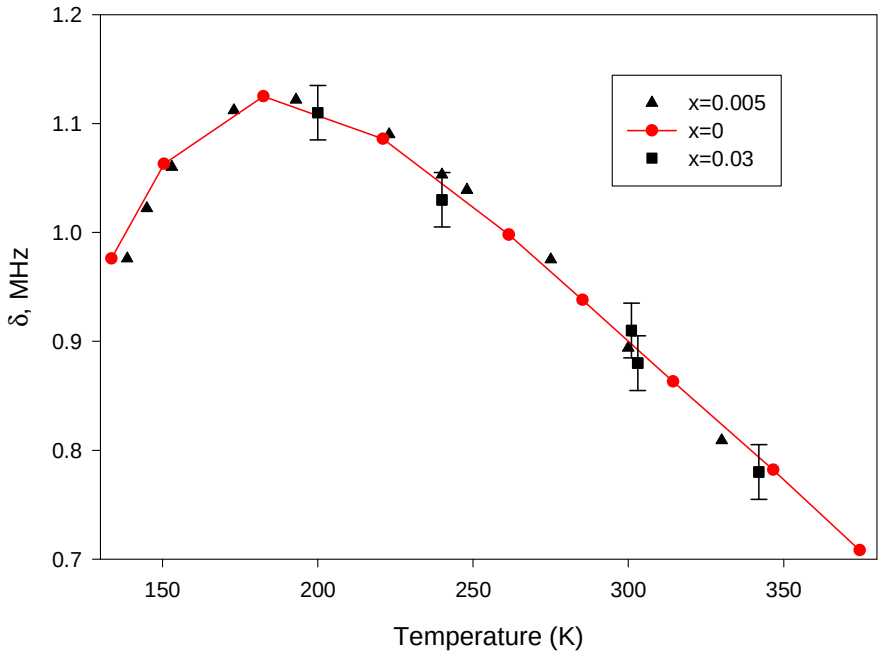

Figure 4.2.20. Temperature dependence of the splitting δ of pure and substituted magnetite above the Verwey transition.

The splitting δ between B-lines reflects the anisotropy of the hyperfine field, which depends on the angle between magnetization and the local trigonal axis. The splitting δ first increases with increasing temperature, attains its maximum at about 180K and then monotonically decreases.

The values of hyperfine fields calculated from the present measurements at T=240K for A and B main lines and for satellite lines are: $B_{hf}(B_1)$=46.22T, $B_{hf}(B_2)$=46.98T, $B_{hf}(A)$=49.68T, $B_{hf}(s_1)$=49.00T, $B_{hf}(s_2)$=49.25T, $B_{hf}(s_3)$=49.49T. The temperature was chosen at which all three satellites are well resolved in spectra (see fig. 4.2.16). The hyperfine fields deduced from the measurements are in agreement with those obtained by DeGrave et al. [DeGra93] from the results of Mossbauer experiments.

The results on temperature behaviour of the resonance frequencies of the main line and satellite lines of tetrahedral Fe^{3+} ions for $Fe_{3-x}Al_xO_4$ with x=0; 0.005 and 0.03 above the Verwey transition have been published [Gama02].

4.2.3.3. Temperature dependence of linewidths of resonance lines above the Verwey transition. Dependence on Al content.

Temperature dependences of the halfwidths Δ of A and B resonance lines taken at a half of their amplitudes are displayed in fig. 4.2.21 for pure and substituted samples.

In a broad interval of temperatures, the Δ(T) dependence is flat. The linewidths for x=0.005 are slightly larger compared to x=0. The linewidths of x=0.03 crystal are considerably larger compared with x=0 and x=0.005 crystals. Moreover, they are much stronger temperature-dependent at temperatures above the spin-reorientation transition and their values cannot be explained by the anisotropy of the hyperfine field, provided that the anisotropy is similar as in compounds with lower content of Al. The most likely scenario is that with lowering of the temperature, the electron density in x=0.03 compound becomes inhomogeneous, leading to a broader distribution of the hyperfine fields.

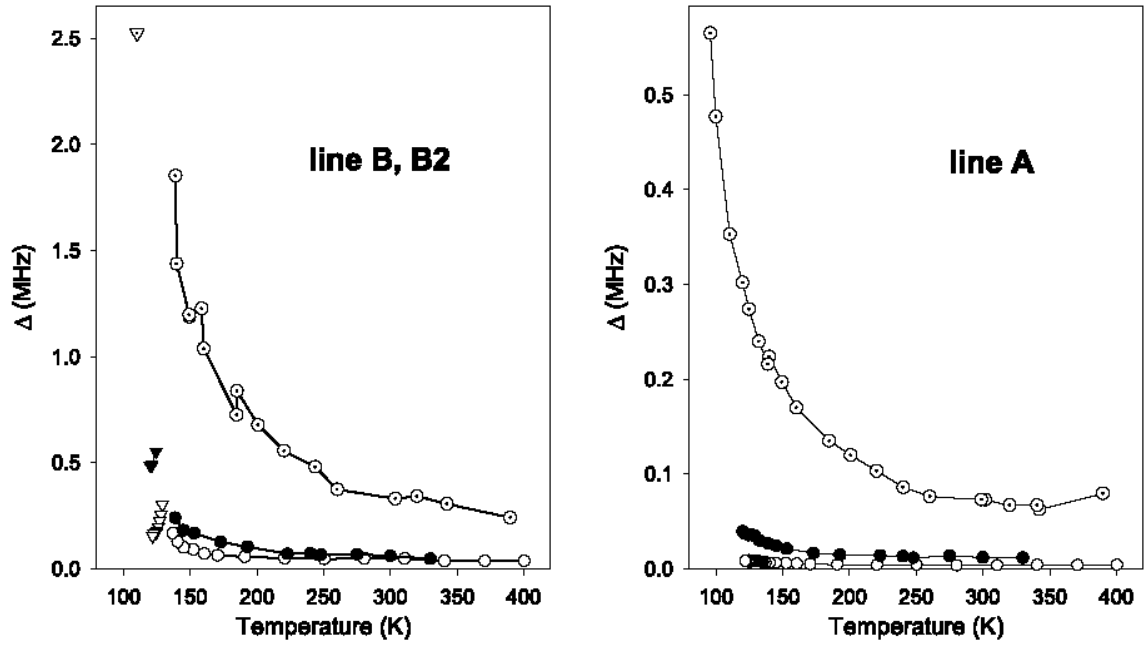

Figure 4.2.21. $Fe_{3-x}Al_xO_4$. Temperature dependences of the widths Δ of the resonance lines taken at a half of their amplitudes for $Fe_{3-x}Al_xO_4$ with x=0; 0.005 and 0.03. Triangles and circles for B sites correspond to temperatures below and above the spin-reorientation transition, respectively. Dotted symbols correspond to the Al concentration x=0.03; full symbols to x=0.005 and open symbols to x=0.

These results have been published [Gama02].

4.2.4. NMR of ^{57}Fe, ^{69}Ga and ^{71}Ga in Ga substituted magnetite.

The influence of Ga substitution is very interesting with regard to its trivalent state. It was surprising that substitution of Ga lowers T_V much weaker than trivalent Al substitution, for example. This fact was explained by the assumption that Al^{3+} ions occupy preferentially B sites while Ga^{3+} ions enter preferentially A-sites (paragraph 3.2.3 for details).

The aim of this paragraph is to present NMR results obtained in the Ga substituted magnetite.

The single crystal $Fe_{3-x}Ga_xO_4$, x=0.05 used in the present study has been prepared by a floating zone technique. NMR spectra have been measured by the spin-echo method using the

phase-coherent spectrometer with an averaging technique and the Fourier transformation. The measurement have been performed at zero external magnetic field and temperature T = 4.2K, 77K and 273K. Attention has been paid to adjustment of the radiofrequency power in order to excite the signal of the nuclei within the magnetic domains only. In the whole temperature region the signal-to-noise ratio has been significantly improved by using the Carr-Purcell pulse sequence.

The NMR spectrum measured in our gallium substituted sample at 273 K, well above the Verwey temperature, is shown in Fig.4.2.22. Comparing with the spectra of the pure sample [Nova00] one can unambiguously resolve the ^{57}Fe NMR lines of A-, B_1-, and B_2-sites. For additional two lines at 70.78 MHz and 55.74 MHz one can calculate the frequency ratio f_{70} / $f_{55} \cong 1.27$. This value exactly corresponds to the ratio of γ-factors of both Ga isotopes: $^{71}\gamma$ / $^{69}\gamma \cong$ 1.27. In addition, taking into account that the ratio of the line amplitudes agrees with the ratio of natural isotopic abundance of both isotopes, we have assigned those lines to ^{71}Ga and ^{69}Ga in tetrahedral A sites. The weak broadening of both lines could be explained by a quadrupolar interaction caused by the local failure of the cubic symmetry of A-sites induced by the Ga substitution. The small satellite S_1 at 62.1 MHz corresponds to the iron resonance in B_1 site in the nearest vicinity of which one A-sited iron was replaced by Ga. This interpretation is similar to the spectra interpretation used in gallium substituted YIG [Step98]. Since no other lines of comparable intensities were found, we can conclude that in our sample Ga ions are predominantly located at *a* sites. Additional detailed measurements in the vicinity of A main line with high data accumulation revealed very weak satellite pattern corresponding to the small amount of Ga ions in *b* sites. The concentration of Ga ions entering B sites has been estimated to be less than 0.006 [Chlan].

The ^{57}Fe NMR spectra measured in Ga substituted sample below the Verwey transition at 77 K and 4.2 K are shown in the Fig.4.2.23. Both spectra are very similar to those measured in the pure magnetite [Nova00ICF]. Slightly lower resolution is due to the general line broadening caused by the small Ga substitution. The shifts of the resonant lines connected with the temperature change agree with the temperature dependence of resonant lines of the pure magnetite sample [Nova00ICF].

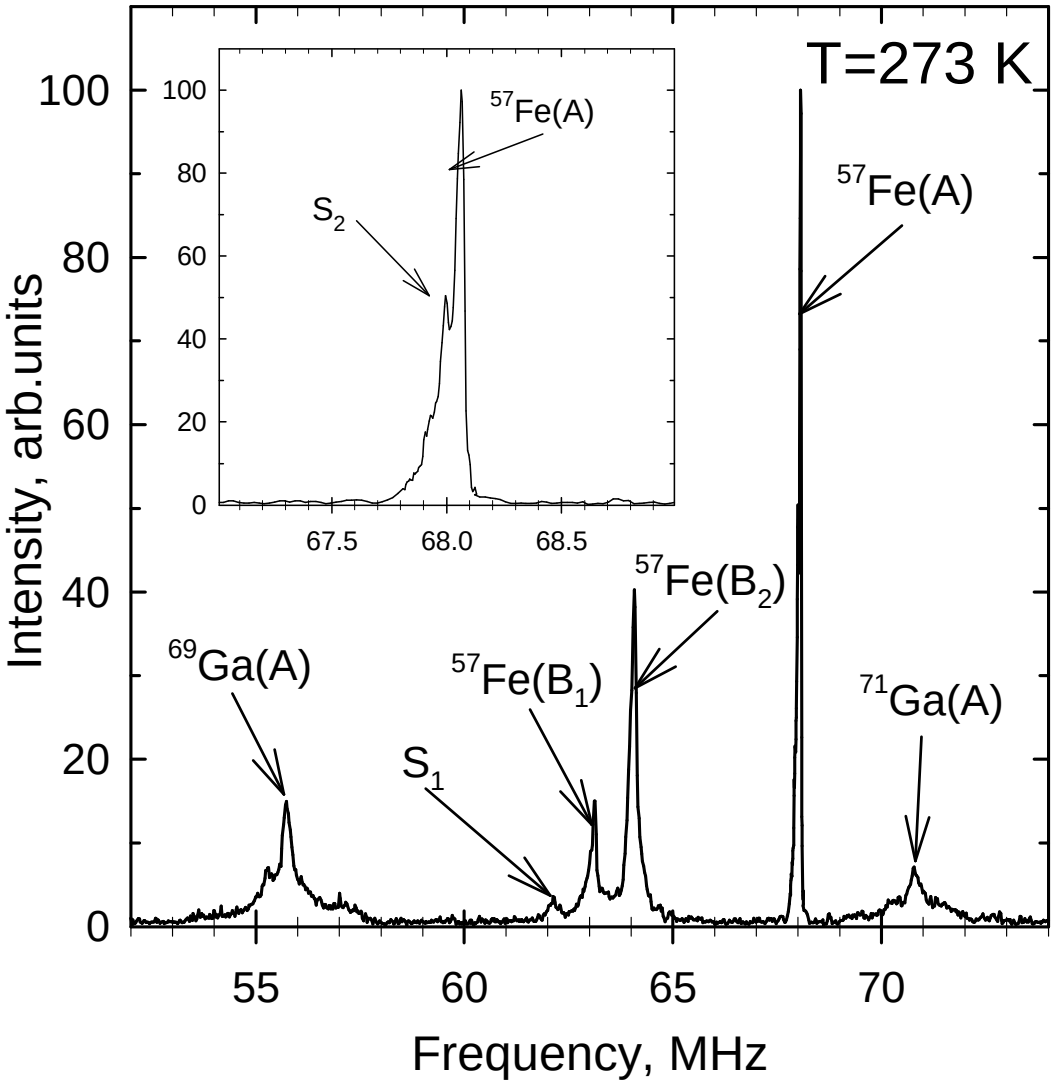

Figure 4.2.22. The ^{69}Ga, ^{71}Ga and ^{57}Fe NMR spectra of the single crystal $Fe_{3-x}Ga_xO_4$, x=0.05 measured at 273 K.

NMR spectra of Ga measured at 77K and 4.2K are shown in the Fig.4.2.24. The line structures in the middle part of the spectra (68-74 MHz) and at the lower frequency side (49-51 MHz) are created by signals of both Ga and Fe nuclei (compare with Fig.4.2.23.). The spectra displayed in Figure 4.2.24 have been measured over the whole region with the rf power optimised for the Ga domain signal excitation. This rf power was considerably lower than the

power needed for the ^{57}Fe domain signal excitation used for obtaining spectra shown in Fig.4.2.23.

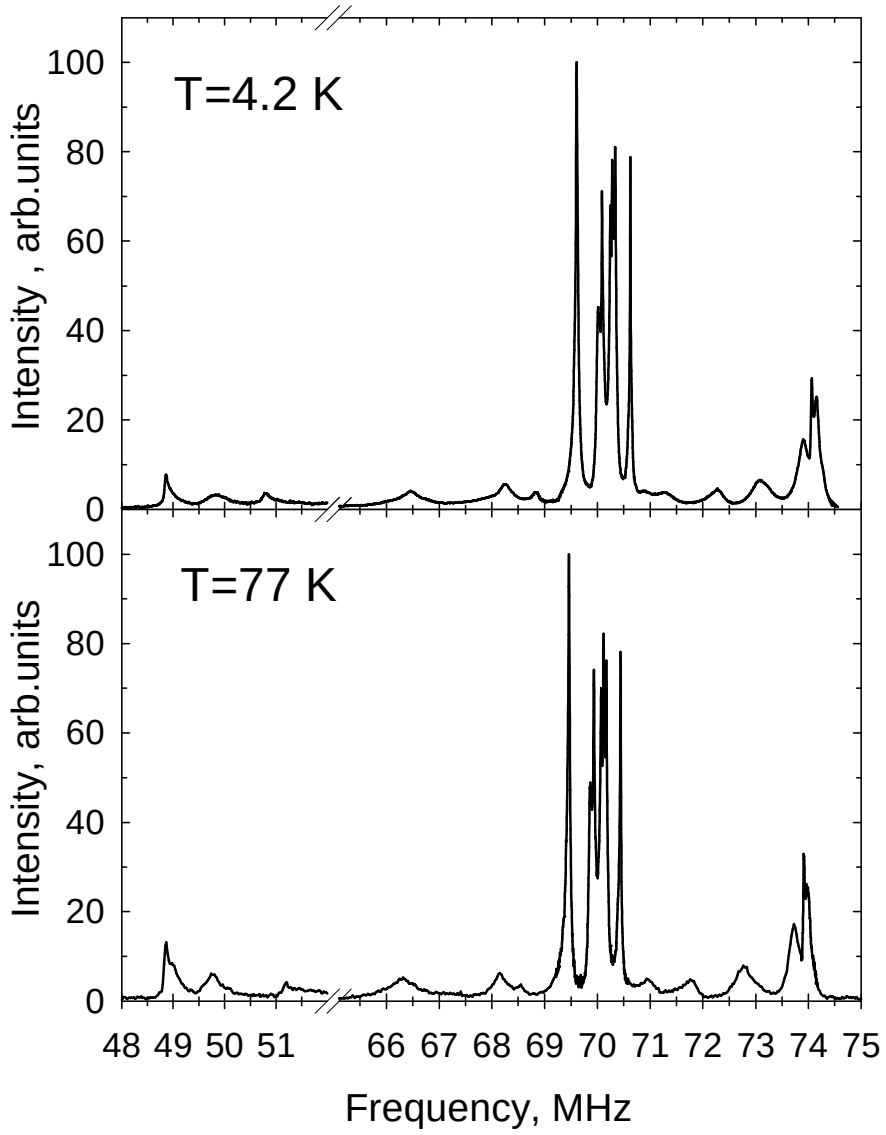

Figure 4.2.23. The ^{57}Fe NMR spectra of the single crystal $Fe_{3-x}Ga_xO_4$, x=0.05 measured at 4.2K and 77K.

As a result, the domain wall signal of iron could be admixed in the above mentioned spectral regions in Fig.4.2.24 with no possibility of its detailed interpretation.

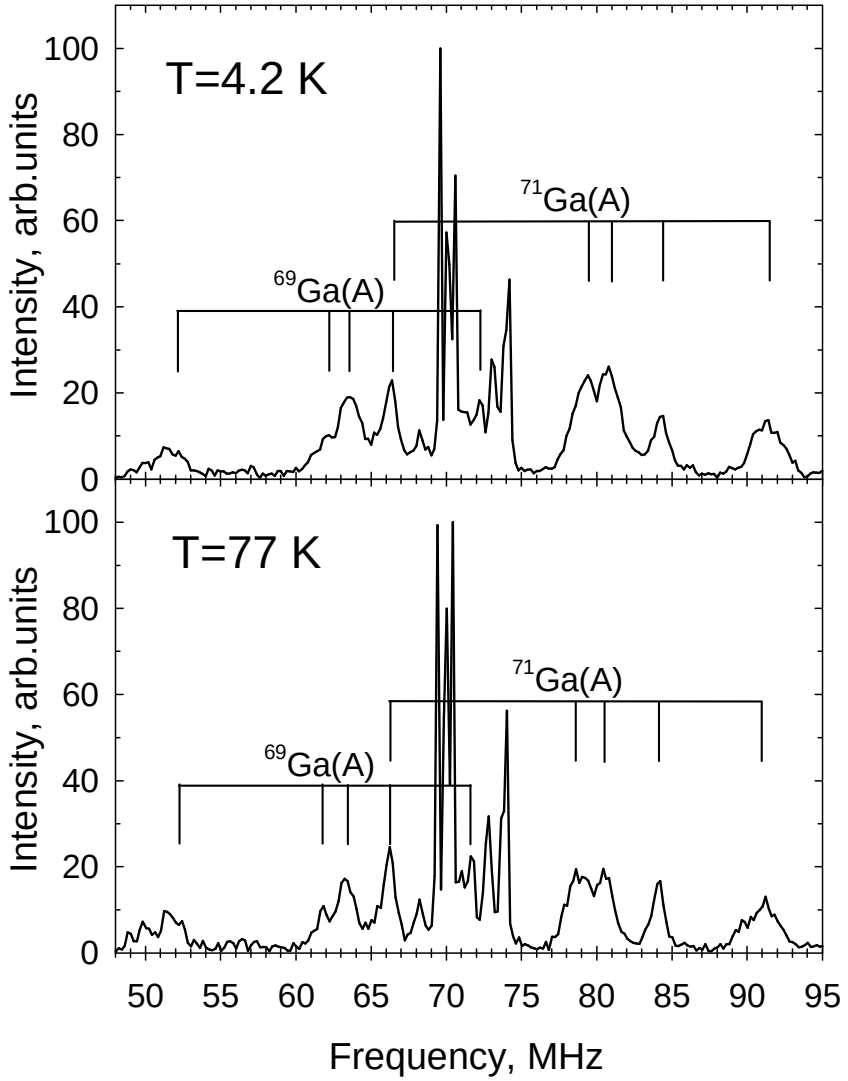

Figure 4.2.24. The ^{69}Ga, ^{71}Ga NMR spectra of the single crystal $Fe_{3-x}Ga_xO_4$, x=0.05 measured at 4.2K and 77 K.

Remaining lines in the Fig.4.2.24 have been most likely induced by Ga nuclei. One can easily identify two groups of those lines (see Fig.4.2.24) connected by the ratio of γ-factors of two Ga isotopes. The pattern constituted by these lines is very similar to that of iron lines from A-sites in Fig.4.2.23. So it seems that the structure of the Ga spectrum is, similarly to the iron spectrum, created by the differences of the local A-sites surroundings below the Verwey temperature. The quadrupolar interaction contributes to line widths only.

These results have been published [Koho05].

4.2.5. Conclusions on studied magnetites.

The study of the influence of substitutions in different crystallographic positions on the hyperfine field in magnetite was carried out on Al and Ga substituted magnetites. The difference in the influence of the substitutions on the Verwey temperature of magnetite was previously explained by the assumption that Al^{3+} ions occupy preferentially B crystallographic positions (octahedral sites) of magnetite while Ga^{3+} ions occupy preferentially A positions (tetrahedral sites) [Brab98]. The series of Al substituted magnetite samples $Fe_{3-x}Al_xO_4$ with Al contents x=0.005, 0.01, 0.02 and 0.03 were measured below and above the Verwey transition in the temperature range $4.2 \leq T \leq 340$ K. Single crystal of Ga substituted magnetite $Fe_{3-x}Ga_xO_4$ with gallium content x=0.05 has been measured at temperatures 4.2, 77 and 273 K. The results of the study can be summarized as follows:

The measurements of aluminum substituted magnetite $Fe_{3-x}Al_xO_4$ with Al contents x=0.005, 0.01, 0.02 and 0.03 below the Verwey transition in the temperature region $4.2K \leq T < T_V$ revealed the following results:

1. Al content up to x=0.03 does not affect positions of the resonance lines (both A and B types) of magnetite at T=4.2K and their temperature dependences below the Verwey transition temperature T_V.

2. In the whole temperature interval studied, the differences of the spectra of x=0.005 crystal and the pure magnetite were found to be small, indicating that Al in the low concentration has only a small effect on the electronic structure of magnetite below the Verwey transition.

3. The resonance lines of substituted samples are broadened at T=4.2K and the broadening increases with increasing Al content. New weak spectral lines within the broad frequency range 35-48 MHz have been observed in all Al substituted spectra at T=4.2K. The lines broaden with increasing Al content. Their origin is not cleared out at the moment.

4. Because of the systematic and significant line broadening and the superimposed A and B spectra, the satellites of A lines caused by Al defects in the nearest B positions are not resolved up to x=0.03.

5. There was not observed systematic or significant change in the temperature behavior of linewidths of B lines below the Verwey transition for Al content x=0.005. However, nearest neighbor B lines have the similar temperature behavior of their linewidths. The line a1+a2 does not change its linewidth at $T<T_V$ as for the case of pure magnetite.

6. Concerning NMR relaxations in Al substituted magnetite, the effect of increasing Al content revealed itself the most in lowering by an order of magnitude of the spin-lattice relaxation times T_1 at T=4.2K as for A and for B lines. The spin-spin relaxation times T_2 for the smallest concentration of impurity (x=0.005) are more than twice lower than those for the pure sample, while the spin-lattice relaxation times T_1 are about twice increased as for A and for B lines compared with the pure sample data.

7. A noticeable difference was observed in the temperature behavior of T_1 and T_2 relaxations of the substituted sample with x=0.005 below the Verwey transition with respect to the pure magnetite. T_1 relaxations of substituted sample at T<20K were twice longer than ones of pure magnetite, while T_2 relaxations were found to be faster than those of the pure magnetite within the same temperature region. As T_1 and T_2 relaxations of the substituted sample within ≈30-80K were observed to be much faster than those of the pure sample. Minimum of T_2 relaxations of A positioned iron ions is at least by 3 orders of magnitude lower than for the pure sample, while the minimum of T_1 relaxation of the same ions is twice lower than for the pure magnetite. Concerning B-positioned iron ions, their both T_1 and T_2 relaxations are at least by an order of magnitude faster than ones of the pure magnetite. In the temperature region from ≈80K up to T_V both T_1 and T_2 relaxations of A-line did not change noticeably, while for B lines both T_1 and T_2 relaxation times somewhat change their temperature behavior compared with the pure sample**.** The estimations of main contributions to relaxation mechanisms performed

earlier for pure magnetite could be applied to the substituted sample with x=0.005 too, because our measurements have revealed that this Al concentration has only a small effect on the electronic structure of magnetite below the Verwey transition. The possible reasons of main differences in temperature behaviour of relaxations of pure and Al substituted samples were pointed out comparing presented data with other experimental results and estimations.

8. The Verwey temperatures of substituted samples were observed to decrease with increasing Al content in agreement with recent reports.

The measurements of aluminum substituted magnetite $Fe_{3-x}Al_xO_4$ with Al contents x=0.005 and 0.03 above the Verwey transition in the temperature region $T_V<T\leq340K$ revealed the following results:

1. Satellite lines of Fe(A) resonance line caused by Al defect in one of the nearest B positions were observed in NMR spectra of substituted samples as below the spin-reorientation transition as above the one up to T≈330K.

2. In the whole interval of temperatures studied, the differences of the spectra of x=0.005 crystal and the pure magnetite were observed to be small, indicating that Al in the low concentration has only a small effect on the electronic structure of magnetite above the Verwey transition.

3. Al content up to x=0.03 did not affect the positions and the temperature behavior of both A- and B-type lines above the Verwey transition up to T=340K.

4. The temperature behavior of satellite lines within the mentioned temperature interval was found to be slightly faster compared to the corresponding main line. This was explained in terms of one missing Fe(A)-O-Fe(B) superexchange interaction caused by the nearest neighbor Al defect in B position.

5. The resonance lines of substituted samples are broadened compared to the pure magnetite above the Verwey transition and the broadening increases with increasing Al content.

6. Close to the spin reorientation transition the lines are additionally broadened and as a consequence the satellites caused by Al are no longer resolved. However, for x=0.005 compound the satellites reappear below T_{SR}.

7. In a broad temperature interval above the Verwey transition the temperature dependence of linewidths is flat. The linewidths of crystal with aluminum content x=0.03 are considerably larger and have much stronger temperature dependence, than linewidths of sample with x=0.005 at temperatures far above the spin-reorientation transition. Their values cannot be explained by the anisotropy of the hyperfine field, providing this anisotropy is similar as in compounds with lower content of Al. The most likely scenario is that with lowering of the temperature the electron density in x=0.03 compounds becomes inhomogeneous, leading to a broader distribution of the hyperfine fields.

The measurements of gallium substituted magnetite $Fe_{3-x}Ga_xO_4$ with Ga content x=0.05 at temperatures 4.2, 77 and 273 K revealed the following results:

1. NMR spectrum of gallium substituted magnetite above the Verwey temperature (T_V~117K) has indicated the preferential presence of Ga substitution in tetrahedral A sites. The concentration of Ga ions entering B sites has been estimated to be less than 0.006 (paragraph 4.2.4). These results together with those obtained for Al substituted magnetite support the assumption of the stronger effect of Al substitution on the Verwey transition because Al^{3+} ions preferentially occupy octahedral *b* sites while Ga substitution prefers tetrahedral *a* sites.

2. The ^{57}Fe NMR spectra of Ga substituted sample below the Verwey transition at 77 K and 4.2 K have been measured. The shifts of the resonant lines connected with the temperature difference agree with the temperature dependence of resonant lines of the pure magnetite sample.

3. NMR spectra of Ga have been measured below the Verwey temperature at 77K and 4.2K. The spectra have been obtained over the whole region with the rf power optimized for the Ga domain signal excitation. Well-resolved structure of Ga lines has been identified and assigned to both Ga isotopes (^{69}Ga and ^{71}Ga). To the best of our knowledge, the magnetite spectra of both Ga isotopes have not been measured previously. Weak quadrupolar interaction contributes to the line broadening only.

5. Summary

The present thesis is devoted to the studying of hyperfine interactions in magnetic iron oxides, namely YIG and magnetite, by means of Nuclear Magnetic Resonance method. The subject of the thesis is to find out and interpret a response induced by nonmagnetic substitutions (Al^{3+}, In^{3+}, La^{3+}, Ca^{2+}, Bi^{3+}, Ga^{3+}) in NMR spectra and relaxations and to contribute to explanation of the influence of the substitutions on a change of the hyperfine parameters of the systems. The studied substitutions were chosen to enter different cationic sublattices of the systems. In particular, in YIG system: Al^{3+} substitutions occupy tetrahedral (*d*) sites, In^{3+} substitutions enter octahedral (*a*) sites, and La^{3+}, Ca^{2+} and Bi^{3+} substitutions enter dodecahedral (*c*) sites. In magnetite system: Al^{3+} substitutions enter octahedral (*b*) sites, and Ga^{3+} substitutions preferentially enter tetrahedral (*a*) sites, while some small amount of Ga^{3+} goes into octahedral (*b*) sites.

The presence of nonmagnetic substitutions in a system gives rise to a satellite structure in NMR spectra. The origin of the satellite lines lies in the fact that a nonmagnetic substitution in the vicinity of the resonating ^{57}Fe nucleus alters its NMR frequency through the change of the hyperfine field, because when Fe^{3+} ion is substituted by the nonmagnetic one, several $Fe^{3+/2+} – O^{2-} – Fe^{3+/2+}$ superexchange interactions become broken, resulting in the change of the magnetic moment value in the vicinity of the substitution. The concentrations of the substitutions in the systems studied were defined from the ratios of amplitudes of satellites and corresponding parent lines.

In the case of YIG system, 1) an effect of Al substitution on ^{57}Fe hyperfine field anisotropy has been systematically studied by means of NMR measurements in an external magnetic field. Analysis of the data yielded the changes of hyperfine parameters induced by Al (paragraph 4.1.1) and enabled to compare the influences of changes in ionic radii and valencies (Table 4.1.1). 2) Effects of trivalent cation substitutions (Al^{3+}(*d*), In^{3+}(*a*),La^{3+}(*c*) on nuclear magnetic relaxations of ^{57}Fe nuclei have been studied by measurements in zero external magnetic fields. Decrease of spin-lattice and spin-spin (except for the higher In content) relaxation rates with increasing concentrations of substituents has been found (paragraph 4.1.2). 3) Effect of Ca^{2+}(*c*) substitution on ^{57}Fe NMR spectra and relaxations has been studied. After an initial constant region, a decrease of a spin-lattice relaxation rate has been observed with increasing Ca content. The onset of the relaxation rate decrease is supposed to correspond to an

induced decrease of an amount of Fe^{2+} ions, while charge compensation is supposed to be reached by other mechanisms for lower calcium contents (paragraph 4.1.3). 4) Hyperfine interaction at iron nuclei in a bismuth-yttrium iron garnet system $Bi_xY_{3-x}Fe_5O_{12}$ has been studied. In addition, for the first time the spectra of completely substituted bismuth iron garnet (BIG) have been obtained. It was expected according to the X-ray diffraction experiments, that the replacement of Y^{3+} (*c*) by Bi^{3+} would lead to a shortening of Fe-O distances in the tetrahedrons while in octahedrons they would lengthen. In this respect the comparison of iron hyperfine fields in BIG and YIG was interesting since the higher covalence related to shorter interatomic distances is believed to lower resonant frequencies. The found spectral shifts of BIG with respect to YIG revealed, however, just the opposite tendency, indicating a substantial impact of the bismuth electron structure on electron transfer in Fe-O-cation triads (paragraph 4.1.4).

In the case of magnetite system, 1) Symmetry consideration of ^{57}Fe NMR for substituted magnetite has been performed (paragraph 4.2.1). 2) Spectra of Al substituted magnetite below, around and above the Verwey transition have been studied. Below the Verwey temperature, the broadening of the main lines with increasing Al content has been detected, their temperature dependencies have been obtained. The decrease of the Verwey temperature with increasing Al content was found to be in agreement with electric conductivity measurements (paragraphs 4.2.2.1-4.2.2.4) It has been also found that the Al substitution significantly affects the relaxation times of resonating iron nuclei. The possible reasons of differences in temperature behaviour of relaxation times of pure and substituted magnetite have been pointed out comparing presented data with results of other experimental methods and estimations (paragraph 4.2.2.5) Above the Verwey transition, temperature dependences of main and satellite lines of Al substituted magnetite have been systematically studied as well as their behaviour in the vicinity of spin-reorientation transition (paragraphs 4.2.3.1-4.2.3.2) Studying of temperature dependences of linewidths of main resonance lines revealed that for higher Al contents their values cannot be explained by the anisotropy of the hyperfine field. As the most likely scenario it was suggested that the electron density becomes inhomogeneous as $T \rightarrow T_V$ (paragraph 4.2.3.3). 3) The studying of Ga substituted magnetite below and above the Verwey transition temperature (T_V) has revealed a well-resolved structure of Ga lines, assigned to ^{69}Ga and ^{71}Ga isotopes. The Ga lines found as well as ^{57}Fe spectra indicate a preference of Ga substitution for the tetrahedral *a* sites (paragraph 4.2.4). These results on Al and Ga substituted magnetites support the assumption of

stronger effect of Al substitution on the Verwey transition because of the preference of Al substitution for octahedral *b* sites in contrast to Ga substitution.

The results obtained in this thesis present a rich set of information on the behavior of a ferrimagnetic system containing nonmagnetic substitutions. The data collected can be used in future investigations of electronic structure and exchange interactions in magnetic oxides.

References

[Abe76] Abe, K., Miyamoto, Y. & Chikazumi, S., J. Phys. Soc. Japan, 41, 1894–1902, (1976)

[Abra61] A.Abragam, The principles of nuclear magnetism, Oxford Claredon Press (1961)

[Abri68] Abrikosov, A.A., Sov. Phys. JETP, 26, 641-646, (1968)

[Adle68] Adler D., Rev. Mod. Phys. 40, 714 (1968)

[Ande50] P.W.Anderson, Phys.Rev. 79 (1950), 350

[Ande56] Anderson P.W., Phys. Rev. 102 1008 (1956)

[Ande63] P.W.Anderson, Exchange in insulators, in Magnetism I. (ed. by G.Rado, H.Suhl), Academic Press, New York (1963)

[Ande64] E.E.Anderson, Phys.Rev. 134A (1964), 1581

[Anis97] Anisimov V I, Aryasetiawan F and Lichtenstein A.I., J. Phys.: Condens. Matter 9, 767 (1997)

[Arag85] R.Aragon, D.Buttrey, J.P.Shepherd and J.M.Honig, Phys.Rev.B 31,430 (1985)

[Arag88] R.Aragon and J.M.Honig, ibid. 37, 209 (1988)

[Beem68] D. Beeman, P. Pincus, Phys. Rev. 166 (1968) 359

[Belo82] Belov, K.P., Goryaga, A.N., Pronin, V.N. & Skipetrova, L.A., JETP Lett., 36, 146–149 (1982).

[Belo93] Belov, K.P., Physics-Uspekhi, 36, 380–391, (1993).

[Belo94] Belov, K.P., Physics-Uspekhi, 37 (6), 563–575, (1994).

[Belo96] Belov, K.P., JETP, 36, 1152–1155, (1996)

[Bert57] F.Bertaut, F.Forrat, C.R.Acad. Sci., Paris 224, (1957), 96

[Bick49] Bickford, L.R., Phys. Rev., 76, 137–138, (1949).

[Bick50] Bickford, L.R., Phys. Rev., 78, 449–457, (1950).

[Bick57] Bickford, L.R., Brownlow, J.M. & Penoyer, R.F., Proc. I.E.E., B104, 238–244, (1957).

[Bloc30] F.Bloch, Z. Physik 61 (1930), 206

[Bloc46] F.Bloch, Phys. Rev. 70 (1946), 460

[Bloo55] A.L.Bloom, Phys. Rev. 98 (1955), 1105

[Boek72] C.Boekema, van der F.Woude, G.A.Zawatzky, Int. J. magnetism 3 (1972), 341

[Boek86] Boekema C., Lichti R.L., Cham K.C.B., Brabers V.A.M., and others, Phys. Rev.B. 33, 210 (1986)

[Bonn75] M.Bonnet, A.Delapalme, H.Fuess, M.Thomas, Acta Cryst. B31 (1975), 2233

[Brab87] M.Brabenec, J.Englich, M.Rotter, P. Novak, J.Sramek, Czech J. Phys. B37 (1987)

[Brab95] Brabers V.A.M. Progress in spinel ferrite research. Handbook of Magnetic Materials, ed. K.H.J.Buschow, Amsterdam: Elsevier (1995)

[Brab98] V.A.M.Brabers, F.Walz and H.Kronmuller, Phys. Rev. B 58, 21 (1998)

[BrabJ99] Brabers J.H.V.J., Walz F. and Kronmuller H., Physica B 266321 (1999)

[BrabJ99] Brabers J.H.V.J., Walz F. and Kronmuller H., J.Phys.:Condens.Matter 11, 3679 (1999)

[BrabJ00] Brabers J.H.V.J., Walz F. and Kronmuller H., J.Phys.:Condens.Matter 12, 5437 (2000)

[Broe68] Broese van Groenou A, Bongers P.F. and Stuyts A.L., Mater. Sci. Eng. 3, 317 (1968/69)

[Brue88] T.Brueckel et.al., Z.Phys.B 72 (1988), 477

[Camp72] Camphausen D L, Coey J M D and Chakraverty B K, Phys. Rev. Lett. 29 657, (1972)

[Camp92] A.G.Campos, Anwendung der ^{57}Fe Kernspinresonanz zur Bestimmung der platzpraferenz von Bi in epitaktischen YIG: Bi Schichten, KFA Juelich (1992)

[Chai95] A.Chainani, T.Yokoya, T.Morimoto, and T.Takahashi, Phys.Rev. B 51, 17976 (1995)

[Chak74] Chakraverty B K, Solid State Commun. 15 1271, (1974)

[Chlan] V. Chlan, E. Gamaliy, H. Stepankova, K. Kouril, J. Englich, J. Kohout, V. Brabers, JMMM, (in print).

[Cox92] P. A. Cox, Transition Metal Oxides, Oxford University Press, Oxford, 1992.

[Cull70] Cullen J.R. and Callen E., J. Appl. Phys. 41, 879 (1970)

[Cull71] Cullen J.R. and Callen E., Phys. Rev. Lett. 26, 236 (1971)

[Cull73] Cullen J.R. and Callen E.R., Phys. Rev. B 7, 397 (1973)

[Degi87] Degiorgi L, Wachter P and Ihle D, Phys. Rev. B 17, 9259 (1987)

[deGra93] E. DeGrave, R.M. Persoons, R.E. Vandenberghe and P.M.A. de Bakker, Phys. Rev. B 47, 5881 (1993)

[Dehe75] G.Dehe, B.Seidel, K.Melzer and C.Michalk, Phys.Status Solidi (a) 31, 439 (1975)

[Dion70] G.F. Dionne, J. Appl. Phys. 41 (1970), 4874

[Doug60] R.L.Douglas, Phys.Rev. 120 (1960), 1612

[Drab71] Drabble J.R., Whyte T.D., Hooper R.M., Solid State Commun. 9, 275 (1971)

[Elli98] S. R. Elliott, The Physics and Chemistry of Solids, John Wiley & Sons, New York, 1998.

[Engl76] J.Englich, PhD thesis, MFF UK Praha (1976)

[Engl85] J.Englich, M.Brabenec, P.Novak, H.Lutgemeier, J.Magn. Magn. Mater. 50 (1985),74

[Engl94] J.Englich, J.Kohout, P.Novak, H.Lutgemeier, IEEE Transaction on Magnetics 30, 972 (1994)

[Engl96] J.Englich, J.Kohout, H.Stepankova, P.Novak, M.Nekvasil, H.Lutgemeier, J. de Phys. Coll. (1996)

[Engl98] J.Englich, P. Novak, H.Lutgemeier, Int. J. of Mod. Phys. B v.12, (1998), 609

[Escu75] P.Escudier, Ann.Phys. (Paris) 9 (1975), 125

[Eule65] F.Euler, J.A. Bruce, Acta Cryst. 19 (1965), 971

[Flet74] Fletcher, E.J. & O'Reilly, W., J. Phys. C, 7, 171–178, (1974).

[Fuji90] T. Fujii, M. Takano, R. Katano, Y. Bando, Y. Isozumi, and T. Okuda, J. Magn. Magn. Mater. 92, 261 (1990)

[Gama02] E.Gamaliy, H.Stepankova, J.Englich, J.Kohout, A.Snezhko, P.Novak, V.A.M.Brabers, J. of Magn. Magn. Mat. 242-245, 732-734 (2002).

[Gama02-1] E. Gamaliy, H. Stepankova, J. Kohout, A. Snezhko, M. Kucera, K. Nitsch, JMMM, 242–245 (2002) 766–768

[Gama02-2] E.Gamaliy, A. Snezhko, H. Stepankova, M. Kucera, K. Nitsch, JMMM, 242–245 (2002), 769–771

[Garc01] J.Garcia, G.Subias, M.G.Proietti, J.Blasco, H.Renevier, J.L.Hodeau, and Y.Joly, Phys. Rev. B 63, 054110 (2001)

[Gasp00] Gasparov L V, Tanner D B, Romero D B, Berger H, Margaritondo G. and Forro L., Phys. Rev. B 62, 7939 (2000)

[Gell57] S.Geller, M.A.Gilleo, J. Phys. Chem. Solids 3 (1957), 30

[Gell64] S.Geller, H.J.Williams, G.P.Espinosa, R.C.Saerwood, Bell Syst. Tech. J. 43 (1964), 565

[Gell74] S. Geller and A. A. Colville, AIP Conference Proceedings No 24, Magnetism and Magnetic Materials 1974, New York 1975 (p. 372)

[Gill83] B.Gillot and F.Jemmali, Phys.Status Solidi A 72, 339 (1983)

[Genn61] P.-G. de Gennes, F. Hartman-Boutron, C. R. Acad. Sci. 253 (1961) 2922.

[Ghos71] S.K. Ghosh, Phys. Rev. B 5 (1971) 174.

[Gona67] R.Gonano, E.Hunt, H.Meyer, Phys.Rev. v.156 (1967), 521

[Grid96] Gridin, V.V., Hearne, G.R. & Honig, J.M., Phys. Rev. B, 53, 15 518–15 521, (1996)

[Gupt02] Gupta, R., et al., Phys. Rev. B, 65, 104430, (2002)

[Hans74] P.Hansen, J. Appl. Phys. 45 (1974), 3638

[Haub61] Haubenreisser W, Phys. Status Solidi 1 619, (1961)

[Harr63] A.Harris, Phys.Rev. 132 (1963), 2398

[Haus76] S.Haussuhl, D.Mateika, W.Tolksdorf, Z. Naturforschg. 31a (1976), 390

[Honi82] Honig J.M., J.Solid State Chem. 45, 1 (1982)

[Honi95] Honig J.M.J., Alloys Compounds 229, 24 (1995)

[Huan04] Huang, D.J. et al., Phys. Rev. Lett. 93, 7, (2004)

[Ihle83] Ihle D. and Lorenz B., Phys. Status Solidi B 116, 539 (1983)

[Ihle86] Ihle D. and Lorenz B., J. Phys. C: Solid State Phys. 19, 5239 (1986)

[Iida76] Iida S., Mizushima K., Mada J., Umemura S., Nakao K. and Yoshida J. AIP Conf.Proc. vol.29, p.388 (1976)

[Iizu82] Iizumi M., Koetzle T.F. and Shirane G. Acta Crystallogr. B 38, 2121 (1982)

[Jeng04] Jeng H.-T., et al, Phys. Rev. Lett. 93, 15 (2004)

[Kako89] Kakol Z., Sabol J., Stickler J., Honig J.M., Phys. Rev. B 46,1975 (1992)

[Kako91] Kakol, Z., Sabol, J. & Honig, J.M., Phys. Rev. B, 44, 2198–2204, (1991).

[Kaku79] Kakudate Y and Mori N, J. Magn. Magn. Mater. 12, 22 (1979)

[Kita79] Kita E., Siratori K., Kohn K., Tasaki A., Kimura S. and Shindo I., J.Phys.Soc.Japan 47, 1788 (1979)

[Koho96] J.Kohout, PhD thesis, MFF UK Praha (1996)

[Koho97] J. Kohout, H. Stepankova, J. Englich, P. Novak, H.Lutgemeier, J. de Phys. IV (France) 7 (1997) C1–449.

[Koho99] J. Kohout, H. Stepankova, J. Englich, P. Novak, M.Kucera, K. Nitsch, H. de Gronckel, J. Magn. Magn. Mater.196–197 (1999) 415.

[Koho00] J. Kohout, H. Stepankova, J. Englich, P. Novak, M.Kucera, K. Nitsch, Acta Phys. Polon. A 97 (2000) 519

[Koho04] J.Kohout, E.Gamaliy, H.Stepankova, J.Englich, P.Novak, V.A.M.Brabers, J.Magn.Magn.Mat. 272-276 e1687-e1688 (2004)

[Koho05] J. Kohout, E. Gamaliy, H. Stepankova, J. Englich, V. Prochazka, V. Chlan, V.A.M. Brabers, JMMM, 290–291 (2005) 1018–1020

[Kovt73] N.M.Kovtun and A.A.Shemyakov, Solid State Commun. 13, 1345 (1973)

[Kozl96] A.Kozlowski, P.Metcalf, Z.Kakol and J.M.Honig, Phys.Rev.B 53, 22 (1996)

[Kram34] H.A.Kramers, Physica 1 (1934), 182

[Kron74] H. Kronmuller et al., Phys. Status Solidi a 24, 487 (1974)

[Krup69] S.Krupichka, Fyzika feritu a pribuznich magnetickych kyslicniku, Academia Praha (1969)

[Lach69] E.de Lacheisserie, J.L.Dorman, Phys. Stat. Sol. 35 (1969), 925

[Leng84] Lenge N., Kronmuller H., Walz F., J.Phys.Soc.Japan 53, 1406 (1984)

[Levi66] H.J.Levinstein, E.M.Gyorgy, R.C.Le Craw, J.Appl. Phys. 37 (1966), 2197

[Li51] Yin-Yuan Li, Phys. Rev. 84 (1951), 721

[Lore75] Lorenz B and Ihle D, Phys. Status Solidi b 69 451, (1975)

[Mads05] Madsen G.K.H., Novak P., Europhysics Letters 69(5) 777-783, (2005)

[Maso81] T.Q.Mason and H.K.Bowen, J.Am.Ceram.Soc. 64, 86 (1981)

[Mats77] Matsui, M., Todo, S. & Chikazumi, S., J. Phys. Soc. Japan, 43, 47–53, (1977)

[Mill29] Millar R.W., J. Am. Chem. Soc., 51, 215-222, (1929)

[Miya71] Myiahara Y., Takajo S, J Phys Soc. Japan 31, 942, (1971)

[Miya72] Y.Miyahara, J.Phys.Soc.Jpn. 32, 629 (1972)

[Mizo66] T.Mizoguchi, M.Inoue, J.Phys.Soc.Japan 21, 1310 (1966)

[Mizo78] Mizoguchi M., J.Phys.Soc.Japan 44, 1501 (1978)

[Mizo78] Mizoguchi M., J.Phys.Soc.Japan 44, 1512 (1978)

[Mizo00] Mizoguchi M., J.Phys.Soc.Japan 69, 1298 (2000)

[Mott74] N.F.Mott, Metal-Insulator Transitions, Taylor&Francis, London (1974)

[Mott90] Mott N.F. Metal-Insulator Transitions 2nd edn(London : Taylor and Francis), (1990)

[Muxw00] A. R. Muxworthy and E. McClelland, Geophys. J. Int., 140, 101–114, (2000)

[Myam93] Y.Myamoto and M.Shindo, J.Phys.Soc.Jpn. 62, 1423 (1993)

[Naga71] Nagaev, E.L., Sov. Phys. Solid State, 13, 961-967, (1971)

[Nage85] S.Nagel, J. Phys. Chem. Solids 46 (1985), 905

[Naka97] Nakamura S.,Li L., Tanaka M., Todo S., Siratori K., J.Phys.Soc.Japan 66, 472 (1997)

[Namt71] M.I.Namtalishvili, O.P.Aleshko-Ozhevskii, I.I.Yamzin, FTT 13 (1971), 2543

[Noff85] J.Noffke, H.Gollish, Phys.Rev. B32 (1985), 7148

[Nova88] P.Novak, J.Englich, H.Lutgemeier, Phys. Rev. B37 (1988), 9712

[Nova95] P.Novak, J.Englich, H.Stepankova, J.Kohout, H.lutgemeier, K. Wagner, W.Tolksdorf, Phys. Rev. Lett. v.75, 3 (1995), 103

[Nova00] P.Novak, H.Stepankova, J.Englich, J.Kohout, and V.A.M.Brabers, Phys.Rev.B 61, 1256 (2000)

[NovaICF00] P.Novak, H.Stepankova, J.Englich, J.Kohout, V.A.M.Brabers, in Proceedings of 8th Int. Conf. on Ferrites, Japan, p.131 (2000).

[Okud89] T. Okuda, T. Katayama, K. Sato, T. Oikava, H. Yamamoto and N. Koshizuka, Proc. of the 5th Symposium on magnetizm and Magnetic Materials, 19-20 April, 1989

[Okud87M] T. Okuda, N. Koshizuka, K. Hayashi, H. Kobani, and H. Yamamoto. IEEE Trans. on Magn., V. MAG-23, #5, 3491-3493, 1987.

[Okud87] T. Okuda, N. Koshizuka, K. Hayashi, T. Takahashi, H. Kotani, and H. Yamamoto. J. Magn. Soc. Jpn. V.11, Supplement, #S1,179-182, 1987.

[Okud90] T. Okuda, T. Katayama, H. Kobayashi, and N. Kobayashi. J. Appl. Phys., V. 67, #9 part 2A, 4944-4946, 1990.

[Okud01] T. Okuda, Mater. Sci. Forum 373–376, 23 (2001)

[Otsu86] Otsuka N., Sato H., J.Solid State Chem. 61, 212 (1986)

[Ozde99] Ozdemir O., Dunlop D., EPSL 165, 229-239 (1999)

[Park97] J.H.Park, L.H.Tjeng, J.W.Allen, P.Metcalf, and C.T.Chen, Phys.Rev. B 55, 12813 (1997)

[Pear62] R.F.Pearson, J.Appl. Phys. 33 (1962), 1236

[Rado75] Rado G.T., Ferrari J.M., Phys. Rev.B 12, 5166 (1975)

[Rado77] Rado G.T., Ferrari J.M., Phys. Rev.B 15, 290 (1977)

[Robe60] C.Robert, Compt. Rend. Acad. Sci. 251 (1960), 2684

[Robe61] C. Robert, J.M. Winter, Comp. Rend. Acad. Sci. 253 (1961) 2925.

[Robe62] C.Robert, F.Hartmann-Bourtron, le Jour.de Phys. Et le Rad., 23 (1962), 574

[Rose85] M.Rosenberg, P.Deppe, H.U.Janssen, V.A.M.Brabers, F.S.Li, and S.Dey, J.Appl.Phys. 57, 3740 (1985)

[Rose96] G.K.Rosenberg, G.R.Hearne, M.P.Pasternak, P.A.Metcalf, and J.M.Honig, Phys. Rev. B 53, 6482 (1996)

[Safa71] A.P.Safantevskii, O.G.Minkina, Y.R.Shilnikov, Bull. Acad. Sci. USSR, Phys.Ser.35 (1975), 1097

[Sahu95] Sahu, S. & Moskowitz, B.M., Geophys. Res. L ett., 22, 449–452 (1995)

[Sama68] Samara G A, Phys. Rev. Lett. 21, 795 (1968)

[Sawa74] G.A.Sawatzky, van der F.Woude, Jour. De Physique Coll. C6, Suppl. 35 (1974), 47

[Seo02] H.Seo, M.Ogata and H.Fukuyama, Phys.Rev.B 65, 085107 (2002)

[Shan76] R.D. Shannon, Acta Cryst. A 32, 751, (1976)

[Sims79] Simsa Z, Phys. Status Solidi b 96 581, (1979b)

[Sira79] Siratori K., Kita E., Kaji G., Tasaki A., Kimura S., Shindo I., Kohn K., J.Phys.Soc.Japan 47, 1779 (1979)

[Sira98] Siratori K., Ishii Y., Morii Y., and others, J.Phys.Soc.Japan 67, 2818 (1998)

[Slic90] C.P.Slichter, Principles of magnetic resonance, Springer Verlag, Berlin Heidelberg (1990)

[Smar56] J.S.Smart, Phys.Rev. 101 (1956), 585

[Smit56] J.Smit, H.Wijn, Ferrites, Ney York, (1956)

[Step94] H.Stepankova, PhD thesis, MFF UK Praha (1994)

[Step98] H.Stepankova, J.Kohout, P.Novak, J.Englich, E. Caspary, H.Lutgemeier, Aust. J. Phys., 51 (1998), 437

[Step98] H. Stepankova, J. Kohout, P. Novak, J. Englich, H. Lutgemeier, M. Trhlik, J. Magn. Magn. Mater. 177–181 (1998) 239

[Step99] H. Stepankova, et al., J. Magn. Magn. Mater. 196–197 (1999) 412

[StepHT99] H.Stepankova, Habilitacni prace, Praha (1999)

[Step00] H.Stepankova, J.Kohout, J.Englich, P.Novak, Hyperfine Int. 131, 3-19 (2000).

[Step03] H. Štěpankova, T. Okuda, E. Gamaliy, A. Snezhko, N. Adachi, and T. Kaneuji, Phys. Stat. Sol. (a) 196, No. 1, 121–124 (2003)

[Step04] H. Stepankova, J. Englich, E. Gamaliy, M. Kucera, M. Marysko, K. Nitsch, P. Novak, JMMM, 272–276 (2004) e1685–e1686

[Subi04] Subias, G., et al., Phys. Rev. Lett. 93, 15, (2004)

[Syon65] Syono Y., Japan. J. Geophys., 4, 71–143, (1965).

[Teru79] Terukov E.I., Reichelt W., Ihle D. and Oppermann H. Phys. Status Solidi B 95, 491 (1979)

[Todo01] S.Todo, N.Takeshita, T.Kanehara, T.Mori, and N.Mori, J.Appl.Phys. 89, 7347 (2001)

[Todo95] Todo S., Siratori K. and Kimura S., J. Phys. Soc. Japan 64, 2118 (1995)

[Tora95] H. Toraya and T. Okuda, J. Phys. Chem. Solids 56, 1317 (1995).

[Turo69] E.A.Turov, M.P.Petrov, Nuclear magnetic resonance in ferro- and antiferromagnetic materials, Nauka, Moscow (1969)

[Verw39] E.J.Verwey, Nature (London) 144, 327 (1939).

[Vons46] Vonsovskii, S.V., J. Phys. 10, 468-475, (1946)

[Walz79] Walz F, Deusch H and Kronm¨uller H, Phys. Status Solidi 53, 519 (1979)

[Walz82] F.Walz et al., Phys. Status Solidi b 110, 471 (1982)

[Walz02] F.Walz, J.Phys.:Condens. Matter 14, R285-R340 (2002)

[Walz03] F.Walz et al., J. Phys.: Condens. Matter 15, 7029-7045 (2003)

[Wats67] R.E.Watson, A.J.Freeman, Hyperfine Interactions (ed. A.J.Freemen, R.B. Frankel), Academic Press, New York (1967)

[Wagn94] K.Wagner, PhD thesis, University of Koln, (1994)

[Wagn95] K.Wagner, H.Lutgemeier, W.Zinn, P.Novak, J.Englich, H.Dotsch, S.Sure, J Mag. Magn. Mat. 140-144 (1995), 2107

[Wagn96] K. Wagner, H. L.utgemeier, W. Zinn, R. Gerhardt, H.Dotsch, M. Kucera, J. Englich, K.Nitsch, P. Novak, J. Magn. Magn. Mater. 161 (1996) 57.

[Weis48] P.R.Weiss, Phys.Rev. 74 (1948), 1493

[Wink81] G.Winkler, Magnetic garnets, Braunchweig/Weisbaden, Vieweg (1981)

[Wojt64] P.J.Wojtovicz, Physics Lett., v.11 (1964), 18

[Woud71] van der F.Woud, G.A.Sawatzky, Phys. Rev. B4 (1971), 3159

[Wrig02] Wright et al., Phys.Rev.B66, 214422 (2002)

[Yama75] Yamada Y. AIP Conf. Proc. vol 24 p 79, (1975)

[Yana81] K.Yanai, M.Mizoguchi and S.Iida, J. Phys. Soc.Japan, 50, 65 (1981)

[Yana84] Yanase A. and Siratori K.J., Phys. Soc. Japan 53, 312 (1984)

[Ye94] Ye, J., Newell, A.J. & Merrill, R.T., Geophys. Res. L ett., 21, 25–28, (1994).

[Yosh77] Yoshida J. and Iida S., J.Phys.Soc.Japan 42, 230 (1977)

[Yosh79] Yoshida J. and Iida S., J.Phys.Soc.Japan 47, 1627 (1979)

[Zhan91] Z.Zhang and S.Satpathy. Phys.Rev.B 44, 24 (1991)

[Zuo90] J.M.Zuo, J.C.H.Spence and W.Petuskey, Phys.Rev.B 42, 845

Appendix

List of publications

1. E. Gamaliy, H. Stepankova, J. Kohout, A. Snezhko, M. Kucera, K. Nitsch, Effect of aluminium substitution in YIGon iron hyperfine field anisotropy, J. Magn. Magn. Mater., 242–245 (2002) 766–768
2. E.Gamaliy, A. Snezhko, H. Stepankova, M. Kucera, K. Nitsch, Nuclear magnetic relaxation in YIG films with nonmagnetic trivalent substitutions, J. Magn. Magn. Mater., 242–245 (2002) 769–771
3. E.Gamaliy, H.Stepankova, J.Englich, J.Kohout, A.Snezhko, P.Novak, V.A.M.Brabers, NMR of ^{57}Fe above the Verwey transition in Al-substituted magnetite, J. of Magn. Magn. Mat. 242-245, 732-734 (2002)
4. H. Štěpankova, T. Okuda, E. Gamaliy, A. Snezhko, N. Adachi, and T. Kaneuji, Nuclear magnetic resonance of ^{57}Fe in bismuth–yttrium iron garnets, Phys. Stat. Sol. (a) 196, No. 1, 121–124 (2003)
5. H. Stepankova, J. Englich, E. Gamaliy, M. Kucera, M. Marysko, K. Nitsch, P. Novak, NMR spectra and relaxations of 57Fe in calcium-doped yttrium iron garnet films, J. Magn. Magn. Mater., 272–276 (2004) e1685–e1686
6. J. Kohout, E. Gamaliy, H. Stepankova, J. Englich, P. Novak, V.A.M. Brabers, NMR of 57Fe below and around the Verwey transition in Al-substituted magnetite, J. Magn. Magn. Mater., 272–276 (2004) e1687–e1688
7. J. Kohout, E. Gamaliy, H. Stepankova, J. Englich, V. Prochazka, V. Chlan, V.A.M. Brabers, NMR of 57Fe, 69Ga and 71Ga in Ga substituted magnetite, J. Magn. Magn. Mater., 290–291 (2005) 1018–1020
8. V. Chlan, E. Gamaliy, H. Stepankova, K. Kouril, J. Englich, J. Kohout, V. Brabers, Nuclear magnetic resonance of ^{57}Fe in Al-, Ga- and Ti- substituted magnetite above the Verwey temperature, J. Magn. Magn. Mater., in print.

Acknowledgments

I would like to thank my supervisor Doc. RNDr Helena Štěpánková, CSc whose personal abilities, experience and energy led me during all my work. Working with her means a lot of satisfaction, feeling deep gratitude for her many-sided help and a lot of good memories.

I would also like to express my sincere gratitude to Prof. RNDr. Jiří Englich, DrSc., to Mgr. Jaroslav Kohout, Dr and to Ing. Alexey Snezhko, Ph.D. for their help I got especially much at my first steps in experimental physics, for useful consultations and permanent interest in my work. I am personally grateful to Jaroslav Kohout for his valuable help at working on anisotropy calculations.

I thank Ing. Pavel Novák, CSc for his important comments of theoretical problems.

I would also like to express my gratitude to Doc. Ing. František Bečvář, DrSc. and to Jitka Hankeová as well as to all colleagues from the Low Temperature Physics Department of Charles University for a creation of friendly and helping working atmosphere.

Finally, I would like to thank my family, especially my husband and parents for their support and understanding through all the years.